UNIVERSITÀ DEGLI STUDI DI PALERMO
PhD Course in Information and Communication Technologies
Engineering department
Scientific-disciplinary sector ICHI-01/C

MODELLING, SIMULATIONS, AND EXPERIMENTAL INVESTIGATION OF ION TRANSPORT IN ION-EXCHANGE MEMBRANES IN HIGH-SALINITY ENVIRONMENT

PhD Candidate:
GIORGIO PURPURA

Course Coordinator:
Prof. MARCO LA CASCIA

Supervisors:
Prof. ANDREA CIPOLLINA
Prof. ALESSANDRO TAMBURINI
Prof. GIORGIO MICALE

Co-supervisors:
Dr.-Ing. ANDREA CULCASI
Dr.-Ing. CHRISTIAN LINNARTZ
Prof. JOVAN KAMCEV

XXXVIII PhD CYCLE
GRADUATION YEAR 2026

“E il mio maestro mi insegnò com’è difficile
Trovare l’alba dentro l’imbrunire”

Ai miei amati genitori, Piero e Cristina

Ai miei Maestri, Giorgio, Andrea ed Alessandro

TABLE OF CONTENTS

Introduction

In recent decades, uncontrolled anthropogenic development has accelerated a range of detrimental social and environmental phenomena that pose existential threats to the survival of the human species. Chief among these is climate change, which affects populations worldwide. The pursuit of a distorted development model, driven by the unregulated exploitation of natural resources, including water, soil, flora, fauna, and even humans, is rapidly pushing mankind to the brink of collapse.

Science and technology, once seen as instruments for improving human life and fostering progress, are often subordinated to the same exploitative logic that threatens our future. A paradigm shift is more necessary than ever. The global scientific community has already issued a stark warning: to prevent severe and irreversible damage to the planet, it is essential to achieve net-zero carbon emissions as soon as possible.

This goal demands a radical rethinking of how goods and services are produced and distributed. Within this ongoing revolution, traditional chemical engineering processes, primarily based on thermal technologies, are increasingly being replaced by innovative systems that embrace circular principles and adopt more efficient and environmentally sustainable solutions. Among the most promising of these emerging solutions are electrochemical technologies, which are rapidly becoming essential across various sectors, from energy production and storage to the synthesis and recovery of chemicals. The main advantages of electrochemical processes over thermal ones are their inherently higher efficiency and their natural compatibility with renewable energy sources.

Broadly speaking, electrochemical technologies enable the interconversion between electrical and chemical energy and can be conceptually represented as assemblies of two electrodes separated by an electrolyte and connected by an external electronic circuit. Their operation relies on a complex interplay of heterogeneous electrochemical reactions and coupled mass and charge transport phenomena.

A significant subclass of electrochemical technologies is represented by electromembrane technologies, all of which feature a specific kind of solid-state electrolytes known as ion-exchange membranes (IEMs). These membranes act as barriers to mass and charge transport, enabling the selective passage of ions based on their charge. This property makes IEMs core components in a wide range of technologies, including electrolysers, fuel cells, flow batteries, membrane reactors, and electrodialysis-based systems. Since IEMs play a central role in determining the performance of these technologies, scientific interest in their properties has surged in recent decades (see Figure 1).

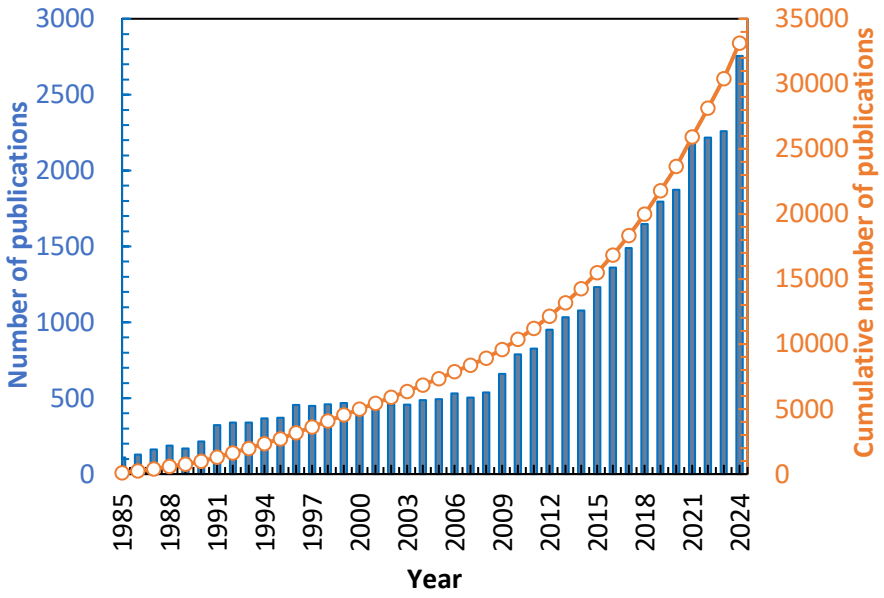

Figure 1 Number of IEM-related publications over the years. Data were collected from Web of Science using the following keywords: "ion exchange membrane", "electromembrane", "electrodialysis", "membrane electrolysis", "bipolar membrane", and "membrane capacitive deionization".

The performance of all technologies relying on IEMs is strongly influenced by the membranes' ability to either transport selectively or reject specific ionic species. For well-established technologies such as ElectroDialysis (ED), IEMs properties like ionic conductivity and permselectivity now represent a bottleneck to further improvement [1–3]. Conversely, emerging electromembrane processes, such as electrodialysis with bipolar membranes (EDBM), still suffer from high Specific Energy Consumption (SEC) and low Specific Productivity (SP), which currently hinder their industrial-scale deployment [4,5]. Consequently, the development of high-performance, next-generation IEMs has become imperative to simultaneously reduce the energy demand of electromembrane technologies and enhance their separation efficiency.

Achieving this goal requires a deep understanding of the fundamental physical laws governing mass and charge transport in these systems. However, despite considerable progress in this area, a substantial gap in fundamental knowledge persists, giving rise to ongoing debate within the scientific community. This gap becomes especially critical when attempting to describe mass and charge transport in IEMs exposed to highly concentrated, multi-ionic solutions, a scenario that has been relatively overlooked in favour of studies on membranes equilibrated with moderately concentrated, single-electrolyte systems.

The present work aims to advance IEMs modeling by conducting a fundamental investigation of ionic transport in IEMs, with a particular focus on highly concentrated systems.

A significant part of the work was devoted to the systematic study of the fundamental theories of thermodynamics and transport phenomena. Particular attention was also dedicated to uncovering and critically examining elements of the current state of the art that remain underexplored or insufficiently disseminated. Furthermore, an important objective was to integrate concepts from traditionally distinct disciplines, bridging fundamental physicochemical theory with more applied, engineering-oriented approaches.

Another fundamental part of the present thesis focused on the development of novel thermodynamic models for the prediction of equilibrium ion distribution in IEMs, and of theoretical and numerical frameworks for the computation of fundamental ionic transport properties from macroscale experimental data.

The models presented herein are framed within a mesoscopic scale, consistent with the continuum hypothesis typically adopted in chemical engineering. In this context, the term *mesoscale* is used to refer to an intermediate length scale between the *microscopic* domain, characterized by atomic and molecular dimensions and typically addressed by fundamental physical theories such as statistical thermodynamics and the kinetic theory of gases, and the *macroscopic* scale, which is commonly adopted in engineering disciplines for tasks such as the conceptual design of equipment and unit operations. The mesoscale considered here thus coincides with the scale inherent to classical thermodynamics, computational fluid dynamics, and transport phenomena. These frameworks serve as foundational theories that effectively bridge the gap between microscopic models, used to estimate mesoscale properties such as activity coefficients and diffusion coefficients based on ionic and molecular characteristics, and macroscopic applications.

Although theoretical modeling forms the core of the study, the modeling activities were rigorously supported by an extensive and carefully designed experimental campaign, which provided the data necessary for the development and validation of the theoretical models.

The structure of the thesis reflects the two main areas of investigation: thermodynamics and transport phenomena. These two aspects are intrinsically interconnected, and a comprehensive study of transport phenomena cannot be achieved without a solid thermodynamic foundation.

The thesis is therefore divided into 3 chapters; the first two, devoted to thermodynamics and transport phenomena in IEMs, are further divided into 3 main sections, focusing on theoretical modeling, experimental characterization and numerical simulations; the third chapter is devoted to the practical implementation of IEMs thermodynamic and transport models, and is divided into 2 main sections presenting real case-study of electromembrane processes implementation in the field of brines valorisation.

In detail, the thesis is structured as follows:

- **Section 1.1** introduces the fundamentals of IEMs thermodynamics and presents the ion-partitioning models developed.
- **Section 1.2** describes the experimental investigation of IEMs equilibrium properties.
- **Section 1.3** presents simulations and validation of the proposed thermodynamic models.
- **Section 2.1** focuses on the fundamentals of transport phenomena in IEMs and introduces the corresponding transport models.
- **Section 2.2** reports the experimental investigation of IEMs transport properties.
- **Section 2.3** presents simulations and validation of the proposed transport models.
- **Section 3.1** focuses on the multi-scale modelling of a specific electromembrane unit for lithium recovery
- **Section 3.2** present the modelling of an integrated process chain for the valorisation of salt bitterns (i.e. the waste solution produced in saltworks).

A graphical representation of the thesis outline is provided in Figure 2.

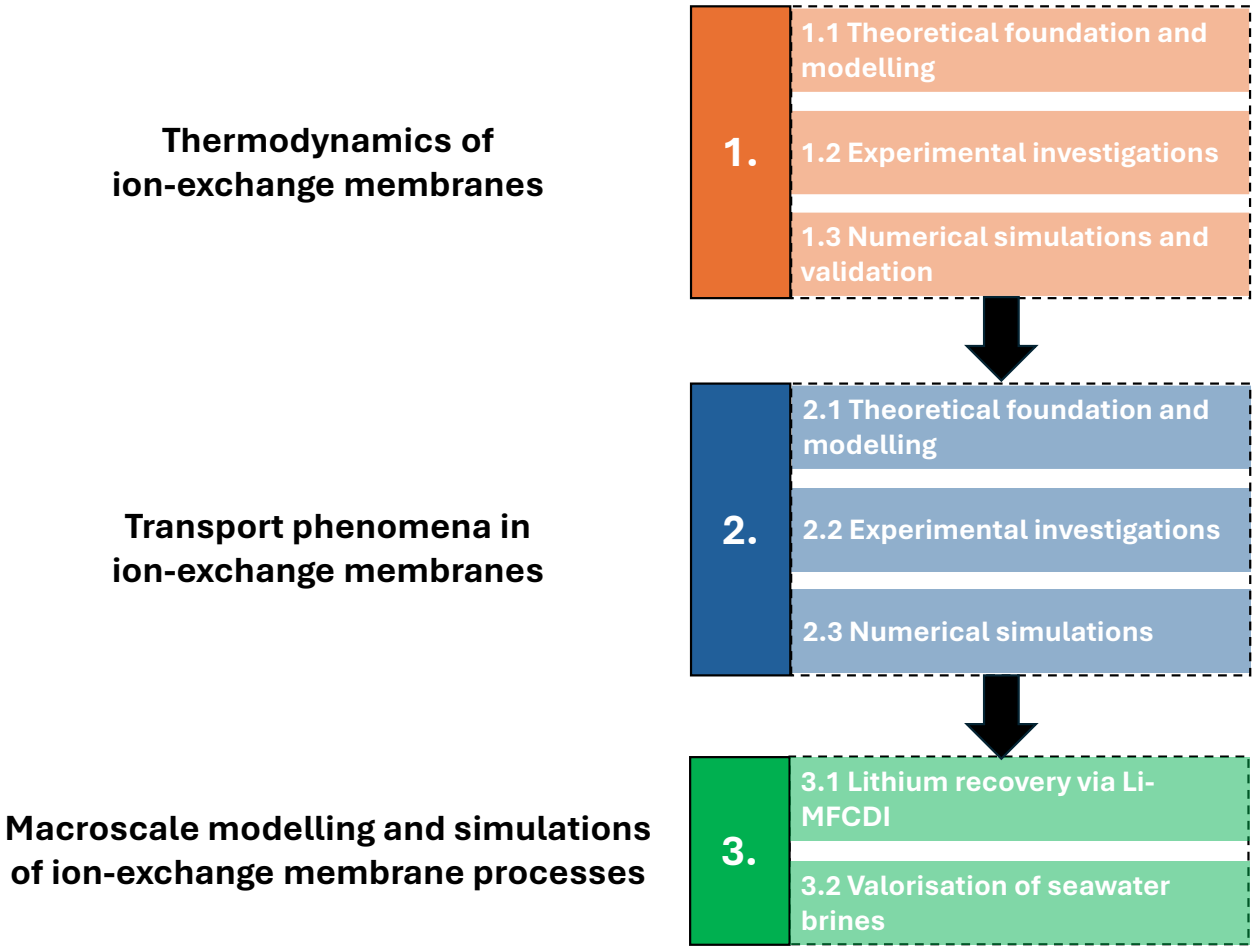

Figure 2 Graphical representation of the thesis outline.

1. Thermodynamics of ion-exchange membranes

The first chapter is devoted to the study of IEMs thermodynamic properties. The chapter is divided into 3 main sections focusing respectively on theoretical modelling, experimental investigation and numerical simulations of IEMs thermodynamics into highly concentrated systems

1.1 Thermodynamics of ion-exchange membranes: theoretical foundations and modelling

The present section focuses on the theoretical foundations and modelling of IEMs thermodynamics. It opens with a brief overview of the structure, synthesis, and applications of IEMs. Hereinafter, fundamental concepts of electrolyte thermodynamics are introduced. These serve as the basis for the thermodynamic modeling of IEMs and will be employed throughout the dissertation. The fourth section presents and critically examines the thermodynamic equilibrium equations relevant to ion transport in these systems. The final section focuses on thermodynamic models for the prediction of ion activity coefficients in IEMs. The state of the art of such models is critically reviewed, and novel modeling approaches are introduced and discussed.

1.1.1 IEMs synthesis and structure

IEMs are a broad class of selective membranes in which the transport of chemically charged species (i.e., ions) is either favoured or suppressed depending on their charge. Based on this fundamental property, IEMs can be broadly classified into Cation-Exchange Membranes (CEMs) or Anion-Exchange Membranes (AEMs), depending on whether they promote respectively the transport of cations or anions. Ions whose transport across the membrane is favoured are usually defined as counter-ions, whereas those whose transport is hindered are termed co-ions. This peculiar property is due to the presence of ionizable chemical groups, integral with the structure of the membrane, that are usually referred to as fixed charges. The selectivity of an IEM is strongly related to its fixed charge density, typically quantified in terms of Ion-Exchange Capacity (IEC), defined as moles of fixed charges per mass of dry membrane [6,7]. Depending on the nature of the fixed chemical groups, IEC can vary, for instance, with the pH of the external electrolyte. However, in this work, only IEMs with invariant IEC were studied.

IEMs are typically made of organic materials. Though inorganic IEMs, such as ceramic or composite IEMs, represent a considerable class of IEMs with various applications [8,9], polymeric IEMs are by far more prominent in terms of volume of production and industrial relevance. These membranes

consist of a polymeric backbone, generally made either of perfluorocarbon or hydrocarbon polymers, functionalized with ionizable groups. Typical functional groups in CEMs include sulfonic (-SO_3H), carboxylic (-COOH), and phosphonic (-PO_3H_2) groups, whereas AEMs are generally functionalized with binary, ternary, or quaternary ammonium groups (-NH_2R, -NHR_2-, NR_3) [6]. To ensure mechanical integrity, IEMs are often reinforced using a backing made of polymeric material as well, such as PE, PP, or PVC fibers [10]. The nature of the backbone and the functional groups determine, to a large extent, the mechanical and chemical properties of the IEMs. Another fundamental characteristic of the IEMs is the microstructure, which depends on the synthesis method. IEMs are conventionally defined as homogeneous when the ion-exchange groups are evenly distributed throughout the membrane structure, in contrast to heterogeneous membranes, consisting of ion-exchange particles incorporated into an inert polymeric matrix. This classification is more of a convention rather than a true description of the IEMs structure, given that, depending on the observation scale, a certain degree of heterogeneity can also be observed in homogeneous IEMs [11,12]. The synthesis method and hence the microstructure can heavily affect IEMs properties in terms of selectivity and ionic conductivity [13]. In the present work, only commercial macroscopically homogeneous IEMs are investigated. Homogeneous IEMs can be obtained through polymerization and polycondensation of suitable functionalized monomers. One of the most common synthesis method consists of a solution-casting step followed by controlled phase-inversion [14]. Synthesis protocols, however, can vary widely in terms of formulation, procedure, and processing conditions, and a comprehensive description of such methods lies beyond the scope of this work. Among the most critical parameters to control during synthesis is the degree of crosslinking, which is often essential to prevent excessive swelling due to water absorption in the membrane matrix. Crosslinking has a profound effect on the microstructure and, in turn, on membrane performance [15,16]. For instance, it is known that the absence of crosslinking in commercial membranes like Nafion can induce phase separation into macroscopic polar and non-polar domains [17]. From a modeling perspective, understanding IEMs morphology is essential for the development of models faithful to reality. Nonetheless, accurately determining the microstructure of such systems through experimental means remains a highly nontrivial task. Consequently, various schools of thought still coexist regarding the physical modeling of IEMs.

1.1.2 IEMs applications

IEMs are employed in a wide range of processes in the field of energy recovery, storage, and conversion, chemical recovery and synthesis, and effluent treatment. A brief and non-exhaustive

overview of the primary electromembrane technologies investigated in this study is presented below. Mathematical models and process simulations of these latter are reported in Chapter 3.

1.1.2.1 Electrodialysis (ED)

ED is the most mature electromembrane technology, being the very first electromembrane process to be implemented on a large industrial scale. The first electrodialysis plants were built between the late 1950s and the early 1960s to perform brackish water desalination. An electrodialysis cell consists of a series of anion- and cation-exchange membranes, arranged in alternating patterns, and divided by spacers that allow electrolytic solutions to flow between them. Each repetitive unit, called cell pair, is then composed of a CEM, a concentrate channel, an AEM, and a dilute channel. The cell pairs are then assembled to form a stack, which can be composed of a few to hundreds of cell pairs, at whose ends are placed two plane electrodes used to apply the electrical potential necessary to deionize the concentrate solution. A schematic representation of an ED unit is reported in Figure 3

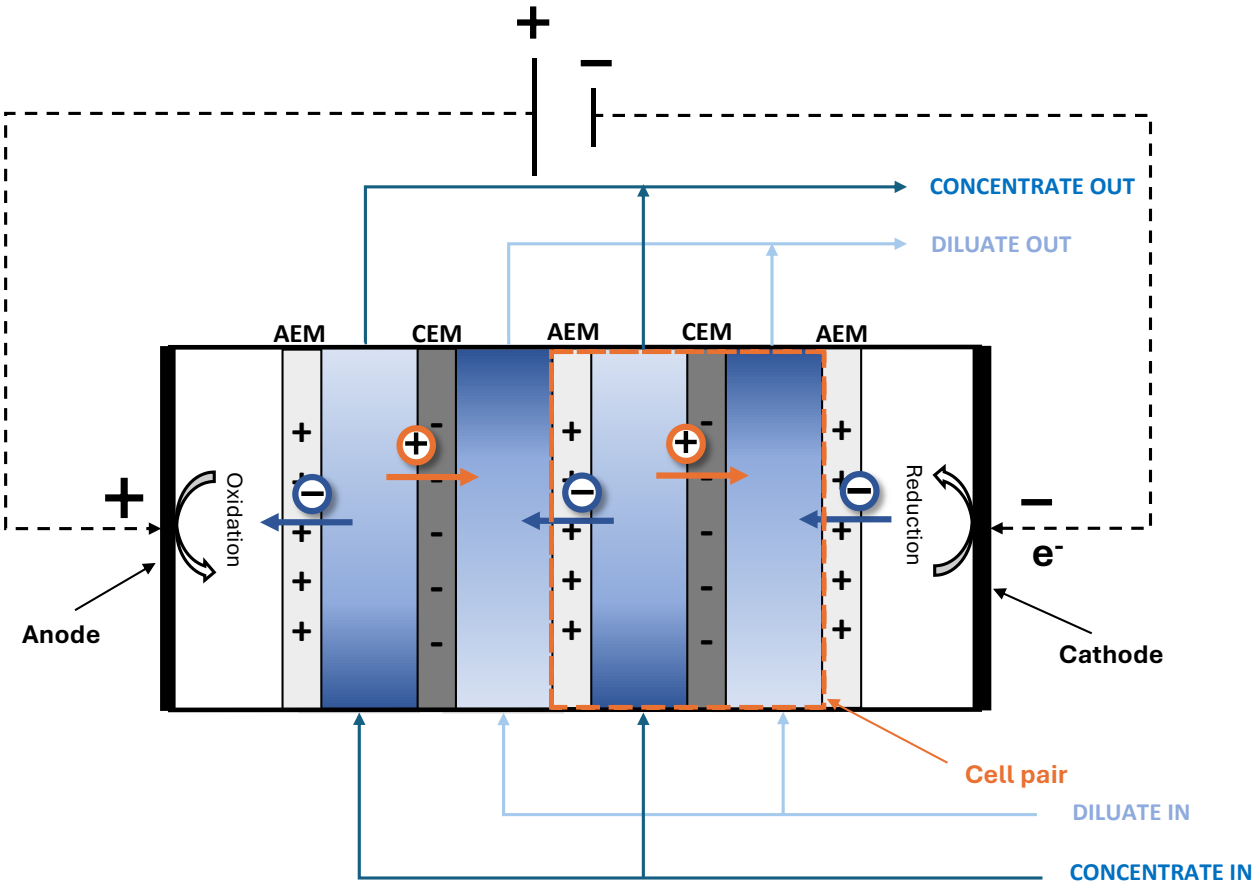

Figure 3 Schematic of an ED unit

When an electrolytic solution is pumped inside the channels, thanks to the applied electric field, the positively charged ions will move towards the cathode across the CEM, while the negatively charged

ions will move towards the anode through the AEM, causing the depletion of ions in the dilute channels. Nowadays, electrodialysis finds several applications in the field of:

- Large-scale seawater and brackish water desalination
- Waste-water treatment
- Food industry

1.1.2.2 Reverse Electrodialysis (RED)

RED is an electromembrane technology formally analogous to ED in structure and functioning principles. However, differently from ED which requires the employment of a power supply, RED is meant to produce electrical energy from the controlled mixing of a dilute and concentrated saline solution, and can be therefore used to power an external load. Thanks to the permselectivity of the IEMs, the concentration difference across two adjacent compartments is transformed into an electromotive force that induces the conductive transport of ions from the concentrated compartment into the dilute one. In other words, RED exploits the salinity gradient between two solutions at different salt concentrations to generate an electrical current that can be used to power an external load [18,19]. Therefore, RED is typically employed to recover energy from waste brine, such as reverse osmosis brines, whenever a dilute saline stream is available.

1.1.2.3 Electrodialysis with Bipolar Membranes (EDBM)

Similarly to RED, Electrodialysis with Bipolar Membranes (EDBM) is an electromembrane technology belonging to the broader class of electrodialysis processes. EDBM is named after the use of a particular type of ion-exchange membrane known as a BiPolar Membrane (BPM), which consists of an Anion-Exchange Layer (AEL) and a Cation-Exchange Layer (CEL), separated by a catalyst layer. When subjected to an electric field, the catalyst promotes the dissociation of water molecules into protons (H^+) and hydroxide ions (OH^-). This feature enables EDBM to be employed in targeted applications such as chemical synthesis and energy recovery from pH gradients [5,20]. A typical EDBM stack is composed of multiple repeating units, called triplets, placed between two flat electrodes. Each triplet includes an AEM, a CEM, and a BPM, separated by spacers that define inter-membrane channels for solution flow. This configuration creates three distinct flow compartments within each triplet: a salt channel, an acid channel, and a base channel. Upon applying an electric potential difference across the stack, the ionic species in the salt solution are forced to migrate in opposite directions towards the electrodes through the membranes, causing a reduction of salt concentration in the salt channel. Simultaneously, within the bipolar membrane, water dissociation occurs, and the generated H^+ ions and OH^- ions migrate through the CEL and AEL, respectively,

increasing their concentration in the acid and base channels. A schematic representation of an EDBM unit is showed in Figure 4.

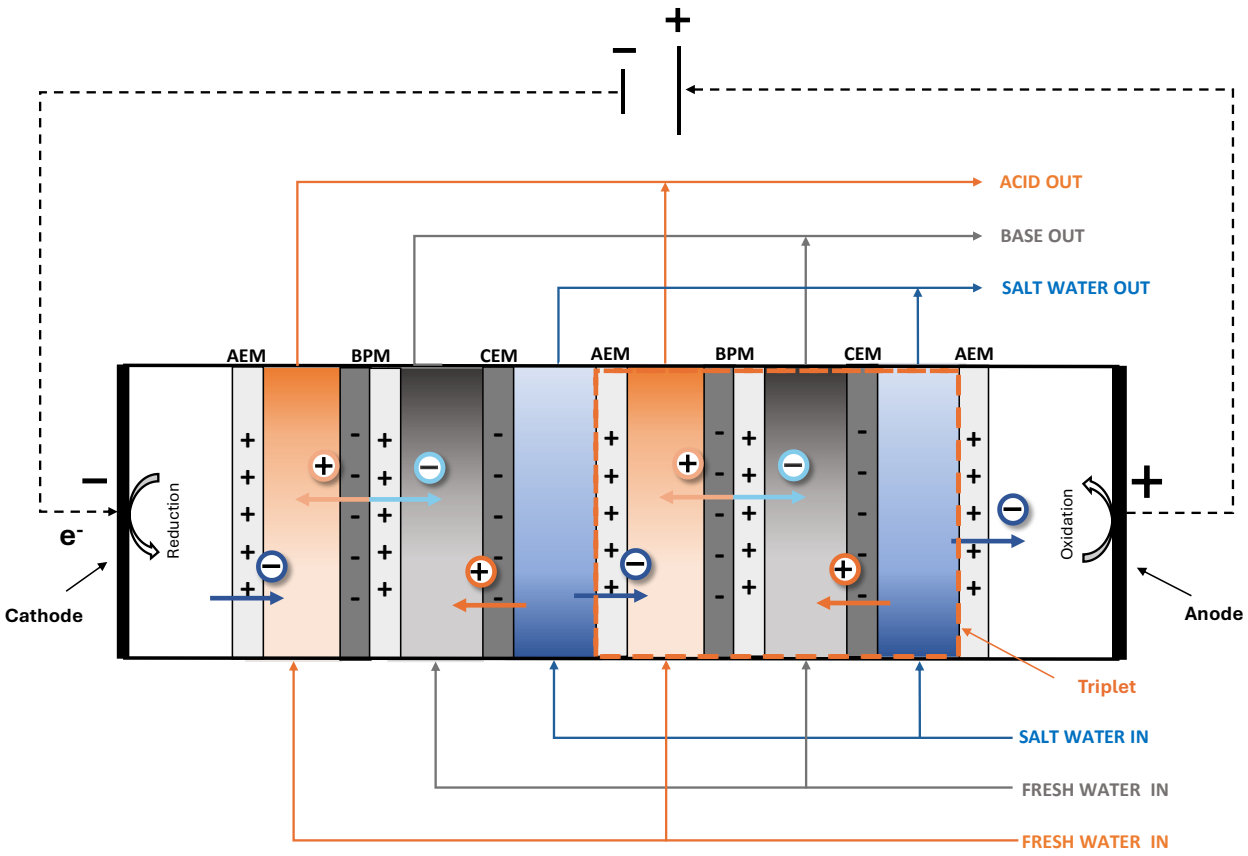

Figure 4 Schematic of an EDBM unit

Analogously for conventional ED, the mechanism of EDBM can be reversed to obtain the so-called REDBM process, which exploits the pH gradient between an acid and an alkaline solution to generate an electrical current. Along with its reversal process, EDBM technology also finds application in the field of flow batteries for the conversion and storage of renewable energies [21].

1.1.3 Fundamentals of electrolyte thermodynamics

Before asking ourselves how a physical system evolves from one state to another, we must know why such a system should evolve. For such a reason, trying to approach transport phenomena without a solid understanding of the thermodynamics of a system will inexorably lead to failure.

Thermodynamics is the part of physics concerned with the study of the energetics of physical systems and of their equilibrium state, i.e., the state toward which any system, let free to evolve, tends. By system, we mean any portion of the universe containing matter, composed of one or more phases, any of which can be defined and characterized by some variables of state (e.g., temperature, pressure, composition). The astounding beauty of thermodynamics lies in its capabilities of describing the

results of physical transformation with a limited understanding of the underlying phenomena. To do that, the entire building of thermodynamics is based on conveniently defined functions, called functions of state, whose variation only depends on the initial and final values of the variables of state. The major outcome of thermodynamics is the definition of fundamental functions of state called Helmholtz free energy and Gibbs free enthalpy, adopted to quantify how much a system is close or far from its equilibrium state. Given a specific homogeneous phase, the free energy (or enthalpy) generally depends on temperature, pressure, and composition of the phase, but more generally it may depend on various variables accounting for other energy contributions (e.g., gravitational, electrostatic, interfacial) [22,23].

1.1.3.1 Chemical and electrochemical potential

For a bulk, electroneutral system, composed of N species, the differential of the Gibbs free enthalpy is defined as follows:

$$dG = VdP - SdT + \sum_{i=1}^{N} \left(\frac{\partial G}{\partial n_i}\right)\Big|_{T,P,n_j \neq n_i} dn_i \tag{1.1}$$

where V and S are the volume and the entropy of the system, P and T are the pressure and the temperature, while n_i is the number of moles of the species *i*. Equivalently, the Helmholtz free energy F can be defined as:

$$dF = -PdV - SdT + \sum_{i=1}^{N} \left(\frac{\partial F}{\partial n_i}\right)\Big|_{T,V,n_j \neq n_i} dn_i \tag{1.2}$$

G and F are generally used to formulate the equilibrium condition of a system respectively at constant T and P or T and V. However, as it will be discussed in section 1.1.4.1, mass transfer equilibrium between two phases at different pressure is typically and conveniently expressed in terms of F.

The partial derivatives appearing in the last term of equations (1.1) and (1.2) correspond to the chemical potentials of the system's component, defined as:

$$\mu_i = \left(\frac{\partial G}{\partial n_i}\right)\Big|_{T,P,n_j \neq n_i} = \left(\frac{\partial F}{\partial n_i}\right)\Big|_{T,V,n_j \neq n_i} \tag{1.3}$$

The chemical potential plays a central role in thermodynamics, as it represents the reversible work required to transfer a given species from one point to another [24]. Importantly, the derivative in

equation (1.3) is taken at constant temperature, pressure, and fixed amounts of all other components, a condition that is crucial when dealing with charged species, as will be discussed in section 1.1.3.7. When the component i is charged, the corresponding work also depends on the electrical state of the phase. Consequently, in ionic systems, the result of equation (1.3) is usually defined as electrochemical potential $\tilde{\mu}_i$, to stress its dependence on the electrical state of the system. Accordingly, in a system where pressure, temperature, and composition are uniform, the reversible work of transfer one mole of the species *i* between two points under the influence of an electric field is given by:

$$w_{el} = \tilde{\mu}_i^{\alpha} - \tilde{\mu}_i^{\beta} = z_i \mathcal{F}\left(\varphi^{\alpha} - \varphi^{\beta}\right) \tag{1.4}$$

Where $\mathcal{F}$ is the Faraday constant, z_i is the valence of the i-th species, and φ is the electrostatic potential of the phase.

1.1.3.2 Conventional electrochemical potential and ionic activity coefficients

The electrochemical potential $\tilde{\mu}_i$ of a charged species, as defined by equation (1.3), is in general a function of temperature, pressure, composition, and electrical state of the phase. Following the conventional expression originally derived for perfect gases, the dependance of $\tilde{\mu}_i$ from the state variables is commonly expressed as follows:

$$\tilde{\mu}_i = \mu_i^{chem} + z_i \mathcal{F} \varphi = \mu_i^{*} + R_g T ln a_i + z_i \mathcal{F} \varphi \tag{1.5}$$

where μ_i^{chem} is the chemical part of the electrochemical potential, μ_i^{*} is the reference state chemical potential of the component (also called secondary reference state), which is a function of T and P, R_g is the universal gas constant, while a_i is the activity of the component. In the latter equation, φ is conventionally called "electrostatic potential". Clearly, if the net charge of a component is zero, $z_i = 0$ and hence $\tilde{\mu}_i = \mu_i^{chem}$. The underlying assumption in equation (1.5) is that the electrochemical potential of a charged species can be split into a chemical contribution, μ_i^{chem}, and an electrical contribution, described by the variable φ. This assumption usually simplifies the modelling of ionic transport, as it enables the explicit definition of an electrical variable amenable to analytical treatment. However, how it will be discussed in section 1.1.3.7, this assumption is both arbitrary and unnecessary when working with non-infinitely dilute systems. On the other hand, the $R_g T ln a_i$ term is used to account for the concentration dependence of the electrochemical potential in non-ideal systems. Therefore, a_i is usually defined as follows [25]:

$$a_i = \frac{\gamma_i C_i}{C_i^*} \tag{1.6}$$

where C_i is the molar concentration of the component, C_i^* is the molar concentration of the same component in the chosen ideal reference state[1], while γ_i is the molar-based activity coefficient of the component[2]. The activity coefficient accounts for the deviation from the ideal condition and it is thermodynamically defined as follows:

$$ln\gamma_i = \frac{1}{R_g T}\left(\frac{\partial G^{ex}}{\partial n_i}\right)\Big|_{T,P,n_j \neq n_i} = \frac{1}{R_g T}\frac{\partial\left(G - G^{id}\right)}{\partial n_i}\Big|_{T,P,n_j \neq n_i} \tag{1.7}$$

where G^{ex} is the excess free enthalpy of the system, while G^{id} is the free enthalpy in the arbitrary, hypothetical ideal state. Noticeably, according to equation (1.7), in the ideal state the activity coefficients are unitary. Hence, defining a secondary reference state corresponds to choose the state at which the activity coefficients are defined to be one [26]. Therefore, the proper definition of the chemical potential always requires the definition of the ideal state as follows [24]:

$$\begin{cases} \mu_i^{chem} = \mu_i^* + R_g T ln\gamma_i C_i \\ C_i \to C_i^* \Rightarrow \gamma_i = 1 \end{cases} \tag{1.8}$$

The previous definition is actually strictly valid in a binary solution, given that the activity coefficient of a given solute can be influenced by the presence of a second solute [25]. Conventionally, in a multi-ionic aqueous solution, two opposite secondary reference states can be adopted: the unsymmetric and the symmetric reference state [27,28]. In the unsymmetric reference state, the activity coefficients are set to one in the limit of all the solutes' concentration tending to zero, or equivalently, when the concentration of the solvent tends to its value in the pure state[3]:

[1] The reference concentration C_i^* depends on the chosen ideal reference state. Since it is constant, for the sake of brevity it is often omitted in the expression of the activity a_i and included in the reference chemical potential μ_i^*

[2] As discussed in 1.1.3.9, activities and activity coefficients can be based on several concentration scales and proper conversion formulas must be employed to pass from a scale to another.

[3] The difficulty of employing a molar scale as the concentration variable becomes evident from the need to define such a hypothetical standard state when developing predictive thermodynamic models. As will be discussed in Section 1.1.3.9, a rigorous approach should be based on the use of mole fractions, which allow for the unambiguous definition of a pure fused electrolyte state.

$$\begin{cases} \mu_i^{chem} = \mu_i^* + R_g T ln\gamma_i C_i \\ C_w \rightarrow C_{w,pure} \Rightarrow \gamma_i = 1 \end{cases} \quad (1.9)$$

where C_w is the solvent (i.e., water) concentration. Conversely, in the symmetric reference state, the activity coefficients of the solutes are set to be 1 in the hypothetical pure fused electrolyte state [27]:

$$\begin{cases} \mu_i^{chem} = \mu_i^* + R_g T ln\gamma_i C_i \\ C_i \rightarrow C_{i,pure} \Rightarrow \gamma_i = 1 \end{cases} \quad (1.10)$$

This latter state is clearly hypothetical and not physically achievable due to the limited solubility of the electrolytes. Nonetheless, this convention is of more general applicability. For instance, it is useful for the development of thermodynamic models for the prediction of excess thermodynamic functions in the presence of mixed solvents.

1.1.3.3 Dependence of electrochemical potential on pressure

When defining the electrochemical potential $\tilde{\mu}_i$, it was stated that it is a function of temperature, pressure, composition, and electrical state. While the dependence on these latter was explicated in equation (1.5), the dependence on T and P was left implicit. In the analysis of transport phenomena, isothermal systems are commonly considered, while isobaric conditions are addressed less frequently. As a result, it is sometimes necessary to explicitly express the dependence of the electrochemical potential on pressure. According to the definition of $\tilde{\mu}_i$ (eq. (1.3)), the following equation can be derived[4]:

$$\left(\frac{\partial \tilde{\mu}_i}{\partial P}\right)\Big|_{T,n_i} = \left(\frac{\partial \mu_i^*}{\partial P}\right)\Big|_{T,n_i} = \upsilon_i \quad (1.11)$$

where υ_i is the partial molar volume of the generic component. For condensed phases, υ_i do not typically change considerably with P. Therefore, by integrating equation (1.11), the following equation can be obtained:

[4] The implicit assumption in equation (1.11) is that $a_i \neq f(P)$, which is not strictly true given that the activity coefficients may show a certain dependence on the pressure [24,31]. However, such dependence is usually negligible in condensed system.

$$\mu_i^* \approx \mu_i^0 + \upsilon_i(P - P^0) \tag{1.12}$$

where μ_i^0 is the primary reference state chemical potential at the reference pressure and temperature P^0 and T^0. Equation (1.12) can then be substituted in equation (1.5) to get a formulation of $\tilde{\mu}_i$ applicable to non-isobaric systems:

$$\tilde{\mu}_i = \mu_i^0 + R_g T ln a_i + z_i \mathcal{F} \varphi + \upsilon_i(P - P^0) \tag{1.13}$$

1.1.3.4 Osmotic coefficient and osmotic pressure

In general, activity coefficients can be defined for all the components of a system. However, for solutions with non-volatile solvents such as water, it is more common and useful[5] to describe the deviation from the ideal behaviour of the solvent by defining a different coefficient, called osmotic coefficient[6], as follows:

$$\phi = \frac{\mu_w^0 - \mu_w}{R_g T \upsilon_w \sum_i C_i} \tag{1.14}$$

From the previous definition, it follows that the solvent chemical potential can also be expressed as:

$$\mu_w = \mu_w^0 - \phi R_g T \upsilon_w \sum_{i \neq w} C_i \tag{1.15}$$

Another fundamental thermodynamic function related to the solvent chemical potential is the osmotic pressure, which is defined as follows[7]:

$$\Pi = \frac{1}{\upsilon_w}(\mu_w^0 - \mu_w) = -\frac{R_g T}{\upsilon_w} ln a_w \tag{1.16}$$

By combining equation (1.15) and (1.16), the traditional definition of osmotic pressure can be obtained:

[5] For moderately concentrated solution of non-volatile solvents, the activity coefficient of the solvent often does not deviate consistently from one. Therefore, its variation is, much more appreciable in a logarithmic than in a linear scale

[6] An analogous definition can be provided for the osmotic coefficient in the molal scale [25]. The two of them are different and proper conversion equation can be obtained according to the procedure reported in Section 1.1.3.9

[7] This latter and most common definition is based on the assumption that υ_s is independent from P.

$$\Pi = \phi RT \sum_i C_i \tag{1.17}$$

1.1.3.5 The Gibbs–Duhem equation

A fundamental property of the electrochemical potential is that it corresponds to the partial molar variable of the free enthalpy G. Therefore, by Euler's first theorem for homogeneous functions, G can be equivalently defined as follows:

$$G = \sum_i n_i \tilde{\mu}_i \tag{1.18}$$

A similar equation can be written for all the other extensive thermodynamic variables like volume [22]:

$$V = \sum_i n_i v_i \tag{1.19}$$

From a mathematical standpoint, this corresponds to state that G and V are Euler homogeneous functions of order 1 with respect to the electrochemical potentials and to the partial molar volumes [29]. Differentiation of equation (1.18) leads to:

$$dG = \sum_i n_i d\tilde{\mu}_i + \sum_i \tilde{\mu}_i dn_i \tag{1.20}$$

If we now substitute equation (1.20) into equation (1.1) we obtain:

$$SdT - VdP + \sum_i n_i d\tilde{\mu}_i = 0 \tag{1.21}$$

which is a form of the well-known Gibbs-Duhem equation valid for bulk, electroneutral systems. Equation (1.21) constitutes a constraint between the thermodynamic variables T, P and $\tilde{\mu}_i$ that reduces the thermodynamic degrees of freedom of the system. For an isothermal transformation, equation (1.21) can be rewritten as follows:

$$\sum_i C_i d\tilde{\mu}_i = dP \tag{1.22}$$

Where the left and right side of the equation have been divided by the total volume V. The isothermal Gibbs-Duhem equation (1.22) can be used to relate the variation of the electrochemical potential of the components to the variation of pressure in non-isobaric systems. In an isothermal, isobaric system, the previous equation can be further simplified as follows:

$$\sum_i C_i d\tilde{\mu}_i = 0 \tag{1.23}$$

According to equation (1.23), in an isothermal, isobaric system, the number of independent electrochemical potentials is $N-1$, where N is the number of components of the system. Therefore, equation (1.23) is commonly employed to express the variation of the solvent chemical potential as a function of the electrochemical potential of all the other components:

$$C_w d\mu_w = -\sum_{i \neq w} C_i d\tilde{\mu}_i \tag{1.24}$$

For an electroneutral system, the previous equation is equivalent to:

$$C_w dlna_w = -\sum_{i \neq w} C_i dlna_i \tag{1.25}$$

When properly integrated, the previous equation can be used to evaluate the activity of the solvent when the activity of all the other components is determined. If we further substitute the definition of osmotic pressure (eq. (1.16)) in the previous equation, the following alternative formulation for the osmotic pressure can be obtained:

$$d\Pi = \frac{R_g T}{C_w \upsilon_w} \sum_{i \neq w} C_i dlna_i \tag{1.26}$$

1.1.3.6 Chemical potential of neutral electrolytes and mean ionic activity coefficient

So far, ionic species have been treated as independent thermodynamic components, and for each of them, a thermodynamic variable, the electrochemical potential, has been introduced. Indeed, ions

derive from the total (or partial) dissociation of neutral electrolytes according to the following stoichiometric relation:

$$M_{\nu_i}N_{\nu_j} \rightleftharpoons \nu_i M^{z_i} + \nu_j N^{z_j} \tag{1.27}$$

where M and N are two generic ionic species, ν_i and ν_j are the stoichiometric coefficients of ions i and j. Since the electrolyte is electrically neutral, ν_i and ν_j are subjected to the following restriction, usually called Guggenheim's equation:

$$z_i\nu_i + z_j\nu_j = 0 \tag{1.28}$$

At equilibrium conditions, the following equilibrium equation must be satisfied between the ions and the electrolyte:

$$\mu_{ij} = \nu_i\tilde{\mu}_i + \nu_j\tilde{\mu}_j \tag{1.29}$$

The former equation can be used to relate the chemical potential of the neutral electrolyte, μ_{ij}, to the electrochemical potentials of the ions formally derived from its dissociation[8] [24,30]. Being a neutral component, μ_{ij} does not depend on the electrical state of the phase. Indeed, if equation (1.5) is substituted in the former equation, the dependence on the electrical potential of the phase vanishes due to the requirement of the Guggenheim's relation (eq. (1.28)):

$$\mu_{ij} = \left(\nu_i\mu_i^* + \nu_j\mu_j^*\right) + R_gTln\left(C_i^{\nu_i}C_j^{\nu_j}\right) + RR_gTln\left(\gamma_i^{\nu_i}\gamma_j^{\nu_j}\right) \tag{1.30}$$

The first term on the right side of eq. (1.30) correspond to the reference state chemical potential of the neutral electrolyte μ_{ij}^*. By defining $\nu = \nu_i + \nu_j$, the former equation can be manipulated to get:

$$\mu_{ij} = \mu_{ij}^* + \nu R_gTln\left(\bar{C}_{ij}\bar{\gamma}_{ij}\right) \tag{1.31}$$

Where $\bar{C}_{ij}$ and $\bar{\gamma}_{ij}$ are respectively the mean ionic concentration and the mean ionic activity coefficient, defined as follows:

[8] Equation (1.27) is derived imposing the dissociation equilibria of the electrolyte. Therefore equation (1.29) tell us that that linear combination of electrochemical potential has a specific physical meaning: it represents the chemical potential of the virtually undissociated part of the electrolyte.

$$\bar{C}_{ij} = \left(C_i^{\nu_i} C_j^{\nu_j}\right)^{\frac{1}{\nu}} \tag{1.32}$$

$$\bar{\gamma}_{ij} = \left(\gamma_i^{\nu_i} \gamma_j^{\nu_j}\right)^{\frac{1}{\nu}} \tag{1.33}$$

The mean ionic activity coefficient $\bar{\gamma}_{ij}$ has a fundamental importance in the thermodynamics of electrolytes. In fact, as it will be discussed in section 1.1.3.7, only neutral combinations of thermodynamic properties can be experimentally determined.

1.1.3.7 Reformulation of traditional electrochemical potential: the quasi-electrostatic potential

The thermodynamic framework presented thus far is formally valid in the case of electrically neutral systems. A thermodynamic phase is said to be electroneutral if the local electrical charge density ρ_e can be assumed to be null everywhere, hence:

$$\rho_{el} = \mathcal{F} \sum_{i=1}^{N} z_i C_i \approx 0 \tag{1.34}$$

where C_i is the molar concentration of the i-th species. This assumption is justified by the huge amount of energy required to charge a macroscopic system[9]: according to Guggenheim, the electric potential required to provide a charge density of around $2 \cdot 10^{-5}$ $C\ m^{-3}$ to a spherical, electrically insulated system barely corresponds to 10^5 V [31]. In other words, according to equation (1.34), the degrees of freedom of an electroneutral system are reduced by one, i.e., it is not possible to arbitrarily vary the concentration of one charged component while keeping all the other constant. The direct consequence of this requirement is that, from a mathematical standpoint, the definition of the electrochemical potential of an ion is not operational [22]. As stated in section 1.1.3.1, the evaluation of the electrochemical potential of a generic component requires taking the partial derivative of G, as shown in equation (1.3), while keeping temperature, pressure, and the number of moles of all other components constant. However, this condition conflicts with the electroneutrality requirement. The direct consequence of this fact is that ions are not thermodynamic *components* of the system but merely *constituents*, in the sense that their concentration cannot be varied arbitrarily. In other words,

[9] Depending on the observation scale, this condition may not be formally true. For instance, at the interface between an electrode and an electrolytic solution, a charge separation occurs in a region of space whose extension depends on the Debye length of the solution [30,32]

the electrochemical potential of an ion is, strictly speaking, theoretically ill-defined [32]. Afar from being a pure mathematical question, this fact stems from an unavoidable physical limitation: it is not possible to experimentally determine, and hence to measure, the variation of the electrochemical potential of a charged species. Indeed, according to equation (1.4), the only measurement that can be made (direct or indirect) is the electric potential difference between two points of a phase of homogeneous composition. Whenever the composition of the system is not uniform, or in general, the chemical environment changes, the difference in the electrochemical potential can still be related to the reversible work of transfer, but this cannot be related to an electric potential difference anymore. In other words, it is not possible to separate the effect of the "chemical" interactions from the "electrical" ones. This stems from the fact that ions, which deviate significantly from the idealized concept of point charges, engage in "chemical" interactions with their surrounding medium. As stated by Guggenheim, "the electrostatic potential difference between two points is admittedly defined in electrostatics, the mathematical theory of an imaginary fluid called electricity". The ultimate consequence of this is that any decomposition of the electrochemical potential into a concentration-dependent part and an electrostatic-dependent one is arbitrary and lacks a physical basis. Therefore, the former and traditional formulation of $\tilde{\mu}_i$ (eq. (1.5)), based on the decoupling of a concentration-dependent term and an electrical-dependent term, is arbitrary and not physically grounded. Given that ion electrochemical potential variation is not experimentally accessible, the same holds for the single ion activity coefficient, formally defined through equation (1.7). The only experimentally accessible properties are those of neutral combinations of ions, such as the mean ionic activity coefficient.

Traditionally, whenever it is useful to define the activity coefficient of charged species, an arbitrary convention is adopted to virtually reduce the mathematical degree of freedom of the system[10]. This fact led Guggenheim to formulate an alternative expression for the electrochemical potential [31]:

$$\tilde{\mu}_i = R_g T ln\lambda_i = R_g T ln(\lambda_i^* \tilde{\gamma}_i C_i) \tag{1.35}$$

Where λ_i is called absolute activity. The difference between the former formulation and equation (1.5) is that while γ_i is improperly assumed to be independent of the electrical state of the phase, $\tilde{\gamma}_i$ is not. By arbitrarily setting λ_i for a certain species to a reference value, all the other absolute activities could be subsequently determined. However, the inconvenience of equation (1.35) compared to equation (1.5) is that no electrical variable is explicitly defined. This may represent a limitation in the description of electrodiffusion. As it will be discussed in section 2.1, traditionally,

1. [10] The most famous of such conventions are the MacInnes convention and the Debye-Hückel convention [22,213], which respectively assume $\gamma_{K^+} = \gamma_{Cl^-} = \gamma_{KCl}$ or $\sum_i \frac{C_i}{z_i} ln\gamma_i = 0$.

the driving force for the ionic current density is expressed in terms of the gradient of an electrical potential. An elegant way to solve the issue was found by Smyrl and Newman with the formulation of the so-called quasi-electrostatic potential [26,33]:

$$\tilde{\mu}_n = R_g T ln C_n + z_n \mathcal{F} \varphi \tag{1.36}$$

Where n identifies a generic species for which the activity coefficient is set to be 1 [34]. In doing so, the electric variable φ is now unambiguously related to the electrochemical potential of a reference species. Indeed, equation (1.36) is thermodynamically consistent: when it is applied to evaluate the electrical work required to move one mole of the species n from a phase α to a phase β of identical composition, it reduces to equation (1.4). Therefore, the quasi-electrostatic potential defined through equation (1.36) can effectively be used to track the electric state of a phase relative to a second phase of equal composition. The term "quasi-electrostatic" arises from the fact that, in the limit of infinitely dilute solutions, any neutral combination of ionic activity coefficients becomes equal to one[11]. Hence, in this limiting condition, equation (1.36) would correspond to equation (1.5) and φ would correspond to the traditional potential defined in electrostatics. Having unambiguously defined the variable φ, the electrochemical potential of any other ionic species can be expressed as:

$$\tilde{\mu}_i = \mu^*_{i(n)} + R_g T ln\left(\gamma_{i(n)} C_i\right) + z_i \mathcal{F} \varphi \tag{1.37}$$

Where the subscript (n) is used to stress the fact that $\gamma_{i(n)}$ correspond to the activity coefficient of the species i when the quasi-electrostatic potential is expressed in relation to the electrochemical potential of the species (n). The arbitrariness of such a definition is apparent from the need to choose a particular reference species. As it will be discussed in section 2.1, this fact will have important consequences in the evaluation of ionic transport properties in concentrated systems.

1.1.3.8 Relation between Newman's and conventional mean ionic activity coefficient

By arbitrarily defining φ according to equation (1.36), we have also univocally identified the activity coefficients of all ionic species, given that the same coefficient has been set to 1 for the reference species (n). As stated in the previous sections, the only measurable properties are those related to neutral combinations of ionic species, such as the mean ionic activity coefficient (see section 1.1.3.6). At this stage, it is essential to examine the relationship between the ionic activity coefficient as defined within quasi-electrostatic theory and the mean ionic activity coefficient, typically measured

[11] This is strictly true if the unsymmetrical convention based on the state of infinite dilution is taken as the secondary reference state for all the ionic solutes.

and reported in the literature for aqueous electrolytes. To address this question, it is important to emphasize that any formally electroneutral linear combination of electrochemical potentials is independent of the electrical state of the phase, and therefore of the convention adopted to define the electrical variable. Therefore, $\tilde{\mu}_i$ can be rewritten as follows:

$$\tilde{\mu}_i = \left(\tilde{\mu}_i - \frac{z_i}{z_n}\tilde{\mu}_n\right) + \frac{z_i}{z_n}\tilde{\mu}_n \tag{1.38}$$

If the electrochemical potentials in the round brackets are substituted with their formulation provided in equation (1.5), while $\tilde{\mu}_n$ outside the brackets being expressed through equation (1.36), the former equation can be rewritten as:

$$\tilde{\mu}_i = \mu^*_{i(n)} + R_g T ln C_i + R_g T ln\left(\gamma_i \gamma_n^{-\frac{z_i}{z_n}}\right) + z_i \mathcal{F}\varphi \tag{1.39}$$

By comparing equation (1.39) with equation (1.37), it is evident that:

$$\gamma_{i(n)} = \gamma_i \gamma_n^{-\frac{z_i}{z_n}} \tag{1.40}$$

Therefore, according to Guggenheim's relation (eq. (1.28)), $\gamma_{i(n)}$ can be related to the mean ionic activity coefficient (defined in eq. (1.33)) as follows:

$$\gamma_{i(n)} = \bar{\gamma}_{in}^{\frac{\nu}{\nu_i}} \tag{1.41}$$

1.1.3.9 Choice of concentration scale

The theoretical framework presented so far is based on the use of molar concentrations as composition variables. For practical reasons, this choice is widespread in the field of transport phenomena. However, molar concentrations are not well suited for rigorous thermodynamic treatments, where molalities or, more commonly, mole fractions are preferred. Consequently, it is often necessary to convert between different concentration scales. The following section provides the formulas required to carry out these conversions:

$$m_i = \frac{C_i}{\rho_{tot} - \sum_{i \neq w} MW_i C_i} \tag{1.42}$$

$$x_i = \frac{MW_w m_i}{1 + MW_w \sum_{i \neq w} m_i} \tag{1.43}$$

$$C_i = \rho_{tot} \frac{x_i}{\sum_{i \neq w} MW_i x_i + MW_w x_w} \tag{1.44}$$

In the latter equations, m_i, x_i and MW_i are respectively the molal concentration, molar fraction and the molar mass of the generic component, while ρ_{tot} is the mass density of the solution, which needs to be evaluated separately by employing a proper equation of state or a semi-empirical predictive model [35,36]. It must also be emphasized that different choices of the composition variable lead to different primary and secondary reference states in the formulation of the electrochemical potentials of the solutes. As a result, the activity coefficient of a given component in one concentration scale generally differs from that in another scale. This fact is often overlooked, leading to gross errors when dealing with highly concentrated systems, where differences between activity coefficients across scales become significantly amplified. The conversion equation can be straightforwardly obtained by considering that the electrochemical potential of a component in a given solution is unaffected by the choice of the concentration scale [24,25]. Hence:

$$\tilde{\mu}_i^{(C)} = \tilde{\mu}_i^{(m)} = \tilde{\mu}_i^{(x)} \tag{1.45}$$

where the superscript (C), (m) and (x) denote respectively the electrochemical potential formulated using the molar concentration, molal concentration, or molar fraction. By substitution of equation (1.5) and properly rearranging, the following equation can be obtained:

$$\frac{m_i \gamma_i^{(m)}}{C_i \gamma_i^{(C)}} = e^{\frac{\mu_i^{*(C)} - \mu_i^{*(m)}}{R_g T}} \tag{1.46}$$

Given that $\mu_i^{*(C)}$ and $\mu_i^{*(m)}$ are independent of the composition, the term on the right side of the latter equation is constant. When approaching the infinite diluted condition, $\gamma_i^{(m)}$ and $\gamma_i^{(C)}$ tend to 1, while according to eq. (1.42) $\frac{m_i}{C_i} \rightarrow \frac{1}{\rho_w}$. Therefore:

$$e^{\frac{\mu_i^{*(C)}-\mu_i^{*(m)}}{R_g T}} = \frac{1}{\rho_w} \tag{1.47}$$

and:

$$\frac{\gamma_i^{(m)}}{\gamma_i^{(C)}} = \frac{C_i}{m_i}\frac{1}{\rho_w} \tag{1.48}$$

The latter equation can then be employed to convert $\gamma_i^{(C)}$ in $\gamma_i^{(m)}$ or vice versa. In a similar way, it is possible to derive the following equation to convert $\gamma_i^{(m)}$ in $\gamma_i^{(x)}$:

$$\frac{\gamma_i^{(x)}}{\gamma_i^{(m)}} = \frac{m_i}{x_i} MW_w \tag{1.49}$$

An analogous conversion formula can be derived to express the molar-based osmotic coefficient of the solvent, as defined in Equation (1.14), in terms of its molal-based counterpart, which is often used as a substitute for the activity coefficient[12]. In the following sections, to avoid unnecessarily intricate notation, the concentration scale of the activity coefficients will not be explicitly specified, except where required to prevent ambiguities.

1.1.3.10 The Born theory of ion-solvent interactions

A fundamental aspect of electrochemistry concerns the study of ion–solvent interactions. These interactions primarily depend on the chemical structure of the solvent molecules, which directly or indirectly determine key physicochemical properties of ionic solutions. Among inorganic solvents, water is by far the most common and important, for both practical and theoretical reasons. Owing to its high dipole moment, water exhibits one of the strongest solvating powers among known molecules. When an electrolyte is dissolved in water, or more generally, in any polar solvent, the solvent molecules surround the ions, forming a series of solvation shells that effectively screen the electrostatic fields generated by the ions. This process, known as ionic solvation, is typically accompanied by a significant decrease in the system's Gibbs free enthalpy. The difference between the free energy of a bare ion in vacuum and that of the same ion in solution is referred to as the hydration free energy, denoted by μ_i^{hyd}. This quantity provides a useful measure of the strength of

[12] It must be kept in mind that, unlike solutes, the secondary reference state of the solvent, and thus its activity, is independent of the concentration scale adopted.

ion–solvent interactions [30,37–39]. The more negative the value of μ_i^{hyd}, the greater the tendency of the ion to be solvated, and the larger the number of solvent molecules that effectively comprise its hydration shell. The hydration free energy depends on both the intrinsic properties of the ion and the structural characteristics of the solvent. A classical physicochemical model used to estimate μ_i^{hyd} is the Born model. In this framework, ions are idealized as charged spheres that interact with the surrounding medium solely through electrostatic forces[13] [30,37]. The evaluation of μ_i^{hyd} is based on a hypothetical thermodynamic cycle in which the ion is first discharged in vacuum, then transferred into the solvent bulk, and finally recharged. The resulting free enthalpy change corresponds to the electrical work required to transfer the ion's charge, under its own electrostatic field, from an infinite distance to the ion surface and vice versa. By modeling the electrostatic potential as that produced by a uniformly charged sphere, Born derived the following expression:

$$\mu_i^{hyd} = \frac{N_a e^2}{8\pi\varepsilon_0} \frac{z_i^2}{r_{B,i}} \left(\frac{1}{\varepsilon} - 1\right) \tag{1.50}$$

Where N_a is Avogadro's number, e is the elementary charge, ε_0 and ε_r are respectively the absolute dielectric constant (or vacuum permittivity) and the relative dielectric constant (or relative permittivity) of the medium, while r_i is the Born radius of the generic species. In the former equation, the effect of the solvent structure is exclusively accounted for by its relative permittivity, which quantifies the ability of solvent molecules to screen an electric field through their orientational polarizability. The greater the polarizability of a molecule, the more effectively it can screen the electric field generated by the ions, thereby stabilising them. As a result, highly polar solvents are typically characterised by high relative permittivity, which, in turn, as shown by equation (1.50), is associated with a strongly negative hydration free energy. On the other hand, the properties of the ion are described by its valence and its Born radius. According to eq. (1.50), the greater the net charge of an ion, the higher the absolute value of μ_i^{hyd}. Conversely, the higher the Born radius, the lower is μ_i^{hyd} in absolute value. Although in the original theory the bare crystal radius of the ions was used to evaluate μ_i^{hyd}, it has been demonstrated that r_i do not correspond to the ionic radius, especially for cations. This discrepancy arises from differences in the distribution of the electronic atmosphere around bare versus solvated ions, due to interactions with the electronic environment of the solvent [37]. In the field of ion-solvent interactions, ions are commonly modelled as empty spherical cavities with a permittivity equal to that of vacuum. The Born radius, in this framework, corresponds to the

[13] This treatment neglects specific short-range interactions between ions and solvent molecules.

effective size of such a cavity, i.e., the region around the ion in which the solvent's permittivity is significantly reduced due to the presence of the ion itself. Another way of explaining it is considering that the solvent molecules in the nearby of the ions are strongly polarized by the local electric field generated by the ions themselves. Consequently, the molecules formally constituting the ionic solvation shell would lose their ability to screen an externally applied electric field. The extent of this polarization depends on the charge density of the bare ion. Therefore, ions with a higher atomic number generally exhibit a larger Born radius and, consequently, a lower hydration free energy. An overview of relevant properties of the ions investigated in this work are reported in Table 1.

Table 1: Relevant properties of some inorganic cations and anions

	Hydration Number [39]	**Crystal radius [Å]**[40]	**Stokes radius [Å]**[40]	**Hydrated radius [Å]**[40]	**Born radius [Å]**[37]	**Hydration free enthalpy [kJ mol^{-1}]**[39]	**Limiting partial molar volume [cm^3 mol^{-1}]**[41]
Li^+	5.2	0.60	2.38	3.82	1.32	-475.0	18.7
Na^+	3.5	0.95	1.84	3.58	1.68	-365.0	18.4
K^+	2.6	1.33	1.25	3.31	2.17	-295.0	28.6
Cs^+	2.1	1.69	1.19	3.29	2.51	-250.0	40.9
Mg^{2+}	10	0.65	3.47	4.28	1.46	-1830	18.0
Ca^{2+}	7.2	0.99	3.10	4.12	1.86	-1505	21.4
Cl-	2.0	1.21	1.21	3.32	3.32	-340.0	49.0
SO_4^{2-}	3.1	2.90	2.33	3.79	2.58	-1080	76.5

1.1.3.11 The Debye-Hückel theory of ion-ion interactions

Another fundamental topic in electrochemistry is the study of interactions among ions dissolved in solution. Understanding and modelling these interactions is of paramount importance, as they directly determine both fundamental thermodynamic and transport properties, namely, the ability of ions to move under the influence of a driving force.

As a result, over the past century, numerous renowned scientists and physical chemists have devoted their efforts to developing physicochemical models capable of describing such interactions in systems of increasing complexity. Among them, Peter Debye and Erich Hückel are widely regarded as the founding figures in the study of ion–ion interactions.

Their most significant contribution was the formulation of a fully predictive physicochemical model that quantifies the strength of electrostatic interactions between ions and the associated excess free energy, from which ionic activity coefficients can be derived. The Debye–Hückel model, named after its developers, is considered a cornerstone of electrochemical theory for ion–ion interactions, and its impact has often been compared to that of the ideal gas law in the field of classical thermodynamics.

Although the original Debye–Hückel model has since been surpassed in terms of predictive accuracy, the fundamental concepts and methodological approach underlying its development continue to serve as the foundation for more advanced models, such as those describing the interactions between mobile ions and fixed charges in IEMs. Similarly to what is done in the development of the Born model, such interactions are related to the change in the ions' free energy when going from a hypothetically ideal state, in which no interactions are present, to the real state. At the basis of the original formulation of the Debye–Hückel model there are some fundamental assumptions [30]:

1. The reference ion object of the thermodynamic analysis is assumed to be a point charge;
2. All the other surrounding ions are smeared out into a continuous charge distribution;
3. The solvent molecules are assimilated to a continuous dielectric medium with constant permittivity;
4. Ions interact only through coulombic interactions.

According to the latter assumption, the ion excess chemical potential can be solely related to the existence of such interactions. Therefore, similarly to what was done in 1.1.3.10 with the Born model, the electrical work required to charge the reference ion can be expressed as:

$$w_i^{el} = \mu_i^{ex} = \frac{N_A z_i e}{2} \varphi_{cloud}|_{r=0} \tag{1.51}$$

where $\varphi_c|_{r=0}$ is the electrostatic potential globally generated by the assembly (or cloud) of surrounding ions at the surface of the reference ion. According to the principle of superimposition of potentials, φ_{cloud} can be expressed as follows:

$$\varphi_{cloud} = \varphi_{tot} - \varphi_i = \varphi_{tot} - \frac{z_i e}{4\pi\varepsilon_0\varepsilon}\frac{1}{r} \tag{1.52}$$

where φ_{tot} is the overall electrostatic potential, φ_i is the electrostatic potential solely generated by the reference ion and r is the radial position.

According to Poisson's equation[14], the electrostatic potential distribution in a certain region of space with spherical symmetry can be related to the electrical charge density as follows:

$$\frac{1}{r^2}\frac{d}{dr}\left(r^2\frac{d\varphi_{tot}}{dr}\right) = -\frac{\rho_{el}}{\varepsilon_0\varepsilon} \tag{1.53}$$

In the original model, the electrical charge density distribution around the reference ion is modelled through a linearized version of the Boltzmann's distribution law [30]:

$$\rho_{el} \approx -\frac{\mathcal{F}^2}{RT}\sum_j C_j^{\infty} z_j^2 \varphi_{tot} \tag{1.54}$$

where C_j^{∞} is the molar concentration of the generic species at the bulk of the system, i.e., at an infinite distance from the reference ion. By substitution of eq. (1.54) into eq.(1.53), the well-known linearized Poisson-Boltzmann equation is obtained:

$$\frac{1}{r^2}\frac{d}{dr}\left(r^2\frac{d\varphi_{tot}}{dr}\right) = -\frac{\mathcal{F}^2}{RT}\sum_j C_j^{\infty} z_j^2 \varphi_{tot} \tag{1.55}$$

[14] The well-known Poisson's equation is actually a form of the Maxwell's law of electrostatic: Being $\vec{E}$ the electrostatic field function of position, according to the Gauss law $\nabla \cdot \vec{E} = \frac{\rho_e}{\varepsilon_0}$. Given that $\vec{E}$ can expressed as $\vec{E} = -\nabla\varphi_{tot}$, we conclude that: $\nabla^2\varphi_{tot} = -\frac{\rho_e}{\varepsilon_0}$ which is the vectorial form of equation **Errore. L'origine riferimento non è stata t rovata.**).

In order to find the electrostatic potential distribution around the central ion, equation (1.55) must be integrated providing suitable boundary condition. Under the point-charge assumption, the lower bound integration limit corresponds to $r = 0$ and the following equation for the total electrostatic potential distribution is achieved:

$$\varphi_{tot} = \frac{z_i e}{4\pi\varepsilon_0\varepsilon}\frac{e^{-\varkappa r}}{r} \tag{1.56}$$

where $\varkappa$ is the Debye screening parameter, defined as follows:

$$\varkappa = \sqrt{\frac{\mathcal{F}^2}{\varepsilon_0\varepsilon R_g T}2I} \tag{1.57}$$

$$I = \frac{1}{2}\sum_j C_j^{\infty} z_j^2 \tag{1.58}$$

and I is the ionic strength of the bulk solution. The Debye screening parameter is a fundamental and ubiquitous factor in electrochemical theory, playing a crucial role in the analysis of potential distribution within electrolyte solutions. It represents the inverse of the characteristic length over which electrostatic interactions are screened in an electrolyte solution. According to eq. (1.57), it is directly related to the ionic strength of the solution, reflecting how increased ion concentration enhances the attenuation of the electric potential around a charged species. In a sufficiently diluted solution ($I \leq 0.01\ M$), the electrostatic potential distribution (eq. (1.56)) can be linearised and substituted in eq. (1.52) and eq. (1.51) to evaluate the excess electrochemical potential as:

$$\mu_i^{ex} = -\frac{N_a(z_i^2 e^2)}{8\pi\varepsilon_0\varepsilon}\varkappa \tag{1.59}$$

By substitution of the latter equation into equation (1.7), the following formulation for the ion activity coefficient can be obtained:

$$ln\gamma_i = -\frac{1}{R_g T}\left[\frac{N_a(z_i^2 e^2)}{8\pi\varepsilon_0\varepsilon}\sqrt{\frac{2\mathcal{F}^2}{\varepsilon_0\varepsilon R_g T}}\sqrt{I}\right] \tag{1.60}$$

From which it is evident that, in the dilute regime under which the model was developed, the ion activity coefficient decreases with increasing ionic strength, approaching one for vanishing I.

Combination of eq. (1.60) according to eq. (1.33) for two oppositely charge ions leads to the following expression for the mean ionic activity coefficient of the corresponding neutral electrolyte:

$$ln\bar{\gamma}_{ij} = -\zeta(z_+z_-)\sqrt{I} \tag{1.61}$$

Where ζ is a lumped parameter including physical constants and stoichiometric coefficients. According to the former equation, the mean ionic activity coefficients scales with the square root of the ionic strength. This result was experimentally validated up to ionic strength of 10 mM [42]. Above this threshold, significant deviance is observed. Indeed, eq. (1.61) is affected by all the simplifying assumptions made, and more accurate results can be achieved by relaxing some of these assumptions.

For instance, the point-charge assumption implies the integration of the linearized Poisson-Boltzmann equation (1.55) in the spatial domain $[0;\infty]$. However, more precisely, the lower bound could be taken to be the radius of the central ion r_0. Integration of the linearized Poisson-Boltzmann equation in the domain $[r_0;\infty]$, leads to the following expression for the electrostatic potential at the ion's surface:

$$\varphi_{tot}(r_0) = -\frac{z_i e}{4\pi\varepsilon_0\varepsilon}\frac{\varkappa}{1+r_0\varkappa} \tag{1.62}$$

Consequently, the corresponding mean ionic activity coefficient has the following expression:

$$ln\bar{\gamma}_{ij} = -\frac{\zeta(z_+z_-)\sqrt{I}}{1+\beta\sqrt{I}} \tag{1.63}$$

where, likewise ζ, β lumps a series of physical constants.

1.1.4 Modelling of aqueous electrolytes–IEMs thermodynamic equilibria

The thermodynamic modelling of equilibrium at the interface between a semipermeable membrane and an electrolyte solution is of considerable practical relevance, not only in the context of conventional membrane processes, but also in various biological disciplines. The distribution of mobile ions between the solution and the membrane drastically affects the performance of all electromembrane processes. Therefore, models able to predict the thermodynamic affinity of mobile species to the membrane are of great interest. The first theoretical treatment of partition equilibria at the solution–membrane interface was proposed by Donnan, who, in 1911, published a seminal paper introducing the model that now bears his name.

Building upon the thermodynamic formulation of equilibrium, this section provides a brief review of the fundamental relations governing partition equilibria at the solution–membrane interface. These relations are extensively employed throughout the present work for both analysis and numerical simulations, and constitute the theoretical foundation for the estimation of membrane activity coefficients from equilibrium experimental data (see section 1.3).

1.1.4.1 Definition of thermodynamic and electrochemical equilibrium.

Let us consider two phases α and β, able to exchange matter across their contact interface. Providing that α and β are not necessarily at the same pressure, the equilibrium condition is formulated by minimising the Helmholtz free energy of the system. Hence:

$$dF^{\alpha} + dF^{\beta} = 0 \tag{1.64}$$

By substitution of eq. (1.2) into (1.64), and assuming the two phases to be in thermal equilibrium (i.e., $T^{\alpha} = T^{\beta}$), the following equation is obtained:

$$-\left(P^{\alpha}dV^{\alpha} + P^{\beta}dV^{\beta}\right) + \sum_{i=1}^{N}\left(\tilde{\mu}_i^{\alpha} - \tilde{\mu}_i^{\beta}\right)dn_i = 0 \tag{1.65}$$

where dn_i are the moles of the generic species exchanged between the two phases. If the transfer process is so slow that P^{α} and P^{β} can be considered at their steady-state value, the summation in the first round bracket in the former equation corresponds to the reversible work exchanged between the system and the surrounding environment, which must be zero at the equilibrium condition [24,31]. Consequently:

$$\sum_{i=1}^{N}\left(\tilde{\mu}_i^{\alpha} - \tilde{\mu}_i^{\beta}\right)dn_i = 0 \tag{1.66}$$

Provided that the former equation must be valid for any quantity of exchanged species, the following equilibrium relation can be derived:

$$\tilde{\mu}_i^{\alpha} = \tilde{\mu}_i^{\beta} \tag{1.67}$$

Ultimately, mass transfer equilibrium is reached when the electrochemical potential of any species is invariant. Importantly, the previous equilibrium condition applies to all and solely the species effectively able to cross the boundary interface between the two phases.

1.1.4.2 Ion partitioning equilibria: the Donnan model

When an IEM is in contact with an aqueous electrolyte, the dissolved ions and the water molecules are free to move from the solution to the membrane (and vice versa). At equilibrium condition, equation (1.67) must be satisfied for all the mobile species. Hence:

$$\mu_{i(n)}^{0,s} + R_g T ln\left(\gamma_{i(n)}^{s} C_i^{s}\right) + z_i \mathcal{F} \varphi^{s} + v_i^{s} P^{s} = \mu_{i(n)}^{0,m} + R_g T ln\left(\gamma_{i(n)}^{m} C_i^{m}\right) + z_i \mathcal{F} \varphi^{m} + v_i^{m} P^{m} \quad (1.68)$$

where the superscript s and m respectively identify the solution phase and the membrane phase[15]. In this regard, it is relevant to highlight that speaking about a *membrane phase* can be rather misleading. Indeed, a thermodynamic phase is defined to be a macroscopically homogeneous and physically distinct portion of matter, characterised by uniform intensive properties and internal thermodynamic equilibrium. For instance, colloidal systems are not to be considered proper thermodynamic phases [23].

While this notation is commonly employed in authoritative reference texts within the field, it may be deemed inappropriate in light of the lack of consensus within the scientific community regarding whether a macroscopically homogeneous IEM should be considered a genuine phase or rather a heterogeneous system comprising distinct hydrophobic and hydrophilic domains [6,12,43–45]. Therefore, in the following, the term *phase* associated with the membrane will refer to the hydrophilic domains containing water molecules and mobile ions. Molar concentration is consistently defined as moles per volume of solution, therefore excluding the volume of space in the membrane occupied by the polymeric chains. This choice is further justified by evidence indicating that the use of concentration values based on the swollen membrane volume results in a diminished predictive accuracy of ionic partitioning models, probably due to an underestimation of the concentration of fixed charges [46,47].

Equation (1.68) is written adopting Newman's definition of electrochemical potential (see section 1.1.3.7), i.e., the quasi-electrostatic potential φ is defined according to equation (1.36), by selecting an arbitrary reference species and setting its activity coefficient to 1. The only requirement for this reference species is to be able to move across the phase boundary. Although the traditional formulation becomes equivalent to Newman's approach when a suitable convention for the activity coefficient is adopted, the latter is rarely employed by membrane engineers and is more commonly found in the work of applied chemical physicists [48–52].

[15] A similar equilibrium relation can be written in terms of molal concentrations and molal-base activity coefficients.

If the same reference states are adopted to formulate $\tilde{\mu}_i^{\alpha}$ and $\tilde{\mu}_i^{\beta}$, and assuming $v_i^s = v_i^{\beta} = v_i$, equation (1.68) can be rewritten as follows:

$$C_i^m = C_i^s \left(\frac{\gamma_{i(n)}^s}{\gamma_{i(n)}^m} \right) e^{-\frac{z_i \mathcal{F}}{RT} \Delta\varphi} e^{-\frac{v_i}{R_g T} \Delta P} \tag{1.69}$$

where $\Delta\varphi$ is the quasi-electrostatic Donnan potential and ΔP is the hydrostatic pressure difference between the membrane and the external solution. The former equation allows us to evaluate the equilibrium concentration in the membrane phase for a given external concentration, if all the other terms are known. Indeed, according to (1.36), a similar equilibrium relation can be formulated for the reference species n:

$$C_n^m = C_n^s e^{-\frac{z_n \mathcal{F}}{R_g T} \Delta\varphi} e^{-\frac{v_i}{R_g T} \Delta P} \tag{1.70}$$

To be thermodynamically consistent, equations (1.69) and (1.70) must also be coupled with the global electroneutrality condition in the membrane phase, which could be expressed as:

$$\sum_i z_i C_i^m + z_{fix} C_{fix} = 0 \tag{1.71}$$

where z_{fix} and C_{fix} are respectively the valence and concentration of the fixed charges in the membrane phase. In principle, z_{fix} depends on the chemical structure of the ionizable functional groups, but in most cases $|z_{fix}| = 1$, while C_{fix} mainly depends on the IEC of the membrane. However, as discussed in section 1.2, C_{fix} varies also with the water content of the membrane.

Disregarding the pressure-related contributions due to solvent partition (see section 1.1.4.3), according to equation (1.71) the quasi-electrostatic Donnan potential is directly related to the concentration of the reference species in the membrane phase, that will inevitably differ from that in solution due to the electroneutrality requirement (eq. (1.71)). Indeed, according to Donnan's theory, the external solution and the membrane differ in the electrical state due to the presence of the fixed charged groups bound to the polymeric backbone of the membrane. Such groups are unable to move across the phase boundaries, and their presence drastically impedes the absorption of co-ions in the membrane phase.

Typically, the equilibrium co-ion concentration in the membrane phase is order of magnitude lower than the external concentration. Accordingly, typical values of $\Delta\varphi$ range between tens to hundreds of

millivolts, with the sign depending on the charge of the fixed counter-ions [13,53,54]. The co-ion exclusion phenomenon is also referred to as Donnan exclusion, and its extent is related to the salt concentration in the external solution, valence of the counter-ions and fixed charges concentration in the membrane phase.

Although the Donnan model constitutes a well-grounded theoretical framework for the description of mobile ion partitioning in IEMs, its practical implementation is substantially limited by the necessity of determining the activity coefficients in the two phases at varying concentration and composition. While $\gamma_{i(n)}^{s}$ can be easily evaluated through robust and extensively validated thermodynamic models, such as the Pitzer model [55–59] or the eNRTL model for aqueous electrolytes [60,61], the activity coefficients in the membrane phase remain elusive and lack a reliable and universally accepted theoretical framework for their accurate determination (further discussion on this topic is reported in section 1.1.5).

For this reason, a simplified version of the Donnan model is frequently adopted, particularly by end-users such as process engineers. This simplified formulation, known as the ideal Donnan model, is derived by neglecting thermodynamic non-idealities in both phases and by assuming that the osmotic effect associated with the pressure difference across the interface is negligible. Consequently, equation (1.69) is rewritten as follows:

$$C_i^m = C_i^s e^{-\frac{z_i \mathcal{F}}{R_g T}\Delta\varphi} \tag{1.72}$$

Noticeably, except for the pressure-related term, equations (1.72) and (1.70) are equivalent as the traditional formulation of the electrochemical potential and Newman's one coincide when approaching the reference state. As it will be discussed in section 1.3, this oversimplified model can be useful to produce a very rough estimation of equilibrium ion concentration but leads to drastic failure in most cases [16,62–64].

By manipulating equation (1.69) the ion partition coefficient K_i^p and the partition selectivity $S_{i,j}^p$ can be defined as follows:

$$K_i^p = \frac{C_i^m}{C_i^s} = \Phi_\gamma \Phi_{\Delta\varphi} \Phi_{\Delta P} \tag{1.73}$$

$$S_{i,j}^p = \frac{K_i^p}{K_j^p} = \left(\frac{\gamma_{i(n)}^s}{\gamma_{i(n)}^m}\frac{\gamma_{j(n)}^m}{\gamma_{j(n)}^s}\right) e^{-\frac{(z_i - z_j)\mathcal{F}}{R_g T}\Delta\varphi} e^{-\frac{(\nu_i - \nu_j)}{R_g T}\Delta P} \tag{1.74}$$

According to the former equations, the partition coefficient and the partitioning selectivity of an ion depend on three contributions: non-ideal (Φ_γ), electrostatic $(\Phi_{\Delta\varphi})$ and osmotic $(\Phi_{\Delta P})$. Among them, the effect of the difference in the electrical state of the two phases is generally the most relevant.

1.1.4.3 Osmotic equilibrium

In section 1.1.4.2, the Donnan equilibrium describing the ion partition between the solution and the membrane was derived starting from the equivalence of the electrochemical potential between the bulk of the solution and the membrane phases. While the latter was extensively studied and investigated, the corresponding partition equilibrium of water has been comparatively less investigated from a theoretical standpoint; however, this does not diminish its importance.

Indeed, according to equations (1.69) and (1.74), a comprehensive modelling of ion partitioning should also include the osmotic effect due to the different pressure existing between the two phases. To find an expression for this contribution, we need to recall that the equilibrium equation must be applied to all the mobile species, including water. Therefore, equation (1.68) can be rewritten as follows:

$$\mu_w^{0,s} + R_g T ln(a_w^s) + \nu_w^s P^s = \mu_w^{0,m} + R_g T ln(a_w^m) + \nu_w^m P^m \tag{1.75}$$

where the subscript w denotes water. If the same reference states are adopted in the formulation of the chemical potential in the membrane and solution phases, and if variation of partial molar volume is neglected, the former equation can be rewritten as follows:

$$\Delta P = \frac{R_g T}{\nu_w} ln\left(\frac{a_w^s}{a_w^m}\right) = \Delta\Pi \tag{1.76}$$

where in the last equality, the definition of osmotic pressure (equation (1.16)) was employed. At this point, it is necessary to focus on the meaning of water partition equilibrium within the membrane, a topic that is often overlooked or insufficiently addressed.

Equation (1.76), derived from the equivalence of the water chemical potential, indicates that, due to the difference in the water activity between the solution and the membrane phase, a pressure difference must arise between the bulk of the solution and the membrane. Since the solvent activity in the membrane phase will inevitably differs from that in the solution, at least due to the presence of the fixed charges, it follows, that, in general, $\Delta P \neq 0$.

Nonetheless, water partitioning in water-permeable membranes is often modelled by imposing equality of water activity on both side of the interface, while assuming continuity of the pressure across the interface [10,65–68]. Furthermore, when the membrane is in contact with two solutions of different composition, ΔP at the two solution–membrane interfaces will generally differ. As a result, a pressure gradient will develop across the membrane.

This seemingly trivial consideration stands in clear contrast with one of the fundamental assumptions of the mostly employed model to describe solvent transport through a membrane, namely, the solution-diffusion model, which assumes the hydrostatic pressure to be uniform across the membrane [69,70]. The supporters of such model suggest that an extra term accounting for the elastic pressure due to the polymer swelling should be added to the definition of the chemical potential of water in the membrane phase, but this term could be simply accounted for when evaluating the water activity [71] and no agreement among the scientific community can be found on the topic. Without purporting to resolve such a complex and debated issue, section 1.3 presents a series of simulations aimed at shedding light on certain physical and mathematical aspects of water partition equilibrium.

1.1.4.4 Extended Donnan model: formulation and analysis of an integrated model for ion and water partition in IEM

In the previous section, the fundamental thermodynamic relations describing ion and water partition at the solution-membrane interface were provided. It is essential to emphasize that a sound thermodynamic model is required not only for the development of predictive tools, but also to provide a theoretical framework through which fundamental insights can be extracted from raw experimental data. From equations (1.69) and (1.76), it is clear that ion and water partitioning equilibria are coupled. Indeed, ion partition coefficients depend on the ΔP term, which in turn depends on the water activity in the two phases. At the same time, the activity of water in the membrane phase, or equivalently its osmotic pressure Π^m, is somehow influenced by the mobile-ions distribution between the two phases. Moreover, mathematical inspection of the former system of equilibrium equations, namely equations (1.69), (1.71) and (1.76), reveals that the system is dimensionally undetermined,

i.e., an equation is missing to solve the system. Therefore, in the following section, our purpose is to formulate an expression to relate water and ion partitioning equations.

At this stage we need to recall that the solvent and the solutes activity in a given phase are related through each other through the Gibbs-Duhem equation (1.25), that in the previous section was rewritten to evaluate the osmotic pressure of the solvent in the given phase. By employing Euler's equation for the total volume (eq. (1.19)), equation (1.26) can be rewritten as follows:

$$d\Pi^m = \frac{R_g T}{1 - \sum_{i \neq w} C_i^m v_i} \sum_{i \neq w} C_i^m d\ln a_i^m \tag{1.77}$$

where $C_i^m v_i$ represents the volumetric fraction of the generic solute in the membrane phase. For the sake of simplicity, in the following we will assume negligible the volume occupied but the ions (i.e., $C_w^m v_w \approx 1$). Moreover, the solutes activity can be rewritten in terms of their activity coefficient, so that equation (1.77) can be rewritten as follows:

$$d\Pi^m = R_g T \sum_{i \neq w} C_i^m d\left(\ln C_i^m + \ln \gamma_{i(n)}^m\right) \tag{1.78}$$

Further manipulation of the former equation leads us to:

$$d\Pi^m = R_g T \sum_{i \neq w} dC_i^m + R_g T \sum_{i \neq w} C_i^m d\ln \gamma_{i(n)}^m \tag{1.79}$$

In order to evaluate Π^m, equation (1.79) must be properly integrated from a reference state, corresponding to the secondary reference state chosen for the activity coefficients, and the generic state characterised by C_i^m. Hence:

$$\Pi^m - \Pi^{*m} = R_g T \int_{C_i^{*m}}^{C_i^m} \sum_{i \neq w} dC_i^m + R_g T \int_{C_i^{*m}}^{C_i^m} \sum_{i \neq w} C_i^m d\ln \gamma_{i(n)}^m \tag{1.80}$$

Regardless of the chosen secondary reference state, Π^{*m} corresponds to the lower bound value of the first integral on the right side of the former equation. Therefore, equation (1.80) can be rewritten as:

$$\Pi^m = R_g T \sum_{i \neq w} C_i^m + R_g T \int_{C_i^{*m}}^{C_i^m} \sum_{i \neq w} C_i^m d ln \gamma_{i(n)}^m = \Pi^{m,id} + \Pi^{m,ex} \quad (1.81)$$

where $\Pi^{m,id}$ corresponds to the ideal value of the osmotic pressure in the membrane phase, while $\Pi^{m,ex}$ is the excess osmotic pressure due to the contribution of the non-ideal phenomena in the membrane phase. In recent works, Biesheuvel and co-workers arrived at a similar formulation but neglected this last term [43,72–74]. While activity coefficients are frequently incorporated in the modelling of ion partition, non-ideal phenomena influencing water partition are often neglected. Such omission, however, represents a rather crude approximation, as non-ideal interactions are expected to significantly contribute to the thermodynamic equilibria in complex, highly charged environments, particularly at high salt concentrations.

This expectation is supported by experimental measurements of ion activity coefficients obtained for a series of commercial IEMs and reported in section 1.2. Further evidence comes from recent studies by Kamcev et al. and Geise et al.,[75,76] who investigated the state of water molecules in custom-made IEMs. Their findings indicate that water molecules can be classified into two main populations, bound and freezable, depending on the strength of their interactions with the fixed charges of the polymeric matrix. As a consequence of these interactions, the two populations exhibit markedly different osmotic activities, with bound water being unable to freeze and incapable of forming hydrogen bonds with other water molecules. In the proposed thermodynamic framework, any possible deviation from ideal thermodynamics should be accounted for by means of the activity coefficients, regardless of the source of such non-ideal interactions. Therefore, if experimental values for C_i^{m} are accessible, equation (1.81) can be combined with equations (1.69), (1.71) an (1.76) to solve the extended Donnan model to evaluate $\gamma_{i(n)}^m$ and $\Pi^{m,ex}$ (see section 1.3).

1.1.5 Modelling of ion activity coefficients in IEMs

In the previous sections, theoretical frameworks for modelling ion and water partitioning equilibria in IEMs were outlined. These models, however, are not fully predictive, as any deviations from ideal thermodynamics are effectively embedded within the ion activity coefficients. It is therefore essential to develop thermodynamic models capable of describing the non-ideal interactions among the system's components, as well as their dependence on the composition of the external electrolyte. Despite the extensive literature on ion partitioning in IEMs, comprehensive and reliable models remain lacking [77]. This gap in fundamental understanding becomes even more critical when dealing with multi-ionic solutions, since most studies up to date have focused on IEMs equilibrated with

single-salt systems. Recently, interest in the characterization and modelling of IEMs in contact with complex multi-ionic solutions has increased, driven by the development of novel electromembrane applications for the selective recovery of raw materials from waste brines [9,72,78]. By elucidating the physical mechanisms of ion partitioning in IEMs, thermodynamic models are not only valuable tools for guiding the design of tailor-made membranes for ion-selective separation processes, but also indispensable for integration into process-level simulations, where they enable reliable prediction of the performance of electromembrane units under realistic operating conditions.

The following section presents and discusses a set of novel thermodynamic models developed for estimating ion activity coefficients in IEMs. These latter were derived as modifications or extensions of existing, yet limited, approaches, and their theoretical formulation is introduced by first outlining the key shortcomings of the currently available models. Parts of this section are adapted and expanded from an author's previously published article [79].

1.1.5.1 Manning's model: current formulation and its main limitations

In recent years, the Manning model, derived from Manning's counterion condensation theory [80], has emerged as one of the most promising frameworks for predicting ion partitioning in IEMs. The foundational version of Manning's model was originally introduced by Gerald Manning in 1969 to describe the colligative behaviour of aqueous solutions of mixed salt-polyelectrolyte aqueous solutions. More recently, Kamcev and collaborators adopted Manning's theory to model ion partitioning in IEMs, suggesting that an IEM in equilibrium with an aqueous solution can be viewed as a condensed polyelectrolyte solution [51,77,81].

In his seminal work, Manning laid the theoretical groundwork of the counter-ion condensation theory, according to which, under certain conditions, a fraction of the counter-ions condenses onto the polyelectrolyte. The description of such phenomenon, akin to ion pairing in concentrated electrolyte solutions, is centered on a dimensionless parameter called the reduced linear charge density, denoted by ξ:

$$\xi = \frac{\lambda_b}{b} = \frac{e^2}{4\pi\varepsilon_0\varepsilon_m k_B T b} \tag{1.82}$$

where λ_b is the Bjerrum length, ε_m is the hydrated membrane relative dielectric constant and b presents the average spacing between fixed charges on the polyelectrolyte chain. This parameter quantifies the extent to which electrostatic fields surrounding fixed charges overlap, indicating whether the local electrostatic interactions are strong enough to induce counter-ion condensation [77].

When ξ exceeds a specific critical threshold (see equation (1.92)), enough counter-ions condense, neutralizing a portion of the fixed charges and lowering the effective linear charge density. These condensed counter-ions are thus localized in a region of space near the charged polymer backbone and no longer participate in osmotic equilibria, leading to a reduction in the activity of the mobile (i.e., uncondensed) ion population. By employing a Debye–Hückel approach on a polyelectrolyte solution with a single salt added, Manning arrived at the following formulation for the counter-ions and co-ions activity coefficients:

$$\gamma_{cou}^{m,(C)} = \bar{\theta}_{cou} exp\left[-\frac{1}{2}\frac{\frac{C_{salt}^{m}}{C_{fix}}}{\frac{C_{salt}^{m}}{C_{fix}} + \frac{\xi}{\xi_c}\left|\frac{z_{cou}}{z_{fix}}\right|(\nu_{cou}+\nu_{co})}\right] \tag{1.83}$$

$$\gamma_{co}^{m,(C)} = exp\left[-\frac{1}{2}\frac{\frac{C_{salt}^{m}}{C_{fix}}\left(\frac{z_{co}}{z_{cou}}\right)^{2}}{\frac{C_{salt}^{m}}{C_{fix}} + \frac{\xi}{\xi_c}\left|\frac{z_{cou}}{z_{fix}}\right|(\nu_{cou}+\nu_{co})}\right] \tag{1.84}$$

where $\bar{\theta}_{cou}$ is the uncondensed fraction of counter-ions, ξ_c is the critical threshold of ξ and C_{salt}^{m} is the neutral salt concentration.

The success of this model lies in achieving good predictive accuracy despite its structural simplicity. Indeed, the model has been shown to provide quantitative predictions of ion partitioning for single-salt systems over a wide range of commercial IEMs, particularly for highly charged membranes with high water content, in the external salt concentration range of 0.1–1 mol L^{-1}.

However, the model showed significant limitations that effectively reduce its applicability. For instance, the model performs poorly at both very low and very high external salt concentrations [16,63]. As discussed later, this reduced accuracy likely arises from the breakdown of certain model assumptions and from unaccounted non-ideal phenomena that depend strongly on the external salt concentration. A further major limitation of the original Manning model is its inability to describe ion partitioning in multi-ionic systems. In fact, equations (1.83) and (1.84) were derived considering only two kinds of mobile ions. Furthermore, in Manning's original formulation, ions are distinguished solely by their valence. Similar to the Debye–Hückel model for dilute aqueous electrolytes presented in section 1.1.3.11, Manning's approach accounts exclusively for electrostatic interactions between mobile ions and the fixed charges. As a result, even accounting for the presence of multiple ions, it would inherently predict identical activity coefficients for all counter-ions of the same valence, disregarding any species-specific effects.

In practice, several types of IEMs exhibit different partitioning selectivity for counterions of similar valence [82–84]. For instance, Galizia et al. [64] investigated ion partitioning in a commercial membrane equilibrated with different single-salt solutions, while Chen et al. [85] examined ion sorption in two commercial CEMs equilibrated with binary salt solutions. Both studies found that, at a fixed ionic charge concentration, counterions with a smaller hydrated radius, and therefore a larger crystal radius, displayed higher partition selectivity. These results suggest that a comprehensive partitioning model should account not only for ion valence but also for ion hydration state. Building on this, a novel multi-ionic formulation of the Manning model was developed incorporating a counterion condensation selectivity rule that reduces the number of calibration parameters while preserving high predictive capability.

1.1.5.2 Multi-ionic extension of Manning's model

Within the proposed work, the multi-ionic extension of Manning's model was derived starting from the original model formulation, where Manning considered a 1:1 electrolyte dissolved in a polyelectrolyte solution and adopted a Debye-Hückel framework to describe the electrostatic interactions between mobile ions and the linearly distributed fixed charges, idealized as an infinite charged line. As such, the underlying assumptions of the model closely resemble those of the Debye-Hückel theory, discussed in section 1.1.3.11.

In order to evaluate the ion activity coefficients, Manning expressed the total electrostatic potential (φ_{tot}) as the sum of that generated by the linear charge distribution (φ_{chain}) and that of the surrounding ionic cloud (φ_{cloud}), following the principle of superposition. Under the assumption of infinite dilution, the following expression for the electrostatic potential of the ionic cloud was derived [80,86]:

$$\varphi_{cloud} = \varphi_{tot} - \varphi_{chain} = -\frac{2z_{fix}e}{4\pi\varepsilon_0\varepsilon_m b} ln\left(b\sqrt{\frac{\mathcal{F}^2}{\varepsilon_0\varepsilon_m R_g T}(C_{cou}\bar{\theta}_{cou} + C_{co})} \right) \tag{1.85}$$

where C_{cou} and C_{co} are respectively the total concentration of counter-ions and co-ions coming from the 1:1 salt dissociation. The former equation represents the base for the traditional formulation of Manning's activity coefficients valid for single-salt solutions (equations (1.83) and (1.84))[83,87–89]. A generalized multi-ionic formulation can be obtained by recognizing that (1.85) is mathematically analogous to eq. (1.52). Therefore, in the general case, the argument of the logarithm term should be replaced with the general expression of the Debye screening parameter (eq. (1.57)).

By using equation (1.85) to calculate the electrical work associated with charging the polyion, the excess molar free enthalpy of the system can be expressed as:

$$\frac{G_{ex}^{m}}{M_w RT} = -\xi m_{fix} z_{fix}^2 \bar{\theta}_{fix}^2 ln\,(\bar{\kappa} b) \tag{1.86}$$

where M_w is the solvent mass of the system, $\overline{\theta}_{fix}$ is the fraction of uncondensed fixed charges and $\bar{\kappa}$ is the modified Debye screening parameter:

$$\bar{\kappa} = \sqrt{\frac{e^2 N_a \rho_s}{\varepsilon_m \varepsilon_0 k_b T} \sum_i z_i^2 \bar{\theta}_i m_i^m} \tag{1.87}$$

Where $\bar{\theta}_i$ is the uncondensed fraction of species i, introduced in the previous expression to account for condensed counter-ions which do not contribute to the total ionic strength of the uncondensed phase. The above relations are formulated using molal concentrations, consistently with the scaling formula introduced in equation (1.42)[16]. It should be pointed out that equations (1.86) and (1.87) are strictly valid in the limit of infinite dilution. Particularly, equation (1.86) can be obtained from the linearization of the excess free energy assuming $\bar{\kappa} b \to 0$ [86] (i.e., when the Debye length $1/\bar{\kappa}$ is far greater than the average distance between fixed charges b). Ultimately, the novel multi-ionic formulation of Manning's activity coefficient can then be obtained from the expression for the excess free energy, by applying equation (1.7) and multiplying the result by the uncondensed fraction of the *i-th* species to take into account the effective reduction in the concentration of the counter-ions due to the condensation [80]:

$$\gamma_i^{m,(m)} = \bar{\theta}_i exp\left[-\frac{\xi m_{fix} z_{fix}^2 \bar{\theta}_{fix}^2 z_i^2 \overline{\theta}_i}{2 \sum_j \overline{\theta}_j m_j^m z_j^2} \right] \tag{1.88}$$

The former expression represents a multi-ionic generalization of the classic Manning formula, applicable both to condensing and non-condensing systems. A similar expression was provided by Wang et al. [62], although they appeared to assume the condensed fraction of the mobile species to be negligible (i.e., approaching 1) when computing $\bar{\kappa}$ (equation (1.87))). This approximation was originally introduced by Manning, who argued that the Debye screening parameter is approximately unaffected by condensation when counter-ion concentrations vastly exceed that of the fixed charges

[16] To be consistent with the hypothesis of infinite dilution, eq. (1.42) was simplified to $C_i \approx m_i \rho_s$

[90], a condition rarely met within IEMs, where these concentrations are typically comparable due to the Donnan exclusion mechanism. For this reason, a more rigorous formulation was adopted herein. The $\overline{\theta}_i$ values in equation (1.87) are (1.88) are related to $\overline{\theta}_{fix}$ by the following charge balance:

$$\sum_i z_i \theta_i m_i^m + z_{fix} \theta_{fix} m_{fix} = 0 \tag{1.89}$$

with:

$$\theta_i = 1 - \overline{\theta}_i \tag{1.90}$$

$$\theta_{fix} = 1 - \overline{\theta}_{fix} \tag{1.91}$$

In equation (1.89), the sum extends over all ionic species, with the understanding that only counter-ions can condense ($\theta_i = 0$ for co-ions). The fixed charges condensed fraction is related to the value of the linear charge density ξ before and after the counter-ion condensation has occurred:

$$\begin{cases} \theta_{fix} = 1 - \dfrac{\xi_c}{\xi} \Leftrightarrow \xi > \xi_c \\ \theta_{fix} = 0 \Leftrightarrow \xi < \xi_c \end{cases} \tag{1.92}$$

where ξ_c is Manning's parameter critical value (i.e., the equilibrium value of linear charge density) that can be related to the valence of the counter-ions and of the fixed charges:

$$\xi_c = \frac{1}{|z_{cou} z_{fix}|} \tag{1.93}$$

Equations (1.92) and (1.93) constitute the mathematical expression of Manning's limiting law, which predicts that, at infinite dilution, condensation occurs only when $\xi > \xi_c$ [77,80]. While widely reported in literature, the limiting law has been almost exclusively applied to single-salt systems. To the best of our knowledge, its application to multi-ionic systems has only been attempted once [62], but the authors did not report the value of ξ_c effectively adopted.

In fact, a key limitation of the Manning's limiting law in multi-ionic contexts is the emergence of inconsistent equilibrium states for counter-ions of different valence. Manning later clarified that in such scenario condensation should occur only for the most highly charged counter-ion species, until the critical threshold ξ_c is reached [86]. This suggests that the actual ξ_c can be determined by

considering the maximum counter-ions valence. However, this leads to complications: when the condensed fraction of the most highly charged counter-ion reaches unity, its Manning activity coefficient vanishes, according to equation (1.88) implying an infinite concentration in the membrane according to the Donnan model (equation (1.69)).

In the same work, Manning discussed whether a threshold value for counter-ions condensation exists even at finite ionic strength. Departing from the limiting law, counter-ions condensation should be viewed as a continuous process, rather than a threshold phenomenon. During this process, each counter-ion should partially condense to minimize the free energy of the system [91]. Due to the intrinsic presence of fixed charges, the infinite dilution condition (i.e., $\varkappa b \ll 1$ [86]) cannot strictly be achieved in IEMs, even when the external solution concentration approaches zero. Hence, the limiting law does not rigorously apply to IEMs unless a large fraction of counter-ions is condensed, leading to a reduction the Debye screening parameter of the system. Despite this, the limiting law has been applied to IEMs owing to its simplicity. In the present work, it has been applied under the assumption that all counter-ions condense simultaneously to reach the critical linear charge density dictated by the most highly charged counter-ion.

However, another inherent limitation of the limiting law is that it does not provide a way to evaluate the condensed fraction of each counter-ion, as equations (1.89), (1.92) and (1.93) are insufficient to determine the entire set of condensed fractions. A feasible approach can be derived from Manning's general theory, according to which a mass-action-like relation can be introduced to relate the condensed fractions of counter-ions:

$$\frac{\frac{\theta_i}{1-\theta_i}}{\frac{\theta_j}{1-\theta_j}} = S_{i,j}^{c} = exp\left(\frac{\Delta\mu_{i,j}^{cond}}{R_g T}\right) \tag{1.94}$$

where $\Delta\mu_{i,j}^{cond}$ is the difference in condensation free energy between the counter-ions i and j, and $S_{i,j}^{c}$ is the corresponding condensation selectivity. Although is not possible to directly measure $\Delta\mu_{i,j}^{cond}$, it may be related to the hydration state of the counter-ions [86]. Since the region near the polymer backbone likely has a reduced dielectric constant, condensed ions are expected to be at least partially dehydrated. Assuming that the condensation free energy corresponds to the energy required for the partial dehydration of the counter-ions, the difference in condensation free energy can be expressed by means of the Born model (equation (1.50)) [37]:

$$\Delta\mu_{i,j}^{cond} = \Delta\mu_{i,j}^{hyd} = \frac{N_a e^2}{8\pi\varepsilon_0}\left(\frac{1}{\varepsilon_c} - \frac{1}{\varepsilon_u}\right)\left(\frac{z_i^2}{r_i} - \frac{z_j^2}{r_j}\right) \tag{1.95}$$

where r_i and r_j are the Born radii respectively of the counter-ion species i and j, while ε_c and ε_u are respectively the relative dielectric constant of the condensed phase and uncondensed phase. Consequently, assuming $\varepsilon_c < \varepsilon_u$ the model predicts higher condensation selectivity for ions with larger Born radii, which correlates with weaker hydration (Table 1). Empirical studies confirm that IEMs tend to preferentially absorb ions with larger crystal or smaller hydrated radii [13,64,85]. Consequently, several attempts were made to apply the Born model to predict partition coefficients in membrane [92–94]. However, the direct application of the Born model requires a way to estimate the dielectric constant in the condensed phase, which is rather unpractical given that the concept of condensed and condensed phases is currently ill-defined [77]. Alternatively, a novel, simplified rule based in line with the Born's model prediction can is proposed:

$$\frac{\frac{\theta_i}{1-\theta_i}}{\frac{\theta_j}{1-\theta_j}} = S_{i,j}^{c} = \frac{r_i}{r_j}\frac{z_j^2}{z_i^2} \tag{1.96}$$

This empirical relation allows estimation of condensation selectivity in a multi-ionic system without adjustable parameters. According to equation (1.96), counter-ions with larger Born radii exhibit higher condensed fractions. By combining, equations (1.89), (1.92) and (1.96) the individual condensed fractions of counter-ions and fixed charges can be evaluated, and subsequently inserted into eq. (1.88) to compute the Manning activity coefficients for all mobile ionic species.

1.1.5.3 Extended peNRTL model: a comprehensive framework for ion activity coefficients

As discussed in sections 2.5.1 and 2.5.2, one of the main limitations of the Manning model lies in its restricted range of concentration validity. Indeed, the model has been primarily validated for external salt concentrations between 0.01 and 1 mol L^{-1}. Outside this interval, several studies have reported a significant decline in its predictive accuracy [63,81]. This discrepancy is often attributed to the breakdown of the model's underlying assumptions, including the idealisation of infinite dilution. As noted by Manning himself, this assumption is only expected to hold for salt concentrations up to approximately 0.1 mol L^{-1}.

This latter limitation is likely related to the exclusive consideration of long-range electrostatic interactions between the mobile ions and the polyelectrolyte chains. While this simplification may be acceptable in dilute solutions, where ion–polymer long-range interactions dominate, it becomes inadequate at higher salt concentrations, where additional effects such as ion–ion electrostatic interactions and short-range (e.g., van der Waals-like) forces can significantly influence the system behaviour. These types of interactions are typically captured by more advanced thermodynamic models for aqueous electrolytes, such as the Pitzer model [58], which extend the concentration range over which the activity coefficients can be reliably calculated.

A first attempt to address these limitations was done by Wells et al. [95] who proposed a modified version of the Manning activity coefficient that integrates the mean ionic activity coefficient of the salt in aqueous solution at the same salt concentration. This correction introduces an additional contribution to the total activity coefficient accounting for ion–ion interactions, but still neglects short-range interactions, typically dominant at very high concentrations.

A more recent and comprehensive extension of Manning's model was developed by Chen et al., who adapted the electrolyte Non-Random Two-Liquid (eNRTL) model, originally formulated for simple electrolyte solutions [27], to mixed salt–polyelectrolyte systems, resulting in the so-called polyelectrolyte NRTL (peNRTL) model [96]. The peNRTL model was successfully employed to describe the salt sorption behaviour of a set of tailor-made IEMs equilibrated with NaCl solutions in the 0.01–1 mol L^{-1} concentration range [97]. The model assumes that various non-ideal phenomena contribute additively to the system's excess free energy. Accordingly, the activity coefficient of a given ionic species in the membrane phase could be expressed as the sum of three distinct contributions:

$$ln(\gamma_i^m) = ln\left(\gamma_i^{m,PDH}\right) + ln\left(\gamma_i^{m,LC}\right) + ln\left(\gamma_i^{m,M}\right) \tag{1.97}$$

Here $\gamma_{PDH,i}^m$ accounts for point-to-point (i.e., ion–ion) long-range electrostatic interactions while $\gamma_{LC,i}^m$ represents the short-range interactions (e.g., van der Waals forces), as described by the standard eNRTL model. The third term, $\gamma_i^{m,M}$ is the Manning activity coefficient which quantifies the electrostatic interactions between mobile ions and the charged polymeric matrix. However, the use of the peNRTL model remained limited, as the original Manning framework was developed exclusively for single-salt systems.

In the present work, $\gamma_i^{m,M}$ is evaluated employing the multi-ionic extension of the Manning model (eq.(1.88)), presented in section 1.1.5.2, so that equation (1.97) can be employed to predict activity coefficients in multi-ionic systems at high concentration.

Regarding the other two contributions in equation (1.97), they are evaluated according to the original version of the peNRTL model.

The point-to-point electrostatic interaction term is evaluated through the Pitzer-Debye-Hückel model [98]; an improved version of the Debye-Hückel model outlined in section 1.1.3.11:

$$ln\left(\gamma_i^{m,PDH,(x)}\right) = -A_\varphi \left[\left(\frac{2z_i^2}{\varrho}\right) ln\left[1+\varrho I^{m,(x)^{1/2}}\right] + \frac{z_i^2 I^{m,(x)^{1/2}} - 2I^{m,(x)^{3/2}}}{1+\varrho I^{m,(x)^{1/2}}}\right] \tag{1.98}$$

In the former expression[17], A_φ and ρ are respectively the Debye-Hückel constant and the closest approach parameter [98], while $I^{m,(x)}$ is the molar fraction-based ionic strength:

$$I^{m,(x)} = \frac{1}{2}\sum_i z_i^2 \bar{\theta}_i x_i^m \tag{1.99}$$

where x_i^m is the molar fraction of species i in the membrane, which can be related to the molal concentrations using equation (1.44). The activity coefficients in molar fraction can likewise be converted to molal-based values via equation (1.49). The PDH term reflects the change in excess free energy due to long-range electrostatic interactions: at low ionic strength, attractive forces dominate, leading to reduced activity coefficients; at high ionic strength, repulsive interactions prevail, increasing the excess free energy and hence the activity coefficients. Importantly, equation (1.99) predicts equal activity coefficients for species of identical valence, since the only ion-specific parameter is the valence.

Instead, short-range interactions are modelled using a local composition approach tailored for charged systems and inspired by NRTL theory of Renon and Prausnitz [99]. The corresponding expressions for the local contribution to the activity coefficients are:

[17] Notably, the summation in equation (1.99), includes the fixed charges, while the factors $\bar{\theta}_i$ account for the fraction of uncondensed ions.

$$\frac{1}{z_c}\gamma_c^{m,LC,(x)} = \frac{X_w G_{cw}}{\sum_i X_i G_{iw}}\left(\tau_{cw} - \frac{\sum_i X_i G_{iw}\tau_{iw}}{\sum_i X_i G_{iw}}\right) + \frac{\sum_{i\neq c} X_i G_{ic}\tau_{ic}}{\sum_{i\neq c} X_i G_{ic}} + \sum_a \frac{X_a G_{ca}}{\sum_{i\neq a} X_i G_{ia}}\left(\tau_{ca} - \frac{\sum_{i\neq a} X_i G_{ia}\tau_{ia}}{\sum_{i\neq a} X_i G_{ia}}\right) - (G_{cw}\tau_{cw} + \tau_{wc}) \quad (1.100)$$

$$\frac{1}{z_a}\gamma_a^{m,LC,(x)} = \frac{X_w G_{aw}}{\sum_i X_i G_{iw}}\left(\tau_{aw} - \frac{\sum_i X_i G_{iw}\tau_{iw}}{\sum_i X_i G_{iw}}\right) + \frac{\sum_{i\neq a} X_i G_{ia}\tau_{ia}}{\sum_{i\neq a} X_i G_{ia}} + \sum_c \frac{X_c G_{ac}}{\sum_{i\neq c} X_i G_{ic}}\left(\tau_{ac} - \frac{\sum_{i\neq c} X_i G_{ic}\tau_{ic}}{\sum_{i\neq c} X_i G_{ic}}\right) - (G_{aw}\tau_{aw} + \tau_{wa}) \quad (1.101)$$

$$G_{ij} = exp(-\alpha_{ij}\tau_{ij}) \quad (1.102)$$

$$X_i = |z_i| x_i^m \quad (1.103)$$

In the previous equations[18], X_i represent the effective molar fraction of species i, with the subscripts c, a and w referring respectively to cations, anions and water. α_{ij} is the nonrandomness factor (equal to 0.2 [97]), while G_{ij} and τ_{ij} are respectively the non-adjustable asymmetric binary interaction parameters between species i and j, which are used to describe the short-range interactions[19][27].

In their work, Chen et al. introduced a secondary solvent to represent interactions with nonpolar segments of the polymer. While theoretically more comprehensive, this approach requires knowledge of the polymer's chemical structure to estimate the molar fraction of the nonpolar segments, an impractical task for commercial membranes. Therefore, in this work, we opted for a simplified model in which absorbed water is the only solvent. Additional details on the estimation of the binary interaction parameters are provided in section 1.3.2.3

.

[18] According to equations (1.100) and (1.101), the chosen reference state for the activity coefficients is the aqueous infinite dilution.

[19] In the summations, terms with $i \neq c$ or $i \neq a$ exclude cationic or anionic species, respectively, while $\tau_{ii} = 0$ by definition. Furthermore, the solvent charge number $|z_i|$ is taken as unity.

1.2 Thermodynamics of ion-exchange membranes: experimental investigations

In the previous section, the development of fully or semi-predictive thermodynamic models for ion partitioning in IEMs has been discussed. The validation, and when necessary, the calibration of these models requires experimental information on the equilibrium properties of IEMs, specifically the distribution of mobile ions between the external saline solution and the membrane, as well as the membrane water content. These latter are determined not only by the composition and concentration of the external solution but also by the intrinsic structure of the membrane. For this reason, dedicated experimental investigations are essential to produce reliable data applicable to the specific IEMs under study.

In the present section, the state of the art concerning the main characterization techniques is briefly reviewed. Subsequently, the experimental procedure adopted for the characterization of the selected set of commercial IEMs is described, followed by a presentation and discussion of the novel experimental results.

1.2.1 State of the art of experimental characterization of ion partition

The experimental characterisation of ion partition is essential for understanding the separation mechanisms of IEMs. As discussed in section 2.1, fundamental transport properties such as ionic conductivity and transport numbers strongly depend on the equilibrium concentration of the mobile species within the membrane. Once the equilibrium concentrations are determined, additional properties of interest, such as partition coefficients, selectivity, and activity coefficients can be derived.

The most widely employed characterisation method is commonly referred to as the *desorption technique*. Already employed by Yasuda et al. in 1968 for the characterization of tailor-made hydrated polymer membranes [100], it has since become a standard technique for IEMs characterization [63,84,101–103]. This method involves two main steps: in the first, the membrane sample is equilibrated with the desired electrolyte solution; in the second, the mobile ions absorbed within the membrane matrix are desorbed in an exchange electrolyte. The choice of the exchange electrolyte is crucial, as it must effectively replace the absorbed counter-ions. The exchange solution is then analysed to quantify the amount of mobile ions released. As discussed in the following sections, this approach also allows for the determination of the IEC of the membrane. Despite being time-

consuming, the desorption technique is relatively simple and does not require sophisticated instrumentation or experimental setups.

An alternative approach is the *ashing technique* [64,104,105]. Similar to the desorption technique, it begins with the equilibration of the membrane in the desired solution. However, in this case, the equilibrated samples are subsequently dried, ashed, and dissolved in a suitable solution subsequently analysed with proper analytical techniques. This method is less commonly employed, as it requires specialized equipment for the ashing step and is typically limited to the quantification of counter-ion concentrations. Co-ion concentrations, in turn, are often determined separately through the desorption technique. Nonetheless, it is sometime adopted because, by bypassing the desorption step, it ensures to reliably measure the overall amount of absorbed counter-ions.

Extensive investigations of mobile ion partitioning in both commercial and tailor-made IEMs have traditionally been carried out in moderately concentrated (up to 1 mol L^{-1}) single-salt solutions, including a variety of salts such as alkali and alkaline earth metal chlorides and sulphates [50,66,81,106]. Only recently some studies have begun to explore IEMs behaviour in highly concentrated or multi-ionic solutions [63,84,107], while highly concentrated multi-ionic mixtures remain largely unexplored.

To address this gap and to collect the experimental data required to validate the proposed models over a wider concentration range [0.1–5 $mol\ L^{-1}$], an extensive experimental campaign was conducted on a set of commercial IEMs equilibrated with both highly concentrated single-salt solutions and binary mixtures.

1.2.2 Experimental characterization procedures

In this section, the detailed rigorous procedure adopted for the experimental determination of the ion equilibrium concentration and water uptake in the investigated IEMs is presented.

1.2.2.1 Materials

Ion partition experiments were carried out on the CEMs Fumasep FKE-50 and Fumasep FKS-50, supplied by Fumatech BWT GmbH (Germany). These non-reinforced membranes are commonly employed in water demineralization technologies such as ED. The CEMs were delivered in dry foils in the H^+ form. Their main specifications are summarized in Table 2. The electrolytes used during the equilibration and desorption steps, including sodium chloride (NaCl ≥ 99%), potassium chloride (KCl, ≥ 99.5%), magnesium chloride ($MgCl_2$ > 99%), calcium chloride ($CaCl_2$, ≥ 96%) and nitric acid (HNO_3 ≥ 99.9%) were purchased from Carlo Erba Reagent (Italy). Solutions were prepared using

DI water (σ <1 μS cm^{-1}), obtained by reverse osmosis treatment of tap water followed by polishing with ion-exchange resins.

1.2.2.2 Samples equilibration

Ions' equilibrium concentration in the investigated IEMs was evaluated through the desorption technique briefly outlined in section 1.2.1. Membrane foils were cut into square samples of variable size. Prior to equilibration, the samples were immersed in DI water for 24 h to remove residual solvents from the polymer matrix; the water was replaced after 6 h.

The samples were then equilibrated for 24 h in 50 g of the desired salt solution, which was periodically renewed to ensure complete equilibration. This equilibration time was selected in accordance with literature data. In particular, Galizia et al. [64] demonstrated that 24 h are sufficient to achieve partition equilibrium for all the investigated salts.

CEM samples were equilibrated in single-salt solutions (NaCl, KCl, $MgCl_2$, $CaCl_2$) and in binary equimolar mixtures (NaCl–KCl, NaCl–$MgCl_2$, $MgCl_2$–$CaCl_2$), over the concentration range 0.1–5 mol L^{-1}. After equilibration, samples were quickly rinsed in DI water to remove surface salt, then blotted with tissue paper. The rinsing procedure is critical to prevent contamination of the subsequent desorption solution.

To validate the reliability of this step, preliminary tests were conducted by varying the number and speed of rinses as well as the operator performing the procedure. In line with previous reports [108,109], no systematic effect on the final results was observed. After rinsing, wet samples were immediately weighed, to avoid weight losses due to drying, using an analytical balance (Ohaus Explorer EX324).

1.2.2.3 Co-ion sorption

To quantify co-ion sorption, after equilibration the samples were immersed in 50 g (or 40 g, depending on the expected IEC) of DI water for desorption of mobile salt. Since membranes with higher IEC exhibit stronger Donnan exclusion and thus absorb fewer co-ions, a smaller water volume was used in such cases to obtain measurable concentrations in the desorption solution.

During preliminary tests, a two-step desorption over 48 h was performed, renewing the water after 24 h. However, negligible additional salt release was detected in the second step, indicating that complete desorption occurs within 24 h. Therefore, subsequent experiments were carried out in a single 24 h step.

The desorption solutions were analyzed for cation and anion content using ion chromatography (IC, Metrohm 882 Compact IC Plus and Metrohm 930 Compact IC Flex).

1.2.2.4 Counter-ion sorption

Counter-ion concentrations were measured using an exchange electrolyte after the removal of co-ions. Samples were immersed for 48 h in 50 g (or 40 g) of exchange solution. Specifically, FKE-50 samples were treated with 0.5 mol L^{-1} HNO_3, while FKS-50 samples were treated with 0.1 mol L^{-1} $CaCl_2$.

Initial trials with 0.1 mol L^{-1} HNO_3 proved that HNO_3 concentration lower than 0.5 mol L^{-1} were insufficient to release divalent counter-ions (Mg^{2+}, Ca^{2+}), due to their higher affinity for the membrane relative to H^+. Conversely, in the case of $CaCl_2$, a lower concentration was enough to achieve complete counter-ions desorption given the strong affinity of Ca^{2+}[20].

Preliminary tests confirmed that two successive desorption steps were sufficient to completely extract counter-ions, since no ions were detected in the third solution. Therefore, the exchange solution was renewed once after 24 h, and all solutions were analyzed by IC.

1.2.2.5 Water uptake and water volume fraction evaluation

After counter-ion desorption, samples were dried in a static oven (Argolab TCN50 Plus) at 40 °C for 48 h, then weighed rapidly to minimize moisture uptake. The water uptake was calculated as:

$$w_u = \frac{M_w}{M_{dry}} = \frac{M_{wet} - \left(M_{dry} + \left(M_{fix.\ cou.} - M_{ex.\ cou.}\right) - M_{salt}\right)}{M_{dry}} \tag{1.104}$$

where M_{wet} and M_{dry} are respectively the wet mass of the sample after the equilibration step and the dry mass of the sample at the end of the ion-exchange procedure. The extra terms at the numerator of eq. (1.104) are included to account for weight variation of the sample due to the ion-exchange procedure. $M_{fix.\ cou.}$ and $M_{ex.\ cou.}$ are respectively the mass of desorbed fixed counter-ions and the mass of exchange counter-ions, introduced in eq. (1.104) to account for the difference in the molar weight between the fixed counter-ions (i.e., those virtually balancing the fixed charges) and the exchange counter-ions (i.e., H^+ or Ca^{2+}). M_{salt} is the total mass of mobile salt released during the desorption steps in DI water. Such term is usually neglected in the literature because low concentration range are typically investigated. However, M_{salt} can be non-negligible when working

[20] Nitric acid was used for the FKE-50 as $CaCl_2$ was among the investigated salt, therefore Ca^{2+} ions could not be used as exchange counter-ions. Conversely, FKS-50 was not tested with $CaCl_2$.

with highly concentrated solutions. It is also important to stress that due to the chosen sequence in the desorption steps, at the end of the procedure the mass of the dry samples M_{dry} depends on the molar weight of the exchange counter-ions. Therefore, when comparing different water uptakes, it is necessary to specify the counter-ion form of the membrane.

From the water uptake it is also possible to derive another important physical quantity which is the water volume fraction in the swollen membrane [81]:

$$\phi_w = \frac{w_u}{w_u + \frac{\rho_w}{\rho_p}} \tag{1.105}$$

In the previous equation ρ_p correspond to the mass density of the dry polymer, while ρ_w is the mass density of pure water. Equation (1.105) is derived by assuming additivity of polymer and water volumes (i.e., neglecting thermodynamic volume effects) and disregarding the volume contribution of mobile ions. Nonetheless, it is widely adopted to estimate water volume fraction, as direct measurements are prone to larger errors, while water uptake can be determined with higher accuracy [81].

1.2.2.6 Mobile ions and fixed charges concentration evaluation

Following the desorption tests, the moles of desorbed ions can be evaluated using the following equation:

$$n_i^m = \frac{\sum_j M_j^{ds} w_{i,j}^{ds}}{MW_i} \tag{1.106}$$

where $w_{i,j}^{ds}$ is the mass fraction of ionic species i in the j-th desorption solution of mass M_j^{ds}, obtained from the chromatographic analysis. The summation is extended to all the desorption steps. Using equation (1.104) the molal concentration of ions in the membrane was obtained as:

$$m_i^m = \frac{n_i^m}{w_u M_{dry}} \tag{1.107}$$

where the product $w_u M_{dry}$ corresponds to the mass of absorbed water M_w.

The evaluation of the molar concentration would require the knowledge of the solution density, according to equation (1.42). Typically, the solution density is assumed to be equal to that of pure

water. A more refined approach, tough still simplified, can be derived by applying Euler's equation (1.19) taking limiting partial molar volumes (i.e., at infinite dilution, see Table 1), giving:

$$C_i^m = \frac{n_i^m}{\upsilon_w n_w^m + \sum_i \upsilon_i n_i^m} \tag{1.108}$$

where n_w^m are the moles of sorbed water which can be straightforwardly evaluated from the mass of sorbed water M_w.

Another important IEM property that can be derived from the ion partition tests is the fixed charge concentration, that can be easily quantified by applying the electroneutrality condition in the membrane [21] (equation (1.34)). Finally, the membrane ion-exchange capacity was evaluated according to the following equation:

$$IEC = m_{fix} w_u \tag{1.109}$$

While fixed charge concentration depends on membrane water uptake, the IEC of strongly acidic/basic membranes (i.e., with fully dissociated fixed groups) is independent of external solution concentration and composition. The values measured during ion sorption tests are reported in Table 2. From equilibrium ion concentrations, partition coefficients and partition selectivity were also determined using equations (1.73) and (1.74).

Table 2 Fumasep FKE-50 and FKS-50 properties. The "measured" quantities are mean values over all investigated concentrations and compositions. The fixed charges concentration, the water uptake and the IEC were determined following the procedure explained in section 1.2.2. All the previous quantities are tabulated in the H^+, except for FKS-50 properties measured in the Ca^{2+} form. The dry thickness was measured using a micrometre; the dry density was determined as the ratio between the dry mass of the samples and their dry volume, evaluated as the product between the average thickness and the dry surface area.

CEM	Source	m_{fix} [mol kg_w^{-1}]	w_u [g_w g_{dry}^{-1}]	IEC [mmol g_{dry}^{-1}]	Dry Thickenss [μm]	ρ_{dry} [g_{dry} cm^{-3}]
FKE-50	Measured	4.24 ± 0.40	0.35 ± 0.02	1.51 ± 0.04	54 ± 1.5	1.35 ± 0.03
	Manufacturer [110]	4.35 ± 2.32	0.33 ± 0.18	1.45 ± 0.05	50 ± 5.0	1.6 ± 0.30
FKS-50	Measured	6.34 ± 1.20	0.22 ± 0.04	1.35 ± 0.08	47.0 ± 2.7	1.29 ± 0.04
	Manufacturer [111]	7.37 ± 2.94	0.18 ± 0.07	1.3 ± 0.10	50 ± 5.0	1.58 ± 0.18

[21] Although the charge density is rigorously defined per unit of volume, in an electroneutral system, the sum of ions equivalent per unit of mass of solvent (i.e., molal equivalents) must be equal to zero anyway

1.2.2.7 Experimental determination of activity coefficients in the membrane phase

Once equilibrium concentrations are known, activity coefficients in the membrane phase can also be evaluated. Unlike partition coefficients or selectivity, which follow directly from definitions, activity coefficients are derived quantities, requiring a thermodynamic framework, such as the Donnan model (section 1.1.4.2) or its extended version (section 1.1.4.4). to be evaluated.

In this case, equilibrium equations must be inverted to calculate activity coefficients. As discussed in section 1.1.3.7, single-ion activity coefficients are not physically meaningful and only neutral combinations can be measured. Following Newman's approach, by defining a reference ion n, the activity coefficients of the other ions can be expressed as by proper combination of equations (1.69) and (1.70):

$$\gamma_{i(n)}^{m} = \gamma_{i(n)}^{s} \left(\frac{C_i^s}{C_i^m}\right)\left(\frac{C_n^s}{C_n^m}\right)^{-\frac{z_i}{z_n}} e^{-\left(v_i - \frac{z_i}{z_n} v_n\right)\frac{\Delta P}{R_g T}} \tag{1.110}$$

In order to solve equation (1.110), the swelling pressure ΔP must be evaluated by solving the full extended Donnan model, including the water partition equation. However, the overall model constitutes a system of non-linear equations which can only be solved numerically. This rigorous approach will be discussed in section 1.3.

Therefore, unless otherwise stated, in this work activity coefficients are evaluated using the simplified expression:

$$\gamma_{i(n)}^{m} = \gamma_{i(n)}^{s} \left(\frac{C_i^s}{C_i^m}\right)\left(\frac{C_n^s}{C_n^m}\right)^{-\frac{z_i}{z_n}} \tag{1.111}$$

Here, $\gamma_{i(\mathrm{n})}^{\mathrm{s}}$ is Newman's activity coefficient of the species i in the external solution with reference to the species n. This can be evaluated through equation (1.41) if experimental values of the mean ion activity coefficient of the corresponding salt are known or, equivalently, by employing a thermodynamic model such as the Debye-Hückel or the Pitzer model. These models do provide a theoretical estimation of single-ions activity coefficients that can be combined through equation (1.40) to evaluate $\gamma_{i(n)}^{s}$.

In the literature, it is more common to provide expressions for the activity coefficients in the form of the mean ion activity coefficient $\bar{\gamma}_{in}^{m}$. However, as explained in section 1.1.3.7, this can be easily converted into $\gamma_{i(\mathrm{n})}^{m}$ by means of equation (1.41) and vice versa.

1.2.3 Experimental results on commercial IEMs

In the following sections, the results of the ion partition experimental campaign on the investigated IEMs are presented and discussed. The experimental data herein showed were employed for the calibration and validation of the models described in section 1.1.5. A more detailed discussion of the validation procedure can be found in section 1.3. Following the procedure explained in section 1.2.2, the CEMs FKS-50 and FKE-50 were equilibrated with single-salt or mixed-salt aqueous solutions of NaCl, KCl, $MgCl_2$, and $CaCl_2$, covering concentrations from 0.1 mol L^{-1} up to 5 mol L^{-1} or the solubility limit of the respective salt. The investigated electrolyte systems were chosen such that Cl^- was the common co-ion. Consequently, differences in the experimental results can be ascribed to the specific nature of the counter-ions.

1.2.3.1 Water uptake

Water uptake is a key property of IEMs, as it exerts a significant influence on ion partitioning [65]. According to equation (1.109), the amount of absorbed water is inversely related to the fixed charge concentration, which in turn governs the extent of co-ion sorption.

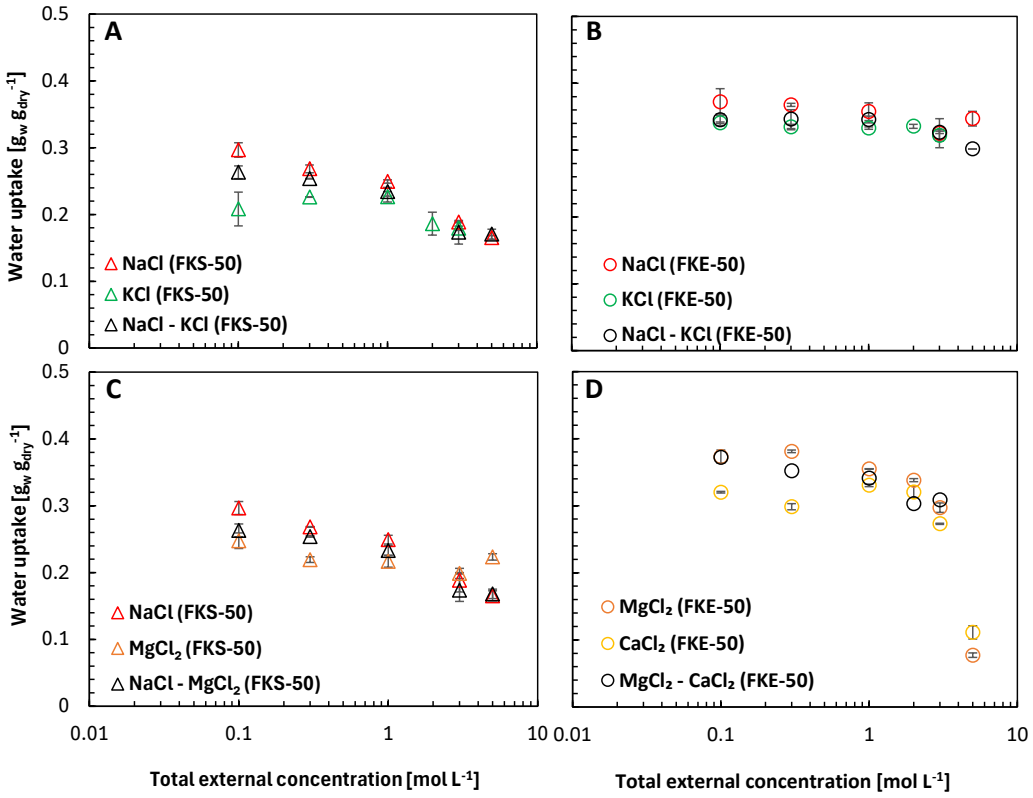

Figure 5 Fumasep FKE-50 (circles) and FKS-50 (triangles) water uptake versus total external concentration for the investigated single-salt and binary equimolar mixtures.

Figure 5 reports the water uptake of the investigated membranes as a function of the external solution concentration. For all the investigated CEMs, water uptake decreases markedly with increasing salt concentration. It is well established that water uptake depends on both the concentration and composition of the external electrolyte [16,64,104]. In particular, the limited uptake of mobile salt into the membrane phase increases the osmotic pressure difference between the external solution and the membrane when the external concentration is increased, thereby reducing water sorption in the IEM through the phenomenon known as osmotic deswelling [112]. At low external concentrations, the water uptake values measured with different salts do not converge to the same value. This behaviour can be attributed to differences in the hydration properties of the counter-ions, which render the membrane more or less hydrophilic depending on the ion. Furthermore, in the case of binary salt mixtures, the measured water uptake generally lies between the values obtained for the corresponding single-salt solutions.

A further noteworthy comparison can be made between the FKS-50 and FKE-50 membranes. At comparable solution concentrations and compositions, FKE-50 exhibits a significantly higher water uptake than FKS-50. This difference is consistent with the higher IEC of FKE-50 (Table 2). Indeed, a higher IEC results in greater water uptake, since a larger minimum number of water molecules is needed to adequately solvate the fixed charges [76]. This phenomenon is widely recognized as a major challenge in the design and manufacturing of commercial IEMs [113–115]. In fact, on the one hand, a high IEC is desirable to increase the fixed charge concentration and thus improve co-ion exclusion; on the other hand, the concomitant increase in water uptake reduces the effective fixed charge concentration, limiting selectivity.

1.2.3.2 Single-salt equilibrium concentration

Figure 6 reports the ion equilibrium concentrations inside the membranes as a function of the external salt concentration. At low external concentrations, co-ion sorption is negligible owing to the Donnan exclusion effect; consequently, the counter-ion concentration is fairly constant and approaching the fixed charge concentration. Notably, the equilibrium concentration of Mg^{2+} and Ca^{2+} in the membrane phase is approximately half that of Na^{+} and K^{+}, due to their divalent charge.

At higher external salt concentrations, co-ion sorption increases due to the weakening of the Donnan exclusion effect, which is associated with a reduction of the Donnan potential. The increase in co-ion sorption is particularly pronounced in the case of divalent cations (Mg^{2+} and Ca^{2+}), since the Donnan potential is inversely related to the valence of the counter-ions. Thus, at the same external concentration, divalent counter-ions give rise to higher co-ion concentrations in the membrane [85].

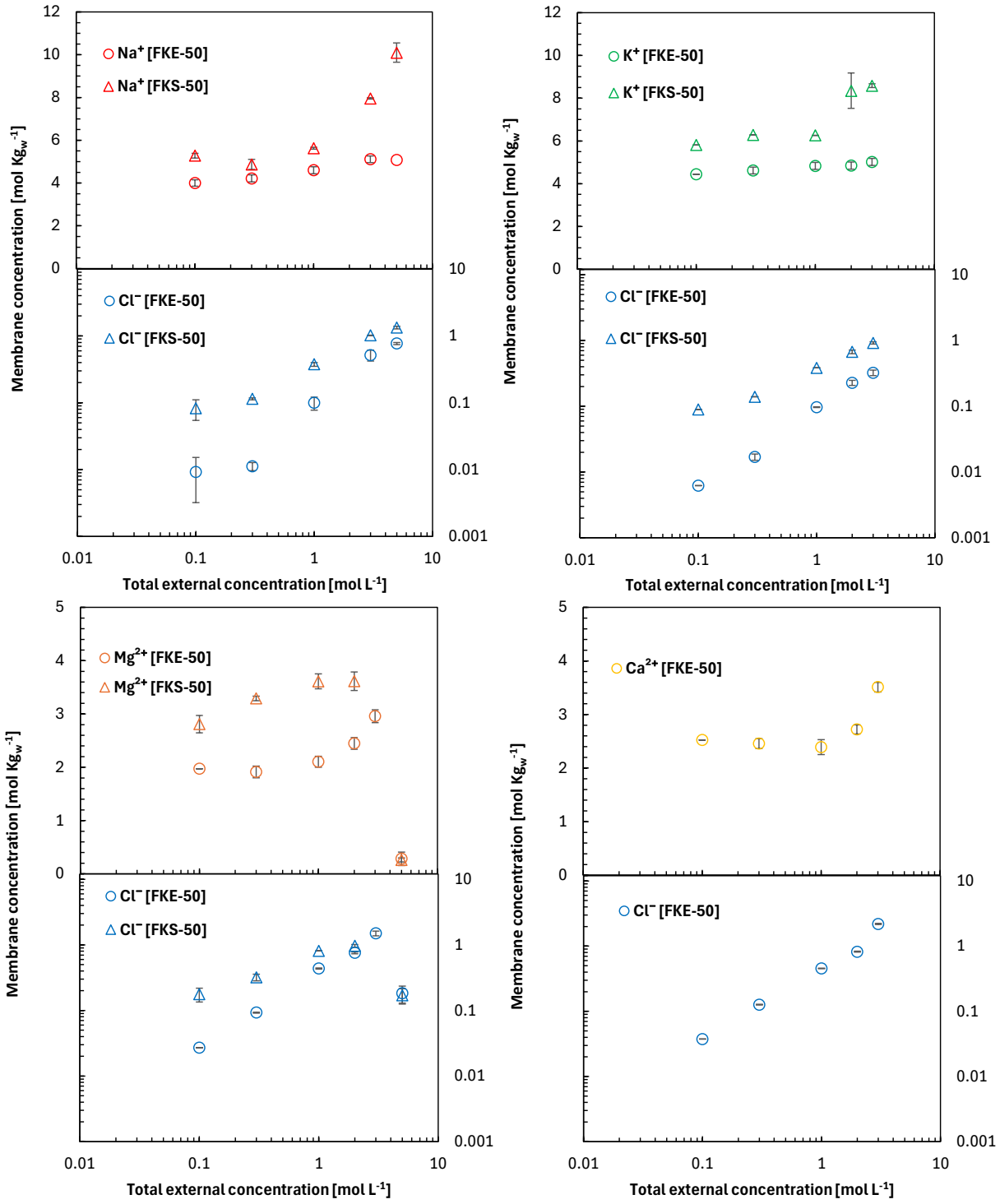

Figure 6 Fumasep FKE-50 (circles) and FKS-50 (triangles) ions molal concentration versus the external salt concentration for single-salt systems containing NaCl (A), KCl (B), $MgCl_2$(C) or $CaCl_2$ (D). The empty circles are the experimental data. The associated error bars were plotted considering the maximum error between the theoretical error evaluated through the error propagation theory and the experimental error on at least two different tests.

Because electroneutrality must be preserved, the co-ion concentration is directly proportional to the amount of absorbed mobile salt, with equal equivalents of counter-ions and co-ions sorbed in the membrane. In absolute terms, FKS-50 exhibits a higher counter-ion concentration than FKE-50, despite its lower IEC. This can be explained by its lower water uptake, as shown in Figure 5. Conversely, the co-ion concentration in the FKS-50 membrane is always lower than in the FKE-50. This result is relatively surprising, given the higher fixed charge concentration of FKS-50 (see Table 2). Indeed, according to the ideal Donnan model, IEMs with higher charge density are expected to absorb a lower amount of co-ions due to electrostatic repulsion. This implies that a partitioning mechanism different from Donnan exclusion is playing a significant role in determining co-ion sorption. Recent studies have highlighted how steric or dielectric exclusion may be relevant in determining IEMs selectivity [47,76,94]. Indeed, according to the Born model (eq. (1.50)), ion partition into the membrane phase is thermodynamically unfavoured due to the lower dielectric permittivity of the membrane phase. This can be physically attributed to dielectric saturation of the water molecules in the membrane phase. Indeed, the water molecules forming the solvation shell of the fixed charges in the membrane phase totally or partially lose their polarizability due to the strong interactions with the charged groups. Consequently, they lose their ability to solvate mobile ions [75,93]. According to Freger [116], such a dielectric exclusion effect would be particularly relevant in IEMs with high IEC, where water molecules polarizability is suppressed to a greater extent. This physical picture is consistent with the higher IEC of FKE-50, suggesting that dielectric exclusion could play a relevant role in determining co-ion partition in this membrane.

Regarding the tests with $MgCl_2$ and $CaCl_2$ at external concentrations above 3 mol L^{-1}, the desorption analysis revealed negligible mobile ion concentrations for both membranes. This result is shown in Figure 11C for FKS-50 equilibrated with pure $MgCl_2$, while for FKE-50 additional measurements at slightly lower concentrations (< 3 mol L^{-1}) were carried out to provide sufficient data for model calibration and validation. Two possible explanations may account for this unexpected phenomenon. First, it may be hypothesized that when equilibrated with highly concentrated Mg^{2+} or Ca^{2+} solutions, the membranes retain the absorbed ions, preventing their release. This could result from scaling phenomena associated with the precipitation of neutral salts inside the membrane matrix, particularly given that $MgCl_2$ and $CaCl_2$ are well-known scaling agents. To support this hypothesis, the extended Donnan–peNRTL model (see sections 1.1.5.3 and 1.3.2.3) was employed to estimate the external concentrations at which salt precipitation would occur in the membrane phase (Figure 7).

In these plots, the solid lines represent the ionic activity products in the membrane, while the dashed line corresponds to the salt solubility product. For both $MgCl_2$ and $CaCl_2$, the precipitation condition

is reached at external concentrations of approximately 3.5 mol L^{-1}, consistent with the experimental observation of negligible ion release.is reached at external concentrations of approximately 3.5 mol L^{-1}, consistent with the experimental observation of negligible ion release.

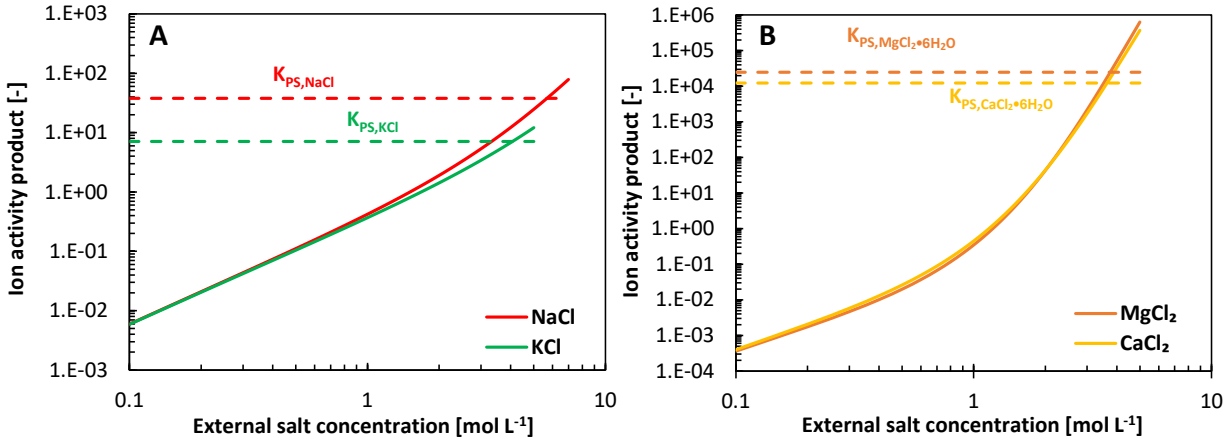

Figure 7 Ion activity product in the membrane phase for the FKE-50 CEM equilibrated with single-salt solution at various salt concentrations evaluated by means of the extended peNRTL model (see sections 1.1.5.3). The dashed lines represent the solubility product of the corresponding salts at 25°C. For the divalent cations Mg^{2+} and Ca^{2+}, the solubility product of the corresponding hexahydrated salt (i.e., $MgCl_2$•6 H_2O and $CaCl_2$•6 H_2O) were considered given their lower solubility.

A second explanation may be offered by considering the presence of nanometric pores, i.e., membrane domains occupied by mobile ions and water molecules. At high external ionic strength, osmotic deswelling could cause the shrinkage of such pores. Since divalent cations are more strongly hydrated than monovalent ones, steric effects associated with their hydration shells could impede their entry into the membrane, explaining the abrupt reduction in their observed desorption.

At present, these interpretations remain speculative. Further dedicated investigations are required to elucidate the mechanisms underlying this intriguing behaviour.

1.2.3.3 Binary salt mixtures equilibrium concentration

Ion partitioning tests were also performed with equimolar binary mixtures, namely NaCl–KCl, $MgCl_2$–$CaCl_2$, and NaCl–$MgCl_2$. The experimental results are presented in Figure 8. For the NaCl–KCl mixture, the counter-ions concentration in both CEMs remained nearly constant up to an external concentration of 1 mol L^{-1}. Beyond this point, co-ion sorption increased, leading to a corresponding rise in counter-ions concentration. The reduction in water uptake (Figure 5) likely contributes to this trend, given that ion concentrations are reported on a water-mass basis. Moreover, Figure 8D shows that K^+ is preferentially partitioned into the membrane. However, notable differences arise between the two CEMs: in FKE-50, the K^+/Na^+ partition selectivity S_{K^+/Na^+} is approximately 1.4, with a slight

decrease at higher external concentrations; in FKS-50, instead, the selectivity increases with concentration.

The preferential partitioning of K^+ over Na^+ has been previously reported [72,85] and is commonly attributed to differences in the hydration states of the two ions. Sorption in the membrane is generally more favourable for ions with larger crystal radii. According to Born's model of ion solvation, ion transfer into a medium of lower dielectric constant is thermodynamically more favourable for ions with larger Born radii [92]. This explains the increase in S_{K^+/Na^+} observed for FKS-50: as water uptake decreases at higher salt concentrations, the dielectric constant of the membrane phase is reduced, further disfavouring Na^+ partitioning, given its higher charge density. In contrast, this change in selectivity appears less relevant for FKE-50, likely due to its limited osmotic deswelling.

Similar considerations apply to the $MgCl_2$–$CaCl_2$ system. The partition selectivity $S_{Ca^{2+}/Mg^{2+}}$ is relatively independent of the external concentration as well and it is higher than 1, consistent with the larger crystal radius of Ca^{2+}. Furthermore, the co-ion concentration trends (Figure 8C) resemble those obtained in the single-salt experiments with counter-ions of the same valence, suggesting that the presence of two counter-ions of equal charge does not significantly alter co-ion sorption.

For the NaCl–$MgCl_2$ mixture, the partition selectivity S_{Mg^{2+}/Na^+} reported in Figure 8E is significantly higher than 1 at low external concentrations but decreases rapidly with increasing total concentration. This behaviour can be explained by the strong electrostatic contribution to ion partitioning, which favours divalent Mg^{2+} over monovalent Na^+. As the external concentration increases, however, the growing co-ion content reduces the Donnan potential, thereby weakening the electrostatic contribution and lowering the observed Mg^{2+}/Na^+. selectivity

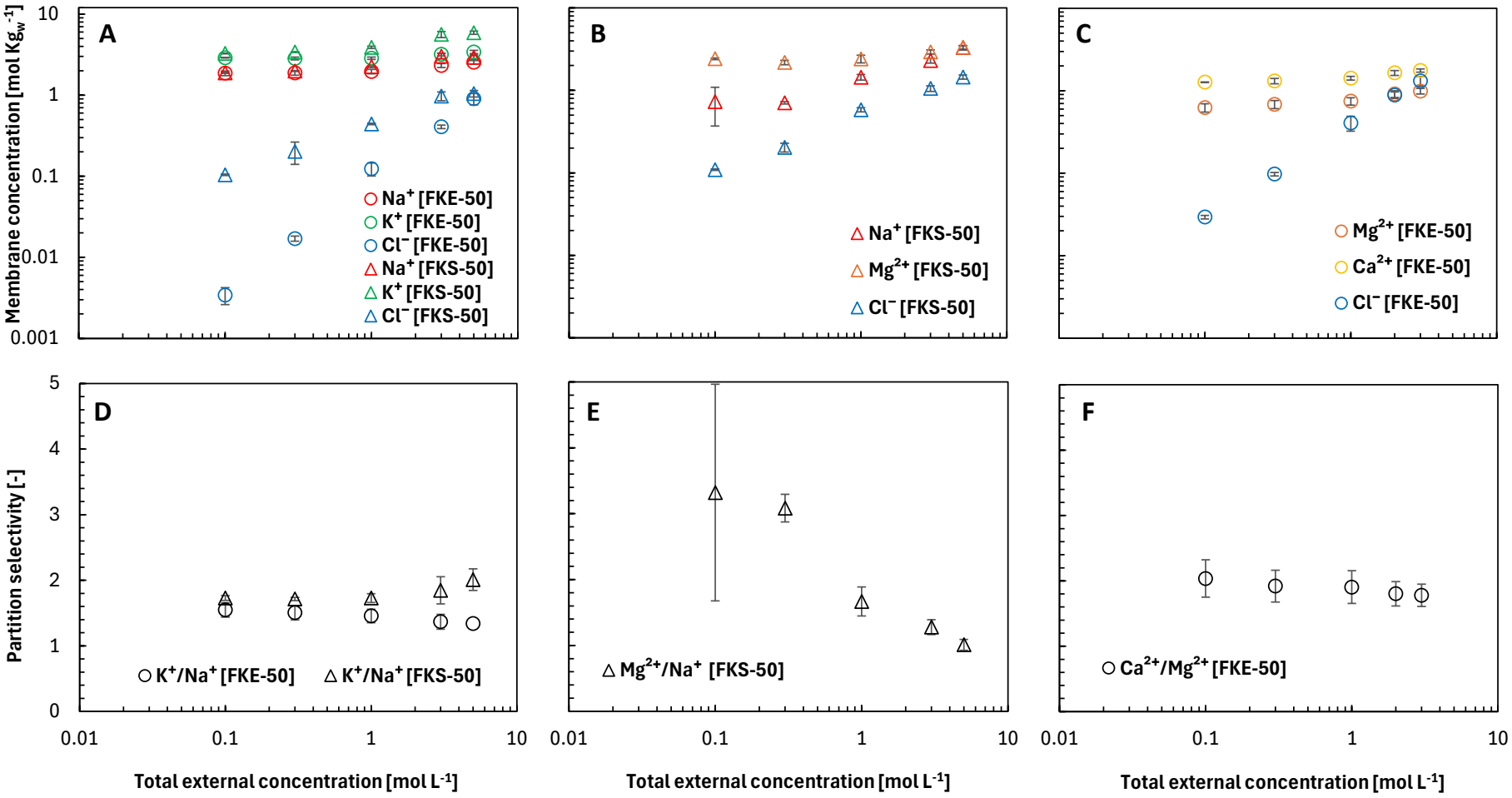

*Figure 8 Membrane equilibrium concentrations (**A,B,C**) and partition selectivity (**D,E,F**) for FKE-50 (empty circles) and FKS-50 (triangles) equilibrated with binary equimolar salt mixtures at various total concentrations.*

1.3 Thermodynamics of ion-exchange membranes: numerical simulations and validation

The present section is focused on the validation of the proposed thermodynamic ion-partitioning models. The experimental partition data presented in section 1.2 are employed both to calibrate the models, when necessary, and to assess the robustness of the different modelling frameworks, particularly under high-salinity conditions and in the presence of multiple ionic species.

It should be emphasized that comprehensive thermodynamic models capable of accurately describing ionic equilibria under a wide range of operating conditions almost invariably require calibration parameters. More than a century has passed since Peter Debye and Erich Hückel introduced the first rigorous theoretical framework for representing thermodynamic non-idealities in aqueous electrolyte solutions. Yet, the complexity of the problem is such that no fully predictive model is currently available for describing ionic interactions in highly concentrated, multi-ionic systems. Even the most advanced and widely adopted approaches, such as the Pitzer and eNRTL models, rely extensively on empirical parameters derived from experimental data. Their effectiveness, however, stems from the solid theoretical foundations that enable them to represent non-ideal interactions in a physically meaningful manner.

This section begins with an evaluation of the extended Donnan model as a theoretical framework to estimate activity coefficients in the membrane phase from ion partitioning data. In the subsequent parts, the conventional Donnan model is applied in combination with the developed thermodynamic models for ion activity coefficients to predict ion partitioning in the investigated IEMs. The calibration procedure is first introduced, followed by a critical comparison among the different models.

1.3.1 Experimental evaluation of activity coefficients via extended Donnan model

In sections 1.1.4.3 and 1.1.4.4 it was shown that, in the rigorous formulation of ion partition equilibria at the solution–membrane interface, water partition is intrinsically coupled to ion partition through the hydrostatic pressure difference ΔP. According to equation (1.73), this term represents an osmotic contribution to the ion partition coefficient. Such a contribution is typically neglected when applying the Donnan model, but this omission inevitably introduces errors in the evaluation of ions' activity coefficients in the membrane phase from experimental partition data.

Furthermore, as discussed in section 2.1.3.6, the application of the extended Donnan model is necessary to rigorously describe water transport across an IEM separating two compartments at different salinity, since it is necessary to evaluate the pressure at both solution-membrane interfaces. Nonetheless, the modelling of water partition still remains largely disregarded.

In order to perform such analysis, the extended Donnan model (See sections 1.1.4.2, 1.1.4.3 and 1.1.4.4) must be solved for $N-1$ activity coefficients $\gamma_{i(n)}^{m}$, the Donnan potential $\Delta\varphi$, the hydrostatic pressure difference ΔP and the osmotic pressure difference $\Delta\pi$, where N denotes the number of mobile ionic species. If C_i^m and C_i^s are determined from ion partition tests, the overall number of unknowns is $N+2$. For each mobile species, including water, an equilibrium equation can be written, while the Gibbs–Duhem equation provides an additional relation between solvent and solute activities. This yields a total of $N+2$ independent equations, and hence the system is mathematically determined.

In the following, the extended Donnan model is applied to the ion partition data collected for the FKS-50 CEM equilibrated with aqueous NaCl solutions at different concentrations. Taking Cl^- as the reference species for the quasi-electrostatic potential, and making explicit the unknown variables, the extended Donnan model equations can be expressed as follows:

$$\gamma_{i,n}^{m} = \gamma_{i,n}^{s}\frac{C_i^s}{C_i^m}e^{-\frac{z_i\mathcal{F}}{R_gT}\Delta\varphi}e^{-\frac{v_i}{R_gT}\Delta P} \tag{1.112}$$

$$\Delta\varphi = \frac{R_gT}{z_n\mathcal{F}}ln\left(\frac{C_n^s}{C_n^m}\right) \tag{1.113}$$

$$\Delta P = \Delta\Pi = \Pi^m - \Pi^s \tag{1.114}$$

$$\Pi^m = \Pi^{m,id} + \Pi^{m,ex} = R_gT\sum_{j\neq w}C_i^m + R_gT\sum_{j\neq w}\int_{C_i^{*m}}^{C_i^m} C_i^m dln\left(\gamma_{i(n)}^m\right) \tag{1.115}$$

Compared to the ideal Donnan model (i.e., equation (1.72)), the above system is significantly more complex and cannot be solved analytically due to the integral equation (1.115) which originates from the Gibbs–Duhem relation. A useful simplification consists in neglecting the excess osmotic contribution in the membrane phase, i.e.:

$$\Pi^m \approx R_g T \sum_{j \neq w} C_i^m \tag{1.116}$$

Although this assumption is quite strong, it has been adopted in some of the most influential works in the field [43,73,74]. Under this approximation, and by using the limiting (i.e., infinite dilution) partial molar volumes reported in Table 1 in equation (1.112), the extended Donnan model was employed to evaluate the hydrostatic pressure, osmotic pressure, and activity coefficients reported in Figure 9.

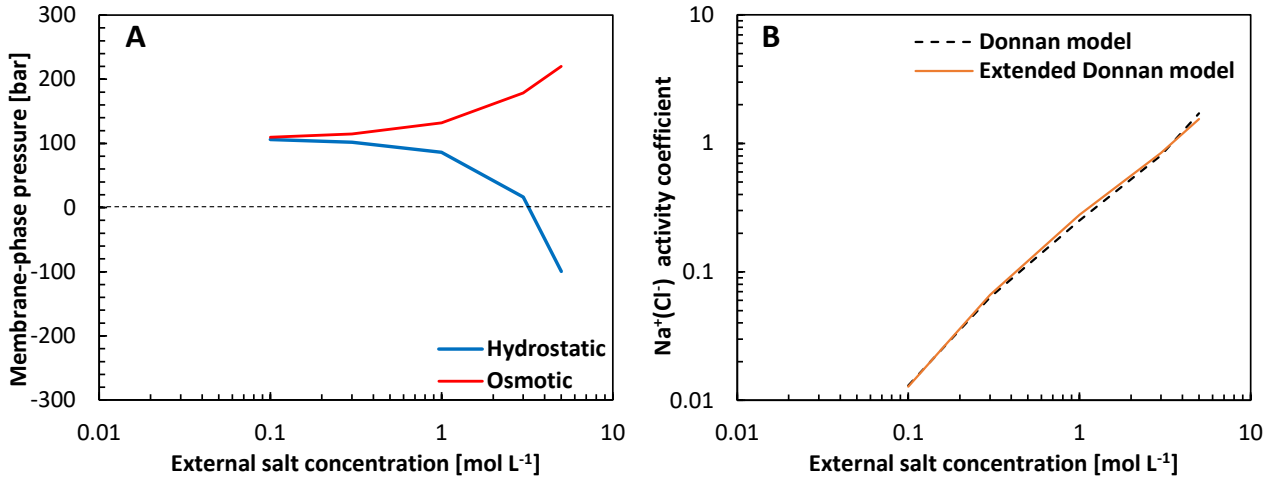

*Figure 9 (**A**) Hydrostatic and ideal osmotic pressure in FKS-50 equilibrated with NaCl solution at various concentration. (**B**) Na^+ Newman's activity coefficient with Cl^- as reference ion in FKS-50 equilibrated with NaCl solutions evaluated from ion equilibrium concentration either through the Donnan model (crosses) or the extended Donnan model (triangles).*

The activity coefficient in the membrane phase $\gamma^m_{Na(Cl)}$ increases with the external salt concentration following a power-law trend. At very high concentrations, it exceeds unity, suggesting unfavourable interactions between mobile ions and fixed charges within the membrane phase. This point is of particular relevance and is further analysed in section 1.3.3. A direct comparison between the traditional and extended Donnan model (Figure 9B) also reveals that the activity coefficient $\gamma^m_{Na(Cl)}$ is only weakly affected by the osmotic contribution in equation (1.112), owing to the small values of the ionic partial molar volumes.

Regarding the hydrostatic pressure in the membrane phase, it remains nearly constant at low concentrations but decreases sharply at high external salt concentrations, following an inverse trend

relative to the osmotic pressure. This behaviour can be rationalised by combining equations (1.114) and (1.116) with the definition of ideal osmotic pressure (equation (1.80)) [22]

$$P^m = P^s + R_g T \sum_{i \neq w} (C_i^m - C_i^s) \tag{1.117}$$

Due to Donnan exclusion, ions' concentration inside the membrane increases sub-linearly with the external concentration. According to equation (1.117), this induces a reduction of the hydrostatic pressure within the membrane to ensure osmotic equilibrium. At high external concentrations, this reduction becomes so pronounced that P^m turns negative. Such an unexpected outcome was admitted possible in a recent work, where Wang et al. [74] investigated osmotic equilibrium in uncharged membranes for reverse osmosis. The authors suggested that the hydrostatic pressure in the membrane can assume negative values due to the concentration difference across the interface, although they did not further elaborate on its physical meaning. From a thermodynamic standpoint, a negative absolute pressure is meaningless. However, mathematically, a negative pressure corresponds to a positive driving force for water partitioning in the membrane, suggesting either the breakdown of model assumptions or the absence of additional terms in the equilibrium equations. It is important to note that Wang et al. also neglected the excess osmotic contribution in the membrane phase. This term is expected to increase in magnitude with external concentration due to strong non-idealities.

A more rigorous treatment therefore requires the use of the full definition of osmotic pressure given in equation (1.115). Applying this equation involves integrating the term $C_i^m dln\left(\gamma_{i(n)}^m\right)$ from the reference state to the experimental point. Mathematically, this can be solved by combining an integration method (e.g., the trapezoidal rule) with a numerical solver. However, this approach requires knowledge of ion activity coefficients over the entire integration domain.

Considering that the reference state for activity coefficients is taken as infinite dilution in water, equation (1.115) can be rewritten as follows:

$$\Pi^m = \Pi^{m,id} + \Pi^{m,ex} = R_g T \sum_{j \neq w} C_i^m + R_g T \sum_{j \neq w} \int_0^{C_i^m} C_i^m dln\left(\gamma_{i(n)}^m\right) \tag{1.118}$$

At this point, two major issues arise. First, a large number of experimental data points would be required to adequately cover the integration range, which is practically impossible since ion

[22] This analysis is actually valid only if the osmotic coefficient in the external solution is assumed to be unitary.

partitioning experiments cannot be performed at concentrations below 0.01 M due to negligible salt uptake in membrane. Second, and more fundamental, because of the fixed charges in the membrane, it is impossible to reach vanishing ion concentrations in the membrane phase, even when approaching infinite dilution in the external solution. This makes the infinite-dilution state experimentally inaccessible and conceptually inconvenient.

One might be tempted to overcome this limitation by selecting a different reference state. For instance, the state in which the IEM is in a particular counter-ion form and equilibrated with pure water. However, this choice would not resolve the problem. Changing the reference state in the membrane phase modifies the definition of the standard chemical potentials (see equation (1.68)) thereby introducing an additional unknown variable into the equilibrium equation. Yet, this unknown is also inherently present when the infinite-dilution reference state is retained. Indeed, by rewriting (1.118) in two separate contributions:

$$\begin{aligned} \Pi^{m,ex} &= \Pi^{m,ex,0} + \Pi^{m,ex,ref} \\ &= R_g T \sum_{j \neq w} \int_{0}^{C_i^{m,ref}} C_i^m \, dln\left(\gamma_{i(n)}^m\right) + R_g T \sum_{j \neq w} \int_{C_i^{m,ref}}^{C_i^m} C_i^m \, dln\left(\gamma_{i(n)}^m\right) \end{aligned} \tag{1.119}$$

with $C_i^{m,ref}$ being the ion concentration in the new arbitrarily chosen reference state, it becomes evident that the second term on the right-hand side of equation (1.119) is experimentally and mathematically accessible, while the first term reduces to a constant ($\Pi^{m,ex,0}$) that embodies a contribution to the excess osmotic pressure which cannot be evaluated from partitioning data alone. Therefore, regardless of the reference state adopted, an additional unknown parameter inevitably appears in the non-ideal formulation of extended Donnan equilibria.

Following the latter formulation, the hydrostatic pressure in the membrane can be rewritten by combining equation (1.115), (1.118) and (1.119):

$$P^m = P^s + \left(\Pi^{m,id} + \Pi^{m,ex,0} + \Pi^{m,ex,ref} - \Pi^s\right) \tag{1.120}$$

From a thermodynamic standpoint $\Pi^{m,ex,0}$ represents the excess pressure energy required to transfer a mole of water molecules from infinite dilution to the chosen reference state in the membrane phase. This term cannot be directly computed from ion-equilibrium concentrations and would require additional experimental information, such as the hydrostatic pressure in the membrane. Although this quantity cannot be measured directly, it might be indirectly inferred from the membrane swelling

degree (i.e., the water volume fraction), provided that a suitable theoretical model (i.e., an equation of state coupling mechanical and thermodynamic properties of the membrane is available.

Supporting this view, several authors [71,117] recently discussed, in reverse osmosis membranes, the necessity of including an additional contribution to the water chemical potential, termed elastic pressure, which is associated with the compression state of polymeric chains. Unlike hydrostatic pressure, elastic pressure can take negative values and has the physical meaning of a mechanical stress. Such additional contribution to the non-ideal chemical potential of water in the membrane phase may correspond to the unknown non measurable contribution to the excess osmotic pressure in the membrane phase $\Pi^{m,ex,0}$.

To conclude this discussion, a sensitivity analysis is reported to assess how different values of the unknown parameter $\Pi^{m,ex,0}$ affect the evaluation of the hydrostatic pressure in the membrane phase:

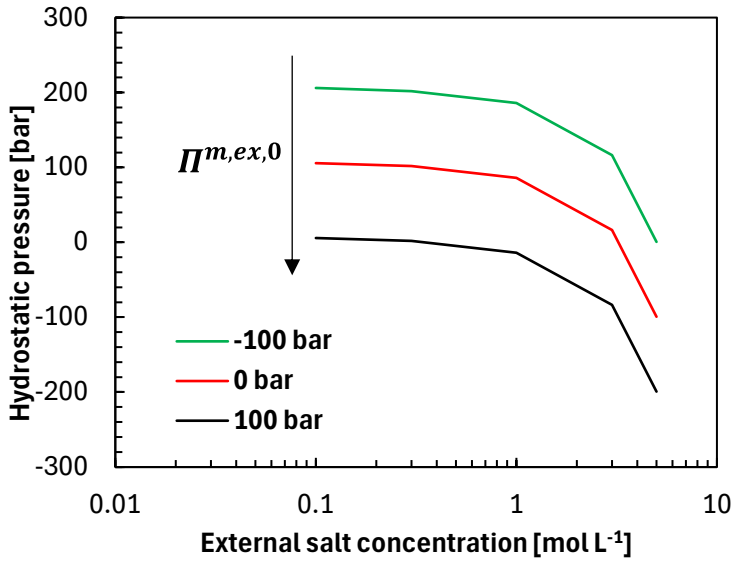

Figure 10 Hydrostatic pressure in FKS-50 at various external salt concentrations with varying $\Pi^{m,ex,0}$

Figure 10 shows that, in order to maintain a positive hydrostatic pressure over the entire concentration range, $\Pi^{m,ex,0}$ must be equal or lower than -10 MPa. In the framework proposed by Freger et al. [71], this would correspond to a negative polymer elastic pressure. According to this physical picture, the membrane would be in a tensile state induced by the uptake of water molecules from the external solution, with stretched polymer chains exerting a compressive effect on water molecules.

1.3.2 Ion partitioning models implementation and calibration

As discussed in section 1.1.5, thermodynamic models typically include parameters that must be either estimated theoretically or determined through calibration against experimental data via a fitting procedure. The following sections present the mathematical implementation of the developed ion partition models, together with the procedure adopted to retrieve the unknown parameters. The discussion of the modelling results is provided in section 1.3.3

1.3.2.1 Models' implementation

The thermodynamic models introduced in section 1.1.5.2 and 1.1.5.3 were implemented on MatLab® to perform ion partition simulations. Their main features are summarized in Table 3.

Table 3 Comparison of tested ion partition models. n indicates the number of counter-ions in the system.

		Ideal Donnan	Donnan-Manning	Donnan-peNRTL
Accounted non-ideal phenomena	Ext. Solution non-ideality	×	✓	✓
	Ion-Chain interactions	×	✓	✓
	Ion-Ion interactions	×	×	✓
	Short-range interactions	×	×	✓
	Calibration parameters	None	ξ	$\xi, \tau_{i,j}, \tau_{j,i}$
	N° of calibration parameters	0	1	$1 + 2n$
	Suggested concentration range	$m^s \gg m_{fix}$	$m^s \ll m_{fix}$	Any
	Model complexity	Simple	Relatively simple	Complex
	Main equations	(1.71)(1.72)	(1.69)(1.71)(1.88)	(1.69)(1.71)(1.88)(1.98) (1.100)(1.101)

Each thermodynamic model for ion activity coefficients was coupled with the Donnan model (equations (1.69) and (1.71)) to solve partition equilibria at the solution-membrane interface and evaluate equilibrium ions' concentration within the membrane. Their predictive performance was then evaluated against the ideal Donnan model, which represents the simplest ion partition model as it neglects all non-ideal effects both in the external solution and in the membrane phase.

In contrast, the Donnan–Manning and Donnan–peNRTL models incorporate non-ideal effects. Specifically, the external solution activity coefficients were computed with the eNRTL model, while those in the membrane phase were estimated either with the extended Manning model or with the extended peNRTL model. Since the membrane activity coefficients depend on the equilibrium ion

concentrations, the resulting system of equations was solved iteratively. The initial guess for equilibrium concentrations was provided by the ideal Donnan model. A schematic representation of the implemented solving algorithms is shown in Figure 11.

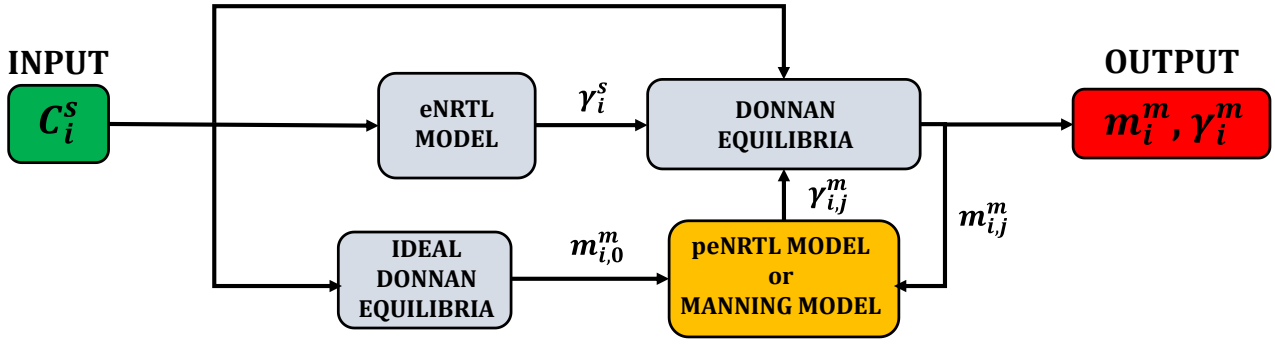

Figure 11 Schematic of the Donnan-Manning and Donnan-peNRTL solution algorithm implemented on MatLab®. As the membrane activity coefficients depend on the equilibrium concentrations, a built-in nonlinear solver was employed. The solver was initialized using the ideal Donnan model. Input molar concentrations were first converted to molal units through equation (1.42)

1.3.2.2 Donnan-Manning model calibration

sections 1.1.5.1 and 1.1.5.2 introduced a novel multi-ionic extension of the Manning model for ion activity coefficients in IEMs. The model relies on the normalized linear charge density ξ, which according to according to equation (1.82), depends only on the relative dielectric constant of the hydrated membrane and on the mean distance between fixed charges along the polymer backbone. Several authors have suggested that the dielectric constant of a hydrated membrane can be estimated as a weighted average of the water and dry polymer dielectric constants, as expressed in equation (1.121) [77]:

$$\varepsilon_m = \phi_w \varepsilon_w + (1 - \phi_w)\varepsilon_p \tag{1.121}$$

where ε_w and ε_p denote the dielectric constants of water and dry polymer, respectively, while ϕ_w is the water volume fraction in the membrane (related to water uptake according through equation (1.105)). For the FKE-50 CEM, all the necessary membrane properties were experimentally determined except for b and ε_p. The latter was fixed at an average value of 6, consistent with the range typically reported for commercial IEMs (2–10). As observed by Kamcev et al., Manning activity coefficient is relatively insensitive to the exact value of ε_p within this range [81,104].

Conversely, the determination of the average distance between fixed charges, is less straightforward. Although some authors attempted correlations with membrane chemical structure and IEC [104,118], such approaches often yielded poor predictions, even for membranes with well-characterized

structures [97]. This is likely to be attributed to the complex structure of the membranes that makes the exact theoretical evaluation of b unfeasible. Consequently, ξ is commonly treated as an adjustable parameter when direct evaluation of b is not feasible. This strategy enables the semi-predictive application of Manning's model under different operating conditions, since ξ is assumed independent of the external solution composition[10,85].

Nevertheless, as the membrane water uptake varies with external concentration, ξ is not strictly constant (see equation (1.82) and (1.121)). In this work, b was therefore treated as an adjustable parameter to capture the influence of water uptake variations on ξ. Following other studies [10,96], calibration was performed by minimizing the Mean Relative Deviation (MRD) between experimental single-salt ion partitioning data presented in section 1.2.3.2 and model predictions, defined as:

$$MRD = \frac{1}{N}\sum_{i}\frac{\left|m_i^{m,exp.} - m_i^{m,pred.}\right|}{m_i^{m,exp.}} \tag{1.122}$$

where N is the number of experimental data points, $m_i^{m,exp.}$ the experimental ion molal concentration in the membrane, and $m_i^{m,pred.}$ the predicted value.

1.3.2.3 Donnan-peNRTL model calibration

The extended peNRTL model presented in section 1.1.5.3, is derived from the eNRTL framework for aqueous electrolytes, where the local excess Gibbs free energy associated with non-electrostatic interactions is expressed in terms of binary interaction parameters τ_{ij} . These parameters can be obtained via the mixing rules reported in equations (1.123)-(1.131), if the corresponding adjustable interaction parameters are known. These latter must be retrieved from experimental equilibrium data through a fitting procedure. The number of interaction parameters grows with the number of ionic and molecular species, but a key advantage of local composition models is that once the parameters are determined for a set of species, they can be applied to any system containing those species, being composition independent.

Accordingly, part of the required water–electrolyte parameters were retrieved from literature on aqueous electrolyte thermodynamics [60]. Table 4 lists the adopted values for the salts considered in this work.

Table 4 Literature eNRTL adjustable binary interaction parameters for water-electrolyte interactions. "w" stands for water component [60]

i-j pair	w-(Na^+, Cl^-)	w-(K^+, Cl^-)	w-(Mg^{2+}, Cl^-)	w-(Ca^{2+}, Cl^-)	(Na^+, Cl^-)-(K^+, Cl^-)	(Mg^{2+}, Cl^-)-(Ca^{2+}, Cl^-)
τ_{ij}	8.865	8.170	10.854	10.478	0.386	0.332
τ_{ji}	-4.541	-4.153	-5.409	-5.291	-0.389	0.220

Differently from the non-adjustable binary parameters that enter equations (1.100) and (1.101) explicitly, the adjustable parameters reported in Table 4 are defined for each couple of molecular and electrolyte component, where *electrolyte* stand for any possible neutral combination of a negative and a positive charged species, while *molecular* stands for any neutral (i.e., not charged) species. In practice, three categories of adjustable binary parameters are defined: electrolyte–electrolyte ($\tau_{ca,ca\prime}$),defined per each couple of electrolytes sharing a common ion, electrolyte–molecular ($\tau_{ca,m}$), and molecular–molecular. For instance, modeling an aqueous NaCl–KCl solution requires four electrolyte–molecular parameters ($\tau_{NaCl,w}$, $\tau_{w,NaCl}$, $\tau_{KCl,w}$, $\tau_{w,KCl}$) and two electrolyte-electrolyte parameters (i.e., $\tau_{NaCl,KCl}$, $\tau_{KCl,NaCl}$).

For CEMs, the fixed charged groups (CG^-) in the polymer matrix must be treated as additional anionic species. Moreover, Yu et al. [97] suggested including a secondary solvent to represent interactions with nonpolar polymer domains, but without knowledge of the precise polymer structure this approach is impractical. To reduce complexity, sorbed water was considered the only molecular component in this work. Moreover, as suggested by Yu et al., electrolyte–electrolyte parameters involving CG^- were set to zero, as their contribution to ion partitioning was shown to be negligible [97].

Under these assumptions, the number of adjustable binary parameters reduces to 2n, where *n* is the number of counter-ions. These correspond to the pairs $\tau_{cCG,w}$ and $\tau_{w,cCG}$, with c denoting a counter-ion sorbed in the membrane. Importantly, the introduction of different co-ions does not increase the number of parameters, since CG^- can only be paired with cations.

Once the adjustable parameters are identified, the following mixing rules yield the non-adjustable binary interaction terms τ_{ij}:

$$Y_c = \frac{X_c}{\sum_{c'} X_{c'}} \tag{1.123}$$

$$Y_a = \frac{X_a}{\sum_{a'} X_{a'}} \tag{1.124}$$

$$G_{cm} = \sum_a Y_a exp\left(-\alpha\tau_{ca,m}\right) \tag{1.125}$$

$$G_{am} = \sum_c Y_c exp\left(-\alpha\tau_{ca,m}\right) \tag{1.126}$$

$$G_{mc} = \sum_a Y_a exp\left(-\alpha\tau_{m,ca}\right) \tag{1.127}$$

$$G_{ma} = \sum_c Y_c exp\left(-\alpha\tau_{m,ca}\right) \tag{1.128}$$

$$G_{ca} = \sum_{c'} Y_{c'} exp\left(-\alpha\tau_{ca,c'a}\right) \tag{1.129}$$

$$G_{ac} = \sum_{a'} Y_{a'} exp\left(-\alpha\tau_{ca,ca'}\right) \tag{1.130}$$

$$\tau_{ij} = -\frac{ln\, G_{ij}}{\alpha} \tag{1.131}$$

where X_c and X_a are the effective molar fractions of the generic cationic or anionic species defined by eq. (1.103).

The fitting procedure followed the same strategy described in section 1.3.2.2. the Donnan–peNRTL model was applied and a multivariable optimization was carried out to minimize the MRD defined in equation (1.122) with respect to experimental single-salt data. The optimization variables included all missing parameters, as well as the fixed-charge distance b calibrated separately for the Donnan–Manning and Donnan–peNRTL models. The final calibrated parameters are reported in Table 5. Further discussion on the results of the calibration procedure is provided in section 1.3.3.1

Table 5 Fitted Manning parameters and peNRTL adjustable binary parameters. CG- stands for the negatively charged groups in the polymeric matrix. The two models were calibrated separately on single-salt tests experimental data. The average ξ was evaluated from b, considering the average water uptake.

Model	i-j pair	τ_{ij}	τ_{ji}	b [nm]	Average ξ
Donnan-Manning	-	-	-	9.630	0.228
Donnan-peNRTL	water - (Na^+, CG-)	-9.492	-3.189	0.135	16.05
	water - (K^+, CG-)	-8.211	-2.939		
	water - (Mg^{2+}, CG-)	-8.164	-2.766		
	water - (Ca^{2+}, CG-)	-7.945	-2.465		

1.3.3 Ion partition models validation

In the following sections, the results of the ion partition models' simulations are presented. Particularly, the Donnan-Manning and Donnan-peNRTL model were applied to simulate ion partition in the FKE-50 CEM. The models' calibration presented in section 1.3.2 was performed on single-salt partition data. Therefore, the results of these simulations are presented first. Subsequently, the models are applied to predict ion partitioning when the CEM is equilibrated with binary salt mixtures. A comparative analysis among the proposed models is done, elucidating the effect of the models' structure on the predictive capabilities, especially at high external concentrations.

1.3.3.1 Single-salt systems

In Figure 12, the experimental ion partition data obtained for the FKE-50 CEM with single-salt solutions are compared with the simulations performed using the Donnan–Manning and Donnan–peNRTL models. The simulations were carried out with the fitting parameters reported in Table 5. The values of ξ were calculated from equation (1.82), adopting an average value for the relative dielectric constant. Since the parameter b could not be experimentally determined, both models were independently calibrated to test their predictive capability under the most favorable conditions. The two fitted values of b minimize the MRD of the respective models, ensuring that any alternative choice would lead to poorer agreement with the experimental data.

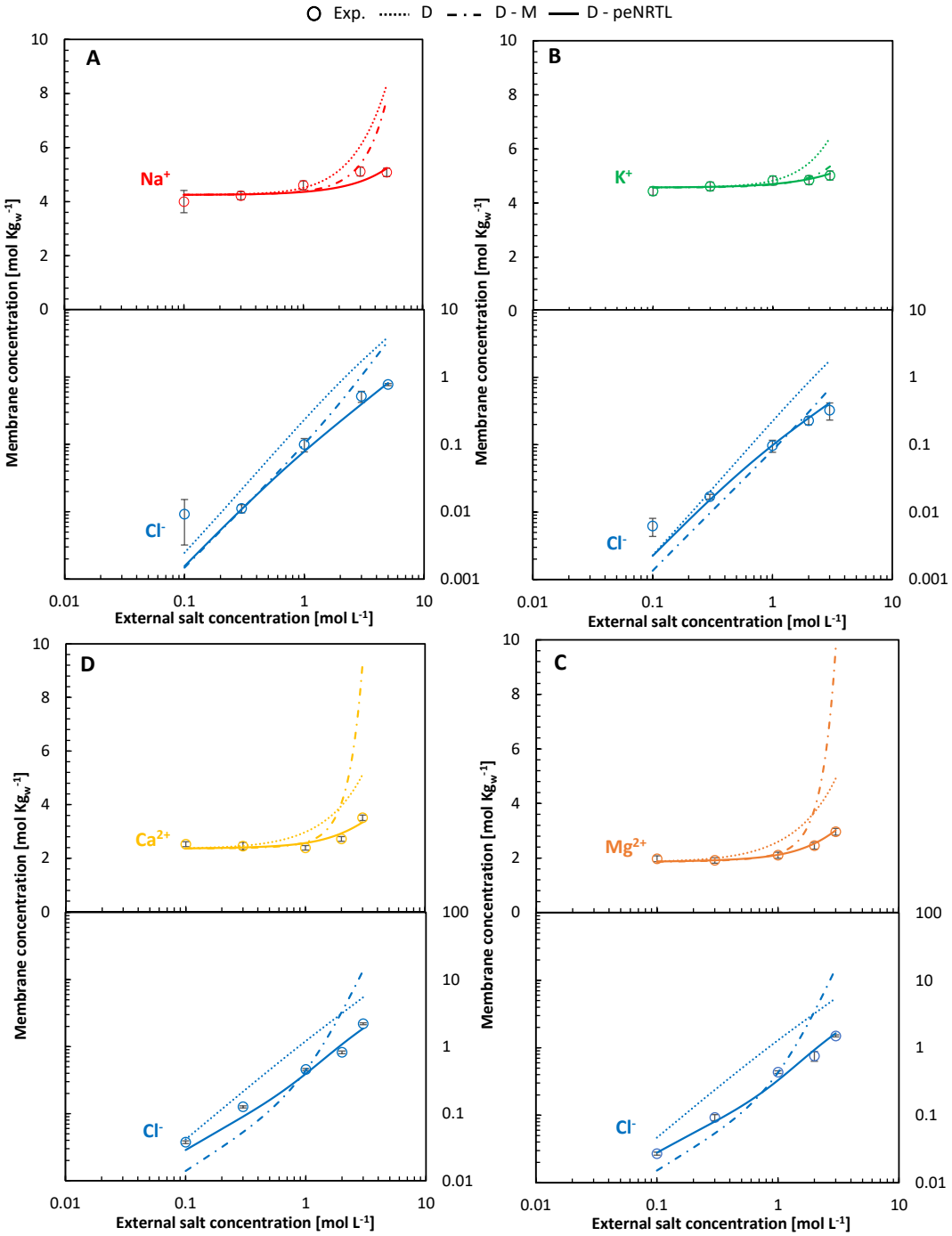

*Figure 12 Ions molal concentration in FKE-50 CEM at various external salt concentration for single-salt systems containing NaCl (**A**), KCl (**B**), $MgCl_2$(**C**) or $CaCl_2$ (**D**).Empty circles indiucate the experimental data. The associated error bars were plotted considering the maximum error between the theoretical error evaluated through the error propagation theory and the experimental error on at least two different tests. The dotted lines represent the predictions of the ideal Donnan model, the dash-dot lines represent the predictions of the Donnan-Manning model while the solid lines are the predictions of the Donnan–peNRTL model.*

A direct comparison of the models in Figure 12 clearly indicates that the Donnan–peNRTL model provides superior predictions at high external concentrations. This outcome can be rationalized by analysing the electrolyte activity coefficients, as shown in Figure 13:

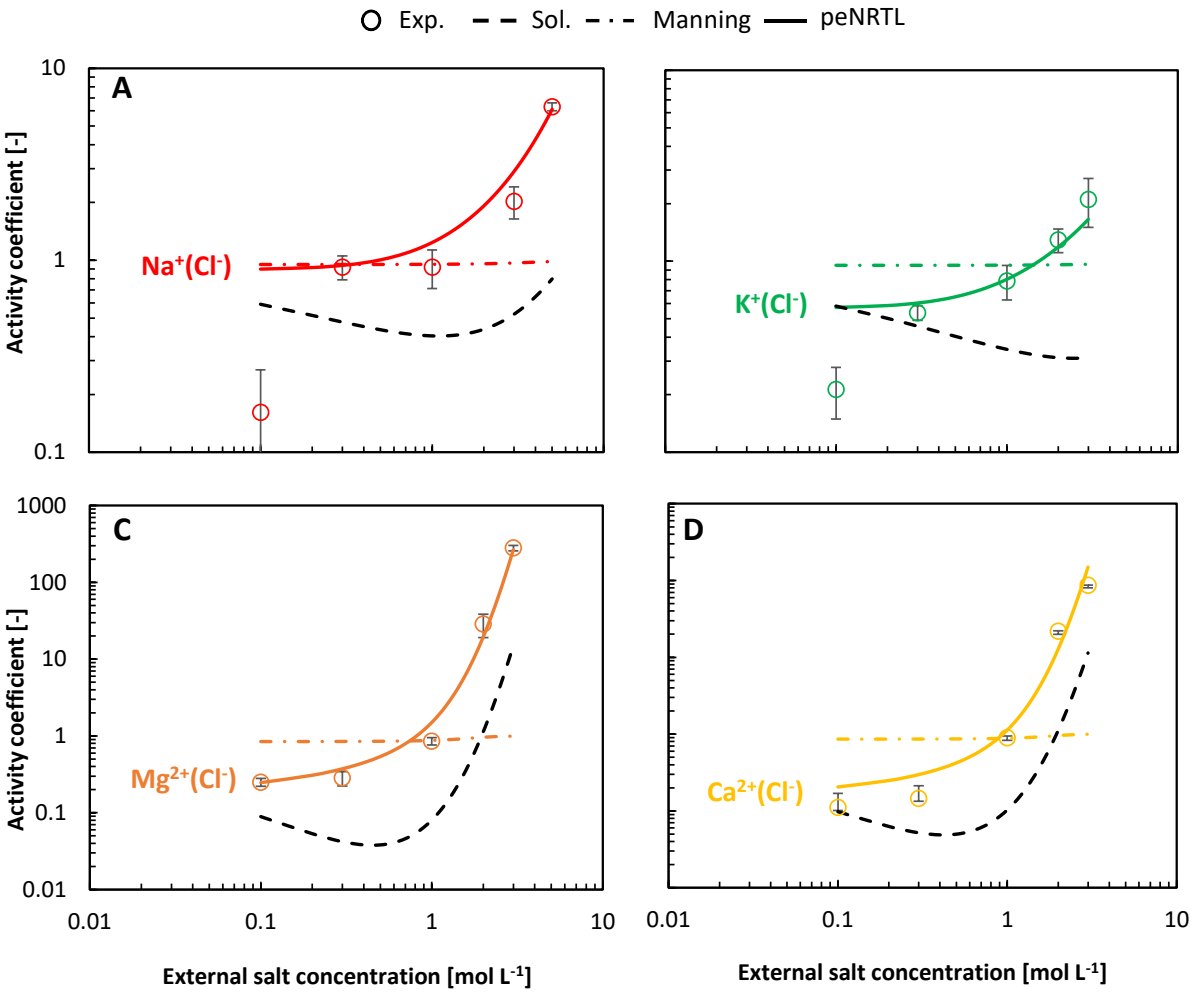

*Figure 13 Newman's activity coefficients in FKE-50 CEM as a function of the external concentration for the single-salt systems containing NaCl (**A**), KCl (**B**), MgCl2 (**C**) or CaCl2 (**D**). The values on the Y axes were evaluated through equation (1.110) taking Cl^- as reference ion. The empty circles were obtained from experimental concentration in membrane, the dash-dot lines are the prediction of the Manning model while the solid lines are the predictions of the peNRTL model. The black dashed lines refer to the external solution activity coefficients and were obtained by applying the eNRTL model.*

At external salt concentrations exceeding 1 mol L^{-1}, the activity coefficients within the membrane are consistently greater than unity for all the electrolytes considered. According to equation (1.88), the Manning model intrinsically fails to predict activity coefficients larger than one. This limitation arises from the functional form of the excess free energy of interaction between mobile ions and the fixed charges (1.86), whose derivative is always negative. Physically, this is caused by the reduction of the Debye length with increasing ionic strength, which causes a strengthening in the electrostatic interactions and a reduction of the electrostatic energy of the system. Counter-ion condensation

further contributes to the lowering of the activity coefficients. Consequently, the fitting procedure converges to ξ values below the condensation threshold in order to minimize the MRD at high external concentrations.

Interestingly, the optimal ξ obtained for the Donnan–Manning model lies below the condensation threshold, whereas the ξ value fitted with the Donnan–peNRTL model is well above ξ_c. In practice, this means that, according to the Manning limiting law (equation (1.92)), counter-ions are totally uncondensed according to the Donnan–Manning model but partially condensed in the Donnan–peNRTL framework.

Such a discrepancy likely reflects the limited applicability of the Manning limiting law, from which ξ is derived. In IEMs, the condition of infinite dilution (i.e., $\varkappa b \ll 1$ [86]) is never strictly satisfied, particularly when equilibrated with concentrated solutions [91]. For this reason, ξ should be regarded as an empirical fitting parameter rather than as a physically meaningful constant when highly concentrated electrolytes are considered.

Most literature studies apply the Donnan–Manning model in a semi-predictive fashion, calibrating ξ against partitioning data up to ~1 mol L^{-1}. Within this range, membrane activity coefficients remain below unity, and the assumptions of the Manning framework hold reasonably well. Consistently, most ξ values reported in the literature exceed the condensation threshold for both monovalent and divalent counter-ions. However, as discussed in 1.1.5.1, Manning's model assumptions break down at higher external concentrations. This is not surprising, since the model only accounts for long-range electrostatic interactions between mobile ions and the linear charge distribution of the polymer chains, neglecting short-range interactions that are likely to become dominant at elevated concentrations.

Figure 13 illustrates that the failure of the Donnan–Manning model at high salt concentrations originates from the rise in solution activity coefficients, which is not mirrored by a corresponding increase in membrane activity coefficients. As a result, the Donnan relation (equation (1.69)), leads to an overestimation of salt uptake in the membrane. This issue was also observed by Galizia et al. [63] when modeling $CaCl_2$ sorption above 1 mol L^{-1} using the Donnan–Manning framework. To overcome this limitation, they introduced an empirical correction to the membrane activity coefficients, estimated via the Pitzer model [58]. The Pitzer formalism successfully captures activity coefficients greater than unity by accounting for short-range ion–ion interactions, which dominate at high concentrations due to the reduced interionic distance. Similar effects are expected within the membrane phase. In fact, when the absorbed salt concentration approaches the fixed-charge density, short-range interactions are likely to outweigh ion–polymer interactions, which cease to dominate.

A quantitative comparison of the three models is reported in Table 6, where the MRD values are listed for each electrolyte system investigated.

Table 6 Mean relative error of the investigated ion partition models. The reported values are calculated by applying equation (1.122) and accounting for the experimental error bars associated with the measurements.

Test	Ideal Donnan	Donnan-Manning	Donnan - peNRTL
NaCl	82.5%	50.0%	6.6%
KCl	72.3%	19.1%	5.1%
NaCl-KCl	56.2%	39.7%	6.2%
$MgCl_2$	102.0%	149.3%	3.5%
$CaCl_2$	73.3%	111.8%	10.6%
$MgCl_2$-$CaCl_2$	83.9%	148.2%	5.7%
Average	78.4%	86.4%	6.3%

The Donnan-peNRTL model clearly outperforms the others, with an average MRD of only 6.3%, significantly lower than the values obtained with the ideal Donnan and Donnan–Manning approaches. Interestingly, for divalent counter-ion systems, the ideal Donnan model provides smaller errors than the Donnan–Manning model, in line with the findings of Galizia et al.[63] at high concentrations. This result supports the hypothesis that, when the mobile salt content in the membrane is very high, ion–polymer interactions lose relevance, and the membrane activity coefficients asymptotically approach those in the bulk solution. In such cases, the basic assumption of the ideal Donnan model becomes valid again, explaining its better performance under these conditions.

By contrast, the Donnan–Manning model retains predictive accuracy only when the mobile salt concentration is low relative to the fixed charges, so that ion–polymer interactions dominate the behaviour of the system. The Donnan–peNRTL model, instead, explicitly incorporates short-range interactions through the local contribution of the non-random two-liquid framework. This feature enables the model to reproduce the increase of membrane activity coefficients at high external concentrations, thereby providing the most accurate description of salt sorption across the entire investigated concentration range.

1.3.3.2 Binary salt mixtures systems

The ion-partitioning data obtained from binary equimolar mixtures, presented in section 1.2.3.3 were used to validate the extended Donnan–peNRTL model for multi-ionic systems. The experimental results are compared with model predictions in Figure 14 .All simulations were performed using the same set of parameters reported in Table 5 which had been calibrated on single-salt systems.

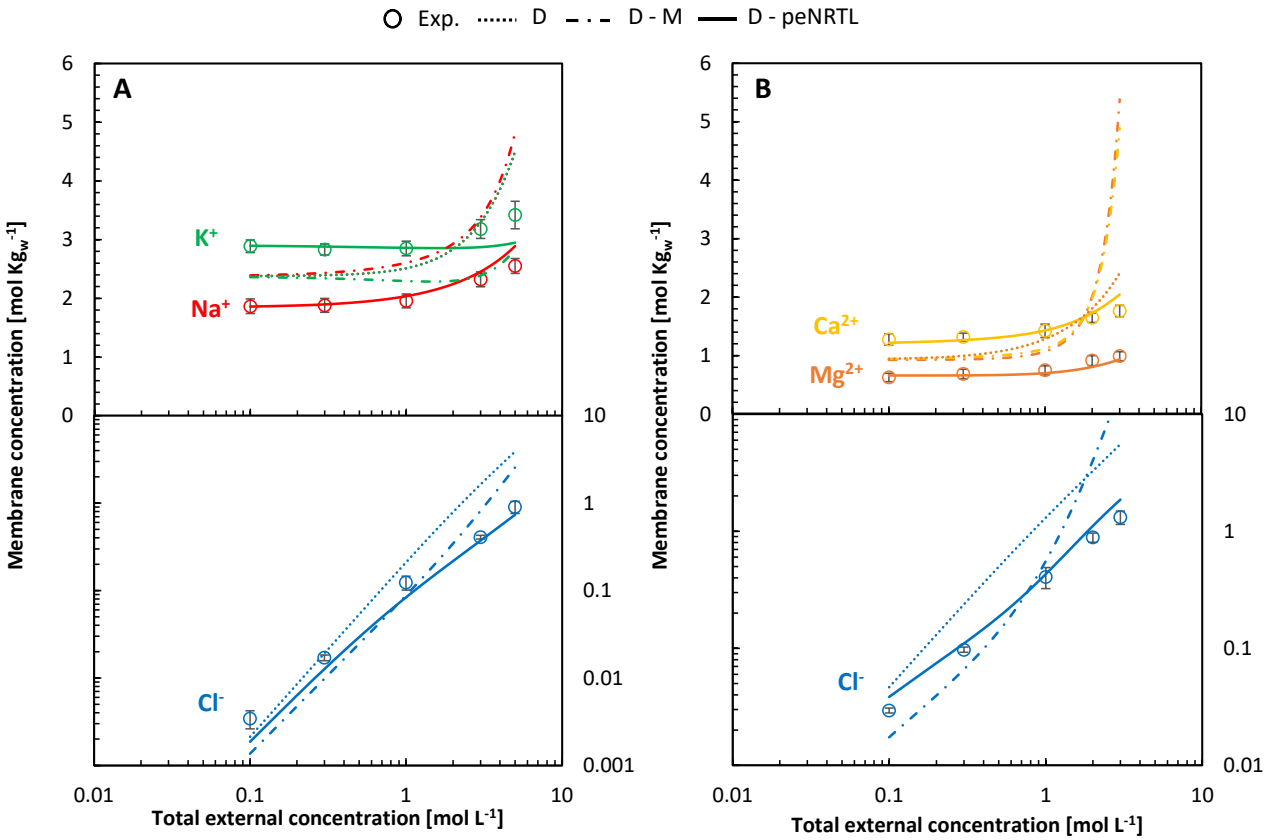

*Figure 14 FKE-50 co- and counter-ions equilibrium molal concentrations in FKE-50 CEM against the total external salt concentration for the two equimolar mixtures of NaCl-KCl (**A**) and MgCl2-CaCl2 (**B**) Empty circles indicate the experimental data, the dotted lines represent the predictions of the ideal Donnan model, the dash-dot lines represent the predictions of the Donnan-Manning model while the solid lines are the predictions of the extended Donnan–peNRTL model.*

Both the ideal Donnan and the extended Donnan–Manning models consistently overestimate the co-ions concentration within the membrane, particularly at total external concentrations above 1 mol L^{-1}, with the largest discrepancies observed for the $MgCl_2$–$CaCl_2$ system. This behaviour stems from the inability of these models to capture the increase in activity coefficients inside the membrane at high external concentrations. In addition, both models fail to reproduce the partition selectivity of counter-ions. Specifically, equation (1.72) implies that the ideal Donnan model predicts identical partition coefficients for counter-ions with the same valence, which is inconsistent with experimental observations.

In the case of the extended Donnan–Manning model, the poor prediction of counter-ion selectivity can be explained by the ξ values obtained during calibration, which were found to be lower than the critical condensation thresholds of the counter-ions. Consequently, the condensation selectivity rule described in equation (1.96) is not practically employed, since counter-ion condensation is not occurring. The resulting differences in equilibrium concentrations of Na^+ vs. K^+ or Mg^{2+} vs. Ca^{2+} are therefore solely dictated by their activity coefficients in the external solution. As shown in Figure 13,

Mg^{2+} and Ca^{2+} have similar activity coefficients in the external solution. Consequently, the Donnan-Manning model lines for these two ions are almost overlapped in Figure 14B.

By contrast, the extended Donnan–peNRTL model accurately predicts both co-ion and counter-ion partition over the entire concentration range investigated. For both NaCl–KCl and $MgCl_2$–$CaCl_2$ mixtures, the counter-ion selectivity is well captured thanks to the incorporation of the condensation selectivity rule (equation (1.96))

To the best of the authors' knowledge, this is the first quantitative prediction of counter-ion distribution between an IEM and a multi-ionic solution at such high external concentrations. The success of the extended peNRTL framework can be attributed to its decomposition of the activity coefficient into three distinct contributions, which significantly broadens the model's range of validity. As shown in Figure 15, the predicted increase in activity coefficients within the membrane prevents the unrealistic rise in mobile ion concentrations that characterizes the Ideal Donnan and Donnan–Manning models.

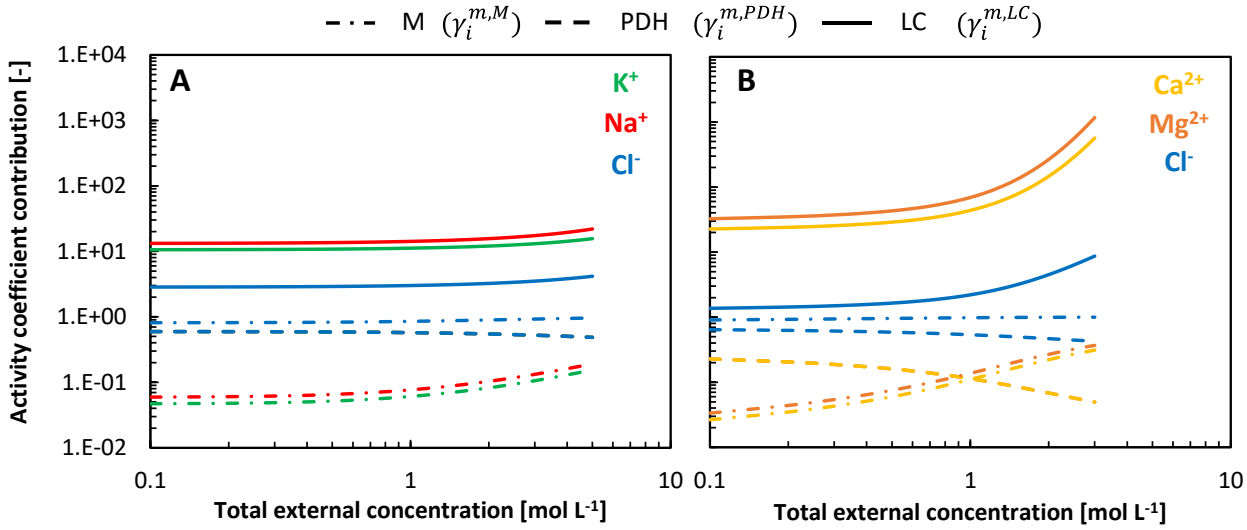

*Figure 15 Contributions to the activity coefficients of the peNRTL model (eq. (1.97)) in FKE-50 equilibrated with binary equimolar solution of NaCl-KCl (**A**) and $MgCl_2$-$CaCl_2$ (**B**) versus the total external salt concentration. The solid lines are the Local Contribution (LC) activity coefficients (eq. (1.100) and (1.101)); the dashed lines are the Manning (M) activity coefficients (eq. (1.88)); the dash-dot lines are the Pitzer-Debye-Hüchel (PDH) activity coefficients (equations (1.98)).*

A closer inspection of the three contributions (Figure 15) provides further insight. The PDH term is always lower than 1 and decreases with increasing concentration, reflecting the strengthening of long-range electrostatic interactions at lower Debye lengths. Noticeably, the PDH contributions overlap for ions of the same charge number (Figure 15 A and B).

The Manning contribution is also lower than 1 but, unlike PDH, it increases with concentration. This effect is linked to counter-ion condensation: while the fraction of condensed fixed charges is constant, the number of absorbed counter-ions rises with increasing co-ion uptake. As a result, the fraction of condensed counter-ions decreases, producing higher Manning activity coefficients.

Conversely, the local contribution is always positive, reflecting short-range repulsive interactions. Its magnitude increases with external concentration, following a trend similar to the co-ion concentration in the membrane. At high concentrations, short-range repulsions intensify due to reduced interionic distances, which explains the stronger and faster rise of the local contribution in the $MgCl_2$–$CaCl_2$ system compared with NaCl–KCl. At low concentrations, when the co-ion content approaches zero, both the local and PDH terms remain nearly constant, as the counter-ion concentration stabilizes. Interestingly, the absolute values of the local and PDH contributions are nearly identical and opposite in sign, so that the two effects cancel each other. Under these conditions, the Manning contribution becomes the dominant factor determining the activity coefficient. This finding suggests that, at external concentrations below 1 mol L^{-1}, co-ion partitioning is mainly governed by ion–polymer chain interactions.

1.4 Thermodynamics of ion-exchange membranes: conclusions

In the previous Chapter, a thorough revision of fundamental IEMs thermodynamic was presented. Some of the most relevant thermodynamic models for ion partitioning in IEMs were critically examinated, highlighting their weaknesses. To address such limitations, novel formulations of the latter models were proposed, extending their applicability to highly concentrated multi-ionic solutions. The proposed models were positively validated against novel experimental data collected on commercial CEMs employed for desalination technologies. The proposed analysis, corroborated by the experimental data, revealed that in high salinity environment, the ion activity coefficients in the membrane phase can achieve values much higher than 1, reflecting the development of strong non-ideal short-range interactions that the existing models cannot properly described.

Moreover, a critical analysis on water partition in IEMs was formulated to highlight some relevant but often disregarded limitations in the traditionally employed modelling approach of ions and water partition in IEMs.

In the future, fundamental research should be carried out to better characterize the physical nature of short-range interactions in the membrane phase, elucidating the influence of the IEMs chemistry and structure on these latter. Regarding water partition, thermodynamic models should be improved to account for the dispersed nature of water molecules in the membrane, for instance including surface energy terms that could contribute to the variation of the hydrostatic pressure of water in the membrane phase.

2. Transport phenomena in ion-exchange membranes

Alongside thermodynamics, transport phenomena represent a central topic in chemical engineering and, naturally, in membrane science. While mass and charge transport in liquid solutions are now relatively well understood, or at least adequately described, the same cannot be said for transport in membrane systems, where the fundamental mechanisms remain only partially clarified, fuelling ongoing debate within the scientific community.

Building upon the concept of IEMs thermodynamics presented in Chapter 1, the following Chapter aims at providing a comprehensive and rigorous theoretical description of mass and charge transport in IEMs.

The Chapter is therefore divided into three main sections, focusing respectively on theoretical modelling, experimental investigations and numerical simulation of mass and charge transport in IEMs

2.1 Transport phenomena in ion-exchange membranes: theoretical foundations and modelling

The modelling of mass and charge transport in IEMs is of fundamental importance, not only because it allows to describe and predict the behaviour of electromembrane units but more importantly also because, by unravelling the relation between IEMs structure and composition to transport properties, it can support the development of next-generation membranes.

Typically, ionic transport in IEMs is described by means of the Nernst–Planck (NP) model, originally developed for liquid electrolytes but often employed also for solid-state electrolyte like IEMs.

In the first part of the present section, the NP model is derived and discussed, focusing on its structural limitations. Hereinafter, a more advanced but scarcely investigated IEMs transport model based on the Maxwell–Stefan (MS) transport theory is presented. The theoretical derivation of this latter and its application to ionic transport in IEMs is thoroughly discussed, focusing on the main differences between the NP and the MS frameworks.

Aiming at shedding light on the physical dependance of transport coefficients from operative conditions, the latter frameworks are employed in sections 2.3 to evaluate primitive transport coefficients from IEMs macroscale transport properties obtained through a dedicated experimental campaign, whose results are reported in section 2.2.

2.1.1 Fundamentals of mass and charge transport

Mass transport phenomena concern the mechanisms by which matter is transferred under the influence of a driving force. In a mixture composed of an arbitrary number of components, the relative motion of these species is generally referred to as diffusion. In ionic systems, i.e., systems in which the constituents are charged species, mass transport is inherently coupled with charge transport. Accordingly, the term *electrodiffusion* is commonly employed to describe this combined process.

2.1.1.1 Fluxes, concentrations scale and reference frames

Electrodiffusion is formally due to the differences in the average velocities of the various components, resulting from the interplay of multiple driving forces, and it is usually quantified in terms of flux, defined as follows [119]:

$$\vec{N}_i^{\#} = C_i(\vec{v}_i - \vec{v}^{\#}) \tag{2.1}$$

where $\vec{v}_i$ and $\vec{v}^{\#}$ are respectively the linear velocity of the generic component and an arbitrary chosen reference velocity, both defined with respect to an inertial reference frame (i.e., a laboratory fixed reference frame).

In equation (2.1), the molar concentration C_i was employed to define the flux. This choice is not mandatory, and other concentration scales, such as mass concentration, could be employed as well. Furthermore, regardless of the chosen concentration scale, multiple definitions of flux are possible. Indeed, the arbitrariness of the electrodiffusive flux definition is apparent in equation (2.1) from the need to select a reference velocity. In principle, the velocity of any component of the system could be taken as reference, but also any linear combination of the components' velocities could be chosen as well. In practice, the choice of the reference frame is guided primarily by convenience [120].

An important consequence of the arbitrariness of the reference frame is that flux densities expressed in different frames and/or concentration scales are not directly comparable, and appropriate conversion relations must be applied to transform fluxes from one frame to another [121,122]. Similarly, transport coefficients defined and evaluated on different reference frames can differ, especially in highly concentrated multi-component systems [22,123]. Therefore, when retrieving transport coefficients from experimental data, it is essential to clearly state the adopted reference frame to avoid misconceptions.

If a laboratory-fixed reference frame is adopted (i.e., $\vec{v}^{\#}$=0), the generic flux becomes:

$$\vec{N}_i = \vec{N}_i^{\#} = C_i\vec{v}_i \tag{2.2}$$

However, in the study of mass transport phenomena, a commonly chosen reference frame is the molar average velocity $\vec{\bar{v}}$ defined as follows:

$$\vec{\bar{v}} = \frac{\sum_{i=1}^{N} C_i\vec{v}_i}{\sum_{i=1}^{N} C_i} = \sum_{i=1}^{N} x_i\vec{v}_i \tag{2.3}$$

where N defines the number of components, including the solvent. By defining the total flux as follows:

$$\vec{N}_{tot} = \sum_{i=1}^{N} \vec{N}_i \tag{2.4}$$

Substitution of equations (2.3) and (2.4) into equation (2.1), the net flux of a generic component with respect to a stationary (i.e., laboratory fixed) reference frame can be evaluated as:

$$\vec{N}_i = \vec{N}_i^{\#} + x_i \vec{N}_{tot} \tag{2.5}$$

According to the latter equation, the flux relative to a stationary reference frame can be evaluated as the sum an electrodiffusive component $\vec{N}_i^{\#}$ and of the molar barycentric velocity contribution $x_i \vec{N}_{tot}$ usually called convective contribution. Importantly, by substituting the definition of $\vec{\vec{v}}$ in eq. (2.1) it is easy to prove that:

$$\sum_{i=1}^{N} \vec{N}_i^{\#} = 0 \tag{2.6}$$

The previous result clearly indicates that there are only $N - 1$ independent electrodiffusive fluxes. It should be pointed out that this outcome is not due to the specific reference velocity adopted, but rather to the coupling of electrodiffusive fluxes due to the definition of the reference velocity.

2.1.1.2 Current density and transport numbers

A fundamental variable describing charge transport in ionic systems is the current density defined as follows:

$$\vec{J}^{\#} = \mathcal{F} \sum_{i=1}^{N} z_i C_i \, \vec{N}_i^{\#} \tag{2.7}$$

Being formally a charge flux, the value of $\vec{J}^{\#}$ depends on the chosen reference frame, i.e., on the chosen $\vec{v}^{\#}$ [22,26,32]. By substituting equations (2.1) and (2.2), eq. (2.7) can be rewritten as follows:

$$\vec{J}^{\#} = F \sum_{i=1}^{N} z_i \vec{N}_i - \mathcal{F} \sum_{i=1}^{N} z_i C_i \, \vec{v}^{\#} \tag{2.8}$$

Further introduction of charge density definition (eq. (1.34)) leads to the following formulation of $\vec{J}^{\#}$:

$$\vec{J} = J^{\#} + \rho_{el}\vec{v}^{\#} \tag{2.9}$$

According to (2.9), the current density in a stationary reference frame can be generally expressed as a sum of an electrodiffusive contribution $\vec{J}^{\#}$, also referred to as *conduction*, and a convective contribution $\rho_{el}\vec{v}^{\#}$. The distinction of the two being solely dependent on the chosen reference frame. Nonetheless, in an electroneutral system, i.e., in a system where the local electroneutrality assumption holds, the local charge density ρ_{el} is zero and the total current density reduces to its conductive component. Consequently, the current density is invariant with respect to the chosen reference frame only under electroneutral conditions. This point will be further discussed in section 2.2.

From the definition of current density $\vec{J}$, the definition of the transport (or transference) number naturally follows:

$$t_i = \frac{z_i\vec{N}_i}{\sum_j z_j\vec{N}_j} = \frac{z_i C_i\vec{v}_i}{\sum_j z_j C_j\vec{v}_j} \tag{2.10}$$

The transport numbers correspond to the fraction of current density carried by a given generic charged component. Although often overlooked by non-specialists, they are inherently dependent on the chosen reference frame, just as current density is. However, unlike current density, this dependence persists even under locally electroneutral conditions. This is simply demonstrated considering that equation (2.10) define the transport numbers with respect to a stationary reference frame, but alternative definitions can be formulated by adopting different frames of reference:

$$t_i^{\#} = \frac{z_i\vec{N}_i^{\#}}{\sum_j z_j\vec{N}_i^{\#}} = \frac{z_i C_i(\vec{v}_i - \vec{v}^{\#})}{\sum_j z_j C_j\left(\vec{v}_j - \vec{v}^{\#}\right)} \tag{2.11}$$

Evidently, in an electroneutral system the denominator of the latter equation is independent of the chosen reference velocity, whereas the numerator is not. Therefore, whenever transport numbers are discussed, it is essential to explicitly specify the adopted reference frame. This notion is indeed of fundamental importance in the experimental evaluation of transport numbers, but it is very often ignored in scientific articles in the field of membrane processes.

2.1.1.3 Constitutive transport equations: thermodynamics of irreversible processes

In the previous sections, the electrodiffusive flux was defined. However, this definition alone provides no insight into the physical origins of $\vec{N}_i^{\#}$. Establishing constitutive equations that relate the

flux of a given component to its underlying driving forces is the primary aim in the study of transport phenomena. The simplest equation describing mass transport, originally formulated for binary mixtures, is Fick's law of diffusion. Within the multicomponent Fickian framework, the diffusive flux of a neutral component is expressed as a function of the concentration gradients of the other components, as given by the following equation:

$$\vec{N}_I^{\#} = -\sum_J D_{I,J}\vec{\nabla}C_J \tag{2.12}$$

where capital subscripts denote neutral components and $D_{I,J}$ are the corresponding binary non-symmetric (i.e., $D_{I,J} \neq D_{J,I}$) Fickian diffusion coefficients. By means of current density and transport number definition (equations (2.7) and (2.11)), the electrodiffusive flux of a generic charged component (i.e., ion) can be defined as follows [22]:

$$\vec{N}_i^{\#} = -\sum_J \sum_K \nu_{i,K} D_{K,J}\vec{\nabla}C_J + \frac{t_i^{\#}\vec{J}^{\#}}{z_i\mathcal{F}} \tag{2.13}$$

Where the index J and K run over the number of independent neutral electrolyte virtually composed by the ionic species constituting the system. The first term on the right-hand side of the latter equation, also called *diffusion-conduction equation*, represents chemical diffusion while the second term represent ionic conduction. In principle, such multicomponent Fickian approach could be employed to describe mass and charge transport in ionic systems, given that in an electroneutral system, the number of independent ionic concentration gradient is $N-2$. Therefore, any arbitrarily chosen set of $N-2$ equivalent neutral electrolytes can be chosen to describe diffusion. However, several problems arise: first the Fickian diffusivities $D_{K,J}$ and the ionic transport numbers are not independent from each other, thus making the integration of such transport equation rather complex. Also, Fickian diffusivities $D_{K,J}$ are not symmetric, resulting in $(N-1)^2$ number of parameters required to describe a multi-component system. Moreover, the use of concentration gradients as driving force, without explicitly accounting neither for electrical coupling among charged components nor the dependence of the transport coefficient on the components thermodynamic activity, makes the Fickian diffusivities $D_{K,J}$ highly dependent on the chosen reference frame, on concentration and even on the chosen set and sequence of equivalent electrolyte in the transport matrix. In addition, such coefficients are simple empirical coefficients and do not truly have a physical meaning, limiting their employment for the development of physicochemical predictive models.

An improved general framework to describe ionic transport in multi-ionic systems is provided by the thermodynamics of irreversible processes. According to this theory, firstly developed by Onsager as extension of classical thermodynamics, any departure from equilibrium gives rise to driving forces and, consequently, to fluxes that result in a net rate of entropy production. The theory relies on two fundamental assumptions: the continuum hypothesis and the local equilibrium hypothesis. Both are inherently linked to the spatial and temporal scales of observation. In particular, the latter assumes that transport phenomena occur over time scales much larger than those of molecular motion, thereby ensuring local thermodynamic equilibrium. This assumption is generally valid as long as the system remains sufficiently close to equilibrium conditions. Under these premises, electrodiffusive fluxes can be related to thermodynamic driving forces through linear phenomenological equations of the form:

$$\vec{N}_i^{\#} = -\sum_j l_{i,j}\vec{\nabla}\tilde{\mu}_j \tag{2.14}$$

where $l_{i,j}$ are the Onsager phenomenological coefficients, which were shown to be symmetric through the Onsager reciprocity relations [22,124]. Moreover, since transport phenomena are inherently spontaneous, the theory of irreversible thermodynamics requires that the transport coefficients $l_{i,j}$ comply with the condition of a positive entropy production rate Ψ, also known as *dissipation function* [22]*:*

$$\frac{ds}{dt} = \Psi = -\frac{1}{T}\sum_i \vec{N}_i^{\#}\vec{\nabla}\tilde{\mu}_i = \frac{1}{T}\sum_i\sum_j l_{i,j}\vec{\nabla}\tilde{\mu}_i\vec{\nabla}\tilde{\mu}_j \geq 0 \tag{2.15}$$

where s is the specific entropy per unit of volume. The inequality establishes that the diagonal elements of the transport matrix must always be positive, whereas the off-diagonal elements, also referred to as *cross-phenomenological coefficients*, may take either positive or negative values [6]

In equation (2.14), the generic electrodiffusive flux depends on the driving force of each component[23]. This reflects the physical coupling of ionic fluxes arising from both long-range and short-range interactions among the different ions.

[23]The driving force corresponds to the ions' electrochemical potential gradient in the absence of externally applied forces (i.e., gravitational or magnetic fields)

As discussed in section 2.1.1.1, all flux densities $\vec{N}_i^{\#}$ are not independent as they are linked through the definition of the reference velocity. Similarly, the driving forces $\vec{\nabla}\tilde{\mu}_i$ must locally satisfy the isothermal Gibbs-Duhem equation:

$$\sum_i C_i \vec{\nabla}\tilde{\mu}_i = \vec{\nabla}P \tag{2.16}$$

Therefore, there are only $N-1$ independent components and driving forces. Consequently, by considering Onsager reciprocity relation, the total number of independent transport parameters required for a general description of ionic transport is $\frac{N}{2}(N-1)$ [32].

2.1.2 The Nernst–Planck model

In section 2.1.1.3, it was shown that, according to thermodynamics of irreversible process, the general description of ionic transport is based on a complex system of transport equations where each flux is coupled with each driving force, thus requiring a considerable number of transport parameters. This clearly limits the practical application of such rigorous transport model in favours of simpler alternative such as the NP model [45,107,125].

2.1.2.1 Model derivation

NP model is the most widely employed framework for describing ionic transport in solution and in IEMs. The derivation of the NP model is based on a fundamental assumption called *principle of independence of ionic fluxes*, according to which short-range interactions among ionic species can be neglected, or equivalently, ions can interact only by means of long-range electrostatic interactions. Consequently, the cross-phenomenological transport coefficients in equation (2.14) (i.e., the off-diagonal elements of the transport matrix) can be neglected:

$$l_{i,j} = 0 \Leftrightarrow i \neq j \tag{2.17}$$

Therefore, the phenomenological transport equation (2.14) can be approximated as follows:

$$\vec{N}_i^{\#} = -l_{i,i}\vec{\nabla}\tilde{\mu}_i \tag{2.18}$$

At this stage, the dependence of $l_{i,i}$ on the concentration is accounted for by introducing the ionic diffusion coefficient D_i according to the following relation:

$$l_{i,i} = \frac{D_i C_i}{R_g T} \tag{2.19}$$

If thermodynamic ideality is assumed, by substituting equation (2.19) and the definition of the electrochemical potential (eq. (1.13)) into eq. (2.18), the traditional isobaric form of the NP equation is obtained:

$$\vec{N}_i^{\#} = -D_i \vec{\nabla} C_i - z_i \mathcal{F} \frac{D_i C_i}{R_g T} \vec{\nabla} \varphi \tag{2.20}$$

The first right-hand side of eq. (2.20) represents ionic diffusion due to concentration gradient, while the second describe ionic migration due to the gradient of electrical potential. Note that, as it is discussed in section 2.1.2.4, *migration* and *conduction* are different charge transport mechanisms.

A fundamental implicit assumption made in the derivation of eq. (2.20) is that diffusion and migration can be described by the same transport coefficient, i.e., that electrochemical mobility and ionic diffusivity must satisfy the so called Nernst-Einstein equation (also called Einstein-Smoluchowski equation)[22,30]:

$$u_i = \frac{D_i}{R_g T} \tag{2.21}$$

where u_i is the electrochemical (or electrophoretic) mobility. Equation (2.21) is valid only if ions' concentration follows a Boltzmannian distribution of the electric potential φ, which is strictly true only if ions do not interact through short-range forces [126]. This requirement, along with the neglection of the cross-phenomenological coefficients, make the NP equation strictly valid only at infinite dilution, i.e., when the Debye length of the system is high enough to prevent any short-range interactions among ions. As discussed in section 2.1.3.7, this condition is plausibly met within the range of validity of the Debye-Hückel theory, i.e., for $I \leq 10\ mN$ [30].

Strictly speaking, the diffusion coefficients appearing in eq. (2.20) should correspond to the ionic mobilities determined under infinite-dilution conditions. These values are inherently independent of concentration, as they represent the mobility of individual ions surrounded exclusively by water molecules. Nevertheless, in order to extend the applicability of the Nernst–Planck model to finite-concentration systems, such diffusivities are commonly treated as concentration-dependent parameters (see 2.1.2.7). The ionic mobilities and diffusivities at infinite dilution are summarized in Table 7.

Table 7 Electrophoretic mobility and ionic diffusivities of some inorganic ions in aqueous solution at infinite dilution and 25°C. Taken from the open-source software for geochemical calculations PhreeqC [127].

	u_i [m^2 mol s^{-1} J^{-1}]	D_i [m^2 s^{-1}]
Li^+	4.2E-13	1.03E-09
Na^+	5.4E-13	1.33E-09
K^+	7.9E-13	1.96E-09
Mg^{2+}	2.8E-13	7.05E-10
Cl^-	8.2E-13	2.03E-09

2.1.2.2 Thermodynamic correcting coefficients for concentrated systems

As discussed in section 2.1.2.1, the theoretical derivation of the NP model relies on several assumptions, such as the equivalence between ionic concentration and thermodynamic activity, that limits its applicability to dilute systems. One consequence of these assumptions is that, when the NP model is applied to concentrated solutions, ionic diffusivities are expected to exhibit a strong dependence on concentration. To mitigate this effect, the NP equation can be modified to include the gradient of the activity coefficient. However, as discussed in section 1.1.3, the decomposition of the electrochemical potential into a concentration term and an electrostatic potential term is inherently arbitrary. To avoid relying on any arbitrary convention, the following formulation employs Newman's quasi-electrostatic potential. Consequently, substitution of eq. (1.37) into eq. (2.18) allows the NP equation to be re-formulated as follows:

$$\vec{N}_i^{\#} = -\frac{D_i C_i}{R_g T}\left[RT\vec{\nabla} ln\left(\gamma_{i(n)} C_i\right) - z_i \mathcal{F}\vec{\nabla}\varphi\right] \tag{2.22}$$

Further manipulation of the former equation leads to [22,32,128]:

$$\vec{N}_i^{\#} = -D_i \Gamma_{i(n)} \vec{\nabla} C_i - z_i \mathcal{F} \frac{D_i C_i}{R_g T}\vec{\nabla}\varphi \tag{2.23}$$

where $\Gamma_{i(n)}$ is the ionic diffusivity thermodynamic corrective factor defined as follows [122]:

$$\Gamma_{i(n)} = 1 + \frac{dln\gamma_{i(n)}}{dlnC_i} \tag{2.24}$$

According to eq. (2.24), the contribution of $\Gamma_{i(n)}$ becomes negligible when approaching the chemical potential secondary reference state at which $\gamma_{i(n)} = 1$. When modelling highly concentrated systems, evaluation of $\Gamma_{i(n)}$ requires the knowledge of experimental values of $\gamma_{i(n)}$ at various concentrations or the implementation of proper thermodynamic models such as the Pitzer model. Further discussion on the evaluation of thermodynamic correcting coefficients to ionic diffusivity in IEMs is provided in section 2.3.1

2.1.2.3 Ionic conduction and diffusion potential

A key advantage of the NP model over the Fickian approach is the explicit dependence of the ionic fluxes on the electrical potential gradient. Indeed, this very term allows to track the effect of the electric field on ionic transport. When such electric field is applied externallys it generates an ohmic conduction current density that can be evaluated by substituting the NP equation into eq. (2.8):

$$\vec{J}^{\#} = -\frac{\mathcal{F}^2}{R_g T}\sum_i z_i^2 D_i C_i \vec{\nabla}\varphi_{ohm} \tag{2.25}$$

where $\vec{\nabla}\varphi_{ohm}$ is the gradient of the externally applied potential. Comparison with the first Ohm's law for ionic conduction[24] allows to identify the NP ionic conductivity:

$$\kappa^{\#} = \frac{\mathcal{F}^2}{R_g T}\sum_i z_i^2 D_i C_i \tag{2.26}$$

Analogously, substitution of the NP equation into eq. (2.10) allows to evaluate the NP transport numbers:

$$t_i^{\#} = \frac{z_i^2 D_i C_i}{\sum_j z_j^2 D_j C_j} \tag{2.27}$$

The overall electric field experienced by each ionic species is not determined solely by the externally applied field but is also influenced by the electric field generated internally by the charged species.

[24] The first Ohm's law, valid for first and second species conductors, states that an electric current density arise in a system due to the application of an external potential gradient, usually called Ohmic potential, according to the following equation: $\vec{J}^{\#} = -\kappa^{\#}\vec{\nabla}\varphi_{ohm}$

The coupling of ionic fluxes arising from long-range interactions can be further understood by noting that the electrical potential in eq. (2.20) generally does not only correspond to the externally applied ohmic potential gradient. This can be readily demonstrated by substituting eq. (2.20) into eq. (2.8) and applying the definition of ionic conductivity (eq. (2.26)):

$$\vec{J}^{\#} = -\kappa^{\#}\left(\vec{\nabla}\varphi + \frac{\mathcal{F}}{\kappa^{\#}}\sum_{i} z_i D_i \Gamma_{i(n)} \vec{\nabla} C_i\right) \tag{2.28}$$

By applying the first Ohm's law (see [24]), it follows that:

$$\vec{\nabla}\varphi_{ohm} = \vec{\nabla}\varphi + \frac{\mathcal{F}}{\kappa^{\#}}\sum_{i} z_i D_i \Gamma_{i(n)} \vec{\nabla} C_i = \vec{\nabla}\varphi - \vec{\nabla}\varphi_{diff.} \tag{2.29}$$

where $\vec{\nabla}\varphi_{diff.}$ is called *diffusion potential*. According to the former equation, such potential originates from concentration gradients due to the difference in the ionic diffusivities[25], and it is directly responsible for the electrical coupling of ionic fluxes. Indeed, in the presence of an electrolyte concentration gradient, ions with opposite charge would diffuse with different velocities due to the difference in the ionic diffusivities. Such difference however induces a charge separation which in turn, according to Poisson's equation (1.53) generates a local electric field accelerating the slower ions and decelerating the faster ones. In practice, the diffusion potential is also responsible for the establishment of a potential difference across any membrane separating compartments at different concentrations.

2.1.2.4 Diffusion-conduction form of the Nernst-Planck equation

Integration of the NP equation in the form of eq. (2.20) requires the knowledge of the potential drop as boundary condition. This can be rather cumbersome in the modelling of galvanostatic systems, where the current density must be set to a specific value and the potential drop is not known a priori. In this case, a more useful form of the NP equation can be obtained by substituting eq. (2.28) into eq. (2.20):

[25] Indeed if $D_i = D_j = \cdots D_n$, due to the local electroneutrality restriction $\sum_i z_i \vec{\nabla} C_i$, the diffusion potential would be null.

$$\vec{N}_i^{\#} = -\sum_j D_{i,j}\vec{\nabla}C_j + \frac{t_i^{\#}\vec{J}^{\#}}{z_i\mathcal{F}} \tag{2.30}$$

In the former equation $D_{i,\mathrm{j}}$ are called cross-diffusion coefficients and are defined as follows:

$$D_{i,j} = D_i\Gamma_{i(n)}\delta_{i,j} + \frac{t_i^{\#}}{z_i}z_j\left(D_i\Gamma_{i(n)} - D_j\Gamma_{j(n)}\right) \tag{2.31}$$

Where $\delta_{i,j}$ is the Kronecker delta which assumes the following values:

$$\begin{cases}\delta_{i,j} = 1 \iff i = j\\ \delta_{i,j} = 0 \iff i \neq j\end{cases} \tag{2.32}$$

Equation (2.30) is called the *diffusion-conduction* form of the NP equation, as the second term on the right-hand side of the equation explicitly account for ionic conduction.Conversely, the first term accounts for *chemical diffusion*, i.e., ionic transport solely due to the presence of concentration gradients.

2.1.2.5 Nernst-Hartley electrolyte diffusion coefficient

In the previous section it was shown that the strength of the NP approach over the Fickian one comes from the description of mass transport in terms of dissociated ions rather than neutral electrolytes. Nonetheless, in some cases, the Fickian approach can be useful owing to its structural simplicity. For instance, integration of transport equations to retrieve transport coefficients from macroscale experimental data in a single-salt system is easier in the Fickian framework (see section 2.3.2). Hence, it is useful to know the relation between the Fickian salt diffusivity and the NP ionic diffusivities. Let us consider a system composed of two oppositely charged ionic species for which the differential form of the local electroneutrality equation is satisfied:

$$\sum_k z_k\vec{\nabla}C_k = 0 \tag{2.33}$$

According to the diffusion-conduction form of the NP equation, chemical (or Fickian) diffusion is described by the first right-hand side term of eq. (2.30). Substitution of equations (2.31) and (2.33) into the former equation leads to:

$$\vec{N}_i^{\#} = -\left(t_i^{\#} D_j \Gamma_{j(n)} + t_j^{\#} D_i \Gamma_{i(n)}\right)\vec{\nabla} C_i + \frac{t_i^{\#}\vec{J}^{\#}}{z_i \mathcal{F}} \tag{2.34}$$

Substituting the expression of the transport number in the NP approach (eq. (2.27)), the following formulation of the NP equation for a binary system can be obtained:

$$\vec{N}_i^{\#} = -\overline{D}_{ij}\vec{\nabla} C_i + \frac{t_i^{\#}\vec{J}^{\#}}{z_i \mathcal{F}} \tag{2.35}$$

where D_{ij} correspond to the Nernst-Hartley diffusion coefficient of the dissociated electrolyte, related to the ionic diffusion coefficients as follows:

$$\overline{D}_{ij} = \frac{D_i D_j\left(z_i^2 C_i \Gamma_{j(n)} + z_j^2 C_j \Gamma_{i(n)}\right)}{z_i^2 D_i C_i + z_j^2 D_j C_j} \tag{2.36}$$

Please note that, depending on the chosen reference species for the quasi-electrostatic potential (i.e., $n = i$ or $n = j$), either $\Gamma_{j(n)}$ or $\Gamma_{i(n)}$ would correspond to 1. In the absence of non-ideal interaction (i.e., $\Gamma_{i(n)} = \Gamma_{j(n)} = 1$), the Nernst-Hartley diffusion coefficient corresponds to the Fickian salt diffusion coefficient. This can be easily demonstrated considering that, in the absence of an ohmic current, due to the local electroneutrality (eq. (2.33)), the following relations hold:

$$\vec{\nabla} C_{ij} = \frac{\vec{\nabla} C_i}{\nu_i} \tag{2.37}$$

$$\vec{N}_{ij}^{\#} = \frac{\vec{N}_i^{\#}}{\nu_i} \tag{2.38}$$

where $\vec{N}_{ij}^{\#}$ and $\vec{\nabla} C_{ij}$ are respectively the neutral electrolyte flux and concentration gradient and ν_i is a stoichiometric coefficient satisfying the Guggenheim's relation (eq. (1.28)). Substitution of the former equations into eq. (2.35) leads to:

$$\vec{N}_{ij}^{\#} = -\overline{D}_{ij}\vec{\nabla} C_{ij} \tag{2.39}$$

which is formally analogous to the first Fick's law for binary diffusion.

2.1.2.6 Accounting for IEMs morphology in mass transport modelling

As previously stated, the NP model is widely employed to describe ionic transport in IEMs. To this regard, it is relevant to highlight some critical aspects of the application of such model to IEMs.

First and foremost, the way the membrane is modelled in equilibrium with the external solution, and the resulting definition of the system under consideration, has significant implications for both the governing equations and the transport parameters. Treating the membrane equilibrated with the external solution as either a one-phase system or a two-phase system, with the latter distinguishing between hydrophobic polymeric domains and hydrophilic, solution-containing domains. This point is further discussed in section 2.1.3.2.

In the former case, our system includes the component *membrane* and the concentration should be consistently defined per unit of volume of swollen membrane. Conversely, in the latter case, concentrations per unit of volume of sorbed solution must be employed. The two concentrations are typically interconverted by means of the water volume fraction of the membrane:

$$C_i^p = C_i^w \phi_w \tag{2.40}$$

In the former equation C_i^p is the concentration per unit of volume of swollen membrane, while C_i^w is the concentration per unit of volume of sorbed solution[26]. The domains of the swollen membrane occupied by the solution are referred to as *pores*, even though there is not unanimous agreement in the scientific community on the proper usage of such term [12,129,130]. As a matter of fact, dense polymer membranes do not have fixed pores as strictly porous membranes, but due to the loose packing of polymer chains and to the water uptake from the external solution, free volumes (i.e., volume not occupied by polymer chains) where water molecules and solvated ions can move are created.

The concentration scale per unit of volume of sorbed solution (i.e., number of moles per volume of pores or free volume) represents the most widely adopted approach and was therefore employed in the present work.

Furthermore, when defining velocities, fluxes, and spatial coordinates, it is necessary to distinguish between fluxes expressed per unit of geometrical or pore surface area, as well as between geometrical

[26] Rigorously. φ_w should take into account also the volume occupied by the sorbed ions, but this contribution is usually neglected.

(i.e., linear) and curvilinear (i.e., following the tortuous path of the hydrophilic domains) spatial coordinates.

The hydrophobic backbones of the polymeric chains act as a geometrical barrier to mass transport, which instead occurs within the hydrophilic channels containing water molecules, solvated ions, and fixed charges. The presence of this impervious solid matrix reduces the fraction of geometrical area available for transport, thereby increasing the interstitial velocity, while also elongating the trajectory of the diffusing species across the tortuous medium, which effectively increases the membrane thickness. These two effects can be accounted for through the ratio of porosity to tortuosity ϵ/τ [131–133]. This geometrical correction factor allows the conversion of interstitial fluxes $\vec{N}_i'$ into apparent fluxes $\vec{N}_i$, when the geometrical area and thickness are employed:

$$\vec{N}_i = \frac{\epsilon}{\tau}\vec{N}_i' \tag{2.41}$$

The correcting coefficient appearing in the former equation can then be incorporated into the ionic diffusivity by defining an apparent diffusion coefficient:

$$D_i = \frac{\epsilon}{\tau}D_i' \tag{2.42}$$

Because of this geometrical effect, the measurable apparent diffusivity D_i is lower than the true interstitial diffusivity. Hence, knowledge of the correction factor ϵ/τ, is required to properly evaluate D_i'.

The porosity ϵ corresponds to the fraction of free volume accessible for transport, which coincides with the volumetric water fraction ϕ_w, and can be readily determined from water uptake measurements (see 1.2.2.5). In contrast, tortuosity τ cannot be measured directly and is generally considered a function of both water volume fraction and the morphology of hydrophilic domains.

For certain classes of materials, including IEMs, commonly employed theoretical or phenomenological models approximate tortuosity as a function of porosity alone. The most widely used relation is the Bruggeman expression [114,134,135]:

$$\tau = \epsilon^n \tag{2.43}$$

with $n < 0$. For a broad range of materials, including IEMs with moderate hydration, Bruggeman's model yields good agreement with experimental data using $n = -0.5$ [134]. Accordingly, ϵ/τ can be rewritten as:

$$\frac{\epsilon}{\tau} = \frac{\epsilon}{\sqrt{\epsilon}} = \sqrt{\phi_w} \tag{2.44}$$

A popular alternative to Bruggeman's model, is the Mackie & Meares model [136]:

$$\frac{\epsilon}{\tau} = \left(\frac{\phi_w}{2 - \phi_w}\right)^2 \tag{2.45}$$

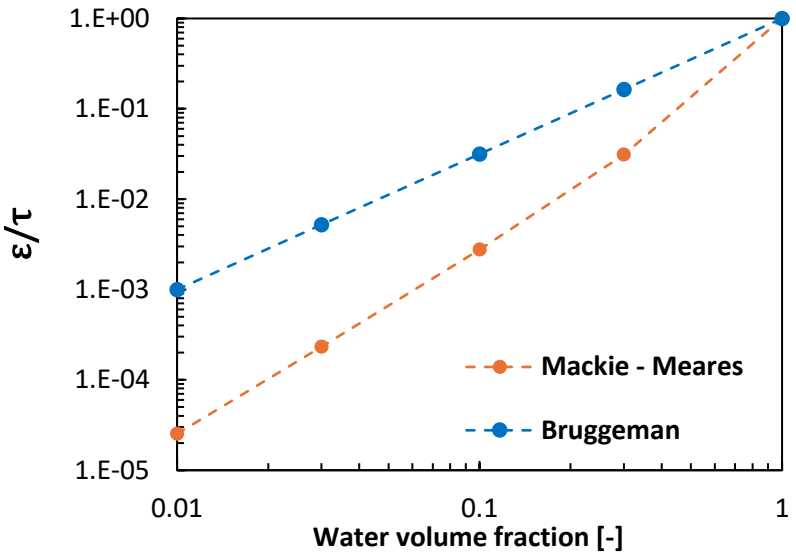

Figure 16 Porosity and tortuosity ratio as a function of water volume fraction in membrane evaluated with Bruggeman's model and Mackie & Meares model

As shown in Figure 16, the two models yield significantly different predictions of the correction factor ϵ/τ, with the discrepancy becoming more pronounced as the water volume fraction decreases. Specifically, the Mackie–Meares model predicts a much sharper increase in tortuosity at low hydration [133]. For membranes with moderate to low water content (i.e., $\phi_w < 0.3$), the deviation between the two models exceeds one order of magnitude. As a consequence, the apparent transport coefficients calculated using Mackie–Meares would be more than two orders of magnitude smaller than the corresponding interstitial values, which appears unrealistic. Therefore, this model is more

suitably applied to highly hydrated membranes (i.e., $\phi_w > 0.3$) [77,137]. Given the moderate water uptake of the IEMs investigated in this work, the Bruggeman model (eq. (2.44)) was adopted in the present work to convert apparent transport parameters into true (i.e., interstitial) values.

2.1.2.7 Limitation of the Nernst-Planck approach

According to its theoretical derivation, the main limitation of the NP model is the neglect of the cross-phenomenological transport coefficients, i.e., the off-diagonal elements of the transport matrix that relate the electrodiffusive flux densities with the driving forces. Consequently, transport of a given species is only related to its own electrochemical potential gradient. From a physical perspective, such assumption corresponds to neglect the mutual coupling among ionic fluxes due to the short-range interactions acting on each component. As we discussed in section 2.1.2.3, within the NP approach ionic fluxes are coupled through the definition of the diffusion potential that arises to satisfy the local electroneutrality condition. However, such coupling is solely due to long-range electrostatic interactions and cannot account for the effect of short-range interactions on the transport rates of each component.

In order to clarify this point, let us perform a virtual experiment in order to measure ionic diffusivities in an aqueous solution of a generic salt at variable concentration C_{ca}. This is typically done by performing two separate tests where salt diffusion and ohmic conduction are quantified (see section 2.2). According to the NP theory, two transport coefficients are enough to describe diffusion and conduction in this system. These are the ionic diffusivities of D_c or D_a or, conversely, the Nernst-Hartley salt diffusion coefficient $\overline{D}_{ca}$ (eq. (2.36) and the ionic conductivity κ (eq. (2.26)). Indeed, according to the Nernst-Einstein assumption, on which the NP model is based, the effect of an electric field or a concentration gradient on the motion of a charged particles must be described by the same coefficient. This clearly introduces a limitation on the values that this transport coefficients can assume. In fact, by combining equations (2.26) and (2.36) a second degree equation is obtained, and real solutions to this equation exist exclusively in the following domain:

$$\overline{D}_{ca} \leq \frac{R_g T}{4\mathcal{F}^2} \frac{\nu_c + \nu_a}{\nu_c \nu_a} \frac{\kappa}{C_{ca}} \tag{2.46}$$

Such inequation clearly states that, taken $\overline{D}_{ca}$ and κ measured at the generic salt concentration C_{ca}, NP ionic diffusivities exist, and hence the NP model can be successfully employed to describe ionic transport, only if experimental data satisfy inequation (2.46).

By way of example, graphical representation of the derived condition of validity of the NP model (i.e., inequality (2.46)) is depicted in Figure 17 at various salt concentrations. In the same figure, values of aqueous NaCl salt diffusivity and ionic conductivity are reported. At a given concentration, the Nernst-Planck model can be used to describe salt diffusion and ionic conduction, i.e., ionic diffusivities can be evaluated from experimental data, only if the experimental data lie below the corresponding dashed line. With increasing concentration, the dashed line moves downward. Consistently, the black dashed line represents the maximum salt concentration at which the NP model can be adopted to simultaneously describe diffusion and conduction. This outcome clearly demonstrate that ionic diffusion and conduction cannot be effectively described by the same transport parameters, especially at high concentration, at which the short-range interactions become dominant. Importantly, the upper limit of validity of the NP model, corresponding to 13 mM for NaCl, lies well below the ionic strength that is encountered in any commercial IEM. This proves that NP ionic diffusivities at nonzero concentrations are ill-defined and the application of the NP model to describe ionic transport in such cases is theoretically, and sometimes practically, unfeasible.

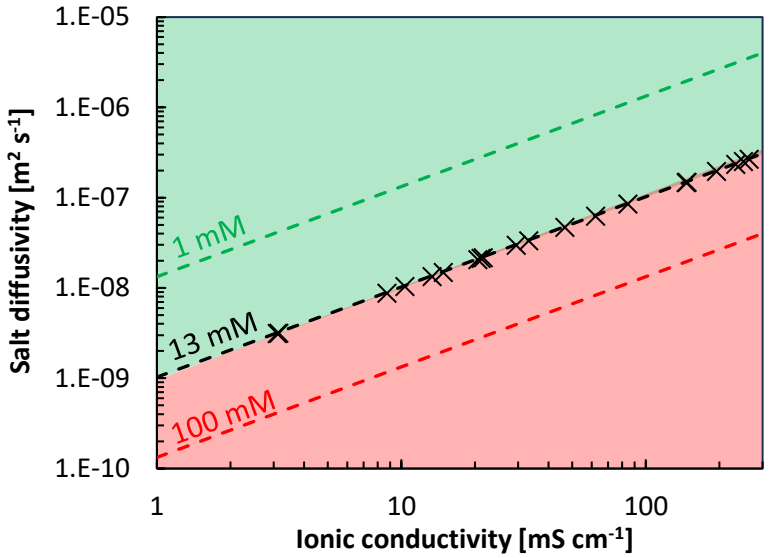

Figure 17 Domain of validity of the Nernst-Planck model in a NaCl aqueous solution. The black crosses represent the experimental values of salt diffusivity and ionic conductivity measured at different salt concentrations ranging from 0.03 M to 5 M. Salt diffusivity was taken from Vitagliano et al.[138] *while ionic conductivity was evaluated through the opensource geochemical software for aqueous solution properties PhreeqC* [127]. *The dashed lines are the graphical representation of inequation (2.46) at a given salt concentration. The green area represents the concentration domain of validity of the Nernst-Planck model. Conversely, the red area represents the concentration domain where the Nernst-Planck model fails in describing diffusion and conduction.*

This outcome is not simply related to the values that ionic diffusivities can assume. Conversely, it is due to a structural deficiency. The upper limit of validity of the NP model shown in Figure 17 is very

close to the upper limit of validity of the Debye-Hückel theory ($\sim 10mM$, see section 1.1.3.11), further suggesting that the failure of the NP model is related to the emergence of strong ion-ion interactions not accounted for. Consequently, allowing ionic diffusivities to become concentration dependent is not sufficient to solve the problem; rather additional composition dependent parameters are required to develop a comprehensive transport model [32].

To prove this, let us perform another virtual experiment and consider two adjacent compartments of an ED unit, containing an aqueous NaCl solution at same concentration, separated by a CEM. By applying an external ohmic potential difference across the membrane we would observe Na^+ ions migrating across the CEM toward the negatively charged electrode, while the Cl^- would be largely blocked. In addition, we would also notice the passage of water molecules in the same direction of Na^+ ions. Such phenomenon, usually called *electro-osmosis,* can be explained assuming that water molecules are entrained by Na^+ ions. In the framework of the NP model such phenomenon is surprising and inexplicable, given that the chemical potential of water is the same on both sides of the membrane.

To understand and model such phenomenon, we need to account for short-range (i.e., non-electrostatic) interactions, relying upon a more sophisticated transport theory, as that presented in section 2.1.3

2.1.3 The Maxwell-Stefan model

The Maxwell-Stefan model was originally derived by Maxwell and Stefan around 1870 to model isothermal diffusion in multi-component gas mixtures. Later, it was extended to liquid mixtures and also more complex media such as IEMs. Today, it remains one of the most sophisticated and comprehensive transport models. Yet, due to its inherent complexity, it is rather unexplored by chemical engineers.

2.1.3.1 Model derivation

The Maxwell-Stefan model is derived from a steady-state momentum balance equation applied to each component of the system [122]:

$$\vec{d}_i = -\sum_{j \neq i} \vec{F}_{i,j} \tag{2.47}$$

In the former equation, $\vec{d}_i$ represents the overall mass transport driving force per unit of volume acting on the generic i-th component, while $\vec{F}_{i,j}$ depicts the generic force per unit of volume exerted

on the i-th component by a different component of the system, with the understanding that the summation is extended to all the components except for the i-th component itself. Note that $\vec{d}_i$ and $\vec{F}_{i,j}$ in principle may represent forces either internal or external to the system.

For an isothermal system, in the absence of any external body force (such as gravity) except electrostatic forces, $\vec{d}_i$ can be expressed as follows [131]:

$$\vec{d}_i = C_i \vec{\nabla} \tilde{\mu}_i \tag{2.48}$$

Conversely, according to its definition $\vec{F}_{ij}$ represents a drag force opposed to the driving force $\vec{d}_i$. The magnitude of such force is taken to be proportional to the relative velocity of the two components, given that two bodies moving with the same velocity cannot exchange momentum. Such proportionality constant is herein called *friction factor* $K_{i,j}$ and defined as follows:

$$K_{ij} = \frac{\vec{F}_{ij}}{\left(\vec{v}_i - \vec{v}_j\right)} \tag{2.49}$$

where $\vec{v}_i$ and $\vec{v}_j$ are the components velocity with respect to any arbitrary reference frame. According to the previous equation, $K_{i,j}$ assumes a specific physical meaning: it quantifies the strength of interaction among a generic couple of different components. Notably, in the considered special scale, there is no distinction among different particles of the same component, and the velocity herein introduced should be intended as the average velocity of the component. Consequently, particles of the same type cannot exchange momentum and hence the friction factor $K_{i,i}$ is not defined. Moreover, due to Newton's third law, or the Onsager reciprocal relations, the friction factors $K_{i,j}$ are inherently symmetric i.e., $K_{i,j} = K_{j,i}$. A pictorial representation of these interaction forces is given in Figure 18.

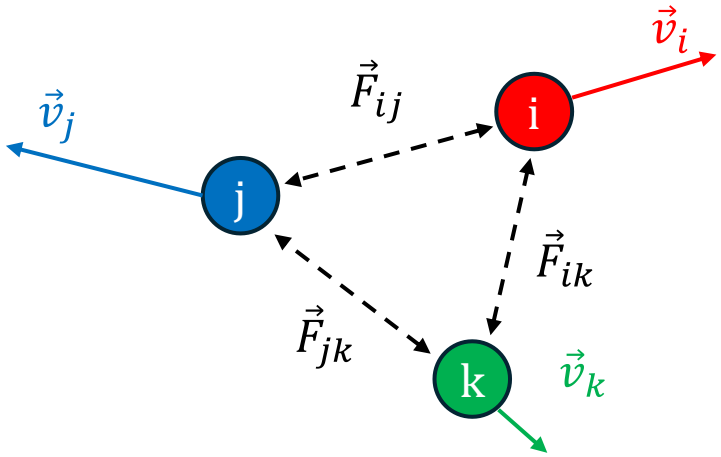

Figure 18 Schematic representation of the interactions between different kind of components in a ternary system.

Importantly, in an inertial system $\vec{F}_{i,j}$ is independent of the chosen reference frame and the same can be said about the relative velocity. Consequently, $K_{i,j}$ is independent of the chosen reference frame as well. Furthermore, by definition, $K_{i,j}$ do not depend on the components' velocities nor on the driving force but do depend on the concentration of the components. Clearly, the more particles of a component per unit of volume are present, the higher is the intensity of the interaction. Therefore, $K_{i,j}$ is expressed as follows [32,139,140]:

$$K_{i,j} = R_g T \frac{C_i C_j}{C_{tot}} f_{i,j} = R_g T \frac{C_i C_j}{C_{tot}} \frac{1}{Đ_{i,j}} \tag{2.50}$$

where C_{tot} is the total molar concentration, while $f_{i,j}$ and $Đ_{i,j}$ are respectively the MS binary friction and diffusion coefficients[27], which exhibit symmetry in the same way as $K_{i,j}$.

By substituting equations (2.48), (2.49) and (2.50) into eq. (2.47), the multi-component Maxwell-Stefan equation is achieved:

[27]Considering that such forces are presented as drag forces, the corresponding transport parameter should be the friction coefficient $f_{i,j}$. Nonetheless, MS diffusivities $Đ_{i,j}$ were defined for historical reasons to be consistent with previously developed transport models.

$$C_i \vec{\nabla} \tilde{\mu}_i = -\frac{R_g T}{C_{tot}} \sum_j \frac{C_i C_j}{Đ_{i,j}} \left(\vec{v}_i - \vec{v}_j\right) \tag{2.51}$$

According to equation (2.51), the motion of the components is coupled due to the exchange friction forces, or equivalently, the motion of a generic component is influenced by the driving force of all the others. Please note that in an isothermal, isobaric system, the former equation can be applied to describe the transport of $N-1$ species, whit N including the solvent. Indeed, summation over i of both sides side of eq. (2.51)) gives:

$$\sum_i C_i \vec{\nabla} \tilde{\mu}_i = -\frac{R_g T}{C_{tot}} \sum_i \sum_j \frac{C_i C_j}{Đ_{i,j}} (\vec{v}_i - \vec{v}_j) \tag{2.52}$$

The right-hand side of the former equation is null due to Newton's third law, while the left-hand side is null due to the Gibbs-Duhem equation. Therefore, the number of transport properties required to apply the MS model is $\frac{N}{2}(N-1)$. This corresponds to the number of parameters required in the phenomenological approach (section 2.1.1.3).

Importantly, one of the major advantages of the MS model is that, since species velocities only appear as differences, the extended MS transport equations are invariant with respect to the choice of reference velocity, thus the MS diffusion coefficients are independent from the reference velocity [26,130]. Furthermore, due to the inclusion of additional transport coefficients that account for the coupling between fluxes, MS diffusivities are inherently less sensitive to variations compared to those derived from the NP or Fickian frameworks.

2.1.3.2 Maxwell-Stefan approach applied to IEMs: the Binary friction model

Application of the MS model (eq. (2.51)) to IEMs is not trivial as it requires some modifications and careful specifications. Of fundamental importance is the choice of the portion of the system subjected to the momentum balance. Concentrations and thermodynamic properties must be defined and employed consistently with this choice.

Traditionally, mass transport phenomena in dense membranes such as IEMs have been described in accordance with the solution-diffusion model [66,70,141]. According to such model, the system cannot support any pressure gradient, and solvent and solutes move down their activity gradient defined for the membrane-solvent mixture. This introduces the problem of defining the molecular mass of the component "membrane". To avoid such inconvenience, mass or volumetric fractions are typically adopted instead of molar concentrations [142]. Yet, this leads us with the unsatisfactory

result of considering the membrane itself as a thermodynamic component of the system in question. Indeed, the component "membrane" is not subjected to partition equilibria with the external solution, and nothing can be said about its chemical potential. Consequently, the Gibbs-Duhem equation cannot be applied to evaluate the water activity in the membrane (see sections 1.1.4.3 and 1.1.4.4). Ultimately, the osmotic pressure of the solvent in the membrane is set to its ideal value.

Apart from thermodynamic considerations, assuming the membrane-solvent mixture as a homogeneous thermodynamic phase can be rather questionable [48,143].

An alternative approach is considering the solution-equilibrated membrane as a two-phase system [144], with the polymer phase distinct from the aqueous, ion-containing phase.

The system under investigation would correspond to the free volume not occupied by the polymer chains where water molecules and solvated ions are located.

The polymeric chains composing the hydrophobic domains and the fixed charges in contact with the solution are considered external bodies which can exert forces on the system. Consistently, the steady-state momentum balance equation (2.47) should include the contribution of such forces. Hence, the MS equation can be rewritten as follows:

$$C_i \vec{\nabla} \tilde{\mu}_i = -\frac{R_g T}{C_{tot}} \sum_{j \neq m} \frac{C_i C_j}{Đ'_{i,j}} \left(\vec{v}'_i - \vec{v}'_j \right) - K'_{i,m} \vec{v}'_i \tag{2.53}$$

In the former equation, known as *Binary Friction* (BF) model [131,145], $K_{i,m}$ is the friction factor describing the overall interaction between the generic mobile component and the membrane matrix, while the prime identifies interstitial quantities.

By means of eq. (2.41) and (2.42), the interstitial velocity can be converted into superficial (i.e., apparent velocity) by including porosity and tortuosity correction into the friction factors and into the MS binary diffusion coefficients (see section 2.1.2.6):

$$K_{i,j} = \frac{K'_{i,j}}{\frac{\epsilon}{\tau}} \tag{2.54}$$

$$Đ_{i,j} = \frac{\epsilon}{\tau} Đ_{i,j}{}' \tag{2.55}$$

Therefore, eq. (2.53) can be rewritten as:

$$C_i \vec{\nabla} \tilde{\mu}_i = -\frac{R_g T}{C_{tot}} \sum_{j \neq m} \frac{C_i C_j}{Đ_{i,j}} \left(\vec{v}_i - \vec{v}_j \right) - K_{i,m} \vec{v}_i \tag{2.56}$$

Note that the velocity of the membrane corresponds to the velocity of the laboratory-fixed reference frame and hence is set to zero. If we sum over i both sides of eq. (2.53), the contribution of the internal forces to the right-side membrane cancel out resulting in the following relation:

$$\sum_i C_i \vec{\nabla} \tilde{\mu}_i = -\sum_i K_{i,m} \vec{v}_i \tag{2.57}$$

The right-hand side of the former equation represent the overall force exerted by the membrane on the system and it is in general non-null. According to the isothermal Gibbs-Duhem equation (2.16), this must imply that:

$$\vec{\nabla} P = -\sum_i K_{i,m} \vec{v}_i \tag{2.58}$$

Equation (2.58) dictates that a pressure gradient develops in the hydrophilic domains to counter-balance the drag forces exerted by the membrane matrix on the mobile species, including water.

To this regard, it should be noticed that the binary friction equation (2.53) inherently accounts for hydrodynamic flow, and superposing additional equations for the flow of water is incorrect [140]. This represents a substantial advantage of the MS approach over the NP one, as the NP equation does not describe water transport directly, necessitating an additional independent equation, such as the Schloegl equation [22,131], to account for it.

It should be emphasized that, rather than being a demonstration of the actual presence of a pressure gradient in the membrane, eq. (2.58) is simply the result of the chosen modelling approach, which is consistent with the fundamental laws of physics and thermodynamics.

2.1.3.3 Transport equation inversion

A shortcoming of the MS approach is that transport equations cannot be directly employed in mass balance, as the velocities and hence the flux densities are not explicit in eq. (2.53). To express explicitly the components' velocity, eq. (2.53) can be manipulated as follows:

$$C_i \vec{\nabla} \tilde{\mu}_i = \sum_{j \neq m} \mathcal{M}_{i,j} \vec{v}_i \tag{2.59}$$

where $\mathcal{M}_{i,j}$ is defined as follows:

$$\begin{cases} \mathcal{M}_{i,j} = K_{i,j} \iff i \neq j \\ \mathcal{M}_{i,j} = -K_{i,m} - \sum_{j \neq m} K_{i,j} \iff i = j \end{cases} \tag{2.60}$$

By defining the corresponding transport matrix $[\mathcal{M}_{i,j}]$, eq. (2.59) can be rewritten as follows:

$$[C_i \vec{\nabla} \tilde{\mu}_i] = [\mathcal{M}_{i,j}][\vec{v}_i] \tag{2.61}$$

Inversion of the former equation leads to:

$$\vec{v}_i = -\sum_{j \neq m} \mathcal{L}_{i,j} C_j \vec{\nabla} \tilde{\mu}_j \tag{2.62}$$

where the coefficients $\mathcal{L}_{i,j}$ is obtained from the negative inverse matrix of $[\mathcal{L}_{i,j}]$:

$$[\mathcal{L}_{i,j}] = -[\mathcal{M}_{i,j}]^{-1} \tag{2.63}$$

Importantly, $\mathcal{L}_{i,j}$ and $\mathcal{M}_{i,j}$ are both symmetric coefficients and, following the former theoretical derivation, they are related to a laboratory-fixed reference frame [32].

By means of eq. (2.5), equation (2.62) can be rewritten as follows:

$$\vec{N}_i = -C_i \sum_{j \neq m} \mathcal{L}_{i,j} C_j \vec{\nabla} \tilde{\mu}_j \tag{2.64}$$

The former equation is structurally equivalent to eq. (2.14), proving that the MS approach is formally equivalent to the Onsager phenomenological approach.

2.1.3.4 Conductivity and transport numbers

By means of eq. (2.7), the ionic current density measured with respect to the laboratory reference frame can be evaluated as follows:

$$\vec{J} = -\mathcal{F} \sum_{i} z_i C_i \sum_{j \neq m} \mathcal{L}_{i,j}\, C_j \vec{\nabla} \tilde{\mu}_j \tag{2.65}$$

In a solution of uniform composition, $\vec{\nabla}\tilde{\mu}_{\mathrm{j}}$ corresponds to $z_j F \vec{\nabla}\varphi$ (see eq. (1.37)). Hence, eq. (2.65) can be rewritten as follows:

$$\vec{J} = -\mathcal{F}^2 \vec{\nabla}\varphi \sum_{i \neq m} z_i C_i \sum_{j \neq m} \mathcal{L}_{i,j}\, z_j C_j \tag{2.66}$$

Comparison with first Ohm's law allows to define ionic conductivity as follows:

$$\kappa = \mathcal{F}^2 \sum_{i \neq m} \sum_{j \neq m} \mathcal{L}_{i,j}\, z_j C_j z_i C_i \tag{2.67}$$

Equation (2.67) is formally analogue to the ionic conductivity defined in the NP framework (eq. (2.26) even though proper distinction should be made. In fact, while ionic diffusivities are directly defined per each component, $\mathcal{L}_{i,j}$ comes from an algebraic combination of all components transport coefficients.

Regarding the ions transport number, it could be straightforwardly defined by combining equations (2.10) and (2.62):

$$t_i = \frac{z_i C_i \sum_{j \neq m} \mathcal{L}_{i,j}\, z_j C_j}{\sum_{i \neq m} \sum_{j \neq m} \mathcal{L}_{i,j}\, z_j C_j z_i C_i} \tag{2.68}$$

2.1.3.5 Salt diffusive transport equation

In section 2.1.2.5, it was shown how to apply the NP model to derive the transport equation for the diffusion of a neutral electrolyte under the effect of a concentration gradient, when no external ohmic potential is applied to the system. Such result is particularly useful as one of the main IEMs experimental characterisation techniques is the standard diffusion test (see section 2.2). At this point, we aim at deriving a similar result starting by employing the binary-friction model.

Let us consider an IEM equilibrated with a strong electrolyte solution. According to eq. (2.53), mobile ions' transport is described according to the following equations:

$$\vec{\nabla}\tilde{\mu}_c = \frac{1}{C_c}\left[K_{c,a}(\vec{v}_a - \vec{v}_c) + K_{c,w}(\vec{v}_w - \vec{v}_c) - K_{c,m}\vec{v}_c\right] \tag{2.69}$$

$$\vec{\nabla}\tilde{\mu}_a = \frac{1}{C_a}\left[K_{c,a}(\vec{v}_c - \vec{v}_a) + K_{a,w}(\vec{v}_w - \vec{v}_a) - K_{a,m}\vec{v}_a\right] \tag{2.70}$$

Where the subscripts c and a identify the mobile cation and anion virtually stemming from the dissociation of the neutral electrolyte and partitioned into the membrane. By multiplying the former equations for the relative stoichiometric coefficients and replacing the velocities with the corresponding ionic fluxes we obtain:

$$\nu_c\vec{\nabla}\tilde{\mu}_c = \frac{\nu_c}{C_c}\left[\frac{K_{c,a}}{C_aC_c}\left(C_c\vec{N}_a - C_a\vec{N}_c\right) + \frac{K_{c,w}}{C_wC_c}\left(C_c\vec{N}_w - C_w\vec{N}_c\right) - \frac{K_{c,m}}{C_c}\vec{N}_c\right] \tag{2.71}$$

$$\nu_a\vec{\nabla}\tilde{\mu}_a = \frac{\nu_a}{C_a}\left[\frac{K_{c,a}}{C_cC_a}\left(C_a\vec{N}_c - C_c\vec{N}_a\right) + \frac{K_{a,w}}{C_wC_a}\left(C_a\vec{N}_w - C_w\vec{N}_a\right) - \frac{K_{a,m}}{C_a}\vec{N}_a\right] \tag{2.72}$$

If no ohmic potential is applied externally, the current density is zero, hence:

$$z_c\vec{N}_c + z_a\vec{N}_a = 0 \tag{2.73}$$

By applying Guggeneim's relation (eq. (1.28)) the former equation can be written as follows:

$$\frac{\vec{N}_c}{\nu_c} = \frac{\vec{N}_a}{\nu_a} = \vec{N}_{ca} \tag{2.74}$$

where $\vec{N}_{ca}$ is the neutral salt flux. Substitution of eq. (2.74) into equations (2.71) and (2.72) leads to:

$$\nu_c\vec{\nabla}\tilde{\mu}_c = \frac{\nu_c}{C_c}\left[\frac{K_{c,a}}{C_aC_c}(C_c\nu_a - C_a\nu_c)\vec{N}_{ca} + \frac{K_{c,w}}{C_wC_c}\left(C_c\vec{N}_w - C_w\nu_c\vec{N}_{ca}\right) - \frac{K_{c,m}}{C_c}\nu_c\vec{N}_{ca}\right] \tag{2.75}$$

$$\nu_a\vec{\nabla}\tilde{\mu}_a = \frac{\nu_a}{C_a}\left[\frac{K_{c,a}}{C_cC_a}(C_a\nu_c - C_c\nu_a)\vec{N}_{ca} + \frac{K_{a,w}}{C_wC_a}\left(C_a\vec{N}_w - C_w\nu_a\vec{N}_{ca}\right) - \frac{K_{a,m}}{C_a}\nu_a\vec{N}_{ca}\right] \tag{2.76}$$

By taking the anion as reference species to define the quasi-electrostatic potential, the neutral salt chemical potential (eq. (1.29)) can be defined as follows:

$$\nu_c \vec{\nabla}\tilde{\mu}_c + \nu_a \vec{\nabla}\tilde{\mu}_a = R_g T \left(\nu_c \Gamma_{c(a)} \frac{\vec{\nabla} C_c}{C_c} + \nu_a \frac{\vec{\nabla} C_a}{C_a} \right) \tag{2.77}$$

where $\Gamma_{c(a)}$ is the thermodynamic correcting factor accounting for the activity coefficient gradient (see section 2.1.2.2). Please note that in the former equation the dependence of the chemical potential on the pressure gradient was neglected. By summing equations (2.75) and (2.76), replacing the left-hand side with eq. (2.77) and multiplying both members by $C_c C_a$, the following equation is achieved:

$$\begin{aligned} R_g T \left(C_a \nu_c \Gamma_{c(a)} \vec{\nabla} C_c + C_c \nu_a \vec{\nabla} C_a \right) \\ = -\left[\frac{K_{c,a}}{C_a C_c} (C_c \nu_a - C_a \nu_c)(C_a \nu_c - C_c \nu_a) + \left(\frac{C_a}{C_c} \nu_c^2 K_{c,w} + \frac{C_c}{C_a} \nu_a^2 K_{a,w} \right) \right. \\ \left. + \left(\frac{C_a}{C_c} \nu_c^2 K_{c,m} + \frac{C_c}{C_a} \nu_a^2 K_{a,m} \right) \right] \vec{N}_{ca} + \left[\frac{C_a}{C_w} \nu_c K_{c,w} + \frac{C_c}{C_w} \nu_a K_{a,w} \right] \vec{N}_w \end{aligned} \tag{2.78}$$

By means of the differential form of the local electroneutrality equation (eq. (2.33)), the concentration gradient of the mobile species can be related as follows[28]:

$$\vec{\nabla} C_c = -\frac{z_a}{z_c} \vec{\nabla} C_a \tag{2.79}$$

Consequently, the left-hand side of the latter equation can be rewritten as follows

$$R_g T \left(C_a \nu_c \Gamma_{c(a)} \vec{\nabla} C_c + C_c \nu_a \vec{\nabla} C_a \right) = R_g T \left(C_c \nu_a - C_a \nu_c \Gamma_{c(a)} \frac{z_a}{z_c} \right) \vec{\nabla} C_a \tag{2.80}$$

Therefore, by applying eq. (2.50) and further manipulating the resulting equation, the following salt diffusion equation is achieved:

$$\begin{aligned} \left(C_c \nu_a - C_a \nu_c \Gamma_{c(a)} \frac{z_a}{z_c} \right) \vec{\nabla} C_a \\ = -\left[\left(\frac{C_a C_w}{C_{tot}} \frac{\nu_c^2}{Đ_{c,w}} + \frac{C_c C_w}{C_{tot}} \frac{\nu_a^2}{Đ_{a,w}} \right) + \frac{(C_c \nu_a - C_a \nu_c)^2}{C_{tot} Đ_{c,a}} + \frac{K_{ca,m}}{R_g T} \right] \vec{N}_{ca} \\ + \left[\frac{C_c C_a}{C_{tot}} \left(\frac{\nu_c}{Đ_{c,w}} + \frac{\nu_a}{Đ_{a,w}} \right) \right] \vec{N}_w \end{aligned} \tag{2.81}$$

where $K_{\mathrm{ca,m}}$ is called equivalent salt-membrane friction factor and defined as follows:

[28]Equation (2.33) is strictly valid if fixed charges concentration gradient in the membrane due to differential swelling is neglected.

$$K_{ca,m} = \frac{C_a}{C_c}\nu_c^2 K_{c,m} + \frac{C_c}{C_a}\nu_a^2 K_{a,m} \tag{2.82}$$

Equation (2.81) is formally analogue to the Nernst-Hartley diffusion equation for a neutral salt (eq. (2.39). However, thanks to the MS approach, the salt diffusion coefficient was decomposed in a series of terms, each of them accounting for a specific kind of interaction affecting the salt transport rate. Indeed, the terms in the square bracket multiplying the salt flux in eq. (2.81) respectively accounts for ion-water interactions, ion-ion interactions and ion-membrane interactions. Moreover, eq. (2.81) directly takes into account the effect of the drag force that water molecules exert on the mobile ions. According to eq. (2.81), a water flux opposed to the salt flux imply a reduction of the salt flux itself. Form a physical point of view, this apparent transport resistance is due to the drag force that water molecules exert on the mobile ions moving in the opposite direction.

2.1.3.6 Osmotic water transport equation

As discussed in the previous sections, one of the main advantages of the MS approach is that it provides a comprehensive approach to model mass transport, including water transport in the membrane. In this section we aim at deriving the transport equation describing water osmotic flux when no ohmic potential gradient is applied externally (i.e., in the absence of an applied current density). By considering a membrane equilibrated with a single-salt solution, water transport equation can be derived from eq. (2.53) as follows:

$$C_w\vec{\nabla}\mu_w = \left[K_{w,c}(\vec{v}_c - \vec{v}_w) + K_{w,a}(\vec{v}_a - \vec{v}_w) - K_{w,m}\vec{v}_w\right] \tag{2.83}$$

Substitution of the water chemical potential expression (eq. (1.13)) leads to:

$$C_w v_w\left(\frac{R_g T}{v_w}\vec{\nabla} ln a_w + \vec{\nabla}P\right) = \left[K_{w,c}(\vec{v}_c - \vec{v}_w) + K_{w,a}(\vec{v}_a - \vec{v}_w) - K_{w,m}\vec{v}_w\right] \tag{2.84}$$

By applying eq. (1.16) the water activity gradient can be expressed in terms of the osmotic pressure gradient as follows:

$$C_w v_w\left(\vec{\nabla}P - \vec{\nabla}\Pi\right) = \left[K_{w,c}(\vec{v}_c - \vec{v}_w) + K_{w,a}(\vec{v}_a - \vec{v}_w) - K_{w,m}\vec{v}_w\right] \tag{2.85}$$

According to the latter equation, the net driving force to water transport in membrane is given by the difference between hydrostatic pressure and osmotic pressure gradient. Notably, the quasi-electrostatic potential gradient does not explicitly appear in the driving force expression. However, it

indirectly affects the water molecules' velocity by influencing the values of the mobile ions' velocity. This further proves that, thanks to the coupling of water and ions' fluxes, in the MS approach no further transport equations are needed to account for osmotic and electro-osmotic water transport.

Assuming $C_w v_w \approx 1$, substituting apparent velocities with fluxes and applying equations (2.74) and (2.50) we arrive at:

$$\left(\vec{\nabla}P - \vec{\nabla}\Pi\right) = R_g T \frac{C_w}{C_{tot}}\left(\frac{\nu_c}{Đ_{c,w}} + \frac{\nu_a}{Đ_{a,w}}\right)\vec{N}_s - R_g T\left[\frac{1}{C_w}\frac{K_{w,m}}{R_g T} + \frac{1}{C_{tot}}\left(\frac{C_c}{Đ_{c,w}} + \frac{C_a}{Đ_{a,w}}\right)\right]\vec{N}_w \qquad (2.86)$$

In order to be solved for $\vec{N}_w$, equation (2.86) must be coupled with the mobile salt transport equation (2.81) and with the local electroneutrality condition (eq.(2.79)) given that the mobile ions concentration profiles in the membrane are, in general, not known a priori. To do so, proper boundary conditions must be provided, i.e., mobile species concentration, hydrostatic pressure and osmotic pressure drop between the solution-membrane interfaces must be imposed in order to determine the mobile species' velocity, or equivalently their fluxes.

In practical applications, $\vec{\nabla}P$ in the membrane can be induced applying a pressure drop between the two compartments separated by the membrane. However, in section 1.1.4.3 it was demonstrated that hydrostatic pressure gradients can also have a thermodynamic origin, being induced by differences in salt concentration in the external solutions facing the membrane. Such values should be determined by imposing the electrochemical potential equilibria at the solution-membrane interface. However, in section 1.3.1 it was shown that, in the absence of experimental values of hydrostatic pressure in the membrane (if achievable), the excess osmotic pressure in the membrane is not univocally determined. Consequently, the hydrostatic pressure in the membrane is determined up to an arbitrary constant ($\Pi^{m,ex,0}$, see Figure 10).

At this point, one could argue that, given that $\Pi^{m,ex,0}$ does not change moving from the left-hand to the right-hand interface (and vice versa), $\vec{\nabla}P$ should not be affected by such arbitrary choice. However, such indeterminacy may cause the hydrostatic pressure in the membrane to assume negative values under certain circumstances. Nonetheless, eq. (2.84) can be solved anyway by defining an overall driving force as follows:

$$\vec{\nabla} P_{tot} = R_g T \frac{C_w}{C_{tot}} \left(\frac{\nu_c}{Đ_{c,w}} + \frac{\nu_a}{Đ_{a,w}} \right) \vec{N}_{ca} - R_g T \left[\frac{1}{C_w} \frac{K_{w,m}}{R_g T} + \frac{1}{C_{tot}} \left(\frac{C_c}{Đ_{c,w}} + \frac{C_a}{Đ_{a,w}} \right) \right] \vec{N}_w \qquad (2.87)$$

where $\vec{\nabla} P_{tot} = \vec{\nabla}(P - \Pi)$. The total pressure P_{tot} indeed is a different way of expressing the water chemical potential in the membrane phase [73,74], and differently form the hydrostatic pressure is univocally determined due to the equality of the water chemical potential at the solution membrane interface.

2.1.3.7 Physicochemical models for interactions among mobile species

In the present section, it was shown how the meaning and value of ionic diffusivities, and transport parameters in general, is not absolute and must always be related to the theoretical structure of the transport model through which they are defined. Indeed, diffusivities are no more than mathematical artifacts used to describe the extent of ions and molecules interactions. However, likewise models, some artifacts are more useful than others.

For instance, NP ionic diffusivities do have a physical meaning only under the assumption of the NP model, i.e., at infinite dilution. Under this condition, they specifically describe the interaction between a mobile ion and the surrounding solvent molecules. At higher concentrations, other interactions become relevant, and nothing can be said about the physical meaning of NP ionic diffusivities. Consequently, any attempt to extrapolate physical information regarding fundamental physical properties from NP model outside its validity domain is likely meaningless.

Most of the NP model limitation can be overcome relaxing the hypothesis of the independence of ionic fluxes. In this regard, the MS theory allow to describe a variety of interactions, allowing to describe complex multi-component systems also at high concentration.

Indeed, the MS binary diffusion coefficients do have a specific physical meaning, as they quantify the strength of interaction among specific couples of components. This not only make such coefficients less concentration-dependent but also make them less dependent from the composition of the system, allowing for an easier modelling strategy. In light of these considerations, once the value of a generic binary diffusion coefficient $Đ_{ij}$ is determined in a given system, the same value may be employed with sufficient accuracy to describe the $i - j$ interactions in a different system [133,146].

For instance, the ion-water MS binary diffusion coefficients $Đ_{iw}$ can be modelled according to the well-known Stokes-Einstein theory, which in the framework of the NP model can be used to estimate ionic diffusivities only in the limit of vanishing concentrations. According to the Stokes-Einstein

theory, the drag forces exerted by the solvent molecules on the mobile ions (and vice versa) is inversely related to the viscosity of the solution, according to the following equation [132,133]:

$$Đ_{i,w} = \frac{\epsilon}{\tau}\frac{Đ_{i,w}^{\infty_0}}{\eta_r} \tag{2.88}$$

where $Đ_{i,w}^{\infty_0}$ is the infinite dilution ion-solvent binary diffusion coefficient, while η_r is the relative viscosity of the solution, i.e., the ratio between the solution and the pure solvent viscosity, and ϵ/τ was used to account for porosity and tortuosity correction in the membrane. The relative viscosity of an aqueous electrolyte typically increases with the ionic strength due to the increased steric interactions among the ions and the solvent. Consequently, $Đ_{i,w}$ typically decreases with the solutes' concentration. According to the Einstein's law, the relative viscosity can be satisfyingly modelled as follows [23]:

$$\eta_r = \frac{(1 + \sum_{i \neq w} C_i \psi_i / 2)}{(1 - \sum_{i \neq w} C_i \psi_i)^2} \tag{2.89}$$

where ψ_i is the effective viscous molar volume of the ions, that is usually fitted from the electrolyte solution viscosity data.

Regarding the ion-ion binary diffusion coefficient $Đ_{i,j}$, its value can be estimated from the theory of ion-ion interactions. Wesseling and Chapman [132,133,147] demonstrated that $Đ_{i,j}$ is roughly inversely proportional to the square root of the ionic strength of the solution, in accordance with the Debye-Hückel theory of ion-ion interaction (see section 1.1.3.11). According to Pinto et al. [146], a better estimation of the ion-ion interaction strength can be provided by including the effect of the finite ions size in the Debye-Hückel equation. Therefore, in the present work, $Đ_{ij}$ is modelled by means of an equation formally analogue to eq. (1.63):

$$Đ_{ij} = -\frac{\epsilon}{\tau}\frac{\zeta_{i,j}\left(z_i z_j\right) I^{c_{i,j}}}{1 + \beta_{i,j} I^{c_{i,j}}} \tag{2.90}$$

where $\zeta_{i,j}$, $\beta_{i,j}$ and $c_{i,j}$ are constant parameters to be fitted on experimental aqueous electrolytes data. Figure 19 shows the agreement between the experimental values and the Stokes-Einstein and Debye-Hückel models' prediction of ion-ion and ion-water MS binary diffusion coefficients for aqueous solutions of NaCl and KCl at various concentrations. The fitting parameters of the two models are reported in Table 8 and Table 9.

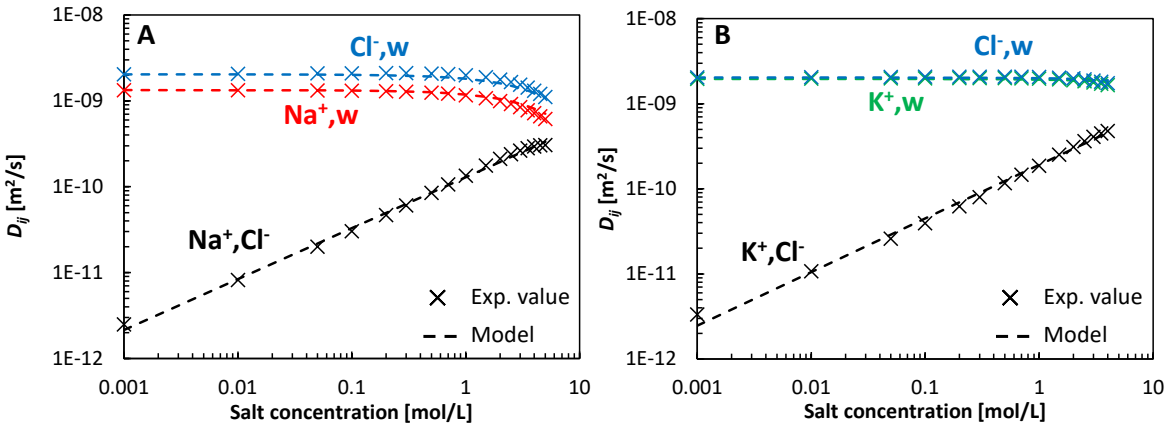

*Figure 19 Maxwell-Stefan binary diffusion coefficients for NaCl (**A**) and KCl (**B**) aqueous solutions at various salt concentration. The crosses represent the experimental values taken from* [147]*, while the dashed lines represent the Stokes-Einstein (eq. (2.88) and (2.89)) and the Debye-Hückel (eq. (2.90)) models fitting applied respectively to ion-water and ion-ion binary coefficients. The corresponding fitting parameters are reported in Table 8 and Table 9*

Table 8 Einstein' model (eq. (2.89)) parameters. Effective viscous radii were fitted to minimize the Mean relative Deviation (MRD) with the experimental data, while the viscous molar volume ψ was evaluated as the corresponding spheric volume divided by the Avogadro's number

	Effective viscous radius [Å]	**Viscous molar volume(ψ_i) [cm³ mol⁻¹]**
Na^+	2.49	39.0
K^+	0.30	0.07
Cl^-	1.41	7.12

Table 9 Fitting parameters of the Debye-Hückel model (eq. (2.90)) for ion-ion binary diffusion coefficients

	$\zeta_{i,j}$ [m³/² mol⁻¹/²]	**$\beta_{i,j}$ [m³/² mol⁻¹/²]**	**$c_{i,j}$ [-]**
Na^+,Cl^-	2.14E-12	2.22E-14	0.593
K^+,Cl^-	2.46E-12	2.22E-14	0.630

2.2 Transport phenomena in ion-exchange membranes: experimental investigations

In section 2.1, two distinct theoretical frameworks for mass transfer, the Nernst–Planck (NP) and the Maxwell–Stefan (MS) models, were investigated. These models allow the evaluation of mass and charge fluxes if the relevant transport coefficients are known. To determine such coefficients from measurable experimental quantities, the transport equations must be applied and solved under specific conditions. However, given the complexity of the topic, experimental determination of fundamental transport coefficients is rarely performed. In most studies, these coefficients are treated as mere adjustable parameters, or simpler models relying on macroscale coefficients are adopted. Consequently, literature data on fundamental transport coefficients in membranes are scarce, especially for multi-component or high-concentration systems. This is especially true for the MS binary diffusion coefficients, which are challenging to determine due to the inherent complexity of the MS framework.

Furthermore, because these transport parameters can depend on the system's concentration and composition, the importance of theoretical models capable of predicting their values across different operating conditions becomes evident. Such models can only be developed, or validated, using reliable experimental data obtained through robust characterization techniques combined with rigorous mathematical analyses.

In the present work, an extensive experimental characterization campaign was performed on a commercial CEM to retrieve fundamental transport coefficients from raw experimental data. In the present section, the adopted characterisation techniques and the experimental results are presented and discussed. Part of the experimental campaign presented in the present section (sections 2.2.1.2, 2.2.2 and 2.2.4) were conducted during a doctoral research stay at the facilities of the chair of chemical engineering at RWTH Aachen university (Germany) under the supervision of prof. Matthias Wessling and Dr. Christian Linnartz.

The data presented herein are then employed in section 2.3 to solve the transport equations in membrane for the unknown transport coefficients.

2.2.1 Ionic conductivity

Ionic conductivity is a fundamental property of IEMs, as it directly affects ohmic losses and, consequently, the overall performance of the electromembrane technologies. According to the NP and MS transport theory, the ionic conductivity of a generic IEM is related to the concentration and

mobility of the species partitioned within the membrane. Therefore, conductivity measurement constitutes a fundamental characterization technique for investigating ion transport in IEMs.

Ionic conductivity is indirectly evaluated by applying Ohm's first law to describe ionic conduction [6,7]:

$$\vec{J}' = -\kappa_m' \vec{\nabla} \varphi_{ohm} \tag{2.91}$$

where $\vec{J}'$ correspond to the interstitial (pore surface area-based) current density. In the absence of concentration gradients, κ_m is independent of the spatial position and the ohmic potential gradient $\vec{\nabla} \varphi_{ohm}$ corresponds to the overall potential gradient. Moreover, if φ_{ohm} is a function of a single spatial variable and $\vec{J}'$ is invariant with the position, eq. (2.91) can be integrated over the membrane geometrical thickness to get:

$$J = \frac{\kappa_m}{\delta} \Delta \varphi_{ohm} \tag{2.92}$$

where δ is the membrane geometrical thickness and the apparent conductivity κ_m is related to the true interstitial conductivity κ_m' as follows (see section 2.1.2.6):

$$\kappa_m = \frac{\epsilon}{\tau} \kappa_m' \tag{2.93}$$

It should be noted that κ_m' and κ_m are often confused in the literature, with the dependence of the apparent conductivity from the porosity and the tortuosity of the membrane frequently left implicit. Multiplying both sides of eq. (2.92) by the geometrical area of the membrane A_m leads to the following equation:

$$R_m = \frac{\Delta \varphi_{ohm}}{j} = \frac{\delta}{\kappa_m A_m} \tag{2.94}$$

Where R_m is the electrical resistance of the membrane and j is the electrical current. According to eq. (2.94), κ_m can be determined by measuring the potential drop and the current.

In the literature several experimental methods are reported to measure the electrical resistance of an IEM. In general, R_m is determined by placing the membrane between two electrodes, imposing a current or potential signal and measuring the system's response. However, there is not a standardized

and widely accepted method and/or procedure to perform such measurements. Thus, the results may vary significantly depending on the chosen experimental setup and procedure [105,109,148].

One of the main factors that can affect the experimental outcome is the configuration of the measurement cell. When the membrane is in direct contact with the electrodes, the setup is referred to as a *direct contact* or *zero-gap* method or configuration. Conversely, when the membrane is separated from the electrodes by electrolyte-filled channels, the setup is referred to as the *difference* configuration.

Another significant factor is the frequency of the applied signal (AC vs. DC). DC measurements are increasingly avoided because the application of a DC current induces concentration polarization at the solution–membrane interface, affecting the measured membrane resistance [3,83,109,144]. Importantly, the derivation of Eq. (2.94) was derived assuming the absence of concentration gradient, which is not guaranteed under polarization conditions. Conversely, AC measurement are usually considered more reliable, given that the application of sinusoidal potential at high frequency prevents concentration polarization phenomena [149].

2.2.1.1 Electrochemical Impedance Spectroscopy

Electrochemical Impedance Spectroscopy (EIS) is an electrochemical technique widely used to investigate the properties of solid-state materials, liquid electrolytes, and both biological and synthetic membranes [150–152]. It can also be applied to complex electrochemical systems such as batteries, electrolyzers, fuel cells, and other devices[153].

In EIS, the system to be investigated is connected to a potentiostat/galvanostat which applies a sinusoidal potential (or current) signal over a range of frequencies. The response of the system is analyzed by means of a frequency response analyzer, and the value of the sinusoidal potential and current are employed to evaluate the impedance of the system as follows:

$$Z(f) = \frac{\hat{\jmath}(\omega)}{\hat{\varphi}(\omega)} \tag{2.95}$$

where $\hat{\jmath}$ and $\hat{\varphi}$ are the sinusoidal current and potential respectively and $Z(\omega)$ is the frequency-dependent impedance of the system under consideration.

The connection to the cell is typically made via four different electrodes leads: Working Electrode (WE), Counter Electrode (CE), Reference Electrode (RE) and Sense Electrode (SE). The WE and CE form the current-carrying path, while the RE and the SE constitute the sensing circuit. Depending on

the way the four leads are connected to the cell, the cell may operate in two-, three-, or four-electrode configurations [152].

The main advantage of EIS over DC methods is that, by measuring the impedance of the system at various frequency, different electrochemical phenomena dominating the system at different frequency range can be investigated with a single measurement, and their effect on the overall resistance of the cell can be evaluated. The impedance of the system $Z(\omega)$ can be decomposed into its real and imaginary parts:

$$Z(\omega) = Z'(\omega) + iZ''(\omega) \tag{2.96}$$

where $Z'(\omega)$ and $Z''(\omega)$ are respectively the resistance and the reactance of the system, while i is the imaginary unit. During an EIS measurement, the value of $R(\omega)$ and $X(\omega)$ are plotted in a diagram called Nyquist plot from which information regarding the electrochemical behaviour of the system can be inferred. An example of Nyquist plot obtained from a high-frequency EIS analysis on an IEM is reported in Figure 20

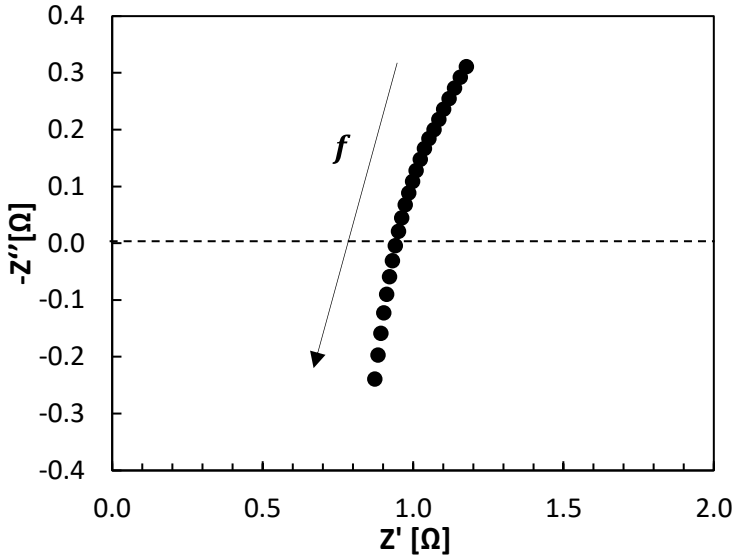

Figure 20 Example of Nyquist plot. The black dots represent the real (Z') and imaginary (Z'') part of the system impedance (Z).

In order to quantify and extrapolate the electrochemical behaviour of the system from an EIS analysis, a suitable equivalent electrical circuit must be employed. Indeed, depending on the structure and on the components of the overall measuring cell, the measured impedance can be a complex function of the frequency. Therefore, a sufficient knowledge of the possible phenomena occurring in the investigated system is required to avoid misinterpreting the EIS results.

An IEM is often modelled with an equivalent electrical circuit (Figure 21) consisting of parallel resistances and capacitances, representing different phenomena, including solution–membrane interfacial effects such as electrical double layer charging and diffusion boundary layer formation [149,151,154].

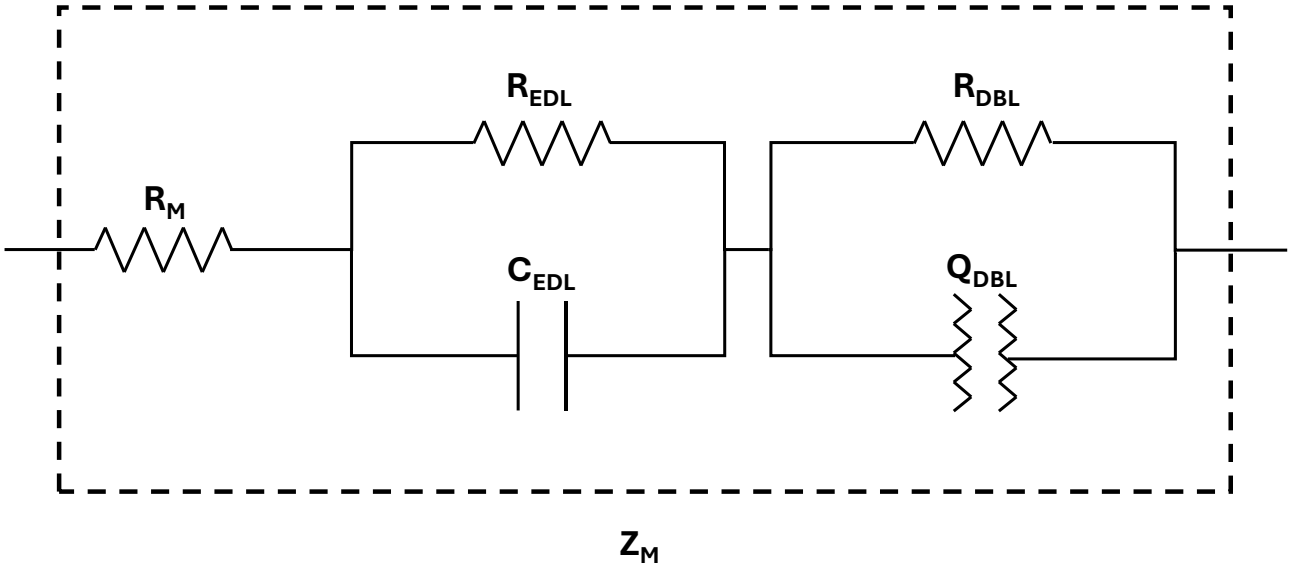

Figure 21 Equivalent electrical circuit of an IEM. R_M, R_{EDL} and R_{DBL} represent respectively the ionic, electric double layer and diffusion boundary layer resistances, while C_{EDL} and Q_{DBL} are the capacitance and the constant phase element describing the capacitive behaviour of the IEM

Such phenomena are heavily affected by the frequency of the imposed electric signal. When a DC signal is applied, the capacitive elements in the equivalent circuit get charged with a time proportional to the time constant of the RC circuit and therefore behave like open branches. Consequently, when $\omega = 0$ the equivalent resistance of the system corresponds to the sum of each of the elements shown in Figure 21. Therefore, DC measurement are not well-suited to measure IEM ionic conductivity as it is not possible to distinguish between the membrane contribution to the overall resistance and the extra contributions due to interfacial phenomena [149]. A clear evidence of this, is that experimental DC measurement performed on IEM contacted with solutions at low salt concentration showed significant increase in the apparent membrane resistance, which must be attributed to the diffusion boundary layer resistance due to the depletion of charge carriers at the interface favoured by the low salt concentrations [109,148].

Conversely, at high frequency, the impedance of the capacitive elements tend to zero, therefore the RC circuit depicted in Figure 21 collapse into short-circuited branches [155]. Under this condition, the reactance of the system is zero and the membrane impedance correspond to its ionic resistance.

If no other elements are included in the sensing circuit, the membrane resistance can be evaluated considering the intercept of the Nyquist plot on the real axis.

Although the advantage of EIS over DC measurement are now quit well recognized, there is still uncertainty regarding the best operative configuration to adopt in order to get reliable results.

In this work, both difference and direct contact methods were investigated and compared.

2.2.1.2 Difference method

In the difference method, the IEM is placed in a two-compartments cell equipped with planar electrodes. The channels facing the membrane are fluxed with an electrolytic solution at given concentration and composition. Depending on the potentiostat leads connection, the method can be employed in a two-electrode or four-electrodes configuration. Usually, the latter is most widely employed as it allows to exclude from the overall impedance of the cell the contributions of the components not situated between the RE and SE tips. However, such configuration needs to employ a couple of reference electrodes (i.e., typically Ag/AgCl electrodes) which are to be placed near the membrane surface by means of glass capillaries called Haber-Luggin capillaries. This complicates the electrochemical cell set-up and may further complicate the evaluation of the bare membrane ionic conductivity [156]. On the other hand, a two-electrode configuration does not allow to exclude from the impedance spectra the contributions from the electrochemical phenomena at the electrode-solution interfaces, which in some cases can influence the quantification of membrane's impedance. The measurements presented in this work were carried out by means of a two-electrode set-up, obtained by short-circuiting respectively WE with the SE and the CE with the RE. A schematic representation of the experimental set-up is depicted in Figure 22, while pictures of the electrochemical cell structure are provided in Figure 23.

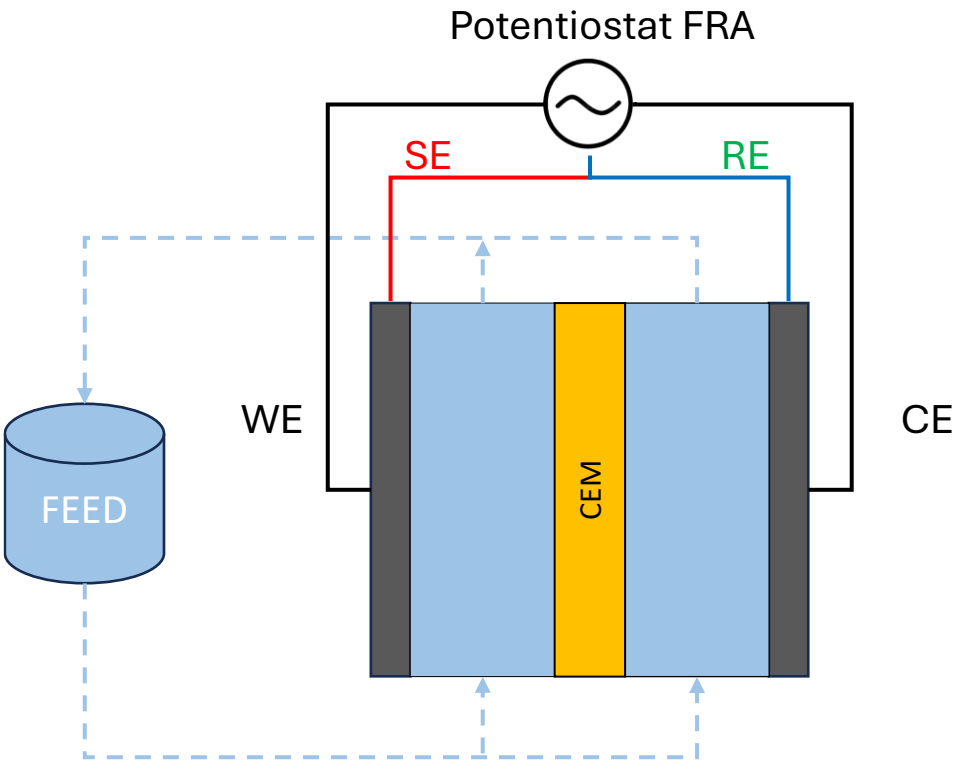

Figure 22 Schematic of the electrochemical cell used to perform EIS using the difference method. A Frequency Response Analyser (FRA) is employed to measure the electrical response signal of the cell and quantify the system impedance.

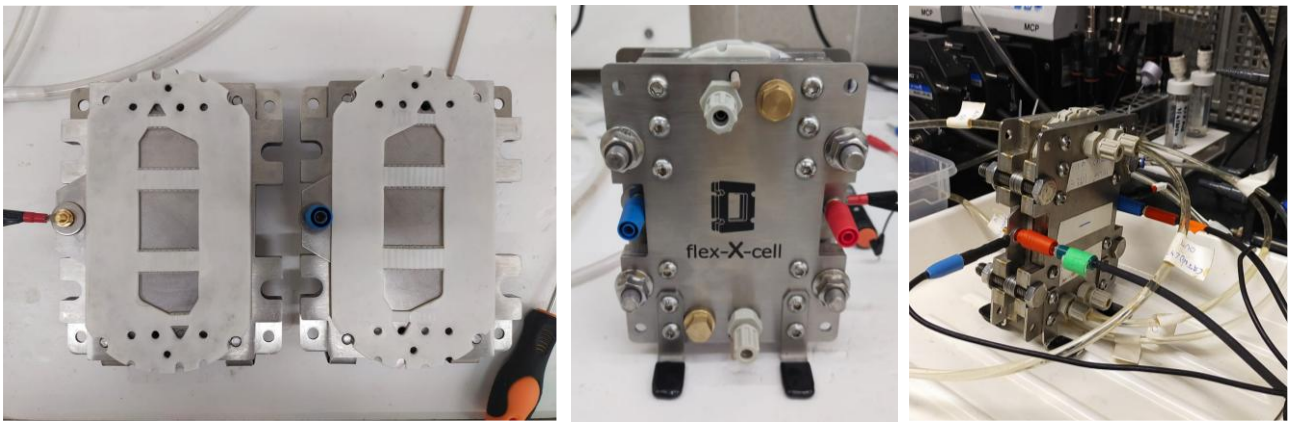

Figure 23 Pictures of the electrochemical cell employed to perform EIS with the difference method

Due to the presence of the liquid electrolyte separating the membrane from the electrode's surface, the membrane resistance cannot be measured directly, as the overall impedance contains contributions from the liquid electrolyte facing the membrane and the blank resistance due to the electronic resistivity of the external circuit, including the leads and the current collectors. Therefore, the membrane resistance must be evaluated by measuring the total resistance of the set-up and subtracting the blank and the liquid electrolyte resistance, measured in a separate test performed without the membrane sample:

$$R_m = R_{tot} - R_B \tag{2.97}$$

In the previous equation, R_{tot} is the overall resistance including the membrane, while R_B is the blank resistance i.e., the cell resistance measured without the membrane sample.

EIS was performed on the FKS-50 CEM (already presented in section 1.2) to evaluate R_m , with a modular electrochemical cell provided by flex-X-cell (RWTH Aachen University, Germany). The cell was equipped with two square graphite sheets as electrodes, placed over two titanium current collectors, and connected to a potentiostat/galvanostat (Iviumstat, The Netherlands) equipped with a Frequency Response Analyzer (FRA). The solution's channels were realized by means of rubber gaskets of 0.5 mm thickness to minimize the distance between the electrodes and the membrane and, consequently, the resistance of the electrolyte. Square membrane coupons of 6x6 cm^2 were sandwiched between two rubber gaskets of 0.5 mm of thickness and clamped between the two electrodes. The membrane active area exposed to the to the graphite electrodes was of 5x5 cm^2. Liquid electrolyte at various salt concentration was prepared by dissolving NaCl or KCl (Carl ROTH + Co. KG GmbH, Karlsruhe, Germany) into DI water. The solution was pumped through the liquid frames of the cell using two gear pumps. The effect of the flow rate on the measured resistance was assessed by changing the pumps' rotational speed between 0 and 200 rpm, but no effect on the measured resistance was observed as expected.

Prior to perform the measurements, membrane's sample were equilibrated for at least 24 hours with the salt same solution used to perform the measurements. After the equilibration time, the thickness of the membrane was measured using a micrometer. The measurements were performed in potentiostatic mode by applying a DC voltage of 0 V vs OCP with a superimposed AC voltage of 10 mV, in the frequency range 50-500 kHz. The tests were performed at controlled ambient temperature of 23°C. An example of the resulting Nyquist plots is reported in Figure 24

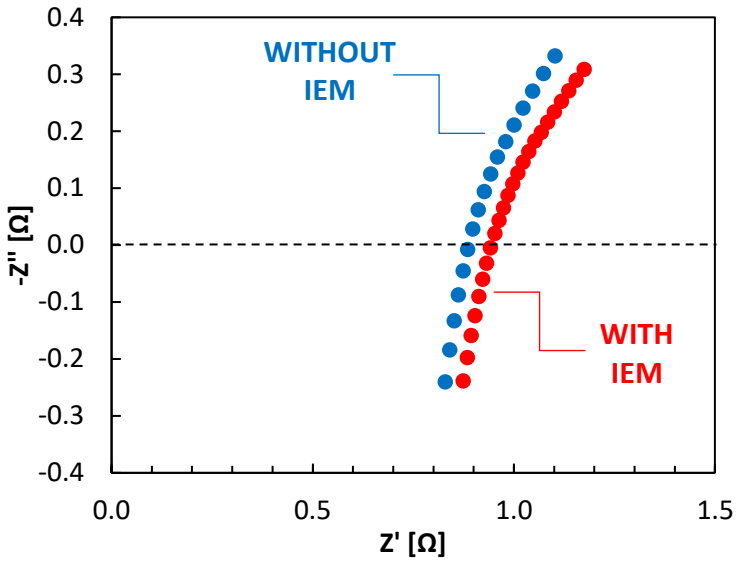

Figure 24 Example of Nyquist plot of FKS-50 CEM in 0.1 M NaCl

After the membrane resistance was evaluated through eq. (2.97), the apparent ionic conductivity κ_m was evaluated by applying equation (2.94). The resulting conductivity is plotted against the external salt concentration in Figure 27. The discussion of the relevant results is reported in section 2.2.1.3.

2.2.1.3 Direct contact method

The direct contact tests reported in the following section were kindly performed by prof. J. Kamcev's collaborators at the facilities of the Chemical Engineering Department of University of Michigan (Ann Arbor).

The direct contact method provides an alternative to the difference method for performing EIS measurements on IEMs. The name stems from the measuring cell configuration, in which the membrane is directly clamped between two planar electrodes, avoiding the interposition of a liquid electrolyte between the membrane and the electrode surfaces. The primary advantage of this technique is that, by eliminating the electrolyte contribution to the overall cell resistance, a more accurate evaluation of the membrane resistance is achieved [105]. This is particularly relevant at very low electrolyte concentrations, where the membrane resistance determined via Eq. (2.97) can be affected by significant cancellation errors due to the large difference in magnitude between the membrane and electrolyte resistances. Direct contact between the membrane and the planar electrodes is realized using a specialized through-plane sample holder, depicted in Figure 25.

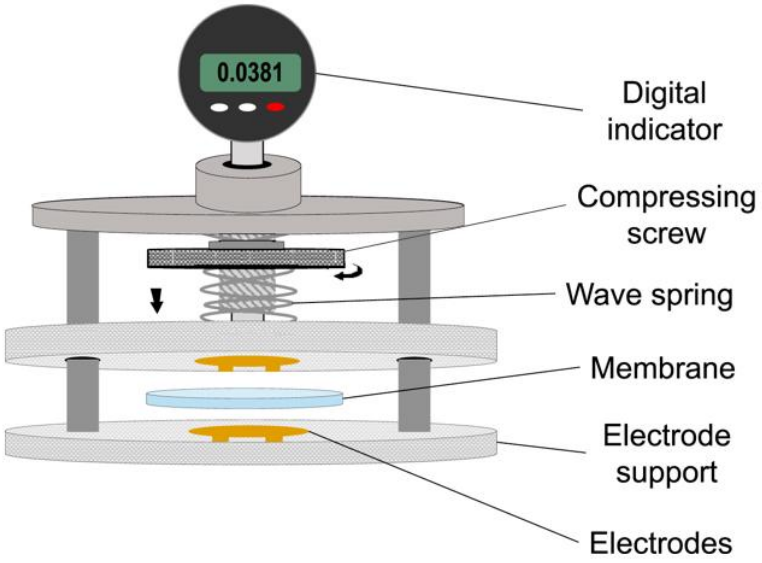

Figure 25 Schematic of the through-plane sample holder used to perform EIS on the investigated CEM with the direct contact method (taken with permission from [105]*)*

Despite the absence of the electrolyte contribution, the measured total resistance still includes contributions unrelated to the membrane. For example, imperfect contact between the membrane and electrodes may introduce additional contact resistances. Moreover, the external circuit, including the potentiostat leads, contributes an additional blank resistance, which must be subtracted to obtain the actual membrane resistance.

To account for such contributions, Diaz et al. [105] proposed a stacking method, in which the total resistance of a direct contact cell with a certain number of stacked membrane samples is measured via EIS.

The measured total areal resistance depends on the total stack thickness as follows:

$$R_{tot}A_m = R_m A_m + R_B A_m = \frac{\delta_{tot}}{\kappa_m} + R_B A_m \tag{2.98}$$

where δ_{tot} and A_m are respectively the overall thickness of the stacked membranes and the active area (i.e., the contact area between the pile and the planar electrodes), while R_B accounts for all the contributions to the total resistance other than R_m. By plotting $R_{tot}A_m$ vs δ_{tot}, κ_m and R_B can be determined through linear fitting, with the slope and intercept corresponding respectively to $\kappa_m$and $R_B A_m$ (see Figure 26).

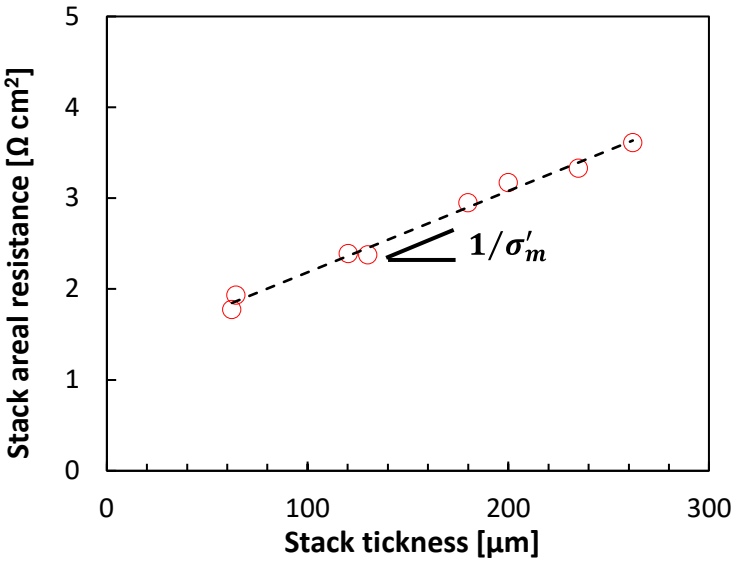

Figure 26 Areal resistance of the stacked membranes vs thickness. The empty circles are the experimental data obtained via EIS with the direct contact method. The dashed line is the linear fitting performed to evaluate the apparent conductivity

The tests were conducted on FKS-50 CEM samples equilibrated in NaCl and KCl solutions at the same concentrations used in the difference method. The apparent conductivity of the CEM, measured with both techniques, is reported in Figure 27

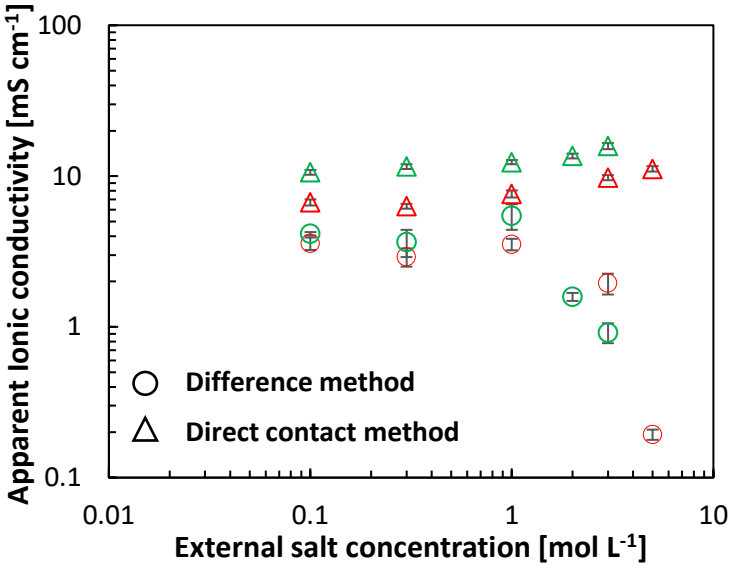

Figure 27 Apparent ionic conductivity of FKS-50 CEM equilibrated with NaCl and KCl, measured with (○) Difference method and (Δ) Direct contact method.

Notably, the apparent conductivity of the CEM in the K^+ form, as measured by the direct contact method, was significantly higher than that in the Na^+ form. This behavior can be attributed to the

smaller hydration shell of K^+, which results in higher ionic mobility. In contrast, this difference becomes only marginal when the conductivity is measured using the difference method.

Moreover, the apparent conductivity measured using the two techniques exhibits notable differences in both magnitude and trend. Independently of the equilibrating electrolyte, the apparent conductivity measured via the difference method is consistently lower than that obtained with the direct contact method. Moreover, κ_m measured with the direct contact method is nearly constant at low external salt concentrations and increases at higher concentrations. Conversely, κ_m measured via the difference method decreases significantly at high external salt concentrations.

According to the NP and MS transport theories (see sections 2.1.2.3 and 2.1.3.4), the membrane conductivity is expected to increase with the concentration of ions in the membrane phase. Assuming that transport coefficients remain approximately constant within the investigated concentration range, an increase in κ_m would be expected at high external concentrations due to the weakening of the Donnan exclusion mechanism, which leads to higher mobile ion concentrations. Conversely, due to the reduced water uptake of the CEM (see Figure 5), a reduction in the apparent conductivity is expected due to the increased τ/ϵ ratio (see eq. (2.93)). Hence, the observed trend of κ_m is the result of the interplay between these opposing phenomena. However, given the limited osmotic deswelling exhibited by the CEM, the increase in the mobile-ions concentration is expected to be the dominant factor influencing the apparent conductivity.

In principle, a reduction in κ_m could also result from decreased ionic mobility due to ion-pairing within the membrane phase, which is favoured at high concentrations [38,88,135]. However, such effects should also be evident in direct contact measurements. Considering this, no physical explanation could be provided for the substantial reduction of κ_m observed with the difference method.

Such reduction could be instead related to a poor cell configuration. Indeed, one of the main issues associated with the difference method is the identification of the active area, i.e., the effective area crossed by the current lines. In practice, this area does not correspond to the contact area between the membrane and the liquid electrolyte. The actual active area in an electrochemical cell depends on the distribution of current lines, which is influenced by the geometrical configuration of the cell and the electrolyte conductivity [148]. If the current distribution is non-uniform, the active area, i.e., the cross-sectional area of the current lines, is not uniquely defined, and Ohm's law cannot be directly integrated to yield eq. (2.94).

The variation of the active area with electrolyte concentration can be attributed to the fringe-field effect, whereby current lines spread beyond the expected electrode area [157]. A graphical representation of this phenomenon is shown in Figure 28.

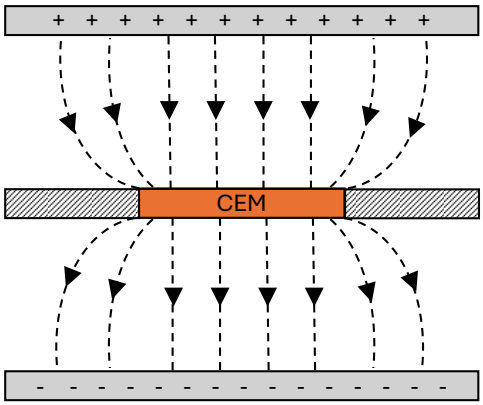

Figure 28 Schematic of fringe-field in a two-compartment cell for IEMs' conductivity measurement. The dashed lines represent the electric field distribution in the two compartments

The fringe-field effect is particularly relevant in low-conductivity media and diminishes at high salt concentrations. Consequently, the effective active area decreases at higher salt concentrations, increasing the total cell resistance and reducing the apparent membrane conductivity. This phenomenon is negligible in direct contact cells, where fringing is minimized due to the small inter-electrode distance.

Therefore, the fringe-field effect can significantly influence IEM conductivity measurements performed with the difference method. Additionally, difficulty in identifying the true active area may explain the poor reproducibility of many experimental results obtained with this method [105].

Considering these aspects, transport simulations reported in section 2.3 are based on the experimental data collected using the direct contact method.

2.2.1.4 Reference frame and conductivity measurement

In the previous sections, two different methods for the experimental evaluation of IEMs' ionic conductivity were presented. To this regard, it is necessary to make a consideration regarding the meaning of the measured ionic conductivity.

In section 2.1.1.2 it was showed how the value of the current density $\vec{J}$ can be generally written in terms of a convective contribution and a conductive contribution, whit this latter being described by Ohm's first law. However, such distinction depends on the arbitrary choice of the reference frame. Therefore, the value of the observed conductive current density $\vec{J}^{\#}$ in principle depends on the chosen reference frame as well. Given that the gradient of the ohmic potential is invariant with respect to the

reference frame, this leads us to the conclusion that the ionic conductivity appearing in Ohm's first law must be dependent on the reference as well. This fact should not be surprising given that $\kappa^{\#}$, like all other transport parameters, is in principle dependent on the reference frame.

However, it was also demonstrated how, in an electroneutral system, $\vec{J}^{\#}$ and then $\kappa^{\#}$ are invariant with respect to the chosen reference frame. Nonetheless, this condition is not strictly respected in IEMs. To clarify this point, let us recall the general definition of $\vec{J}$:

$$\vec{J} = F\sum_{i=1}^{N} z_i \vec{N}_i^{\#} + \mathcal{F}\sum_{i=1}^{N} z_i C_i \vec{v}^{\#} \tag{2.99}$$

where N corresponds to the number of system's components. Typical modelling strategies based on the NP model strictly speaking do not consider the membrane as a component of the system when writing down the transport equations. Consequently, ionic conductivity is always written by considering contributions only from mobile ions [108,118,158,159]. However, in doing so, the second summation at the right-hand side of eq. (2.99) (corresponding to the charge density) would assume a non-null value. Therefore, $\vec{J} \neq \vec{J}^{\#}$. This fact should be kept in mind when extrapolating transport parameters from experimental data. Given that the molar or mass average velocity is typically taken as reference velocity for the evaluation of the diffusive fluxes $\vec{N}_i^{\#}$ [128], $\vec{J}^{\#}$ should be employed consistently to evaluate the corresponding ionic conductivity $\kappa_m^{\#}$. However, when measuring the impedance of an IEM placed between two stationary electrodes, the current density measured by the potentiostat is inherently referred to a stationary reference frame as well. In other words, the experimentally accessible quantity is $\vec{J}$ and not $\vec{J}^{\#}$. To the best of the author's knowledge, this fact is not taken into account in the reference literature, and had possibly led to misestimation of IEMs conductivity, especially in the case of IEMs with non-negligible water permeability.

Two possible strategies can be implemented to solve this inconsistency: the measured $\vec{J}$ can be corrected to account for the convective current to evaluate $\vec{J}^{\#}$ or, alternatively, a laboratory-fixed stationary reference frame (i.e, $\vec{v}^{\#} = 0$) can be employed when measuring the diffusive fluxes.

Therefore, if the uncorrected experimental ionic conductivity κ is employed, the ionic flux evaluated in the NP framework should not be corrected for the barycentric flux velocity (see section 2.3.2).

Importantly, in the MS framework presented in section 2.1.3.2, such issue is not relevant as the Binary-Friction model inherently adopts a stationary-reference frame for the transport equations.

2.2.2 Ionic transport numbers

Transport numbers represent the fraction of the current carried by a given ionic species under the effect of an externally applied electric field. In IEMs, transport numbers are typically determined through a standard permselectivity test, in which the membrane is placed between two electrolytes at different concentrations and the pseudo-steady-state transmembrane potential is measured using two reference electrodes [6,7,160]. However, this technique only provides an average transport number and is not suitable for evaluating individual ionic transport numbers in multicomponent systems.

Therefore, an alternative approach based on ED selectivity tests was investigated [82,83]. The method relies on the use of a four-compartment ED cell in a closed-loop configuration, where the central compartments are separated by the membrane under investigation. A schematic of the experimental setup is depicted in Figure 29.

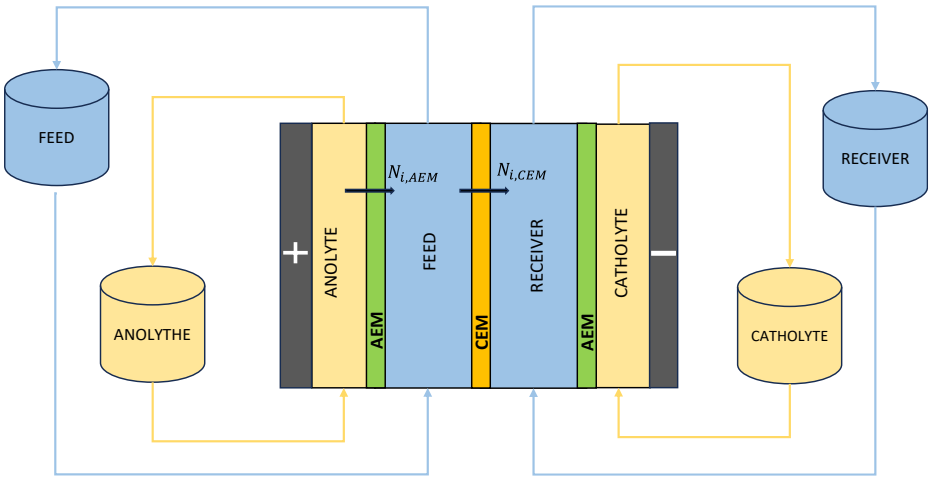

Figure 29 Schematic of the four-compartment ED cell used to measure transport numbers in the investigated CEM

In the preliminary tests, the FKS-50 CEM was used to separate the feed and receiver channels, which were circulated with aqueous NaCl solutions of equal concentration, ranging from 0.1 to 5 M. The solutions were pumped at a flow rate of 400 mL min^{-1} from two external 50 mL reservoirs using gear pumps. The electrode compartments were separated from the feed and receiver chambers by two Fumasep FAB-PK-130 AEMs (Fumatech BWT GmbH, Germany), characterized by a high proton-blocking capacity. The effective active area of the IEMs was 5×5 cm^2. The anolyte and catholyte consisted of $FeCl_2$ and $FeCl_3$ solutions, respectively, prepared by dissolving the salts in 0.01 M HCl (pH=2). Graphite sheets were selected as electrode material. The Fe^{2+}/Fe^{3+} redox couple was specifically chosen to reduce the applied potential due to its low thermodynamic redox potential and low electrode overpotential [161], thus minimizing water splitting at the electrodes.

The tests were performed in galvanostatic mode, applying a fixed current for a defined time interval. Under these conditions, ions were driven from the feed compartment toward the adjacent compartments across both the AEMs and the CEM. Conductivity, pH, and temperature were monitored in-line, while final ion concentrations in the compartments were determined via chromatographic analysis.

By applying a mass balance to a generic component in the feed compartment, the following expression can be derived:

$$\frac{d\left(V_F C_{i,F}\right)}{dt} = A_m\left(N_{i,AEM} - N_{i,CEM}\right) \tag{2.100}$$

where A_m is the membrane area, V_F and $C_{i,F}$ are respectively the volume and concentration of the feed compartment, while $N_{i,CEM}$ and $N_{i,AEM}$ are the total ionic fluxes across the CEM and the AEM.

When considering the counter-ion (Na^+), $N_{i,AEM}$ can be neglected since AEMs largely exclude the passage of cations. This assumption was confirmed experimentally, as Na^+ concentrations measured in the anolyte at the end of each test were negligible. In addition, the total mass of the solutions in each compartment, measured with precision balances, showed negligible variation, confirming the absence of significant water transport. Equation (2.100) can therefore be simplified to:

$$V_F \frac{dC_{cou,F}}{dt} = -A_m N_{cou,CEM} \tag{2.101}$$

The duration of the tests was selected to induce a concentration variation in the feed compartment of about 5%, sufficient to be experimentally detectable but not large enough to trigger significant diffusive fluxes across the CEM. Under these conditions, $N_{i,CEM}$ is essentially driven by conduction. Since current density was kept constant under galvanostatic operation, Eq. (2.101) can be expressed as:

$$V_F \frac{\Delta C_{cou,F}}{\Delta t} \simeq -A_m \frac{t_{cou}^m J}{z_{cou}\mathcal{F}} \tag{2.102}$$

where t_{cou}^m is the transport number of the counter ion in the membrane and Δt is the test duration. Accordingly, t_{cou}^m can be determined as:

$$t_{cou}^{m} \simeq -\frac{z_{cou}\mathcal{F}}{J}\frac{V_F \Delta C_{cou,F}}{A_m \Delta t} \tag{2.103}$$

Equation (2.103) can, in principle, be applied to determine the transport numbers of the counter-ions in the investigated CEM. If Cl^- is the only co-ion presents, its transport number can be straightforwardly evaluated as:

$$t_{co}^{m} = 1 - \sum_{k \neq co} t_k^m \tag{2.104}$$

This approach has several advantages. First, it can be applied to multi-ionic systems. Moreover, changes in the composition of the feed and receiver compartments are prevented because:

- Leakage of $Fe^{3+}$and Fe^{2+} from the electrodic compartments is strongly impeded to the strong electrostatic and dielectric exclusion provided by the AEMs
- The proton-blocking AEMs and relatively high pH in the electrodic compartments prevent significant H^+ crossover
- Cl^- is the only anion present in the system

In addition, the limited concentration gradient across the CEM allows transport numbers to be evaluated at well-defined electrolyte concentrations and compositions. However, even if the bulk concentrations of the feed and receiver compartments are initially equal, the concentrations at the solution–membrane interfaces can differ due to concentration polarization induced by the applied current density [45,162].

Concentration polarization typically occurs at phase boundaries because of differences in transport numbers between external solution and IEM, which induce a compensating diffusive flux. In steady-state, this diffusive flux balances the difference in conductive fluxes in the two phases, leading to interfacial concentrations that deviate from bulk values. The extent of polarization can be quantified by polarization coefficients ϑ_i defined as [162,163]:

$$\vartheta_i = \frac{C_i^{s,int}}{C_i^{s,\infty}} \tag{2.105}$$

where $C_i^{s,int}$ and $C_i^{s,\infty}$ are respectively the concentrations of the generic component at the solution-side of the interface and at the bulk of the solution.

According to the Nernst film theory, the concentration gradient is localized within the diffusion boundary layer (DBL), whose thickness depends on the hydrodynamics of the system [6,45]. By neglecting diffusive flux through the membrane, ϑ_i is usually estimated as [163,164]:

$$\vartheta_i = 1 - \frac{(t_i^m - t_i^{s,\infty})J\delta_{DBL}}{|z_i|\mathcal{F}D_i^s C_i^{s,\infty}} \tag{2.106}$$

where δ_{DBL} is the thickness of the DBL, $C_i^{s,\infty}$ and $t_i^{s,\infty}$ are the concentration and transport number evaluated at the bulk of the solution, while D_i^s is the ionic diffusion coefficient in the solution.

To minimize polarization, the applied current density must be properly adjusted as a function of $C_i^{s,\infty}$ and on δ_{DBL}. or a qualitative estimation, δ_{DBL} was calculated using the Levêque equation [163–165]:

$$\delta_{DBL} = \frac{h_s}{1.47}\left(\frac{d_s D_i^s}{h_s^2 v_s}\right)^{1/3} \tag{2.107}$$

where h_s and d_s are respectively the height and width of the feed channel and v_s is the fluid velocity that can be evaluated from the flow rate. The resulting $\delta_{DBL}$was 78 μm. In principle, eq. (2.107) applies to non-fully developed laminar flows, in the absence of mixing promoters. In the present case, custom-made spacers were introduced to enhance mixing, making the previous result a conservative estimation. For consistency reason, the total channels' cross-sectional area was employed to evaluate v_s from the flow rate. All the relevant data are reported in Table 10.

Table 10 Geometrical properties of ED cell feed and receiver channels

Channel height [cm]	Channel width [cm]	Flow rate [mL min^{-1}]	Fluid velocity [cm s^{-1}]
5.00	0.20	400	6.67

By applying a current density of 4 A m^{-2} with a bulk NaCl concentration of 0.1 M, a ϑ_i of 0.985 was obtained for the counter-ion (Na^+), confirming that polarization effects could be neglected under these operating conditions. For tests at higher bulk concentrations, the applied current density was proportionally increased to maintain constant test durations of 50 or 100 minutes.

2.2.2.1 Results and discussion

The transport numbers of Na^+ and Cl^-, obtained from eqs. (2.103) and (2.104), are reported in Figure 30.

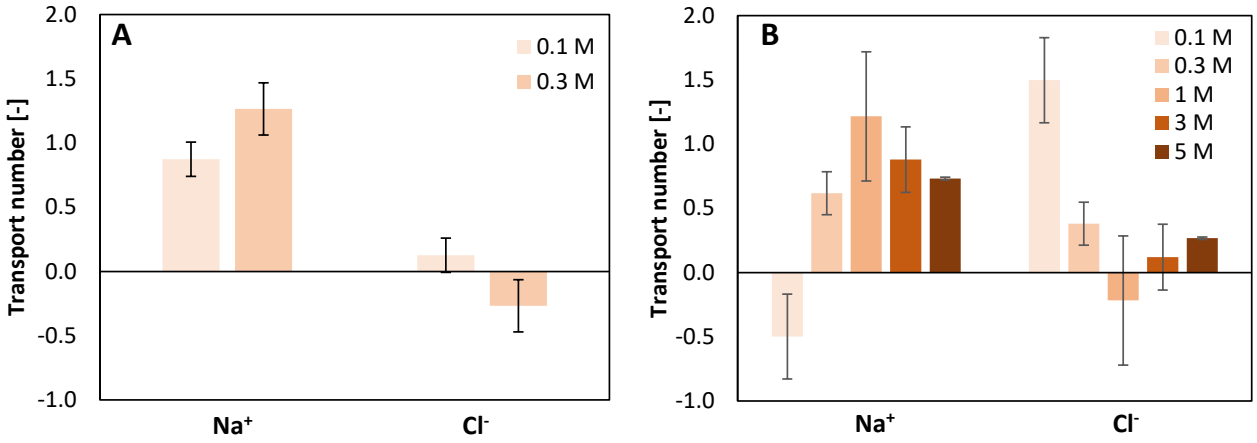

*Figure 30 Na^+ and Cl^- transport numbers evaluated through the four-compartment ED cell, with test duration of (**A**) 50 minutes and (**B**) 100 minutes with variable applied current density (4,12,40,120 or 200 A m^{-2} respectively corresponding to initial feed and receiver salt concentration of 0.1,0.3,1,3 and 5 mol L^{-1}). The error bars are evaluated as the standard deviation of at least 3 separate measurements.*

As shown in Figure 30 the measured transport numbers are of the same order of magnitude as the associated experimental error, rendering the results inconclusive. To identify the origin of the uncertainty, a parametric analysis was performed using error propagation theory, which states that the standard deviation of a derived variable can be expressed as:

$$\varpi_g = \sqrt{\sum_{x_i} \left(\frac{\partial g}{\partial y_i} \varpi_{y_i} \right)^2} \tag{2.108}$$

where $g(\vec{y})$ is the derived variable, y_i are the measured variables, and ϖ_{y_i} and ϖ_g are the corresponding errors. By applying the former equation to eq. (2.106), the following expression for the theoretical error in transport numbers is obtained[29]:

$$\varpi_{t_i} = \frac{z_i \mathcal{F}}{j \Delta t} \sqrt{\Delta C_{i,F}{}^2 \varpi_V^2 + 2 V_F^2 \varpi_C^2} \tag{2.109}$$

Where ϖ_V and ϖ_C are the experimental errors associated with volume and concentration measurement. Using eq. (2.102), the applied current j can be expressed in terms of the expected variation of concentration in the feed compartment:

[29] Equation (2.109) can be obtained under the assumption that t and j are error-free

$$j \cong -z_i \mathcal{F} V_F \frac{\Delta C_{i,F}}{\Delta t} \tag{2.110}$$

Thus, eq. (2.109) can be rewritten as follows:

$$\varpi_{t_i} \simeq \sqrt{\left(\frac{\varpi_V}{V_F}\right)^2 + \left(\frac{\varpi_C}{\Delta C_{i,F}}\right)^2} \tag{2.111}$$

The latter equation enables estimation of the theoretical error on t_i^m, given the experimental uncertainties (ϖ_V and ϖ_C) and the chosen operative conditions (V_F and $\Delta C_{i,F}$). Specifically, ϖ_V and ϖ_C depend on the specific measurement method. By setting $V_F = 50\ mL$ and $\varpi_V = 0.5\ mL$, a typical value for graduated cylinders, a parametric analysis can be performed on ϖ_{t_i} by varying ϖ_C and $\Delta C_{i,F}$. The results of such analysis are reported in Figure 31

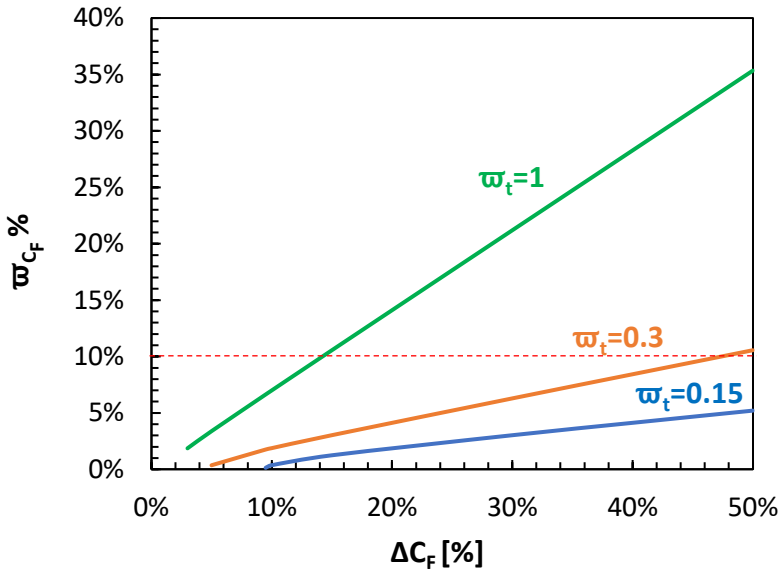

Figure 31 Parametric analysis on transport numbers theoretical error. The solid lines represent the theoretical standard deviation associated with the transport number measurement. The red dashed lines represent the experimental error typically associated to the chromatographic analysis.

Figure 31 demonstrates that, at a fixed ϖ_{t_i}, the acceptable concentration error (measured chromatographically) must decrease as $\Delta C_{i,F}$ decreases. In other words, the smaller the concentration variation in the feed compartment, the more accurate the concentration measurement must be to reliably determine t_i^m. Given that realistic values of ϖ_C are about the 10% of the sample concentration, achieving a standard deviation of 0.3 on t_i^m, would require $\Delta C_{i,F}$ to be around 47% of the initial feed concentration, conditions that clearly violate the assumption of negligible

concentration gradients. This analysis therefore shows that accurate determination of transport numbers with the investigated method is not feasible under the required conditions.

2.2.3 Salt permeability

The determination of the neutral salt diffusive transport rate represents a fundamental method for characterizing IEMs. Two main experimental approaches are commonly employed for this purpose: the desorption rate measurement from a salt-loaded membrane sample, and the direct transport measurement using a two-compartment cell [100,103,106]. The latter method is generally preferred, as it is easier to implement and enables a more straightforward mathematical treatment of the results.

In the present work, salt diffusive fluxes and permeabilities across the FKS-50 CEM were quantified using a custom-designed two-compartment diffusion cell. Experiments were carried out with both single-salt solutions and equimolar binary mixtures, including NaCl, KCl, and $MgCl_2$. The compositions and concentrations of the feed solutions were chosen to be consistent with those used in the thermodynamic characterization (see section 1.2).

Prior to each test, the feed compartment was filled with 140 mL of salt solution, while the receiver compartment was filled with 150 mL of DI water. Circular membrane coupons (diameter of 4.7 cm) were equilibrated in the feed solution for at least 24 h, followed by immersion in DI water for 24 h to desorb mobile salt prior to testing. During the experiments, both compartments were vigorously stirred using mechanical stirrers to minimize external mass-transfer resistances. The conductivity of the receiver solution was monitored in-line with a sampling frequency of 60 s^{-1} to track the concentration change as a function of time. After 30 min, the cell was disassembled, and the membrane thickness was measured using a micrometer.

The transport rate across the membrane was evaluated by applying a mass balance to the receiver compartment:

$$\frac{d\left(V_R C_{salt,R}\right)}{dt} = C_{R,i}\frac{dV_R}{dt} + V_R\frac{dC_{i,R}}{dt} = N_i A_m \tag{2.112}$$

Under pseudo-steady state conditions, N_i is constant, thus eq. (2.112) can be simplified as:

$$N_i \simeq \frac{\bar{V}_R}{A_m}\frac{\Delta C_{i,R}}{\Delta t} + \frac{\bar{C}_{i,R}}{A_m}\frac{\Delta V_R}{\Delta t} \tag{2.113}$$

where $\bar{V}_R$ and $\bar{C}_{i,R}$ denote the average volume and salt concentration in the receiver compartment. The volume variation in the receiver compartment due to osmotic water transport can be expressed in terms of water flux N_w, yielding:

$$N_i \simeq \frac{\bar{V}_R}{A_m}\frac{\Delta C_{i,R}}{\Delta t} - \bar{C}_{i,R}N_w \tag{2.114}$$

Here, N_w was independently determined in separate osmotic water transport experiments (see section 2.2.4). The validity of the pseudo-steady-state assumption was confirmed by the linearity of the conductivity–time profiles (see Figure 32)

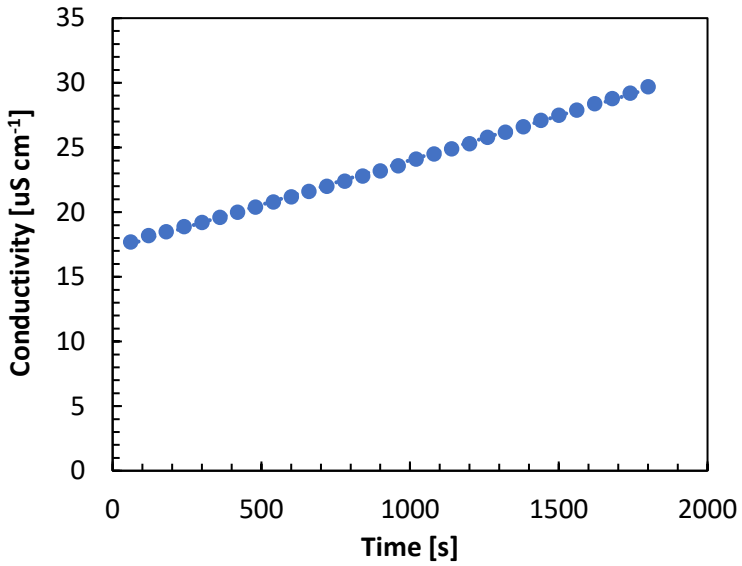

Figure 32 Variation of receiver compartment conductivity as a function of time during a salt diffusion test with feed concentration of 0.1 mol L^{-1} NaCl

At low salt concentration, solution conductivity increases proportionally with salt concentration [30]. Therefore, a linear conductivity–time relationship demonstrates that the salt flux remains constant throughout the experiment. For single-salt tests, concentration variations were determined through a linear calibration of conductivity. Accordingly, eq. (2.114) was reformulated as:

$$N_i \simeq \frac{\bar{V}_R}{A_m}\frac{\Delta C_i}{\Delta \kappa}\frac{\Delta \sigma_R}{\Delta t} - \bar{C}_{i,R}N_w \tag{2.115}$$

Where $\Delta\sigma_R/\Delta t$ is the slope of the conductivity-time curve, while $\Delta C_i/\Delta\kappa$ was obtained from the calibration procedure. Conversely, for equimolar binary mixtures, the final concentrations in the receiver compartment were determined by chromatographic analysis.

Salt permeability was then derived from the calculated fluxes according to:

$$p_{s,i} = \delta\frac{N_i}{\Delta C_i} = \delta\frac{N_i}{C_{F,i}} \tag{2.116}$$

2.2.3.1 Results and discussion

The salt permeabilities of single-salt and equimolar binary solutions tests are reported in Figure 33.

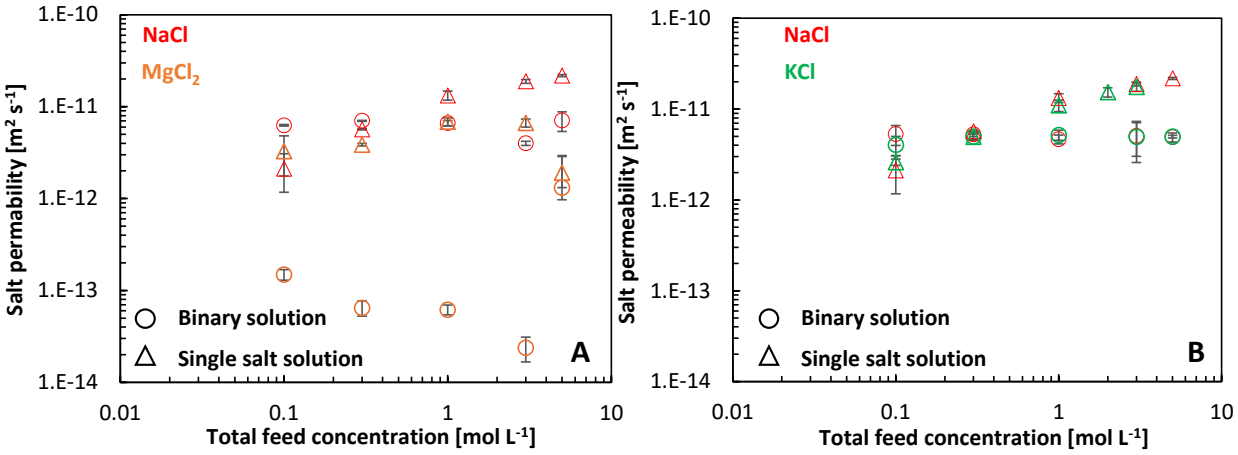

*Figure 33 Salt permeability in FKS-50 CEM equilibrated with (**Δ**) single-salt or (○) binary equimolar solutions of (**A**) NaCl and $MgCl_2$ or (**B**) NaCl and KCl.*

NaCl and KCl showed similar salt permeability in the investigated CEM, with an increasing trend with the external concentration. Since the permeability obtained from eq. (2.115) represents a macroscopic parameter influenced by both partitioning and diffusivity within the membrane [10,137], the observed increase can be attributed to either enhanced partition or higher effective diffusivity. Conversely, $MgCl_2$ permeability showed a decreasing trend at high salt concentration. This reduction is noteworthy, as co-ion transport typically dominates salt transport in IEM [128]. A plausible explanation lies in the reduced water uptake of membranes equilibrated with $MgCl_2$, which would lower the apparent diffusivity (see section 1.2.3.1). Moreover, such decrease is in agreement with the

abrupt reduction of mobile ion concentration observed in Figure 6, suggesting that the reduction in salt permeability could be due to thermodynamic reasons.

In the case of equimolar mixtures, NaCl and KCl permeabilities were comparable to each other but consistently lower than in single-salt experiments, and they remained nearly independent of the external concentration. Conversely, for the NaCl–$MgCl_2$ mixture, $MgCl_2$ permeability was strongly suppressed, a result that cannot be explained solely by thermodynamic arguments, since the partition selectivity of Mg^{2+} over Na^+ exceeds unity (see Figure 6)

Given that diffusion is primarily governed by co-ion transport, the interaction of chloride with two different counterions may hinder ion mobility and reduce salt flux. The assumption that different inter-ionic interactions can affect the value of salt permeability is consistent with the reduced discrepancy between single- and binary-salt permeabilities at low concentrations, i.e., at low chloride content in the membrane phase. This further suggests that the effect of the These findings are consistent with literature reports on multi-ionic transport through nanofiltration membranes, showing that salt permeability can be strongly affected by the presence of multiple ionic species [166].

2.2.4 Water permeability

Part of the water permeability experimental campaign was carried out in in collaboration with Mrs. Valeria Guenther, PhD student at the chair of chemical engineering of RWTH Aachen university.

Water permeability is typically defined to quantify the transport rate of water across IEMs. In electromembrane processes, undesired water crossover represents a parasitic phenomenon, and commercial IEMs are generally engineered to minimize water transport [167]. Water permeability can be evaluated either by measuring water flux under an applied hydrostatic pressure difference or under a salt concentration gradient [106,128]. The latter approach requires an apparatus similar to that used for salt permeability measurements. In the present study, water permeability was determined by means of direct osmosis experiments in a custom-made two-compartment cell (Figure 34).

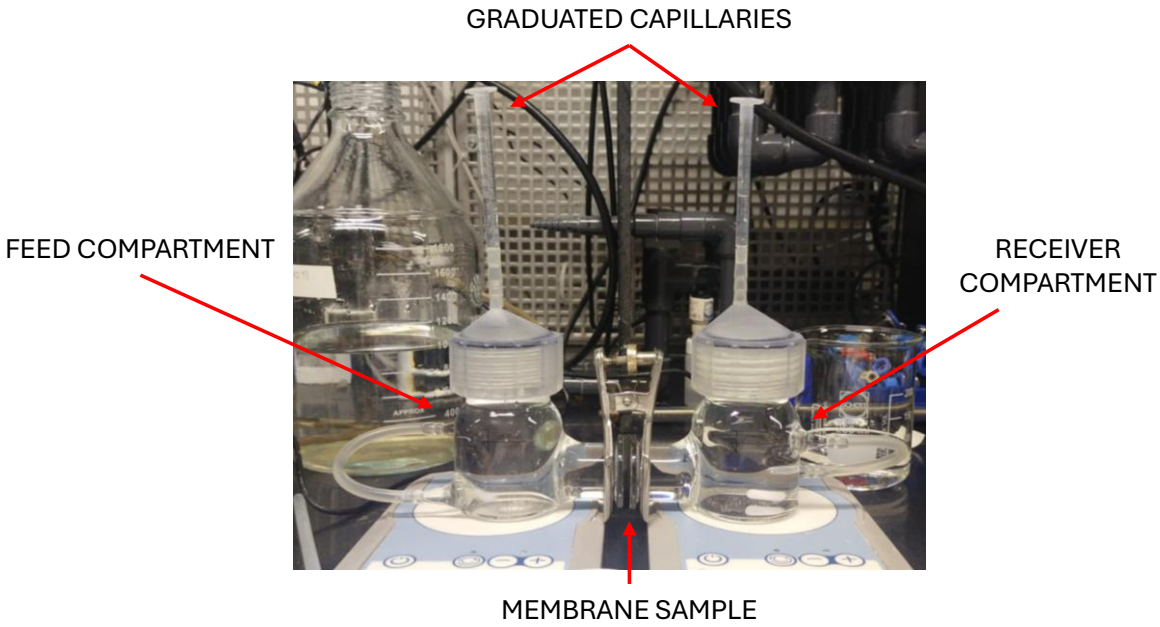

Figure 34 Picture of the two-compartment cell employed to perform water permeability tests

The experiments were conducted in batch configuration. At the beginning of each test, the feed and receiver compartments were filled with salt solution and DI water, respectively, and sealed with conical caps equipped with graduated capillaries for monitoring volume changes. The two compartments were separated by circular membrane coupons with an active area of 7.1 cm². Before testing, FKS-50 membranes were equilibrated in the feed solution for 24 h, followed by immersion in DI water for 24 h to desorb mobile salt.

Special care was taken during cell assembly to avoid entrapped air bubbles, as their presence can significantly alter the results [128]. To this end, 3D-printed conical caps were employed to allow smooth filling of the compartments without bubble formation. Another potential source of error was membrane deformation induced by the osmotic pressure difference between the two compartments, which could produce apparent volume changes unrelated to water transport. To prevent this effect, a rigid support was placed in direct contact with the membrane sample. During the tests, the solutions were stirred with magnetic stir bars. The overall test duration was approximately 40 min, with a data acquisition rate of 1 point per minute. The water flux was quantified by applying a volume balance to the receiver compartment, assuming constant density:

$$\frac{dV_R}{dt} = -N_w A_m \tag{2.117}$$

Under pseudo-steady-state conditions, the former equation can be reformulated as:

$$N_w = -\frac{1}{A_m}\frac{\Delta V_R}{\Delta t} \tag{2.118}$$

where $\Delta V_R/\Delta t$ can be evaluated from the slope of the V_R vs t plot (see Figure 35)

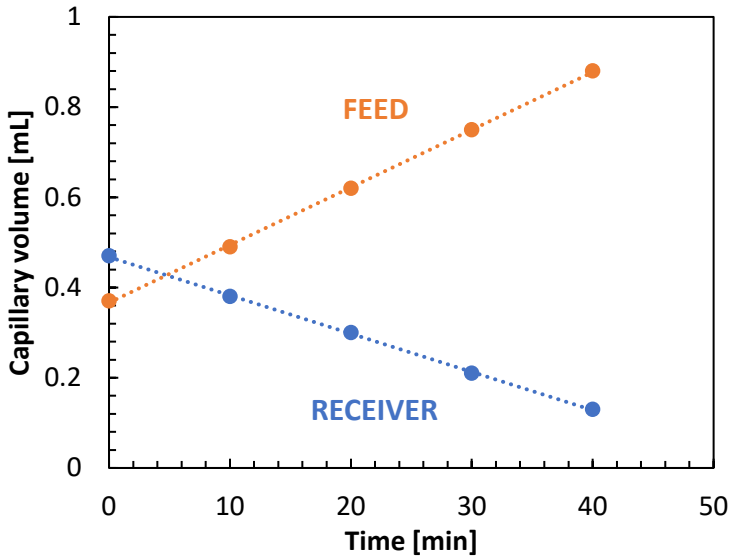

Figure 35 Liquid volume in the capillaries of feed and receiver compartments as a function of time for a generic water permeability test. The solid dots are the experimental data while the dotted lines are linear fittings.

Subsequently, the water permeability was calculated according to:

$$P_w = \delta\frac{N_w}{\Delta\Delta} = \delta\frac{N_w}{\Pi_F} \tag{2.119}$$

with Π_F being the osmotic pressure of the feed solution. The results are reported in Figure 36

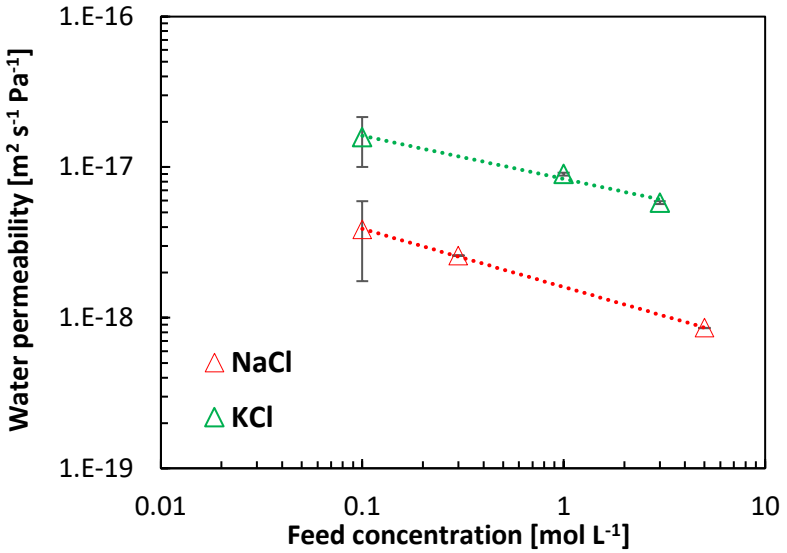

Figure 36 Water permeability of FKS-50 equilibrated with NaCl and KCl solutions at various concentrations. Dotted lines represents power law fittings.

The measured water permeability of membranes equilibrated with NaCl and KCl decreases similarly with the external concentration as can be appreciated by the slope of the lines in Figure 36. This trend is typical for IEMs in contact with concentrated salt solutions and is usually attributed to osmotic deswelling [167]. This result can be rationalized considering that the FKS-50 swells similarly in the Na^+ and K^+ form. However, a difference of nearly one order of magnitude was observed between NaCl and KCl water permeabilities. This discrepancy can be rationalised by considering ion–water interactions: Na^+ ions, diffusing in the opposite direction to water flux, have higher hydration energy and coordination number compared to K^+. Consequently, stronger drag interactions between Na^+ and water molecules lead to a reduced effective water transport in NaCl solutions, resulting in lower observed permeability

.

2.3 Transport phenomena in ion-exchange membranes: numerical simulations

In section 2.2, the main experimental techniques employed for IEMs characterization were presented. Directly measurable quantities, such as ionic fluxes, allow for the evaluation of macroscopical membrane parameters, such as salt and water permeabilities, that cannot immediately be related to primitive thermodynamic or transport properties, either because of experimental procedure design or because of the complexity of solution of the rigorous transport equations. Consequently, macroscale parameters are easy to implement in macroscale process models, but are typically dependent on numerous variables. This makes them strongly dependent on the chosen process conditions and also useless to develop fundamental physicochemical predictive models.

In the present section, the NP and MS transport theories are employed to retrieve fundamental transport parameters from raw experimental data. Transport equations are rigorously integrated accounting for concentration variation and thermodynamic effect on transport rate, thus accounting for phenomena typically neglected in the relevant literature. The proposed physical-mathematical framework is applied to single-salt solutions, but the theoretical structure of the modelling strategy is well-suited to be applied to multi-ionic systems.

Finally, the retrieved transport parameters are presented and discussed within the framework of the proposed models.

2.3.1 Evaluation of thermodynamic correcting coefficients

In section 2.1.2.2, it was discussed that, in order to properly implement transport equations in highly concentrated systems, gradients in the activity coefficients must be accounted for. This leads to the traditional formulation of the thermodynamic corrective coefficient, $\Gamma_{i(n)}$ defined in eq. (2.24). A different formulation, particularly useful in multi-ionic systems, can be obtained by considering that, in principle, activity coefficients depend on the concentration of all but one component[30], i.e., $\gamma_{i(n)} = f\left(C_i, C_j, \dots, C_n\right)$. Accordingly, the total differential of $ln\gamma_{i(n)}$ can be expressed as [122]:

[30] Due to the Gibbs-Duhem equation, the thermodynamic degrees of freedom of an isothermal, isobaric system composed of N components is $N-1$.

$$dln(\gamma_{i(n)}^{m}) = \sum_{j \neq w} \left. \frac{\partial ln\gamma_{i(n)}^{m}}{\partial lnC_j^m} \right|_{C_{k \neq j} = cost} dlnC_j^m \tag{2.120}$$

where the subscript $C_{k \neq j} = cost$ indicates that the partial derivatives are taken with all concentrations but C_j held constant. By applying the chain rule, the former equation can be rewritten as:

$$dln\gamma_{i(n)}^{m} = \left(\sum_{j \neq w} \left. \frac{\partial ln\gamma_{i(n)}^{m}}{\partial lnC_j^m} \right|_{C_{k \neq j} = cost} \frac{dlnC_j^m}{dlnC_i^m} \right) dlnC_i^m \tag{2.121}$$

Substituting eq. (2.121) into eq. (2.24), $\Gamma_{i(n)}$ can be rewritten as:

$$\Gamma_{i(n)}^{m} = 1 + \sum_{j \neq w} \chi_{i,j}^{m} \frac{dlnC_j^m}{dlnC_i^m} \tag{2.122}$$

where:

$$\chi_{i,j}^{m} = \left. \frac{\partial ln\gamma_{i(n)}^{m}}{\partial lnC_j^m} \right|_{C_{k \neq j} = cost} = \frac{C_j^m}{\gamma_{i(n)}^{m}} \left. \frac{\partial \gamma_{i(n)}^{m}}{\partial C_j^m} \right|_{C_{k \neq j} = cost} \tag{2.123}$$

The coefficient $\chi_{i,j}$ defined in the former equation quantifies the dependence of $\gamma_{i(n)}$ on the concentration of the j-th ionic species. Notably, water is excluded from the summation in (2.122) due to the Gibbs-Duhem relation. However, given that the fixed charges concentration can change with the external salt concentration due to the membrane osmotic de-swelling, the electroneutrality condition cannot be invoked to further reduce the system's degrees of freedom. Consequently, eq. (2.122) must include all mobile ions. It is worth noting that $\gamma_{n(n)}$ is, by definition, equal to unity, thus $\Gamma_{n(n)} = 1$.

For a membrane equilibrated with a binary electrolyte solution containing two mobile species c and a, (with a chosen as the reference species) $\Gamma_{c(a)}$ becomes:

$$\Gamma_{c(a)}^{m} = 1 + \chi_{c,c}^{m} + \chi_{c,a}^{m} \frac{C_c^m}{C_a^m} \frac{dC_c^m}{dC_a^m} \tag{2.124}$$

By applying the differential form of the electroneutrality condition (equation (2.33)), the former equation reduces to:

$$\Gamma_{c(a)}^{m} = 1 + \chi_{c,c}^{m} - \chi_{c,a}^{m} \frac{z_c C_c^m}{z_a C_a^m} \tag{2.125}$$

At this point, it should be stresses that $\Gamma_{c(a)}^{m}$ is almost always approximated to 1, and to the best of the author's knowledge in only one work $\Gamma_{c(a)}^{m}$ was effectively estimated in a IEM [128]. In this work, the authors made use of the original formulation of Manning's model to evaluate $\Gamma_{c(a)}^{m}$ but as discussed in Chapter 1, Manning's model fails in describing nonideal interactions both at very high and very low salt concentrations. In order to reduce reliance on semi-empirical models, the coefficients $\chi_{c,c}$ and $\chi_{\mathrm{c,a}}$ can, in principle, be extracted from ion partition equilibrium data, which provide information on how $\gamma_{c(a)}$ varies with the concentration (see section 1.2.2.7). However, from an experimental standpoint it is not possible to vary the concentration of individual mobile ions independently, as the only independent variable is the bulk salt concentration. Nevertheless, in the present work, we propose to obtain approximate values of $\chi_{\mathrm{c,c}}$ and $\chi_{\mathrm{c,a}}$ by plotting $\gamma_{c(a)}^{m}$ vs C_c^m and C_a^m and estimating the slope of the corresponding curves (see Figure 37).

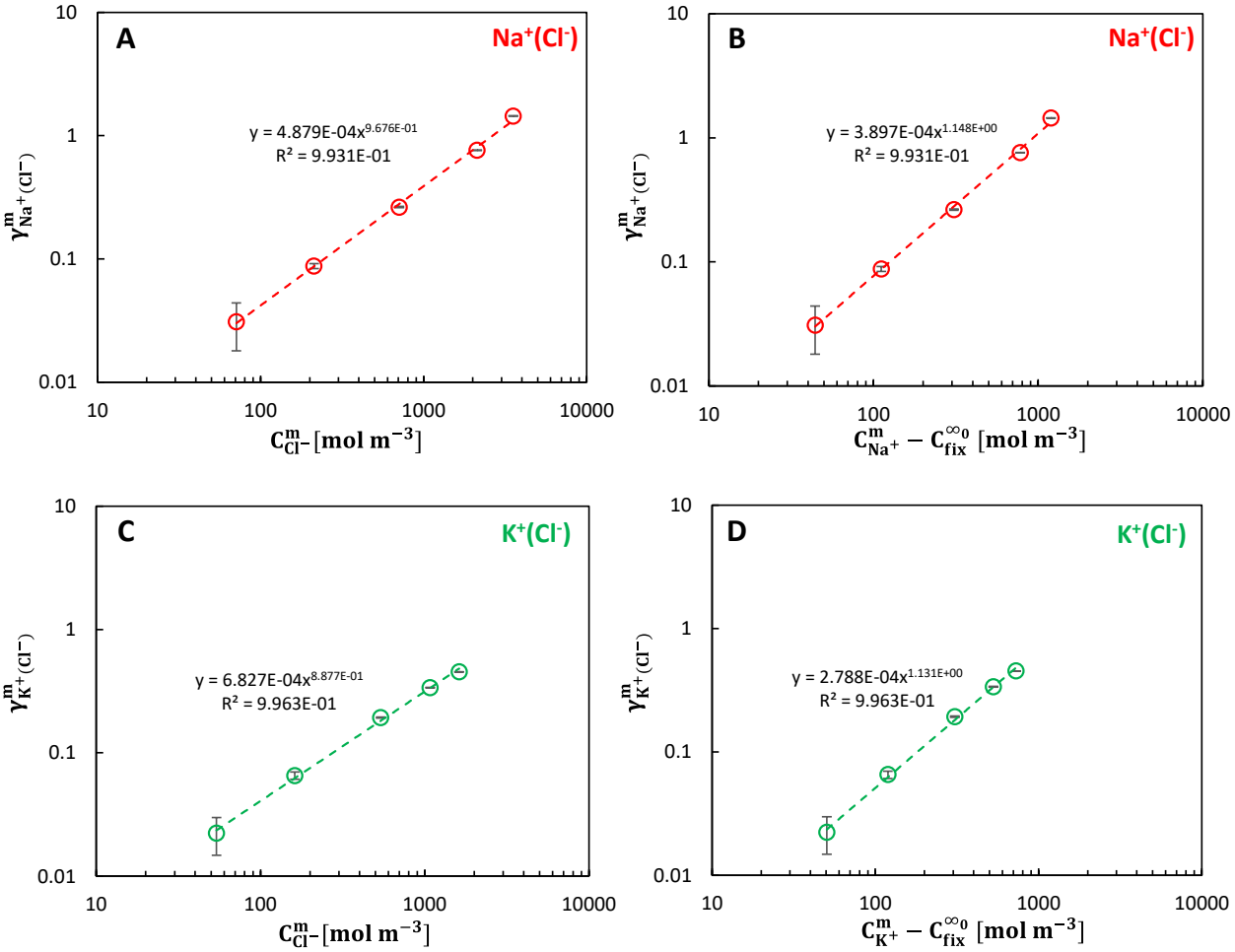

*Figure 37 (**A** and **B**) Na^+ and (**C** and **D**) K^+ activity coefficients in FKS-50 CEM, with Cl^- as reference ion. The values are plotted against (**A** and **C**) Cl^- concentration or against (**B** and **D**) the difference between the counter-ion and concentration and the fixed charges concentration evaluated at external infinite dilution. The empty circles are the experimental values evaluated from ion partitioning data reported in section 1.2.3.2, with the procedure reported in section 1.2.2.7. The dashed lines represent the fitting performed with power law functions.*

The experimental values reported in Figure 37 were fitted with the following power law functions:

$$\gamma^m_{c(a)} = a_1 (C^m_a)^{b_1} \tag{2.126}$$

$$\gamma^m_{c(a)} = a_2 \left(C^m_c - C^{\infty_0}_{fix}\right)^{b_2} \tag{2.127}$$

where a_1, b_1,a_2,b_2 are fitting constants and $C^{\infty_0}_{fix}$ represent the fixed charge concentration evaluated at external infinite dilution, i.e., with the membrane equilibrated with pure DI water in the corresponding counter-ion form. The value of the fitting constant is reported in Table 11

Table 11 Activity coefficients power laws fitting constants

	a_1 [-]	b_1 [-]	a_2 [-]	b_2 [-]	$C_{fix}^{\infty 0}$ [mol m^{-3}]
$Na^+(Cl^-)$	3.90E-04	1.15E+00	4.88E-04	9.68E-01	4.30E+03
$K^+(Cl^-)$	2.79E-04	1.13E+00	6.83E-04	8.88E-01	5.13E+03

By applying fitting equations (2.126) and (2.127), the coefficients $\chi_{c,c}^m$ and $\chi_{c,a}^m$ were evaluated as:

$$\chi_{c,a}^m = b_1 \tag{2.128}$$

$$\chi_{c,c}^m = \frac{b_2}{C_c^m - C_{fix}^{\infty_0}} \tag{2.129}$$

By substituting the former equations into eq. (2.125), $\Gamma_{c(a)}^m$ can be evaluated as:

$$\Gamma_{c(a)}^m = 1 + \frac{b_2}{C_c^m - C_{fix}^{\infty_0}} - b_1 \frac{z_c C_c^m}{z_a C_a^m} \tag{2.130}$$

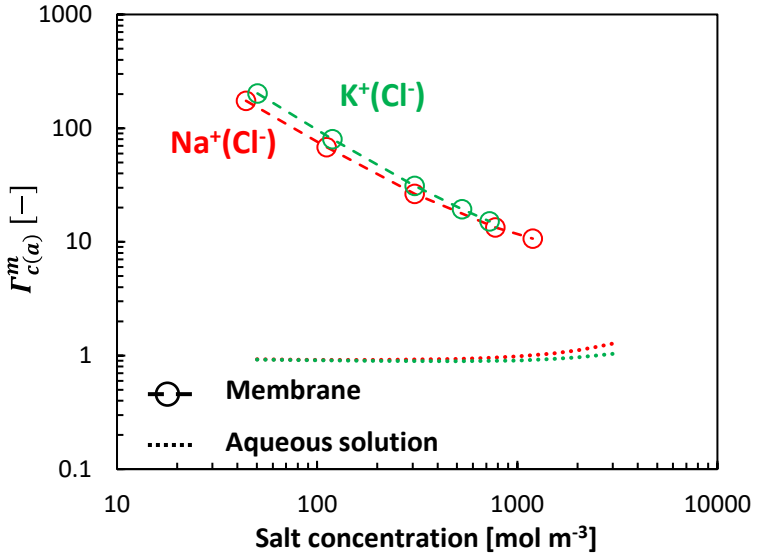

Figure 38 Na^+ and K^+ thermodynamic corrective coefficients of at various salt concentrations (Cl^- was taken as reference species) in FKS-50 CEM (dashed lines with circles) and in aqueous solution (dotted lines). The value of $\Gamma_{c(a)}^m$ was evaluated by applying eq. (2.130) and using the experimental equilibrium values of C_c^m and C_a^m. (the point at lower salt concentration in the membrane corresponds to an external salt concentration of 0.1 mol L^{-1})

In Figure 38, the thermodynamic corrective coefficient is reported as a function of the salt concentration in the membrane, corresponding to the co-ions concentration for 1:1 salts. Interestingly, $\Gamma_{c(a)}^m$ increases as the co-ion concentration in the membrane approaches zero, i.e., when the external

salt concentration decreases. This behaviour is the opposite of that in aqueous salt solution, where deviations from ideality (i.e., $\Gamma^m_{c(a)} > 1$) typically emerge at high salt concentrations. Mathematically, this stems from the fact that the experimentally measured activity coefficient in the membrane phase does not approach unity even at low external salt concentration; on the contrary, it decreases markedly (see Figure 37). This trend, commonly reported in the literature [63,81], is due to the fact that, when approaching the infinite dilution state in the external solution, the presence of the fixed charges prevents to reach a similar state in the membrane phase. This observation is consistent with eq.(1.111):

$$\lim_{C^s_c, C^m_a \to 0} \gamma^m_{c(a)} = \lim_{C^s_c, C^m_a \to 0} \gamma^s_{c(a)} \left(\frac{C^s_c}{C^m_c}\right)\left(\frac{C^s_a}{C^m_a}\right)^{-\frac{z_c}{z_a}} \neq 1 \tag{2.131}$$

Given that for a CEM equilibrated with NaCl or KCl, $C^m_c \to C^{\infty_0}_{fix}$ and $\gamma^s_{c(a)} \to 1$ when the external salt concentration approaches zero, the former inequality would be violated only if:

$$\lim_{C^s_c, C^m_a \to 0} C^m_a = C^s_c C^s_a \tag{2.132}$$

which is not verified experimentally. From a thermodynamic viewpoint, this behaviour can be rationalised by noting that electrostatic interactions with the fixed charges strongly depress the activity coefficient of counter-ions (see section 1.3). These interactions are progressively screened as the co-ion concentration in the membrane increases, producing a corresponding increase in the counter-ion activity coefficient.

2.3.2 Evaluation of transport coefficients in the Nernst–Planck framework

In the following sections, the transport properties obtained from the experimental campaign on the FKS-50 CEM, presented in section 2.2, are combined with thermodynamic data (see section 1.2) to estimate the ionic diffusivities within the framework of the NP model. In a single-salt system, two independent experimental measurements are required to determine the two unknown ionic diffusivities. A common choice is the combination of salt permeability and ionic conductivity tests (see sections 2.2.3 and 2.2.1) [158]. In an IEM equilibrated with a single-salt solution, the NP ionic conductivity can be expressed as:

$$\kappa^m = \frac{\mathcal{F}^2}{R_g T}\frac{\epsilon}{\tau}(z_c^2 D_c'^m C_c^m + z_c^2 D_a'^m C_a^m) \tag{2.133}$$

However, while ionic conductivity is measured at a given mobile-ion composition in the membrane phase, salt permeability tests are performed under a concentration gradient. This makes the combination of the two experimental datasets non-trivial.

2.3.2.1 Salt diffusion equation integration

The first step in evaluating ionic diffusion coefficients is the integration of the neutral salt transport equation across the membrane. As discussed in section 2.1.2.5, within the NP framework ionic diffusion in a single-salt system under a concentration gradient can be described as[31]:

$$\vec{N}_a^{\#} = -\frac{\epsilon}{\tau}\frac{D_c'^m D_a'^m\left(z_c^2 C_c^m + z_a^2 C_a^m \Gamma_{c(a)}^m\right)}{z_c^2 D_c'^m C_c^m + z_a^2 D_a'^m C_a^m}\vec{\nabla} C_a = -\bar{D}_{ca}^m \vec{\nabla} C_a^m \tag{2.134}$$

where $\vec{N}_{\mathrm{a}}^{\#}$ and $\vec{\nabla} C_{\mathrm{a}}$ denote the anion flux and concentration gradient within the membrane phase, respectively, while $\bar{D}_{\mathrm{ca}}$ is the apparent Nernst-Hartley diffusion coefficient of the neutral salt (including the geometrical corrective coefficient ϵ/τ). Importantly, in the former equation $\bar{D}_{ca}^m$ is an unknown function of the salt concentration. Equation. (2.134) could equivalently be expressed in terms of the cation flux and concentration gradient, as these are directly related to $\vec{N}_{\mathrm{a}}^{\#}$ and $\vec{\nabla} C_a^m$ through the zero-current condition and the local electroneutrality constraint.

Notably, the transport coefficient that can be derived from eq. (2.134) depends on the choice of the reference frame for the salt flux $\vec{N}_a^{\#}$. Within the solution–diffusion approach, the barycentric velocity is typically taken as reference and, to avoid defining an ill-posed molar concentration for the membrane component, the mass barycentric velocity is adopted, and fluxes and driving forces are expressed in terms of mass variables. However, in this latter case coupling the corresponding value of $\bar{D}_{\mathrm{ca}}$ with eq. (2.133)) is not rigorous, since ionic mobilities in conductivity measurements are expressed in molar terms.

Alternatively, if the membrane is formally excluded as thermodynamic component, the barycentric molar velocity can be easily defined (See eq. (2.3)), and eq. (2.134) can be reformulated as:

[31] Equation (2.134) is valid if the anion is taken as reference species for the quasi-electrostatic potential

$$\vec{N}_a - \frac{C_a^m}{C_{tot}^m}\vec{N}_{tot} = -\bar{D}_{ca}^m \vec{\nabla} C_a^m \tag{2.135}$$

with $C_{tot}^m = C_a^m + C_c^m + C_w^m$[32] and $\vec{N}_{\mathrm{tot}} = \vec{N}_{\mathrm{a}} + \vec{N}_{\mathrm{c}} + \vec{N}_{\mathrm{w}}$. Here, $\vec{N}_{\mathrm{a}}$ represent the flux in a stationary (membrane-fixed) reference frame, consistent with the flux measured in standard salt permeability tests (see section 2.2.3), and the $\bar{D}_{ca}^m$ evaluated via eq. (2.135) is now referred to a non-stationary reference frame.

For clarity, eq.(2.135) can be reformulated as:

$$\frac{dC_a^m(x)}{dx} = -\frac{1}{\bar{D}_{ca}^m(C_a^m)}\left(N_a - \frac{C_a^m(x)}{C_{tot}^m(x)}N_{tot}\right) \tag{2.136}$$

Under pseudo-steady state and in planar geometry, the molar fluxes appearing in eq. (2.136) are invariant with the position. Also, N_w and N_a have opposite signs, since water and salt move in opposite directions. To determine the unknown function $\bar{D}_{ca}^m = f(C_a^m)$[33], eq. (2.136) must be coupled with the electroneutrality and Euler's equations ((2.33) and (1.19)) and solved with boundary conditions consistent with the experimental configuration of salt permeability tests:

$$\begin{cases} C_a^m(0) = C_{a,0}^m \\ C_c^m(0) = C_{c,0}^m \\ C_a^m(\delta) = 0 \end{cases} \tag{2.137}$$

where δ is the geometrical thickness of the membrane, while $C_{a,0}^m$ and $C_{c,0}^m$ are respectively the equilibrium anion and cation concentration at the feed-side interface. Traditionally, $\bar{D}_{ca}^m(C_a^m)$ is evaluated by solving eq. (2.136) under the assumption of linear concentration profile across the membrane[128,168], an approximation valid only for moderate concentration gradients. When $C_a^m(0) \gg C_a^m(\delta)$, osmotic water flux and variations of diffusion coefficients make such assumption unreliable.

In this work, an alternative numerical procedure was employed, based on a stepwise evaluation $\bar{D}_{ca}^m = f(C_a^m)$. The concentration domain in which $\bar{D}_{ca}^m = f(C_a^m)$ is to be evaluated is discretized into sufficiently small intervals ΔC_a^m in which $\bar{D}_{ca}^m$ is approximated as constant. Hence, $\bar{D}_{ca}^m$ and C_a^m can

[32] C_w^m can be evaluated as a function of C_a^m and C_c^m by means of the Euler's equation (1.19) assuming constant partial molar volumes

[33] In a single-salt system, the salt concentration can be univocally related both to the anion concentration and the cation concentration

we conceptualized as vectors of N elements, with N being the number of sub-intervals, i.e., $\overline{D}_{ca}^{m} = \left[\overline{D}_{ca}^{m(0)}, \overline{D}_{ca}^{m(1)}, \dots, \overline{D}_{ca}^{m(i)}, \dots, \overline{D}_{ca}^{m(N)}\right]$ and $C_a^m = [C_a^{m(0)}, C_a^{m(1)}, \dots, C_a^{m(i)}, \dots C_a^{m(N)}]$ with i representing the interval, and $C_a^{m(0)} = C_a^m(\delta) = 0$. Consequently, eq. (2.136) can be integrated numerically and $\overline{D}_{ca}^{m(0)}$ can be evaluated with a numerical solver by imposing the boundary conditions (2.137). To evaluate $\overline{D}_{ca}^{m(1)}$ eq. (2.136) can be integrated again in the sub-interval $C_a^m = [C_a^{m(0)}, C_a^{m(1)}, C_a^{m(2)}]$ considering that now $\overline{D}_{ca}^{m(0)}$ is known from the previous integration. Such iterative procedure can be carried out by progressively increasing the integration step until $\overline{D}_{ca}^{m(N)}$ is evaluated. To do that, N different experimental points should be determined. To circumvent the problem, experimental values of N_a, N_w, $C_{a,0}^m$ and $C_{c,0}^m$ can be fitted as functions of the external feed salt concentration. The fitting functions for the FKS-50 CEM equilibrated with NaCl and KCl are reported in Figure 39 and Figure 40.

For both NaCl and KCl, $C_a^{m(0)}$ was set to the equilibrium value corresponding to an external salt concentration of 10^{-3} mol L^{-1} while N was set to 200. To assess the dependence of the of the results from the lower concentration bound and from the number of discretization intervals, several simulations were also performed at different values of $C_a^{m(0)}$ (from 10^{-5} to 10^{-3}) and N (from 10^2 to 10^5), but no significant numerical effects were observed.

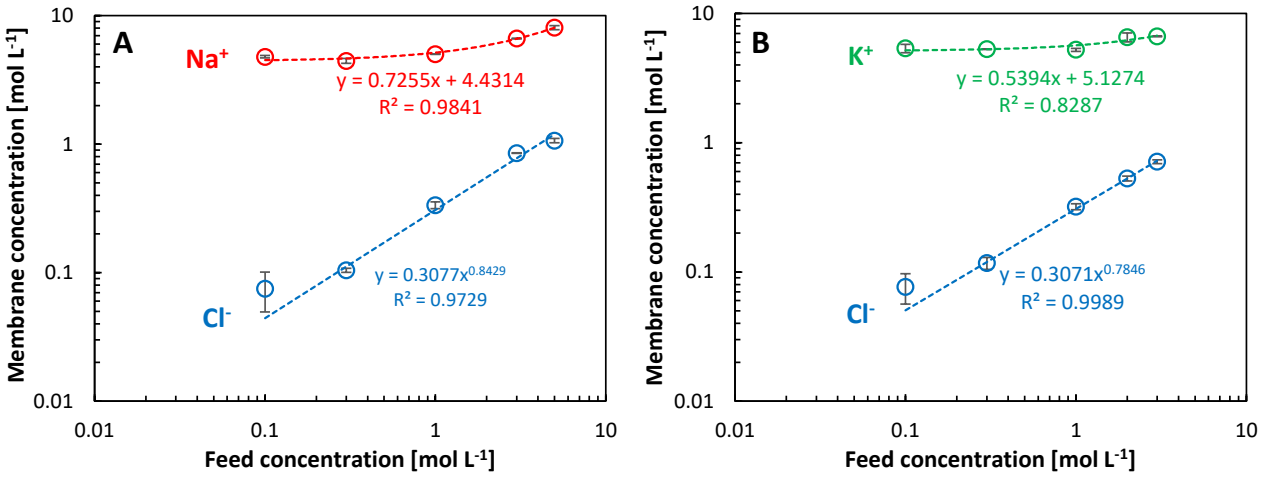

*Figure 39 Mobile ions concentration in FKS-50 equilibrated with aqueous solutions of (**A**) NaCl and (**B**) KCl. The empty circles are the experimental data evaluated from ion partitioning tests, while the dashed lines are the power law fittings.*

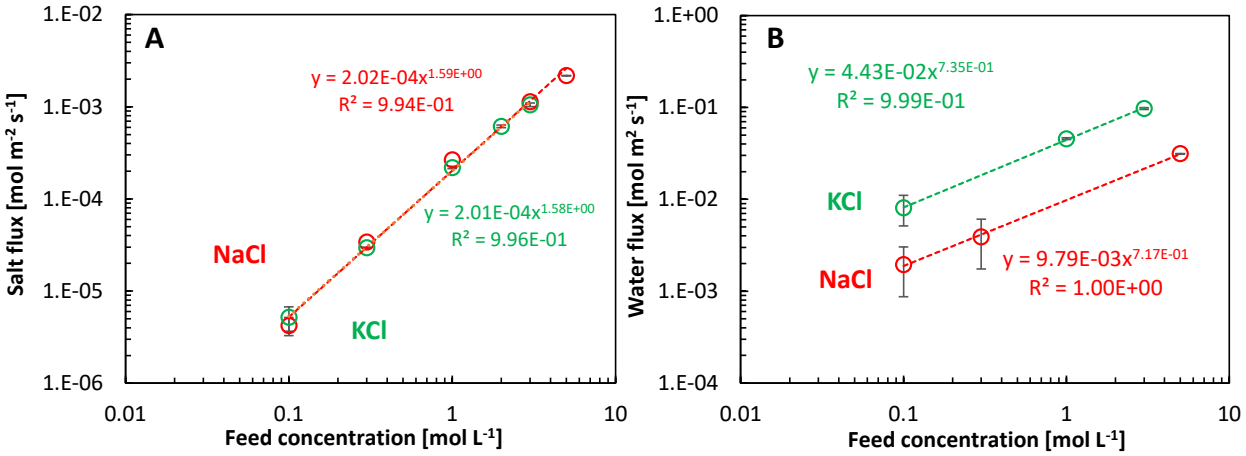

*Figure 40 (**A**) Salt and (**B**) water fluxes across FKS-50 separating a DI water receiver compartment from a feed compartment filled with single-salt solutions at variable concentration of NaCl and KCl. The empty circles are the experimental data evaluated from ion partitioning tests, while the dashed lines are the power law fittings.*

Integration of eq. (2.136) enables the evaluation of $\bar{D}_{ca}^{m}$ in a molar barycentric velocity reference frame. However, as discussed in section 2.2.1.4, this valued cannot be directly combined with eq. (2.133), since conductivity measurements refer to a stationary (membrane-fixed) frame unless corrected for the convective current contributions.

Accordingly, $\bar{D}_{ca}^{m}$ should be evaluated with respect to the membrane-fixed reference frame by integrating the following equation:

$$\frac{dC_a^m(x)}{dx} = -\frac{N_a}{\bar{D}_{ca}^m(C_a^m)} \tag{2.138}$$

Eq. (2.138) can be solved for $\bar{D}_{ca}^m$ following the same numerical strategy as above. Figure 41A-D report the resulting concentration profiles and diffusion coefficients in both reference frames.

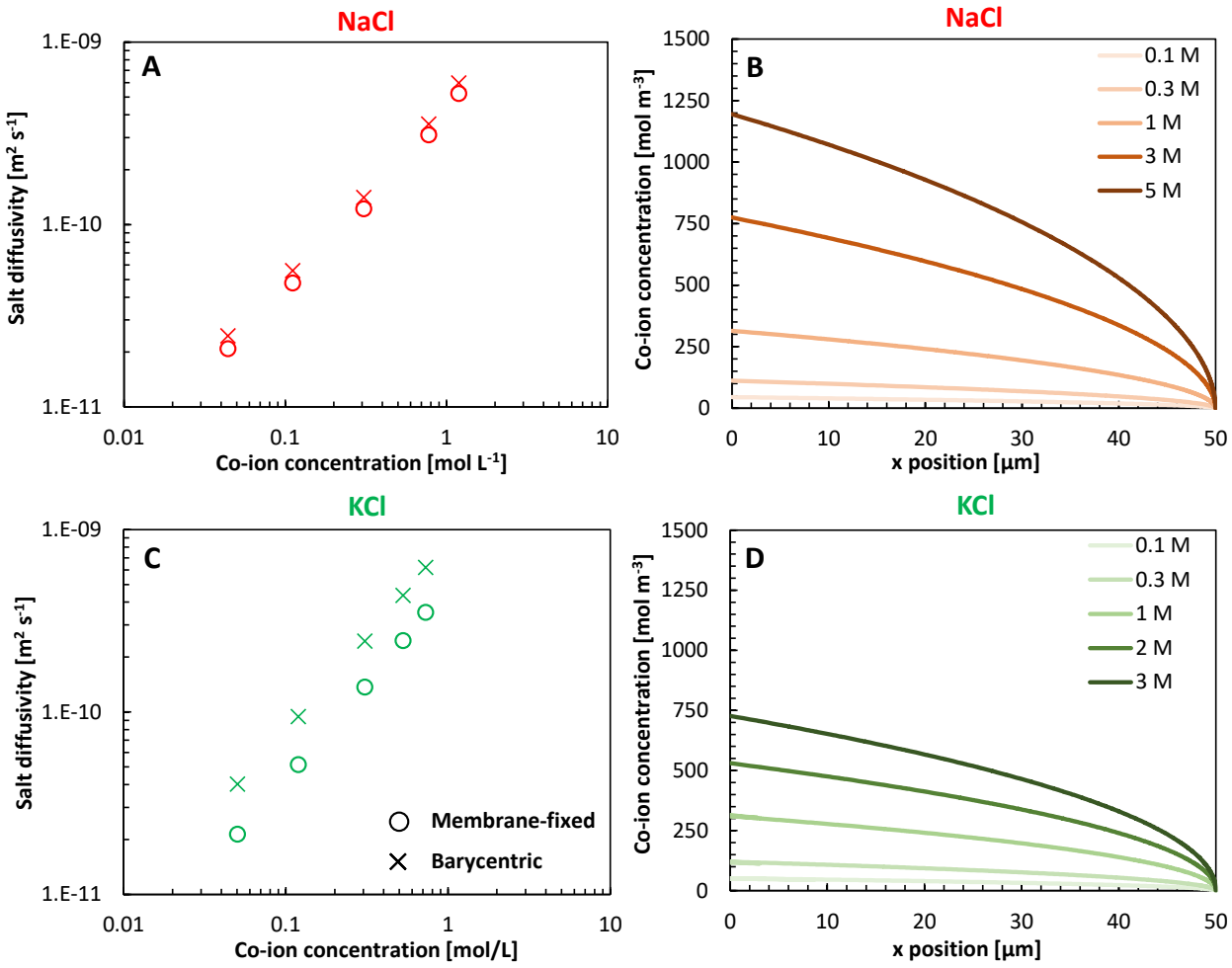

*Figure 41 (**A**) NaCl and (**C**) KCl Nernst-Hartely apparent diffusion coefficient in FKS-50 (equilibrated with single-salt solutions at different concentrations), as a function of the mobile ions concentration in the membrane phase. The empty circles are the values of diffusivity in the membrane-fixed reference frame while the crosses are the values in the molar barycentric reference frame. Figures (**B**) and (**D**) show co-ions concentration profile in FKS-50 in a salt diffusion tests with the feed-side interface ($x = 0$) contacted with single-salt solutions of NaCl and KCl at various concentrations, ranging from 0.1 to 5 mol L^{-1}.*

As previously discussed, the concentration profile depends on the variation of the transport coefficients with the concentration itself. Figure 41 B and D clearly show that the concentration profiles are non-linear, indicating a significant variation of the salt diffusion coefficient with the co-ions' concentration (see Figure 41 C and D). In particular, the sign of the concavity of the concentration profile is directly related to the variation of the mass transport resistance: a negative

concavity indicates that transport resistance increases at lower concentrations. As a matter of fact, the apparent diffusion coefficients of NaCl and KCl increase by more than one order of magnitude as the external salt concentration rises from 0.1 to 3 mol L^{-1}. Such result confirms that assuming a linear concentration profile in the evaluation of the salt diffusion coefficient would have led to gross errors.

Notably, while the difference between the diffusion coefficients obtained in the membrane-fixed and molar barycentric reference frames is relatively small for NaCl, in the case of KCl the value of $\bar{D}_{ca}^{m}$ in the barycentric reference frame is almost twice that obtained in the membrane-fixed frame. This discrepancy originates from the higher osmotic water flux observed during KCl diffusion experiments. Such evidence highlights the importance of carefully converting transport coefficients between reference frames, especially when osmotic water fluxes are non-negligible. For consistency with the conductivity measurements, the values of $\bar{D}_{ca}^{m}$ in the membrane-fixed reference frame are adopted in the following sections to evaluate ionic diffusivities.

2.3.2.2 Results and discussion

Once $\bar{D}_{ca}^{m}$ is determined, NP ionic diffusivities can be evaluated by combining equations (2.133) and (2.134), provided that the geometrical correction factor ϵ/τ and the thermodynamic correction coefficient $\Gamma_{c(a)}^{m}$ are known. In this work, ϵ/τ was estimated via Bruggeman's model (eq. (2.44)), while $\Gamma_{c(a)}^{m}$ was derived from ion partition data (see section 2.3.1). The resulting ionic diffusivities are reported in Figure 42.

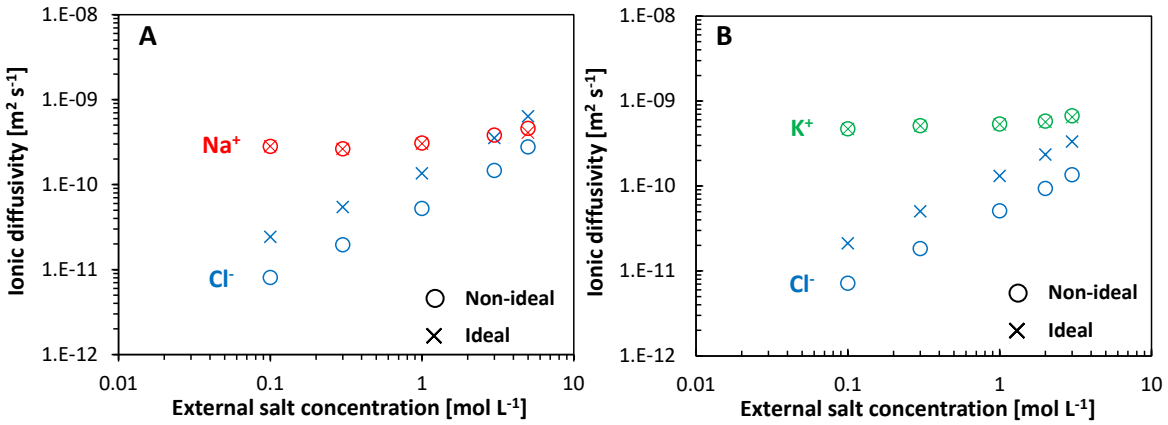

*Figure 42 Nernst-Planck ionic diffusivities in the membrane-fixed reference frame of mobile ions in FKS-50 CEM equilibrated with aqueous solution of (**A**) NaCl or (**B**) KCl at various concentrations. Empty circles represent the diffusivities not corrected for the thermodynamic correcting coefficient (i.e., $\Gamma_{c(a)}^{m} = 1$), while crosses adopt the values of $\Gamma_{c(a)}^{m}$ evaluated in section 2.3.1.*

Importantly, the reported values are already corrected for both geometric and thermodynamic effects and therefore reflect the intrinsic diffusivities of the mobile ions in the membrane. Counter-ion

diffusivities (i.e., $D^m_{Na^+}$ and $D^m_{K^+}$) are nearly constant at low external salt concentrations and lower than their infinite-dilution counterparts $D^{\infty_0}_{Na^+}$ and $D^{\infty_0}_{K^+}$ (see Table 7), with a similar trend ($D^m_{K^+} > D^m_{Na^+}$ and $D^{\infty_0}_{K^+} > D^{\infty_0}_{Na^+}$). However, at higher concentrations, counter-ion diffusivities exhibit a slight increase, a trend opposite to that of the Maxwell–Stefan ion–water binary diffusion coefficient (Figure 19) suggesting that ion–solvent interactions alone cannot account for the observed behaviour.

In contrast, co-ions diffusivity $D^m_{Cl^-}$ increase markedly with salt concentration, mirroring the behaviour of ion–ion Maxwell–Stefan coefficients (see Figure 19), thus suggesting that the origin of such increase can be related to inter-ionic interactions.

Moreover, correcting for the thermodynamic corrective coefficient significantly alters co-ion diffusivities, while leaving counter-ion values essentially unaffected. This occurs because $\Gamma^m_{c(a)}$ only influence the values of $\overline{D}^m_{ca}$, which is dominated by co-ions diffusion coefficient. In fact, $\overline{D}^m_{NaCl}$, $\overline{D}^m_{KCl}$ and $D^m_{Cl^-}$ vary with the concentration in a similar fashion.

It must be stressed that NP ionic diffusivities in membranes should be interpreted as pseudo-binary coefficients, implicitly associated with the dominant "third component" (the membrane matrix). Moreover, at high salt concentrations, the NP model neglects cross-correlated transport effects and therefore the extracted diffusivities progressively lose physical significance. Consequently, caution must be exercised when employing the NP framework to interpret the mechanistic origin of ion transport phenomena.

2.3.3 Evaluation of transport coefficients in the Maxell–Stefan framework

In the previous section, the application of the NP model to determine the diffusivities of mobile ions in an IEM equilibrated with a single-salt solution was discussed. This approach is relatively straightforward to implement, since only one transport coefficient per mobile ion is required to adequately describe electrodiffusion within the NP framework.

In contrast, the MS transport coefficients are considerably more challenging to predict and to determine experimentally. The main difficulty arises from the fact that multiple diffusion coefficients must be identified, all of which may, in principle, contribute to the measurable flux of a given component. As a result, experimental data on MS diffusivities are extremely scarce, particularly in IEMs.

As outlined in section 2.1.3, the number of transport coefficients required to describe mass and charge transport within the MS framework is given by $\frac{N}{2}(N-1)$, where N denotes the number of components. In the Binary-Friction model, derived from the application of the MS equations to IEMs, the membrane is considered as an additional fixed component exerting a drag force on the mobile species (i.e., water and ions). Consequently, the number of required coefficients becomes $\frac{(N+1)}{2}N$. In this expression, one additional component is formally introduced to account for frictional interactions between the mobile species and the membrane matrix. For an IEM equilibrated with a single-salt solution, three mobile components are present (water, counter-ions, and co-ions), leading to a total of six required transport coefficients. A schematic representation of the transport coefficients matrix is reported in Figure 43

j \ i	c	a	w	m
c		-	-	-
a	K_{ca}		-	-
w	K_{cw}	K_{aw}		-
m	K_{cm}	K_{am}	K_{wm}	

Figure 43 Matrix of Maxwell-Stefan friction factors for an IEM equilibrated with a single-salt solution. c, a, w, and m denote cations, anions, water molecules, and the membrane component, respectively. Note that the matrix is symmetric, and that the main diagonal elements are undefined according to the Stefan–Maxwell theory

The direct determination of all six transport coefficients would require an equivalent number of independent experimental measurements, a task that is both overly complex and scarcely feasible. Nevertheless, by analogy with semi-empirical thermodynamic models such as peNRTL (section 1.1.5.3), at least three of these parameters can be estimated from equivalent binary diffusion coefficients measured in aqueous solutions. In fact, MS diffusivities exhibit a weaker dependence on composition and concentration compared to NP diffusivities, thereby enabling the estimation of binary diffusion coefficients for a given pair of components from experiments performed in separate systems.

In particular, ion–water and ion–ion MS binary diffusion coefficients are well-documented in aqueous salt solutions and can be satisfactorily described by classical models such as Stokes–Einstein and Debye–Hückel [132,133] (see section 2.1.3.7). This reduces the number of unknown transport coefficients to three, namely $K_{c,m}, K_{a,m}, K_{w,m}$, which can be obtained by combining salt-diffusion and water-permeability experiments with ionic conductivity measurements and subsequently applying the corresponding MS transport equations, namely equations (2.67), (2.81) and (2.87).

2.3.3.1 Salt diffusion and osmotic water transport equations integration

Neutral salt diffusion and osmotic water transport in a single-salt permeability test can be described through eqs. (2.81) and (2.87) which, under pseudo steady-state conditions and in planar geometry can be reformulated as:

$$\begin{aligned}\left(C_c^m \nu_a - C_a^m \nu_c \Gamma_{c(a)}^m \frac{z_a}{z_c}\right)\frac{dC_a^m}{dx} = \\ = -\left[\left(\frac{C_a^m C_w^m}{C_{tot}^m}\frac{\nu_c^2}{Đ_{c,w}} + \frac{C_c^m C_w^m}{C_{tot}^m}\frac{\nu_a^2}{Đ_{a,w}}\right) + \frac{(C_c^m \nu_a - C_a^m \nu_c)^2}{C_{tot}^m Đ_{c,a}} + \frac{K_{ca,m}}{R_g T}\right] N_{ca} \\ - \frac{C_c^m C_a^m}{C_{tot}^m}\left(\frac{\nu_c}{Đ_{c,w}} + \frac{\nu_a}{Đ_{a,w}}\right) N_w\end{aligned} \tag{2.139}$$

$$\frac{dP_{tot}^m}{dx} = R_g T \frac{C_w^m}{C_{tot}^m}\left(\frac{\nu_c}{Đ_{c,w}} + \frac{\nu_a}{Đ_{a,w}}\right) N_{ca} - R_g T\left[\frac{1}{C_w^m}\frac{K_{w,m}}{R_g T} + \frac{1}{C_{tot}^m}\left(\frac{C_c^m}{Đ_{c,w}} + \frac{C_a^m}{Đ_{a,w}}\right)\right] N_w \tag{2.140}$$

The two equations must be solved by adopting the following boundary conditions:

$$\begin{cases} C_a^m(0) = C_{a,0}^m \\ C_c^m(0) = C_{c,0}^m \\ C_a^m(\delta) = 0 \end{cases} \tag{2.141}$$

$$\begin{cases} P_{tot}^m(0) = P^s(0) \\ P_{tot}^m(\delta) = P^s(\delta) - \Pi^s(\delta) \end{cases} \tag{2.142}$$

where $P^s(0)$ and $P^s(\delta)$ correspond to the hydrostatic pressure applied in the external compartment (i.e., atmospheric pressure) while $\Pi^s(\delta)$ correspond to the osmotic pressure of the solution in the feed compartment. To be solved eqs. (2.81) and (2.87) must be coupled with the differential form of the local electroneutrality equation (eq. (2.33)) and with Euler's equation (eq. (1.19)). Notably, all the transport coefficients appearing in equation (2.139) are apparent transport coefficients, whose dependence on the membrane microstructure can be expressed through the Bruggeman correction factor.

The previous set of equations can be employed to predict the water and salt flux across the membrane if the corresponding transport coefficients are known. Conversely, if the fluxes are experimentally determined, an equivalent number of transport coefficients can be determined.

Provided that the concentration dependence of binary transport coefficients including water and mobile ions is known, the remaining coefficients, i.e., $K_{\mathrm{ca,m}}$ (see eq. (2.82).) and $K_{w,m}$ can be determined by applying the numerical method proposed in section 2.3.2.1,

2.3.3.2 Results and discussion: Binary diffusion coefficients

Integration of eqs. (2.139) and (2.140) for the FKS-50 membrane contacted with NaCl or KCl solutions at various concentrations allows for the evaluation of the salt concentration and total pressure profiles depicted in Figure 44.

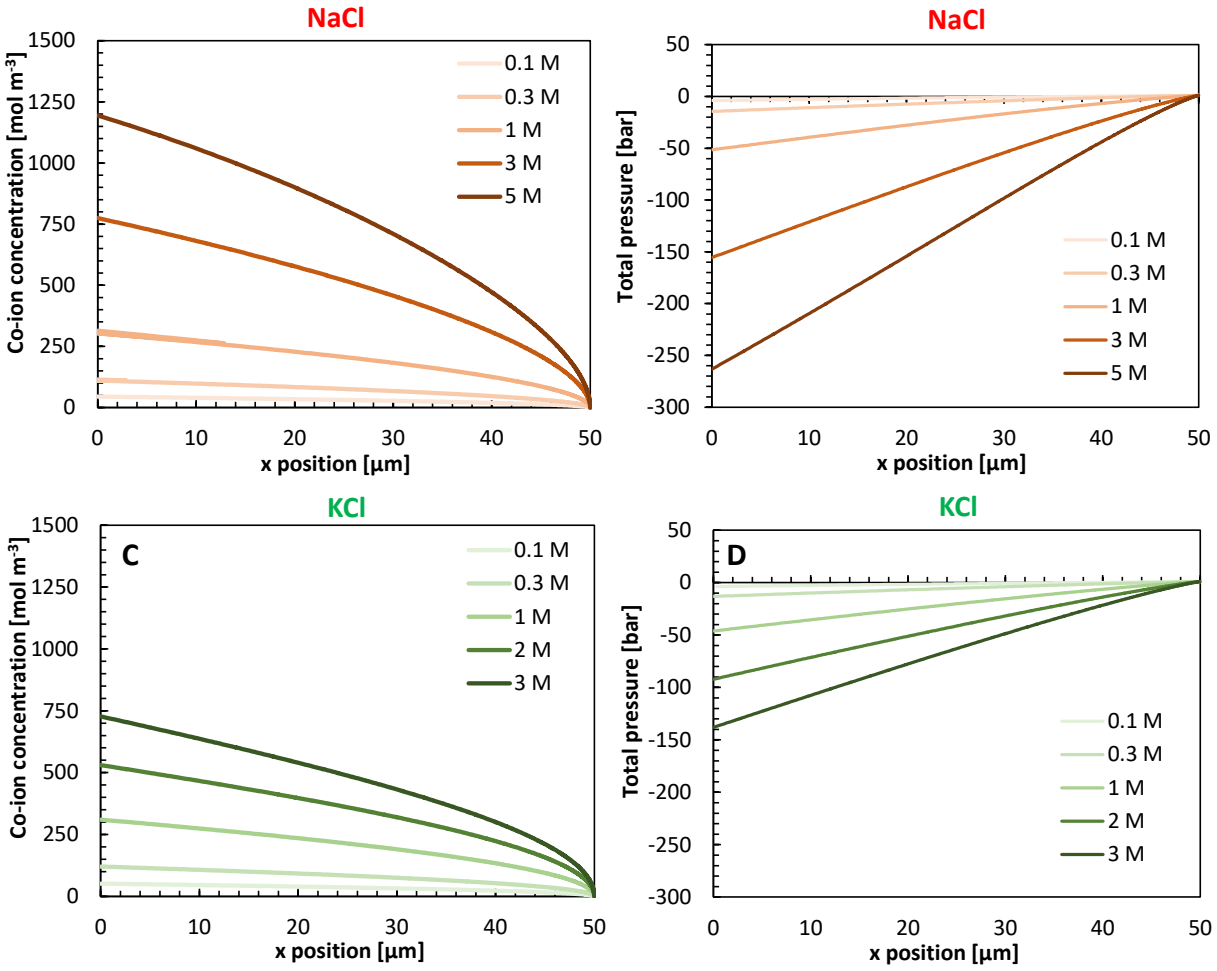

*Figure 44: **(A)(C)** Co-ions concentration profile and **(B)(D)** total pressure profile in FKS-50 in a salt diffusion tests with the feed-side interface ($x = 0$) contacted with single-salt solutions of NaCl and KCl at various concentrations, ranging from 0.1 to 5 mol L^{-1}. The receiver compartment was filled with DI water.*

Mobile salt concentration profiles are equivalent to those achieved applying the NP model, therefore similar considerations hold. Notably, the total pressure as an opposite trend. In fact, as the hydrostatic pressure in the external compartment correspond to the atmospheric pressure, the water chemical potential at the feed-side interfaces is lower due to the higher salt concentration. Moreover, the total pressure is almost everywhere negative. As previously stated, differently from the hydrostatic pressure, the total pressure is a thermodynamic variable and can reasonably assume negative values if the water osmotic pressure is higher that the hydrostatic one [74]. However, without accounting for non-ideal thermodynamic phenomena, it is not possible to separate rigorously the two contributions, unless the excess osmotic pressure is neglected.

Integration of eqs. (2.139) and (2.140) allow also for the evaluation of the unknown transport coefficients as a function of the co-ions concentration in the membrane, as depicted in Figure 45.

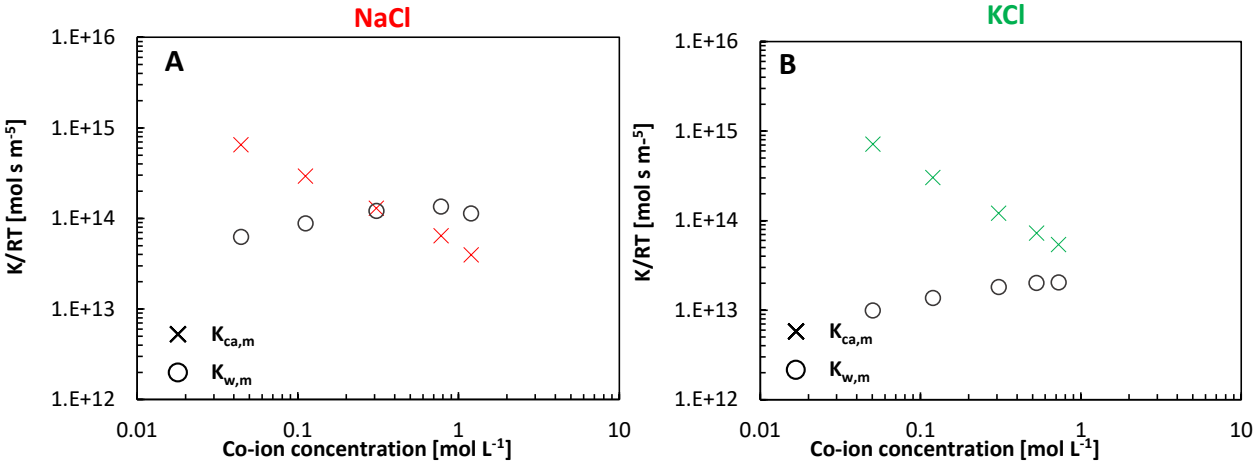

*Figure 45 (**A**) NaCl and (**B**) KCl equivalent salt-membrane friction factor (×) and water-membrane friction factor (○)in FKS-50 (equilibrated with single-salt solutions at different concentrations), as a function of the co-ions concentration in the membrane phase.*

Strictly speaking, the water-membrane friction factor increases with the co-ions' concentration. However, increasing the external concentration from 0.1 mol L^{-1} to 5 mol L^{-1} (3 mol L^{-1} in the case of KCl) makes $K_{w,m}$ increase only twofold. In recent works, Biesheuvel and Dykstra [43,72,74] assumed this factor to be constant. According to the present simulations, such assumption seems to be reasonable. Slight changes in the water-membrane friction factor could be attributed to a variation in the strength of interaction with the fixed charges caused by the increased salt content [76].

Conversely, the equivalent salt-membrane friction factor for NaCl and KCl considerably decreases with increasing mobile salt concentration in the membrane phase. $K_{ca,m}$ formally represent the neutral salt diffusive transport resistance due to the interactions between the mobile ions and the fixed charges. Therefore, a reduction of $K_{ca,m}$ implies a weakening of such interactions at high co-ion

concentration. In order to separate the contributions due to counter-ions and co-ions and evaluate the coefficients $K_{c,m}$ and $K_{a,m}$, eq. (2.82) must be combined with the ionic conductivity expression (eq. (2.67)). The corresponding results are reported in Figure 46.

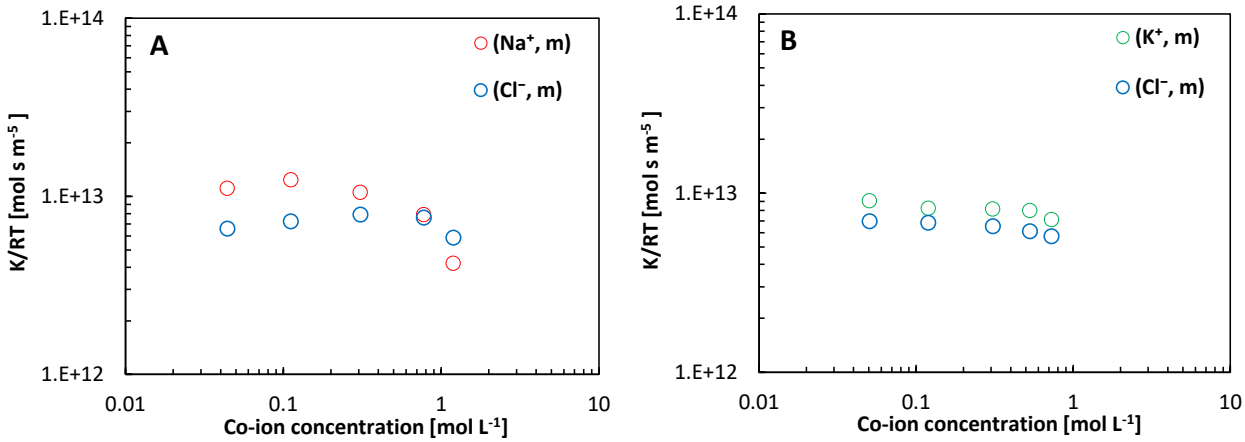

*Figure 46 Ion-membrane friction factors in FKS-50 CEM equilibrated with aqueous (**A**) NaCl and (**B**) KCl as a function of the co-ion concentration in the membrane phase.*

For the case of NaCl, $K_{Na^+,m}$ shows a considerable decrease at high co-ion concentration, conversely $K_{Cl^-,m}$ increases at low co-ion concentration apparently reaching a maximum value around 0.5 mol L^{-1}. Notably, when the CEM is equilibrated with aqueous solution of KCl, ion-membrane friction factors exhibit a different trend: $K_{K^+,m}$ and $K_{Cl^-,m}$ slightly decrease with increasing co-ion concentration.

Given that the magnitude of friction factors is inherently dependent on the mobile-ions concentration, it is useful to convert friction factors into binary diffusivities to rationalize such trend. Indeed, it should be noted that, although $K_{c,m}$ and $K_{a,m}$ are corrected for geometrical and thermodynamic effects, they still depend on the mobile-ion concentration. In principle, the general definition of the friction factor K_{ij} (eq. (2.50)) could be extended to ion–membrane interactions. However, this would require defining the "concentration" of the membrane component, which is not straightforward. To circumvent this issue, some authors [43] propose to treat the membrane friction factor as concentration-independent. Such an assumption, however, appears questionable, since the momentum exchanged between two species is inevitably related to the number of interacting particles.

To reduce the concentration dependence of $K_{c,m}$ and $K_{a,m}$ a binary ion–membrane diffusion coefficient can be introduced as:

$$Đ_{i,m} = \frac{R_g T}{K_{i,m}} \frac{C_{tot}^m}{C_i^m C_{fix}} \tag{2.143}$$

This definition relies on the assumption that the dominant drag force arises from the interactions between mobile ions and the fixed charged groups, rather than with the polymer backbone—a plausible hypothesis given the charged nature of the solutes. Through eq. (2.143), the ion–membrane friction factors can be reformulated as ion–membrane binary diffusion coefficients (see Figure 47).

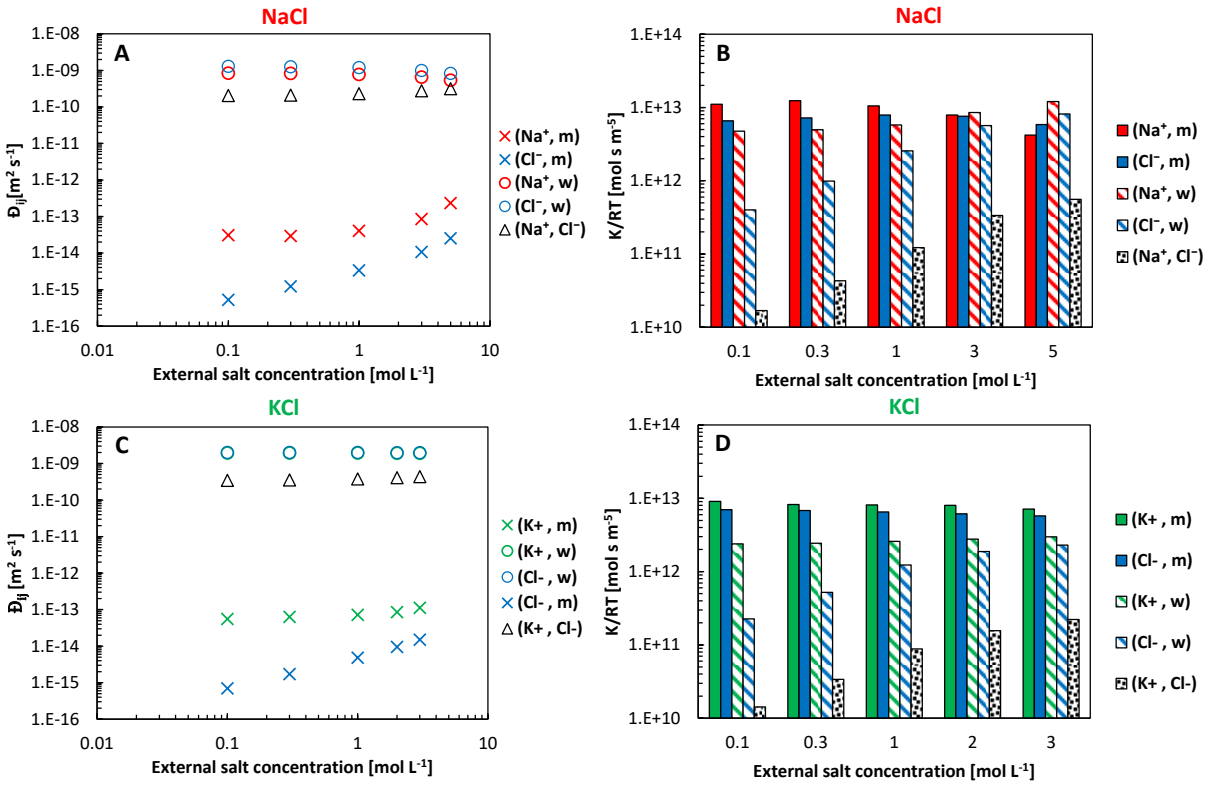

*Figure 47 (**A**),(**C**) Ion-ion, ion-water and ion-membrane MS binary diffusion coefficients in FKS-50 CEM equilibrated with aqueous NaCl and KCl at various concentrations. (**C**),(**D**) Ion-ion, ion-water and ion-membrane MS binary friction factors in FKS-50 CEM equilibrated with aqueous NaCl and KCl at various concentrations. A key advantage of the MS framework is that it decouples the transport resistances into species-specific contributions, thereby providing a clearer physical interpretation of the system.*

Figure 47 A and B show the ion-membrane binary diffusion coefficients in comparison to ion-ion and ion-water binary diffusivities, while Figure 47 C and D compare the related friction factors. Notably, ion-membrane diffusivities are order of magnitudes lower than the other binary diffusivities, implying that the strength of interaction with the fixed charges is much higher compared to the interactions among the mobile ions and between the mobile ions and the water molecules.

Nonetheless, ion-water friction factors are not negligible, especially at high external salt concentration, when the mobile ions concentration in the membrane phase is increased due to the weakening of Donnan exclusion mechanism. Therefore, not accounting for their contribution in the evaluation of salt transport resistance could lead to significant errors.

More in detail, the counter-ion–membrane binary diffusion coefficients are barely constant at low salt concentration, while showing a moderate increase at external concentrations above1 mol L^{-1}. In contrast, the co-ion–membrane diffusion coefficients show a marked increase with the external salt concentration.

Such trends mirror that of ion-ion binary diffusion coefficients in aqueous solution (see Figure 19). This suggest that the Debye–Hückel framework can be employed to rationalize these results. Indeed, at high ionic strength electrostatic interactions are screened due to the increase in the Debye screening parameter. Consequently, a reduction in $Đ_{i,m}$ is expected at high external concentration.

However, there are at least two considerations that undermine the validity of such analysis. First, $Đ_{a,m}$ appears to be much more sensitive on the ionic strength compared to $Đ_{c,m}$ and $Đ_{c,a}$. Moreover, if interactions among co-ions and the membrane were primarily electrostatic, $Đ_{a,m}$ would be expected to be negative, in accordance with eq. (2.90). In fact, since both co-ions and fixed charges are like-charged, the interaction force $\vec{F}_{a,m}$ in the momentum balance is expected to be repulsive, leading naturally to a negative value of $Đ_{a,m}$, as it is reported for like-charged ions in aqueous solutions [133].

Such unexpected behaviour could be only explained assuming that interactions between co-ions and the fixed-charges are mediated by counter-ions, provided that these latter are located in a region of space closer to the charged functional groups. Simulations performed by different authors [169,170] demonstrated how counter-ions binding (i.e., condensation) may determine a net inversion of charge on the surface of a polyelectrolyte, consequently affecting the interactions with the co-ions. Moreover, it is relevant to note that there is a slight difference between $Đ_{a,m}$ measured when the membrane is in the K^+ or in the Na^+ form, further suggesting that counter-ions can influence the interactions between co-ions and fixed charges.

Unfortunately, most of the studies on ion transport in IEMs focus on counter-ions, and only a few have investigated co-ion diffusivities. To the best of the author's knowledge, this is the first attempt to estimate binary diffusivities from experimental data within the proposed theoretical framework and further investigations will be required to fully elucidate the physical basis of the observed trends.

2.3.3.3 Results and discussion: mass and charge transport resistance analysis

The evaluation of the MS binary diffusivities enables a separate analysis of the contribution of each type of interaction to the overall salt-transport and charge-transport resistances. For this purpose, eq. (2.139) can be conveniently reformulated as:

$$\frac{dC_a^m}{dx} = -(R_{s,i-w} + R_{s,i-j} + R_{s,i-m})N_{ca} = -R_{tot}N_{ca} \tag{2.144}$$

Where R_s is the total salt transport resistance and $R_{s,i-w}$, $R_{s,i-j}$, and $R_{s,i-m}$ represent the salt transport resistances respectively due to ion-water, ion-ion and ion-membrane interactions, and are defined as follows:

$$R_{s,i-w} = \frac{\left(\frac{C_a^m C_w^m}{C_{tot}^m}\frac{\nu_c^2}{Đ_{c,w}} + \frac{C_c^m C_w^m}{C_{tot}^m}\frac{\nu_a^2}{Đ_{a,w}}\right) - \frac{C_c^m C_a^m}{C_{tot}^m}\left(\frac{\nu_c}{Đ_{c,w}} + \frac{\nu_a}{Đ_{a,w}}\right)\frac{N_w}{N_{ca}}}{\left(C_c^m\nu_a - C_a^m\nu_c\Gamma_{c(a)}^m\frac{z_a}{z_c}\right)} \tag{2.145}$$

$$R_{s,i-j} = \frac{\frac{(C_c^m\nu_a - C_a^m\nu_c)^2}{C_{tot}^m Đ_{c,a}}}{\left(C_c^m\nu_a - C_a^m\nu_c\Gamma_{c(a)}^m\frac{z_a}{z_c}\right)} \tag{2.146}$$

$$R_{s,i-m} = \frac{\frac{K_{ca,m}}{R_g T}}{\left(C_c^m\nu_a - C_a^m\nu_c\Gamma_{c(a)}^m\frac{z_a}{z_c}\right)} = \frac{\frac{C_{fix}}{C_{tot}^m}\left(\frac{C_a^m\nu_c^2}{Đ_{c,m}} + \frac{C_c^m\nu_a^2}{Đ_{a,m}}\right)}{\left(C_c^m\nu_a - C_a^m\nu_c\Gamma_{c(a)}^m\frac{z_a}{z_c}\right)} \tag{2.147}$$

Note that R_s is formally the inverse of salt permeability P_s, which is typically defined as:

$$P_s = \delta\frac{N_{ca}}{\Delta C_{ca}^m} \tag{2.148}$$

Where ΔC_{ca}^m is the difference between the mobile salt concentration in the membrane phase at the solution-membrane interface facing respectively the feed and receiver, which correspond to C_a^m when the membrane is equilibrated with a 1:1 salt. Given that salt diffusion always occurs under the effect of a concentration gradient, P_s is always an average quantity. By integrating eq. (2.148), and comparing the result with eq. (2.145), P_s can be expressed as follows:

$$P_s = \int_{C_{a,R}^m}^{C_{a,F}^m} \frac{dC_a^m}{R_s} = \int_0^{C_{a,F}^m} \frac{dC_a^m}{\sum_i R_{s,i}} \tag{2.149}$$

To quantify the contribution of each salt transport resistance to the total salt permeability, individual salt permeabilities can be defined as follows:

$$P_s = \sum_i P_{s,i} = \sum_i \int_0^{C_{a,F}^m} \frac{R_{s,i}}{\left(\sum_j R_{s,j}\right)^2} dC_a^m \tag{2.150}$$

The relative contribution to the salt permeability can be then evaluated as:

$$p_{s,i} = \frac{P_{s,i}}{\sum_i P_{s,i}} \tag{2.151}$$

Analogously, individual contributions to the ionic conductivity can be defined starting from eq. (2.67), and recalling that the MS transport matrix $[\mathcal{L}_{i,j}]$ can be written as:

$$[\mathcal{L}_{i,j}] = -\frac{[\mathcal{M}_{i,j}]^+}{det([\mathcal{M}_{i,j}])} \tag{2.152}$$

Where $[\mathcal{M}_{i,j}]^+$ is the adjugate matrix of $[\mathcal{M}_{i,j}]$, that for a membrane equilibrated with a single-salt solution assume the following form:

$$[\mathcal{M}_{i,j}] = \begin{bmatrix} -(K_{c,a} + K_{c,w} + K_{c,m}) & K_{c,a} & K_{c,m} \\ K_{a,c} & -(K_{a,c} + K_{a,w} + K_{a,m}) & K_{a,m} \\ K_{w,c} & K_{w,a} & -(K_{w,c} + K_{w,a} + K_{w,m}) \end{bmatrix} \tag{2.153}$$

where $K_{c,a} = K_{a,c}$, $K_{w,a} = K_{a,w}$, $K_{w,c} = K_{c,w}$.

Consequently, the ionic conductivity κ^m assume the following form:

$$\kappa^m = \frac{N(K_{c,w}, K_{a,w}, K_{c,a}, K_{c,m}, K_{a,m}, K_{w,m})}{D(K_{c,w}, K_{a,w}, K_{c,a}, K_{c,m}, K_{a,m}, K_{w,m})} \tag{2.154}$$

where N and D are homogeneous polynomials, respectively of order 2 and 3 in K_i, for which the Euler's rule applies:

$$\kappa^m = -\sum_i K_i \frac{\partial \kappa^m}{\partial K_i} = -\frac{1}{D^2}\sum_i K_i \left(N \frac{\partial D}{\partial K_i} - D \frac{\partial N}{\partial K_i} \right) \tag{2.155}$$

Where the minus is added to account for the fact that $\frac{\partial K_i}{\partial \kappa^m}$ is negative. From eq. (2.155) it follows that individual contribution to the ionic conductivity can be expressed as follows:

$$\kappa_i^m = -K_i \frac{\partial \kappa^m}{\partial K_i} \tag{2.156}$$

κ_i^m quantifies how much the effect of a specific kind of interaction (represented by the friction factor K_i) contribute to the overall ionic conductivity. For comparison purposes, the contributions to salt-transport resistance and ionic conductivity are reported in Figure 48.

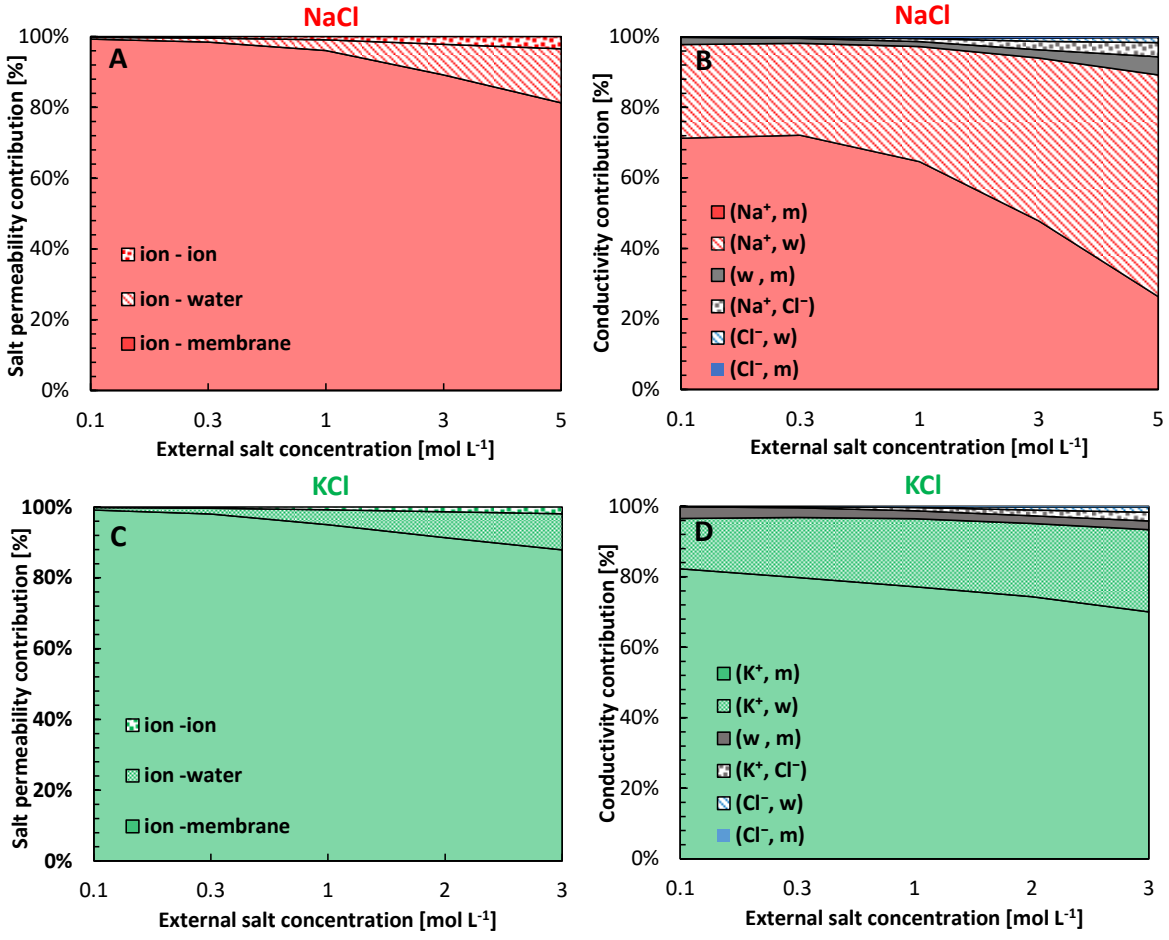

*Figure 48(**A**), (**C**) Ion-ion, ion-water and ion-membrane relative salt permeabilities in FKS-50 CEM equilibrated with aqueous NaCl and KCl at various concentrations. (**B**), (**D**) Maxwell-Stefan ionic conductivity contributions in FKS-50 CEM equilibrated with aqueous NaCl and KCl at various concentrations.*

Salt-transport permeability is primarily governed by the drag forces exerted by the membrane on the mobile components. However, at sufficiently high salt concentrations, ion–water interactions exert a significant influence on the overall permeability, while ion–ion contribution satay negligible in the entire concentration range. The contribution of ion-water interactions to the salt permeability of NaCl and KCl reach a value respectively of 15% and 10% at 5 mol L^{-1}. Such increase must be ascribed both to an increase in the ion-water interactions, due to the increased viscosity of the solvent, and to the weakening of the ion-membrane interactions, which is evident from the reduction of the salt-membrane equivalent friction factor $K_{ca,m}$ (Figure 45).

A similar trend is observed for ionic conductivity (Figure 48 B and D). At low salt concentrations, conductivity is primarily governed by the counter-ion−membrane interactions, even though counter-ion−water interactions in NaCl and KCl- equilibrated membrane respectively account for 27% and 14% of the overall conductivity. At higher external salt concentrations, however, the role of counter-ion−membrane interactions become less dominant, and the other contributions become significant. For instance, at 5 mol L^{-1} NaCl and 3 mol L^{-1} KCl, counter-ion − water interactions contribute to the overall ionic conductivity respectively for the 63% and 24%.

Interestingly, water-membrane interactions do contribute to the overall ionic conductivity even though the solvent does not directly contribute to the ionic current. Given that water is a neutral component, one would expect $K_{\mathrm{w},m}$ to have no influence on the ionic conductivity of the membrane. Such result can be rationalized considering that the transport rate of mobile ions is directly related to the solvent velocity, as the drag force that water molecules exert on the mobile ions is proportional to the difference between their velocity and that of the solvent, which in turn is related to $K_{\mathrm{w},m}$. In other words, transport coefficients of neutral components do have an indirect effect on the ionic conductivity of the membrane. Such effect is only implicit in the NP approach, given that solvent properties are not directly taken into account.

Regarding ion-ion interactions, their contribution to the overall ionic conductivity is negligible over the entire concentration range investigated, reaching a maximum value of 4% and 2.5% respectively at 5 mol L^{-1} of NaCl and 3 mol L^{-1} of KCl.

These findings suggest that neglecting mutual interactions among mobile components can lead to a gross misinterpretation of the physics of charge and mass transport in IEMs. Recently, Freeman et al. [171] , performed molecular dynamics simulations to assess the effect of mobile components correlated motion on the overall ionic conductivity. According to their findings, when the IEMs are equilibrated with concentrated salt solutions, correlated motions among the mobile components can

become significant. This highlights the necessity of considering such effects when interpreting experimental measurements of transport coefficients [172,173].

A theoretical framework based on the NP model to not allow to account for such mutual coupling, and therefore NP diffusivities do not assume a clear and specific physical meaning. Rather they represent the global effect of several physical contributions. Consequently, NP diffusivities cannot be used to describe ion-membrane interactions. To demonstrate this point, it can be useful to compare the NP diffusivities with the MS ion-membrane diffusivities $Đ_{i,m}$. When the other transport resistances are neglected, the MS equation (2.56) becomes:

$$C_i \vec{\nabla} \tilde{\mu}_i = -\frac{R_g T}{Đ_{i,m}} \frac{C_{fix}}{C_{tot}} \vec{N}_i \tag{2.157}$$

Which can be rewritten as:

$$\vec{N}_i = -\frac{C_{tot}}{C_{fix}} Đ_{i,m} \left(\Gamma_{i(n)} \vec{\nabla} C_i + \frac{z_i \mathcal{F}}{R_g T} C_i \vec{\nabla} \varphi \right) \tag{2.158}$$

Which would correspond to the NP equation if:

$$\frac{C_{tot}}{C_{fix}} Đ_{i,m} = D_i \tag{2.159}$$

Figure 49 shows the comparison between NP diffusivities D_i and the MS binary diffusivity $Đ_{i,m}$ corrected for $\frac{C_{tot}}{C_{fix}}$ according to eq. (2.159).

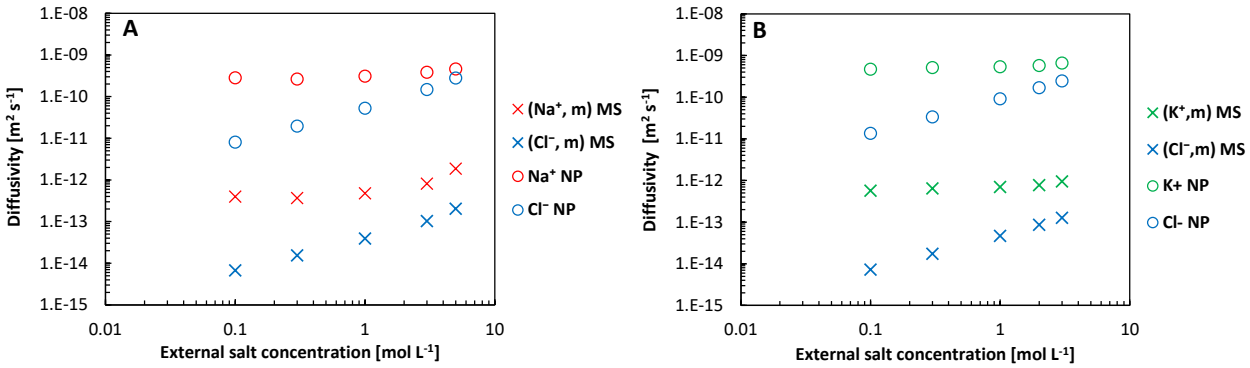

*Figure 49 Corrected ion-membrane Maxwell-Stefan binary diffusivity and Nernst-Planck ionic diffusivities in FKS-50 equilibrated with (**A**) NaCl and (**B**) KCl at various concentration.*

Although the trend of NP and MS diffusivities with the salt concentration is similar, NP ionic diffusivities are orders of magnitude higher than the MS ion-membrane binary-diffusion coefficients. This must be attributed to the fact that NP diffusivities accounts for the overall effect of the interactions exchanged between the mobile-ions and all the other components. Consequently, associating NP solely to the interactions with the fixed charges would lead to gross misestimation of such interactions. This further confirms that the application of the NP model to non-dilute systems is intrinsically misleading, and attributing NP diffusivities solely to the interactions with the fixed-charges is improper.

2.4 Transport phenomena in ion-exchange membranes: conclusions

In the previous Chapter, a thorough revision of fundamental transport models in IEMs was presented. Some of the mostly employed transport models for IEMs were critically examinated. In particular, it was demonstrated that, in a high salinity environment, the Nernst-Planck description of ionic transport lacks of physical meaning, and it may even become unfungible due to its assumptions.

To overcome such limitations, a more rigorous framework based on the Maxwell-Stefan transport theory was proposed.

A series of independent experimental tests were conducted on a commercial CEM aiming at determining information on interactions among components in the membrane phase, in particular the interactions between mobile components and fixed charges.

The proposed physic-mathematical framework allowed the binary diffusivity in the membrane phase for each couple of components at various co-ion concentration to be quantified. Such analysis revealed that the transport properties of IEMs, such as the ionic conductivity, are affected not only by ion-membrane interactions, but also by ion-water interactions, the latter often disregarded in the literature. In addition, it was demonstrated that the ionic conductivity of the IEMs also depends on water-membrane interactions.

Further fundamental research should be carried out to develop fundamental physic-chemical models, for predicting binary interactions in the IEMs, that can provide useful support for the design of next-generation membranes with improved transport properties. To this regard, the proposed framework constitutes a valid benchmark for the validation of such predictive models based on reliable experimental data.

3. *Macroscale modelling and simulations of ion-exchange membranes processes*

In the former Chapters, fundamental thermodynamic and transport models were developed and investigated. These typically describe the behavior of physical systems at the lowest space and time scales considered in chemical process engineering and are of paramount importance to develop accurate and reliable multi-scale models, accounting for multiple physical phenomena occurring in each process at scales. Chemical process engineering largely relies on multi-scale process models, not only to predict the performance of industrial processes but also to guide the choice of the best operating configuration and condition.

The following Chapter is devoted to the development of multi-scale models of electromembrane processes for the valorization of saline streams. In particular, two case studies are examined in sections 3.1 and 3.2: the modeling of an electromembrane unit for the recovery of lithium from a geothermal brine and the modelling of an integrated process for the valorization of a seawater bittern.

3.1 Case study 1: Lithium recovery from seawater via Lithium-selective Membrane Flow Capacitive De-Ionization

The present section is adapted from a previously published paper [174].

As one of the most sought-after commodities worldwide, lithium plays a crucial role in modern industry. The rapid expansion of the Li-ion battery market has dramatically increased the global demand for lithium, which is projected to reach 2.43 million tons per year by 2030 [175]. However, conventional lithium production relies heavily on environmentally harmful mining practices, and its trade is highly sensitive to geopolitical instabilities, as only a few countries, mainly Australia, Argentina, and China, hold the largest global reserves [176].

To alleviate the pressure on natural lithium resources and satisfy the growing market demand, new and unconventional lithium sources are currently being explored. Among these, geothermal brines and seawater bitterns, naturally enriched in lithium, are promising and environmentally sustainable alternatives [78,177,178]

The exploitation of all these potential sources requires efficient processes capable of fractionating complex, multi-ionic solutions. Despite significant research efforts, a scalable, selective, and environmentally benign method for lithium recovery is still lacking. The main challenge lies in the selective extraction of lithium ions from brines that contain much higher concentrations of chemically similar cations, such as sodium, potassium, and magnesium [179].

Electro-driven separation technologies, such as ED and Capacitive De-Ionization (CDI) have recently attracted growing attention for the selective recovery of valuable raw materials from concentrated brines [72,180]

Among electrochemical separation techniques, Flow Capacitive De-Ionization (FCDI) [181–183] has emerged as a promising alternative to conventional CDI. In FCDI, extensive experimental work has been devoted to improving process efficiency and optimizing operational parameters [184,185]. The key difference between CDI and FCDI lies in the electrode design. In both systems, ions migrate from the bulk solution toward the electrode compartments, where they are adsorbed within the porous electrode structures that act as electrochemical capacitors. However, in traditional CDI, fixed porous electrodes are employed, making the process inherently non-continuous: once saturated, the electrodes must be regenerated through short-circuiting or polarity reversal to release the adsorbed ions [186].

FCDI overcomes this limitation by replacing fixed electrodes with flowing slurries composed of carbon-based particles circulated through channels embedded in the current collectors [187]. The carbon slurry can be externally regenerated and recirculated, enabling continuous operation and improved process stability.

In 2023, Saif et al. [188] introduced a novel configuration of FCDI, termed Lithium Membrane Flow Capacitive Deionization (Li-MFCDI), in which a Lithium-Selective Membrane (LiSM) was incorporated to selectively recover lithium from synthetic multi-ionic geothermal brines. containing Li^+ together with competing cations such as Na^+, K^+, and Mg^{2+}. Despite these promising outcomes, the influence of key operating parameters, such as applied voltage and electrode flow rate, on process performance was not further investigated, leaving significant room for optimization in terms of energy efficiency and separation selectivity.

In the following sections, we propose a simple yet robust model for the Li-MFCDI process, emphasizing the multi-ionic transport phenomena across ion-exchange membranes, which are central to lithium selectivity. The model is designed to be flexible and applicable to saline streams of varying compositions. First, the governing equations and assumptions are presented. Then, simulation results are compared with the experimental data reported by Saif et al.[188] to validate the model. Finally, a parametric study is conducted to evaluate the influence of key operating variables on process performance, considering three lithium-selective membranes: the glass-ceramic Ohara AG-01, the monovalent-selective polymeric Selemion CSO, and an idealized LiSM combining the best properties of both.

3.1.1 Unit description & process configuration

The Li-FCDI unit consists of four distinct compartments: two central compartments (feed and receiver) with identical volumes of 10.75 mL, and two outer electrodic compartments, which were machined directly into graphite plates. The feed and receiver compartments are separated by a LiSM with an effective active area of 10.75 cm^2, while the electrodic compartments are isolated from the solution chambers by AEMs. The main geometrical characteristics of the cell are summarized in Table 12.

Table 12 Geometrical properties of Li-MFCDI unit

Property	Electrode channel (el)	Solution channels (s)
Width - d [cm]	0.2	3.7
Height - h [cm]	0.2	1.0
Length - L [cm]	27.5	3.7*

**Solution channels are circular; thus, the length corresponds to the width (diameter) of the channels*

The LiSM employed in the experimental campaign is the commercial lithium-conductive glass-ceramic membrane AG-01 (Ohara Corporation, Japan). The AEMs used (FAB-PK-130, Fumatech BWT, Germany) are dense, mechanically reinforced polymeric membranes with high proton-blocking capability, commonly adopted in ED and EDBM processes [5]. The key properties of the IEMs used in this study are reported in Table 13.

Table 13 Relevant properties of FAB-PK-130 and Ohara AG-01 membranes.

	δ [μm]	R [Ω cm^2]	w_u [g_w g^{-1}_{dry}]	IEC [mmol g^{-1}_{dry}]	C_{fix} [mmol g^{-1}_w]
FAB-PK-130	125±15[189]	7±2[190]	0.1±0.05[190]	0.85±0.015[190]	5[189]
OHARA AG-01	250[188]	12900*	-	-	-

* The value was fitted from experimental data

The values of membrane areal resistance and ionic conductivity reported in Table 13 are taken from the manufacturer's technical datasheet. The experiments were conducted in a closed-loop configuration over a period of seven days, under an applied external potential of 1.2 V. The initial compositions of the feed, receiver, and flow-electrode compartments are summarized in Table 14.

Table 14 The initial composition of feed, receiver and flow electrodes. The flow electrode is a 10 wt. % slurry of YP50F activated carbon.

	NaCl [g L^{-1}]	KCl [g L^{-1}]	LiCl [g L^{-1}]	$MgCl_2$ [g L^{-1}]	HCl [g L^{-1}]
FEED	26.170	0.195	0.096	0.196	0
RECEIVER	0	0	0	0	3.646
FLOW ELECTRODE	1.000	0	0	0	0

Based on the circulation pathway of the flow electrodes, FCDI systems can be operated in different configuration. In this work, the Single Cycle (SC) configuration (Figure 46), was adopted. In the SC configuration, the flow electrodes are circulated in a closed loop between the cathodic and anodic compartments. and charging and discharging phases, corresponding respectively to the electro sorption and desorption of charged species within the Electric Double Layers (EDLs) of the carbon particles, occur simultaneously in the electrode compartments. This simultaneous operation minimizes electrostatic energy dissipation and thereby enhances the overall energy efficiency of the process [184–186]. The feed and receiver solutions were recirculated externally in separate reservoirs under a closed-loop configuration, as shown in Figure 50. During operation, the feed solution becomes progressively depleted in Li^+ ions, which migrate across the LiSM toward the receiver compartment. The total volumes and flow rates of all solutions employed in the experiments are summarized in Table 15.

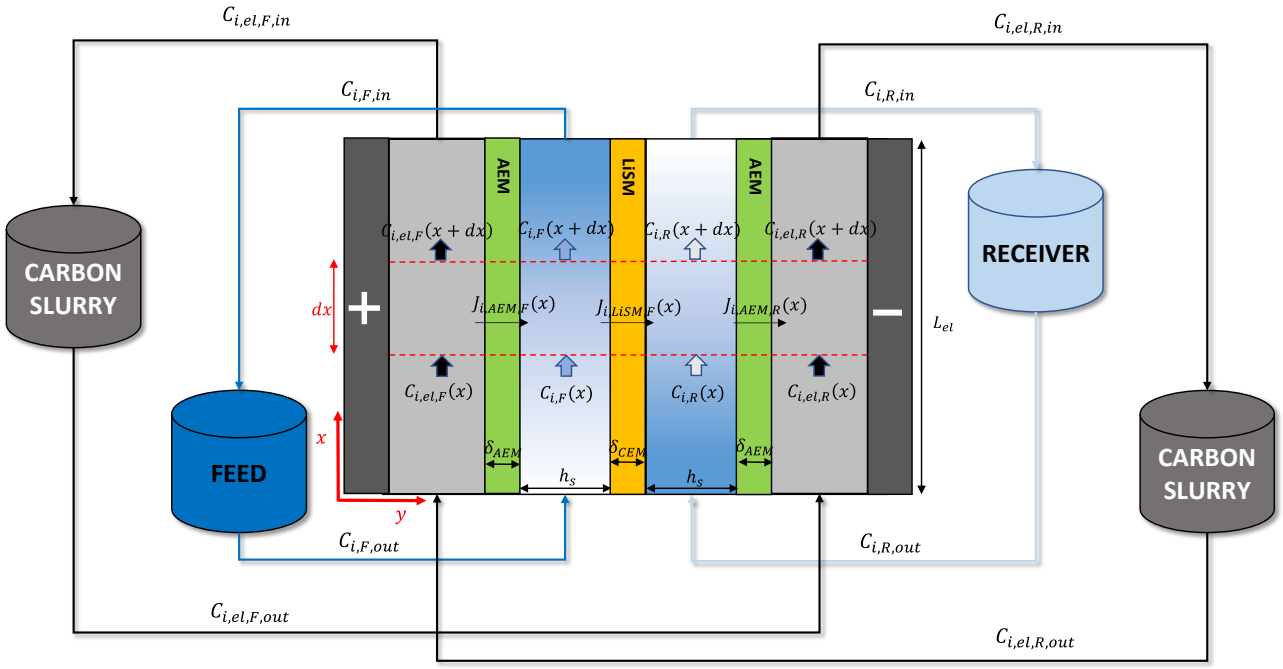

Figure 50 Schematic representation of the Li-MFCDI cell with SC configuration.

Table 15 Feed, Receiver and flow electrode flow rates and total volume

	Feed	Receiver	Flow electrodes
V [L]	2	0.2	0.25
Q [mL min^{-1}]	10	10	100

3.1.2 Multi-scale process model of the Li-MFCDI unit

The Li-MFCDI unit is modelled through a one-dimensional (1D) pseudo–steady-state framework with distributed parameters along the flow direction (x-axis in Figure 50). Although the experimental configuration operates in closed-loop mode, thus being intrinsically unsteady, the transient dynamics of the cell is assumed negligible compared to those of the external reservoirs. Consequently, all process variables within the Li-MFCDI cell are treated as time-invariant.

Water transport across the membranes in the y-direction is neglected, as no measurable variation in the external solution volumes was observed experimentally. Diffusive fluxes superimposed on the convective flow along the x-direction are also disregarded, and constant fluid density is assumed. Furthermore, non-ideal thermodynamic phenomena are disregarded, and no Faradaic reactions are considered to occur within the electrode compartments.

3.1.2.1 Mass balance in channels

To determine the concentration profiles along the flow channels, species mass balances are formulated for each compartment. The cell is discretized into 100 elements along the x-direction, and differential mass balances are applied to each element as follows:

$$Q_F \cdot \frac{dC_{i,F}}{dx} = \left(N_{i,F}^{AEM} - N_i^{LiSM}\right) \cdot d_{el} \tag{3.1}$$

$$Q_R \cdot \frac{dC_{i,R}}{dx} = \left(N_i^{LiSM} - N_{i,R}^{AEM}\right) \cdot d_{el} \tag{3.2}$$

$$(1 - \varsigma_{el}) \cdot Q_{el} \frac{dC_{i,el,F}}{dx} = -N_{i,F,diff}^{AEM} \cdot d_{el} \tag{3.3}$$

$$(1 - \varsigma_{el}) \cdot Q_{el} \frac{dC_{i,el,R}}{dx} = N_{i,R,diff}^{AEM} \cdot d_{el} \tag{3.4}$$

where $C_{i,F}$ and $C_{i,R}$ are the molar concentrations (mol m^{-3}) of the species i respectively in the feed and receiver channels at the generic x position; $C_{i,el,F}$ and $C_{i,el,R}$ denote the concentrations in the electrodic compartments respectively facing the feed and receiver compartments; Q_F, Q_R and Q_{el} represent the volumetric flow rates (m^3 s^{-1}) of the feed, receiver and flow electrodes streams, respectively; d_{el} is the electrode-channel width, and ς_{el} is the volumetric fraction of suspended solids in the flow electrodes.; $N_{i,F}^{AEM}$ and $N_{i,R}^{AEM}$ are the total ionic fluxes (mol m^{-2} s^{-1}) of the i-th species across the AEMs adjacent to the feed and receiver compartments, while $N_{i,F,diff}^{AEM}$ and $N_{i,R,diff}^{AEM}$ denote their diffusive components. N_i^{LiSM} represents the ionic flux across the LiSM. The active mass-transfer surface, corresponding to the AEM-facing area of the electrode channels, was assumed uniformly distributed along the flow direction, neglecting the effect of electrode-path tortuosity for simplicity.

The right-hand sides of Equations (3.1) and (3.2) account for all ionic transport mechanisms through the IEMs, including diffusion and migration, whereas in Equations (3.3) and (3.4) only diffusive contributions are considered. Since no Faradaic processes occur, the conductive flux component is assumed to be fully electro-sorbed within the carbon particles' electric double layers (EDLs), thus not altering the bulk ionic concentration in the electrode solution.

These governing equations are solved for each ionic species and channel to compute the concentration profiles within the Li-MFCDI unit, given appropriate boundary conditions and flux expressions across the membranes, with this latter depending on the kind of IEM considered.

3.1.2.2 Transport equations

The LiSM employed in the experimental campaign is a glass–ceramic membrane consisting of an amorphous glassy matrix in which lithium-ion–conductive crystalline particles are dispersed. The ion transport mechanism in this type of LiSM follows the so-called *vacancy diffusion* or *hopping* mechanism [191]. Within the membrane, which behaves as a solid-state ionic conductor, mobile ions migrate by jumping between adjacent lattice sites under the influence of an applied electric field. The transport rate of each ionic species depends on its activation energy for hopping, which in turn is governed by the ionic radius and the size of the lattice cavities [192].

The lithium selectivity of the LiSM arises from the specific size of the vacancies in the crystal lattice, which are designed to closely match the ionic radius of lithium. This structural compatibility lowers the activation energy for lithium hopping compared to other cations, thereby enhancing Li^+ transport. Conventional diffusion through the membrane is assumed negligible due to the extremely low diffusivities typical of glassy materials. Consequently, the ionic transport across the LiSM can be described as purely conductive and expressed by the following relationship:

$$N_i^{LiSM} = \frac{t_i^{LiSM} \cdot J}{z_i \mathcal{F}} \tag{3.5}$$

Where t_i^{LiSM} denotes the transport number of ion $i$within the LiSM, which was calibrated against experimental data.

In contrast, ionic transport through the anion-exchange membranes (AEMs) was modelled according to the ideal Nernst–Planck (NP) framework (see section 2.1.2). Assuming a linear concentration profile within the membrane, Eq. (5.30) can be rewritten as:

$$N_i^{AEM} = N_{i,diff}^{AEM} + N_{i,cond}^{AEM} = -\sum_{j=1}^{n} D_{i,j}^{AEM} \frac{\left(C_j^{AEM,-} - C_j^{AEM,+}\right)}{\delta_{AEM}} + \frac{t_i^{AEM} \cdot J}{z_i \mathcal{F}} \tag{3.6}$$

where N_i^{AEM} is the total ionic flux of the i-th species across the AEM, $N_{i,diff}^{AEM}$ and $N_{i,cond}^{AEM}$ are the diffusive and conductive components of the total flux, t_i^{AEM} is the average transport number in membrane, δ_{AEM} is the membrane thickness, $C_j^{AEM,-}$ and $C_j^{AEM,+}$ are the molar concentrations of the j-th species in membrane respectively at the right and left interfaces and $D_{i,j}^{AEM}$ are the cross-diffusion coefficients defined in eq. (2.31).

The transport numbers in AEMs, t_i^{AEM}, can be related to the diffusivities and average concentrations of the mobile species within the membrane by:

$$t_i^{AEM} = \frac{z_i^2 D_i^{AEM} \bar{C}_i^{AEM}}{\sum_j z_j^2 D_j^{AEM} \bar{C}_j^{AEM}} \tag{3.7}$$

where $\bar{C}_i^{AEM}$ is the average concentration of species $i$within the membrane. Equation (3.7) can also be applied to bulk solutions by replacing the diffusivities and concentrations in the membrane with those in the liquid phase. To apply eq. (3.6), the equilibrium concentrations of the mobile species at both membrane–solution interfaces must be determined. Assuming ideal behaviour for all phases, such equilibrium concentrations can be estimated from the composition of the solution at the membrane interface using the ideal Donnan model (see section 1.1.4.2). A qualitative representation of the concentration and potential profiles across a generic AEM is shown in Figure 51.

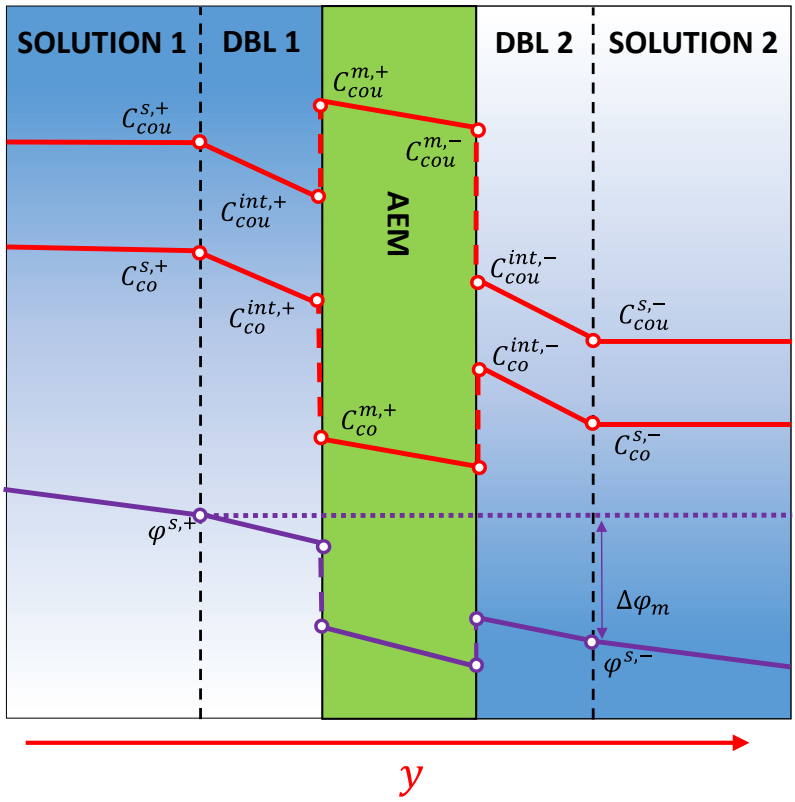

Figure 51 Qualitative representation of concentration and potential profile across a generic AEM. The superscript + and – denote, respectively, the left and right side of the membrane, according to the chosen y direction. The subscripts "cou" and "co" refer to a generic counter-ion and co-ion in a multi-ionic solution. The superscript s, m and int refer to, the bulk solution, membrane phase and solution-membrane interface, respectively.

3.1.2.3 Concentration polarization phenomena

Interfacial concentrations typically deviate from bulk concentrations due to concentration polarization effects (see also section 2.2.2) [45,193], These effects can be quantified through the polarization coefficients, defined in eq. (2.105)

In the conventional approach (eq. (2.106)), polarization coefficients are evaluated by performing a steady-state mass balance across theDBL, where salt diffusion is described by Fick's law using an average diffusion coefficient [194]. Although this method is adequate for single-salt systems, it becomes cumbersome and less accurate in multi-ionic environments.

A more rigorous formulation can be derived by incorporating the diffusion–conduction form of the Nernst–Planck equation (eq. (2.30)) into the mass balance at the DBL. By neglecting the contribution of diffusive transport through the membrane, typically negligible due to the high permselectivity of the membranes and the relatively low ionic concentrations [193], the following expressions for the polarization coefficients are obtained:

$$\vartheta_i^+ = 1 - \frac{\frac{\left(t_i^m - t_i^{s,+}\right)J}{z_i\mathcal{F}} - \sum_{j\neq i}\frac{D_{i,j}^s}{\delta_{DBL,j}^+}C_j^{s,+}\left(1-\vartheta_j^+\right)}{\frac{D_i^s}{\delta_{DBL,i}^+}C_i^{s,+}} \tag{3.8}$$

$$\vartheta_i^- = 1 + \frac{\frac{\left(t_i^m - t_i^{s,-}\right)J}{z_i\mathcal{F}} - \sum_{j\neq i}\frac{D_{i,j}^s}{\delta_{DBL,j}^-}C_j^{s,-}\left(1-\vartheta_j^-\right)}{\frac{D_i^s}{\delta_{DBL,i}^-}C_i^{s,-}} \tag{3.9}$$

In the previous equation, the superscripts + and - denote the left and the right sides of the IEM corresponding to the direction of current density, t_i^s and t_i^m re the ionic transport numbers in the bulk solution and in the membrane, respectively, while $\delta_{DBL,i}$ is the DBL thickness.

The main difference between this formulation and the traditional one lies in the additional term in the numerator, which accounts for the electrical coupling between the ionic fluxes, an effect that becomes particularly relevant in concentrated or multi-ionic systems. Equations (3.8) and (3.9) can be written for each ionic species, yielding a linear system that can be solved to evaluate the polarization coefficients at both membrane interfaces.

In the absence of turbulence promoters and for non-fully developed flow conditions, the DBL thickness can be estimated using Leveque's correlation (2.107) [164,165]. This correlation is

applicable to the feed and receiver channels but not to the electrode compartments. In the latter, the complex geometry and flow structure, combined with the non-Newtonian nature of flow electrodes, would require dedicated CFD analyses to derive Sherwood number correlations for estimating $\delta_{DBL,i}$.

Nevertheless, according to the correlation proposed by Rommerskirchen et al. [182], the DBL thickness in the electrode compartments is less than 3% of that in the feed and receiver channels. Therefore, under the present operating conditions, concentration polarization in the electrode compartments can be considered negligible compared to that occurring in the solution channels. As a result, only polarization phenomena in the feed and receiver channels are accounted for in this study.

3.1.2.4 Circuital equations

To evaluate the ionic fluxes (equations (3.5) and (3.6)) and solve the mass balances in each compartment, the current density associated with the conductive term of the fluxes must be determined. Owing to the distributed nature of the model, the current density profile along the x-direction can be obtained by solving an equivalent distributed electrical circuit, where each electrical element (i.e., resistances, capacitances, and electromotive forces) corresponds to one physical component of the unit cell (i.e., membranes, electrodes, and solution channels). A qualitativerepresentation of the potential profile inside the cell and the corresponding equivalent circuit elements is shown in Figure 52.

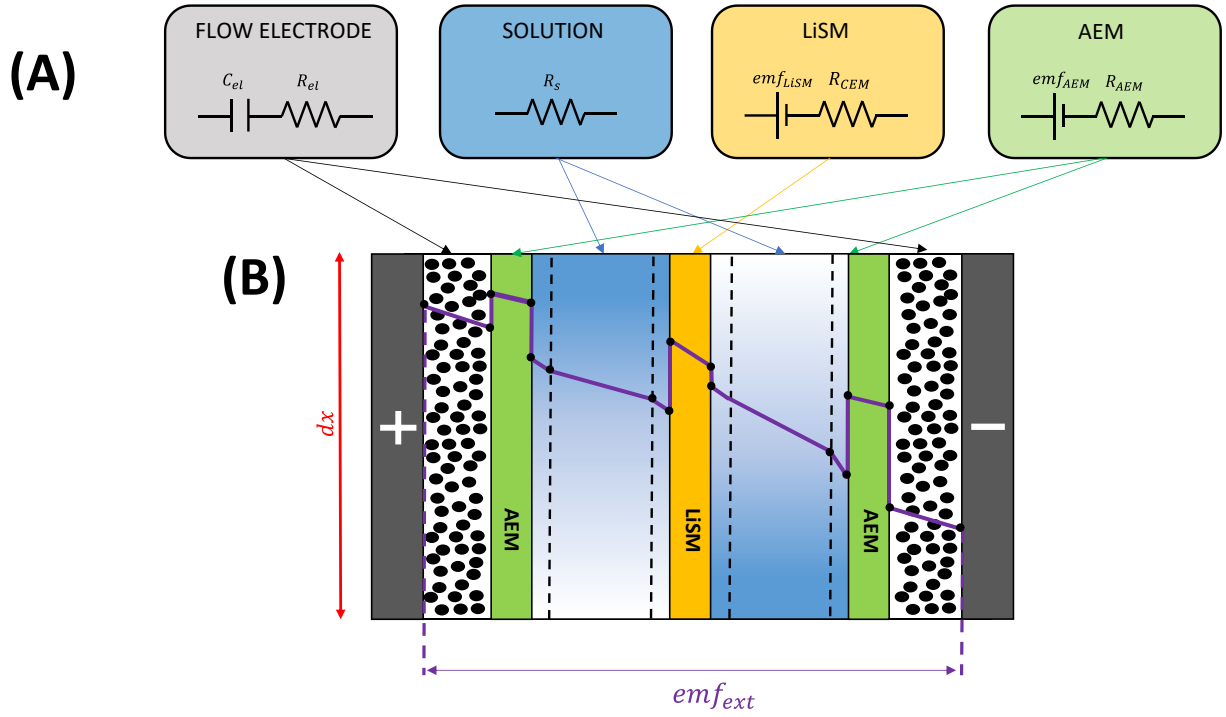

*Figure 52 (**A**) Equivalent electrical components for flow electrodes, ion-exchange membranes and solutions. (**B**) Qualitative potential profile across the electrodes*

Assuming that the current collectors behave as equipotential surfaces, the overall equivalent circuit can be represented as a distributed parallel circuit composed of multiple branches, each subjected to the same applied voltage, as illustrated in Figure 53. Consequently, unless otherwise specified, all the electrical variables introduced hereafter are distributed along the x-direction.

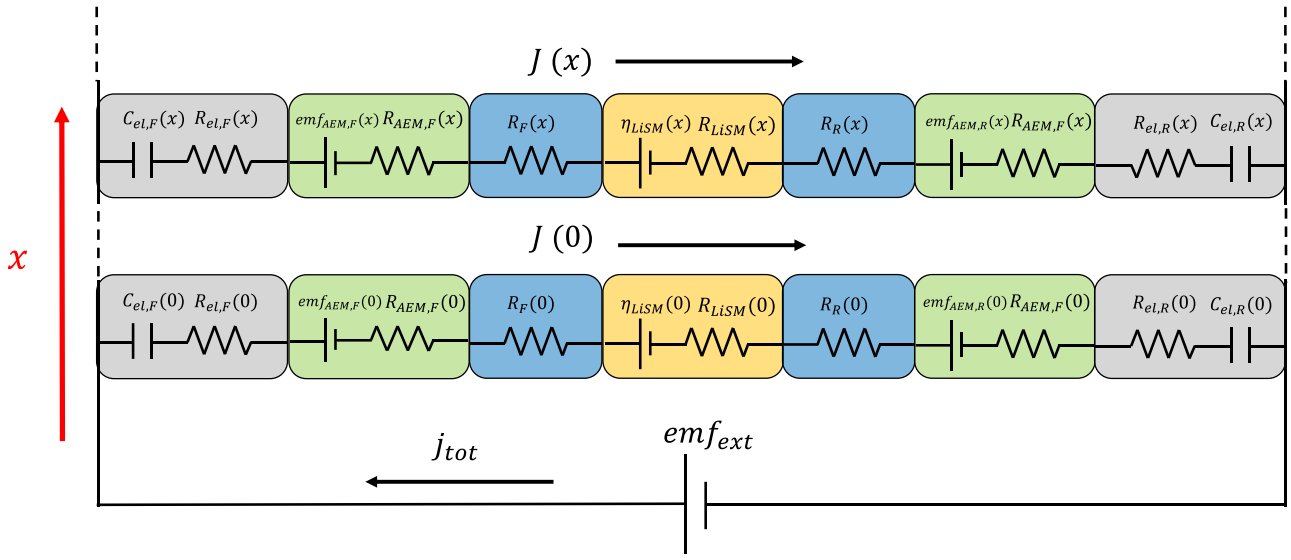

Figure 53 Equivalent electrical circuit of the Li-MFCDI cell, with the x-direction discretisation of all variables.

For the flow electrodes, several equivalent circuit models have been proposed to describe the electrical response associated with the porous carbon particles [195]. According to the so-called

vertical ladder model, which applies to systems containing particles with a non-uniform pore size distribution and operating at low current frequencies, the flow electrodes can be conveniently represented as a parallel network of resistors and capacitors in series (as depicted in Figure 53), This model typically reproduces the capacitance values reported by the manufacturer for the specific carbon material [196,197].

The potential drop across each flow electrode can thus be expressed as:

$$\Delta\varphi_{el} = \frac{\sigma_{el}}{C_{el}} + R_{el}J \tag{3.10}$$

where C_{el} is the specific capacitance of the carbon particles per unit of mass, σ_{el} is the charge density accumulated on the carbon particles at the generic x position, and R_{el} is the equivalent areal resistance.

The resistive behaviour of the flow electrodes arises from multiple factors, including the carbon loading, salt concentration, flow rate, and the intrinsic properties of the carbon material. The equivalent conductivity adopted in this work was measured by Porada et al. [198] for a carbon slurry of similar composition to the one used in this study (10% YP50F in 1 g L^{-1} NaCl) for a carbon slurry of similar composition (10 wt.% YP50F in 1 g L^{-1} NaCl). This conductivity primarily reflects the electronic conductivity of the carbon particles, which represents the dominant contribution to the total areal resistance. Following their approach, the equivalent resistance of the flow electrodes can be expressed as:

$$R_{el} = \frac{h_{el}}{\kappa_{el}} \tag{3.11}$$

where h_{el} is the electrodic channel depth, and κ_{el} is the carbon slurry equivalent conductivity, assumed constant. The physical properties of the slurry were taken from literature sources and are summarized in Table 18.

The electrical behaviour of the membranes can be modelled as a series combination of a resistance and an electromotive force. Accordingly, the total potential drop across a membrane can be written as:

$$\Delta\varphi_m = R_m J - emf_m \tag{3.12}$$

where R_m is the membrane areal resistance, while emf_m represents the membrane electromotive force, arising from the concentration gradient between the adjacent solutions. Here, the subscript m denotes to a generic membrane, including the LiSM.

Assuming ideal thermodynamic behaviour, linear concentration profiles within the membrane, and average ionic transport numbers, $\Delta\varphi_N$ and $\Delta\varphi_P$ can be evaluated using the Nernst equation [7]:

$$emf_m = -\Delta\varphi_N - \Delta\varphi_P = -\frac{R_g T}{\mathcal{F}} \sum_i \frac{t_i^m}{z_i} ln\left(\frac{C_i^{s,-}}{C_i^{s,+}}\right) - \frac{R_g T}{\mathcal{F}} \sum_i \frac{t_i^m}{z_i} ln\left(\frac{\theta_i^-}{\theta_i^+}\right) \tag{3.13}$$

Where $\Delta\varphi_N$ and $\Delta\varphi_P$ are the bare Nernst contribution (i.e., without concentration polarization) and the polarization contribution. Although emf_m is formally defined as an electromotive force, its sign depends on the concentration difference between the two adjacent compartments, and it may act as a net voltage drop in case of a negative sign.

The feed and receiver channels behave as simple ohmic resistors and can be described through Ohm's law:

$$\Delta\varphi_s = \frac{h_s}{\kappa_s} J \tag{3.14}$$

Where h_s is the height of the solution channels (see Table 12) and κ_s is the conductivity of the solution evaluated as a function of the solution composition by applying the McCleskey model [199].

The current density in each branch of the equivalent circuit can be obtained by applying Kirchhoff's second law, which states that the sum of voltage drops along each branch equals the applied electromotive force emf_{ext}:

$$emf_{ext} = \sum_i \Delta\varphi_i = \Delta\varphi_{el,F} + \Delta\varphi_{AEM,F} + \Delta\varphi_F + \Delta\varphi_{LiSM} + \Delta\varphi_R + \Delta\varphi_{AEM,R} + \Delta\varphi_{el,R} \tag{3.15}$$

By substituting eq. (3.10)-(3.14) into eq. (3.15) and rearranging terms, one obtains:

$$emf_{ext} = \frac{\sigma_{el,F} + \sigma_{el,R}}{C_{el}} + R_{tot}J + \Delta\varphi_{N,tot} \tag{3.16}$$

where R_{tot} is the sum of areal resistances of flow electrodes, membranes and solutions, $\Delta\varphi_{N,tot}$ is the total non-ohmic potential contribution. The charge densities accumulated on the carbon particles at the front and rear electrodes, $\sigma_{el,F}$ and $\sigma_{el,R}$ are related to the current density through the charge balance equation:

$$J = -\frac{Q_{el}w_{el}}{d_{el}}\frac{d\sigma_{el,F}}{dx} = \frac{Q_{el}w_{el}}{d_{el}}\frac{d\sigma_{el,R}}{dx} \tag{3.17}$$

where w_{el} is the mass concentration of the suspended activated carbon. Equations (3.16) and (3.17) form a system of ODEs that can be solved numerically, together with the mass balances and transport equations, to determine the charge and current density profiles along the flow direction. Finally, the total current can be obtained by integrating the local current density:

$$j_{tot} = \int_0^{L_{el}} J d_{el} dx \tag{3.18}$$

3.1.2.5 Mass balance in tanks

The set of equations presented in the previous sections can be solved to obtain the steady-state concentration and current density profiles inside the cell. However, the lithium recovery process is intrinsically non-stationary, as in the closed-loop configuration, the concentration of each species in the storage tanks changes over time. The following mass and charge balances are then applied to the tanks to evaluate the change in concentration of each species and charge density onto the carbon particles over time:

$$V_F \frac{dC_{i,F,out}}{dt} = Q_F\left(C_{i,F,in} - C_{i,F,out}\right) \tag{3.19}$$

$$V_R \frac{dC_{i,R,out}}{dt} = Q_R\left(C_{i,R,in} - C_{i,R,out}\right) \tag{3.20}$$

$$\frac{V_{el}}{2} \frac{dC_{i,el,F,out}}{dt} = Q_{el}\left(C_{i,el,F,in} - C_{i,el,F,out}\right) \tag{3.21}$$

$$\frac{V_{el}}{2} \frac{dC_{i,el,R,out}}{dt} = Q_{el}\left(C_{i,el,R,in} - C_{i,el,R,out}\right) \tag{3.22}$$

$$\frac{V_{el}}{2} \frac{d\sigma_{el,F,out}}{dt} = Q_{el}\left(\sigma_{el,F,in} - \sigma_{el,F,out}\right) \tag{3.23}$$

$$\frac{V_{el}}{2} \frac{d\sigma_{el,R,out}}{dt} = Q_{el}\left(\sigma_{el,R,in} - \sigma_{el,R,out}\right) \tag{3.24}$$

In the previous equations, V_F, V_R and V_{el} are, the total volume of feed, receiver and carbon slurry, respectively, Q_F, Q_R and Q_{el} are their volumetric flow rates, while $C_{i,F,out}$, $C_{i,R,out}$, $C_{i,el,F,out}$ and $C_{i,el,R,out}$ are the ionic concentrations of the i-th species in the solutions and electrodic tanks, corresponding to the inlet concentration in the unit (i.e. concentration evaluated at $x = 0$), $C_{i,F,in}$, $C_{i,R,in}$, $C_{i,el,F,in}$ and $C_{i,el,R,in}$ are the tanks' inlet concentrations, corresponding to the outlet concentrations from the unit (i.e., evaluated at $x = L$), $\sigma_{el,F,out}$ and $\sigma_{el,R,out}$ are the charge densities accumulated onto the carbon particles in the two electrodic tanks, corresponding to the inlet charge densities in the two electrodic compartments, while $\sigma_{el,F,in}$ and $\sigma_{el,R,in}$ are the tanks' inlet charge densities, corresponding to the charge densities accumulated at the outlet of the unit's electrodic compartments.

3.1.2.6 Results and discussion

To apply the model presented in the previous sections, the transport numbers in the LiSM and the ionic diffusivities in the AEMs, which are specific properties of the membrane/ionswere determined through a fitting procedure based on the experimental time–concentration profiles measured in the receiver tank. Conversely, the areal resistance of the Ohara AG-01 membrane was directly derived from the experimental current–voltage curve. The input membrane parameters are summarized in Table 13 whereas the optimized fitting parameters are listed in Table 16.

For comparison purposes, the model was also used to predict the process performance employing different types of LiSMs. The properties of the LiSMs considered for comparison are summarized in Table 17.

Table 16 FAB-PK-130, Ohara AG-01, Selemion CSO and Ideal LiSM parameters obtained from experimental data fitting.

	Na^+	K^+	Li^+	H^+	Mg^{2+}	Cl^-
D_i^{AEM} [$m^2 s^{-1}$]	0	0	0	6.7E-10	0	1.12E-10
t_i^{AG-01}	0.400	0.009	0.310	0	0.041	0.240
t_i^{CSO}	0.989	0.006	0.004	0	0.001	0
$t_i^{IDEAL\ LiSM}$	0.319	0.322	0.273	0	0.086	0

Table 17 Properties of the Selemion CSO and of the ideal LiSM. For the sake of comparison, the main properties of the Ohara membrane (already reported in Table 13) are reported below as well.

	δ_{iem} [μm]	κ_{iem} [mS cm^{-1}]	R_{iem} [Ω cm^2]	w_u [$g_w\ g_{dry}^{-1}$]	IEC [mmol g_{dry}^{-1}]	C_{fix} [mmol g_w^{-1}]
SELEMION CSO	100	4.35	2.3	0.2-0.25	2	8.9
IDEAL LiSM	100	4.35	2.3	0.2-0.25	2	8.9
OHARA AG-01	250	0.1	250	-	-	-

Transport parameters for the comparison LiSMs were similarly obtained from the experimental data reported by Nie et al. [200] and are provided in Table 16. Further discussion about the fitting procedure can be found elsewhere [163].

3.1.2.7 Model validation

The model was validated against experimental data previously reported for a Li-MFCDI unit employing the Ohara AG-01 membrane, under the operating conditions summarized in Table 14 and Table 15. The applied voltage was 1.2 V, and the main results are presented in Figure 54. Since the feed volume was ten times larger than that of the receiver, no appreciable concentration variation occurred in the feed tank after seven days; thus, only the receiver concentration profiles are shown.

As illustrated in Figure 54A, the model accurately reproduces the experimental data, confirming its reliability. The concentration profiles in the receiver tank are nearly linear, indicating that ion transport across the LiSM is predominantly driven by conduction rather than diffusion. Consequently, the slope of each profile reflects the transport number of the corresponding ionic species: the steeper the slope, the higher the ionic transfer through the membrane. Given the dense, non-porous nature of the ceramic LiSM, purely diffusive transport is expected to be strongly hindered. Hence, the model successfully captures the conductive ion transport and quantitatively predicts the receiver concentration evolution.

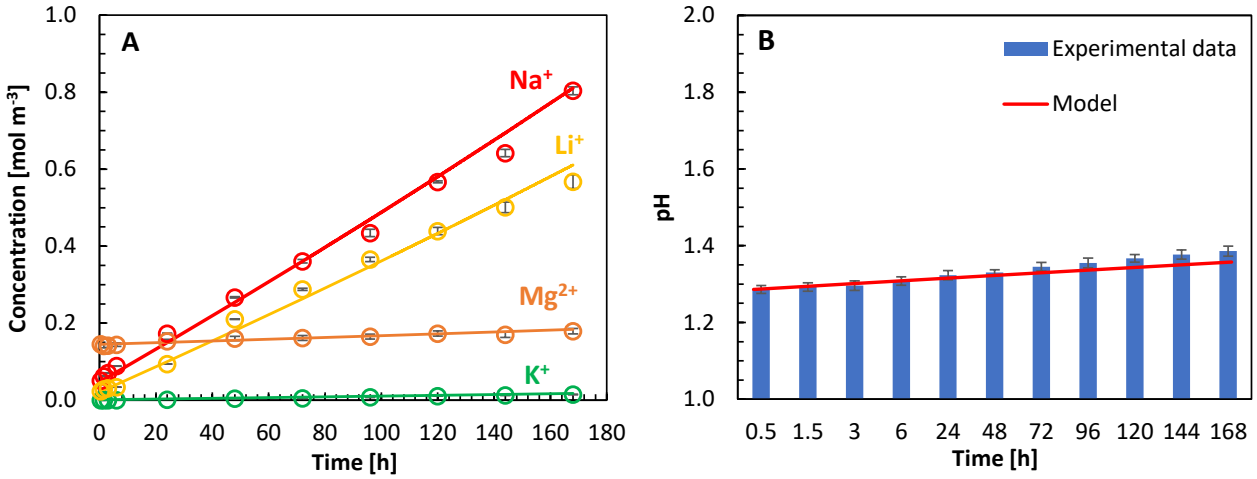

*Figure 54 (**A**) Concentration of species in the receiver tank vs time. The empty circle represents the experimental data while the solid lines represent the model prediction. (**B**) Receiver compartment pH versus time. The blue columns represent the experimental data while the solid red line represents the model prediction. Membrane: Ohara AG-01.*

The pH evolution in the receiver compartment was also monitored, as shown in Figure 54B. As the receiver contained 0.1 M HCl, protons could, in principle, migrate through the adjacent membranes via diffusion or migration. The model captures the slight pH increase observed experimentally; however, the change remains negligible ($\Delta H^+ < 0.01$ M after 7 days). Since proton diffusion through the LiSM is largely suppressed, this small variation must arise from proton transfer across the adjacent AEM. Nonetheless, the FAB-PK-130 AEM is known for its excellent proton-blocking capability [190], which effectively minimizes H^+ crossover. Consequently, under the present conditions, the use of HCl as a supporting electrolyte does not significantly influence the specific energy consumption.

The simulated current under potentiostatic operation remained nearly constant at ~0.05 mA, consistent with the experimental observations. This confirms the stability of the system's electrical behaviour and supports the use of a pseudo-steady-state modelling approach.

To further elucidate the effect of the various resistive components on the overall potential, Figure 55A shows the breakdown of the total voltage drop. The main contribution originates from ohmic losses, while interfacial polarization effects are negligible, an expected outcome given the very low current density (~0.1 A m^{-2}). In agreement with theoretical prediction, polarization phenomena become relevant only at higher current densities. The overall Nernst potential contributes negatively, providing an additional electromotive force to the external voltage. This behaviour results from the adopted configuration, in which the LiSM separates a concentrated feed from a dilute receiver, resembling the operating principle of an Assisted Reverse Electrodialysis (ARED) cell [201].

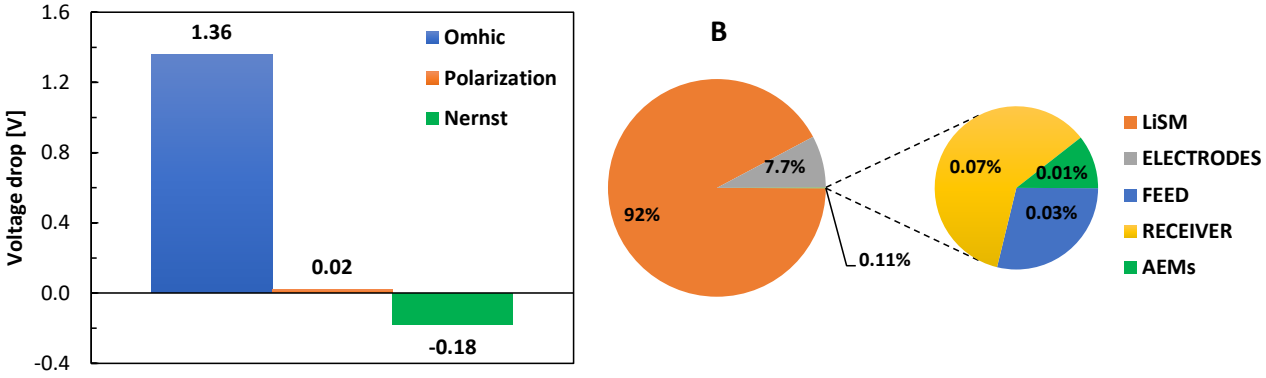

*Figure 55 (**A**) Average voltage drops in the Li-MFCDI unit. (**B**) Ohmic drops percentage contributions. Membrane: Ohara AG-01.*

The capacitive contribution to the total voltage drop is not shown, as the flow electrodes were modelled as ideal capacitors during charge and discharge. Under steady-state conditions and assuming symmetric charge distribution, the net capacitive potential drop is therefore zero, an assumption consistent with previous findings indicating that electrode capacitance has minimal impact in closed-loop configurations [202]. The analysis indicates that system energy losses are primarily governed by ohmic resistances. As shown in Figure 55B, the LiSM accounts for more than 90% of the total areal resistance, owing to the extremely low ionic conductivity of the Ohara AG-01 membrane. Unlike polymeric membranes, this dense ceramic does not absorb water, which drastically limits ion mobility within the membrane phase. The second major contribution arises from the electrical resistance of the electrode compartments, while all other sources are negligible. In conventional FCDI systems, the dilute compartment often contributes significantly to ohmic losses due to its low conductivity; in contrast, the use of a diluted HCl solution in the receiver stream here minimizes such losses, thanks to the high proton mobility.

3.1.2.8 Effect of voltage and flow rates

To assess the influence of the applied voltage and the solution flow rate on the lithium recovery process, a parametric analysis was carried out. Although the model assumes the absence of faradaic reactions at the electrodes, a reasonable approximation as long as the applied potential remains moderate, the effect of the applied voltage on lithium recovery was nevertheless investigated. The performance of the Li-MFCDI unit was evaluated in terms of Specific Energy Consumption (SEC) and Specific Productivity (SP), expressed respectively in kWh kg^{-1} of recovered lithium and kg m^{-2} $year^{-1}$:

$$SEC = \frac{\int_0^{t_{tot}} emf_{ext} \cdot j_{tot} dt}{\Delta C_{Li,R,out} V_r MW_{Li}} \tag{3.25}$$

$$SP = \frac{\Delta C_{Li,R,out} V_r MW_{Li}}{A_m t_{tot}} \tag{3.26}$$

In equations (3.25) and (3.26), $\Delta C_{Li,R,out}$ is the variation of the lithium molar concentration in the receiver tank, MW_{Li} is the lithium mole mass A_m is the membrane area while t_{tot} is the overall test duration. All simulations were conducted over a 7-days period using the same initial concentrations adopted for model validation. The results are shown in Figure 56 A and B.

At 1.2 V and a flow rate of 10 mL·min^{-1}, the estimated SEC was 12.7 kWh·kg$^{-1}_{Li}$, with a SP of 7.9 kg$_{Li}$·m^{-2}·year^{-1} (equivalent to 0.131 mol$_{Li}$·m^{-2}·h^{-1}). According to the simulations, the SEC could be reduced to 2.3 kWh·kg$^{-1}_{Li}$ by lowering the applied voltage to 0.5 V. Conversely, increasing the applied voltage leads to a simultaneous rise in both SEC and SP by approximately 10.6 kWh·kg$^{-1}_{Li}$ and 5.8 kg$_{Li}$·m^{-2}·year^{-1} (0.096 mol$_{Li}$·m^{-2}·h^{-1}) per volt, respectively. This relatively moderate increase, compared to similar systems [203] , arises from the high lithium selectivity of the employed LiSM. Indeed, enhanced selectivity is typically associated with low ionic conductivity and, consequently, reduced ion recovery. In contrast, high ionic conductivity yields higher productivity but lower separation selectivity.

Simulation results indicate that doubling productivity by increasing the applied voltage entails a fourfold rise in SEC. Both SEC and SP increase with voltage due to the linear growth of current density, which enhances ohmic losses and lithium transport simultaneously. The nearly linear trends of SEC and SP are likely an artifact of the ideal selectivity assumption for the AEMs. In reality, SP would tend to level off at higher voltages due to lithium back-diffusion from the receiver to the electrode compartment. Nevertheless, even at 8 V, the maximum lithium recovery remains below 16%, and the corresponding concentration gradient would generate a negligible diffusive flux, given the low lithium concentration in the receiver and the very low partition coefficient of lithium in conventional polymeric IEMs [64,204].

Therefore, assuming ideal AEM behaviour (i.e., no cation diffusion except for H^+) is not expected to cause a significant deviation from experimental results. Finally, although Faradaic reactions are not included in the model, this simplification remains valid since potential electrode reactions are not directly coupled to lithium transport across the LiSM.

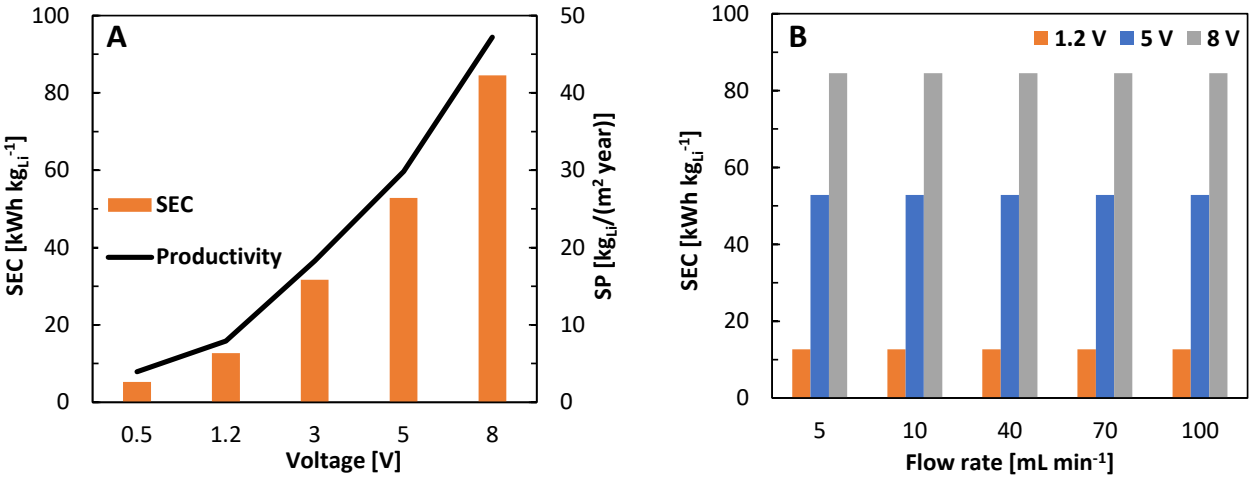

*Figure 56 (**A**) Specific energy consumption (SEC) and lithium Specific Productivity (SP) versus applied voltage at flow rates of 10 mL min^{-1} (See Table 15). (**B**) SEC versus feed and receiver flow rates at different applied voltages*

The effect of the feed and receiver flow rates on lithium recovery performance was also investigated. Simulations were carried out by simultaneously varying the flow rates in both compartments. The resulting SEC values at different flow rates and applied voltages are shown in Figure 56B. According to the model, the SEC is only marginally affected by the flow rate, showing a slight decrease at higher flow rates and voltages. Specifically, increasing the flow rate from 5 to 100 mL min^{-1} reduces the SEC by only 0.8%, a variation that would likely be compensated by the additional pumping power required. Therefore, under the investigated operating conditions, the solution flow rate does not represent an effective optimization variable. This behaviour can be explained by considering that the influence of flow rate on SEC is mainly associated with concentration polarization phenomena, which tend to reduce the effective electromotive force. While improved mixing mitigates polarization effects, these remain negligible under the present low-current-density conditions. Nonetheless, accurate modeling of polarization remains essential, as its impact may become significant when polymeric membranes are employed. Furthermore, since higher flow rates would increase pumping energy demand, operating at high flow rates is ultimately disadvantageous from an energy efficiency standpoint.

3.1.2.9 Effect of flow electrodes' composition

In conventional FCDI systems, the flow electrodes play a crucial role in determining overall process performance. Variations in their composition can significantly influence operation, as different types of activated carbon exhibit distinct conductivities and capacitances depending on factors such as pore size distribution, specific surface area, and intrinsic electronic conductivity [205–207]. To investigate

the effect of flow electrode composition, simulations were carried out using several commercially available activated carbons. The main properties of the flow electrodes considered are summarized in Table 18.

Table 18 Carbon slurry properties (taken from literature). The volumetric fraction of activated carbon in the slurry (ς_{el}) was evaluated from the available data according to the procedure reported elsewhere [163].

Activated Carbon	C_{el} [F g^{-1}]	S_{BET} [m^2 g^{-1}]	ρ_{bulk} [g mL^{-1}]	κ_{el} [mS cm^{-1}]	ς_{el} [-]
YP-50F	28.6 [208]	1692 [208]	0.30 [208]	0.004 [198]	27%
YEC-200D	183.7 [205]	2054 [205]	0.40 [209]	0.016 [185]	22%
Norit SX Ultra	65.0 [210]	1082 [210]	0.32 [211]	0.024 [185]	26%

The simulation results are presented as Productivity vs. SEC curves in Figure 57. For all investigated activated carbons, productivity exhibits a linear relationship with SEC. As a result, the maximum achievable productivity corresponds to the highest attainable SEC, typically determined through a techno-economic analysis. The observed linear trend indicates the absence of significant detrimental phenomena under the investigated operating conditions, except for ohmic losses and diffusive fluxes. At a fixed SEC, the productivity achieved with YEC200D and Norit SX Ultra activated carbons is nearly identical and only slightly higher than that obtained with YP-50F, the material adopted by Saif et al. This improvement can be ascribed to the higher electronic conductivity of these carbons, as reported in Table 18The productivity difference between the reference and comparison materials becomes more pronounced at higher SEC values, as ohmic losses increase with current density. Nonetheless, the maximum difference, observed at 8 V, does not exceed 6%. This limited variation is mainly due to the relatively high resistance of the LiSM used in the system, compared to that of the flow electrodes. The influence of LiSM properties, such as ionic conductivity, will be further analysed in section 3.1.2.10.

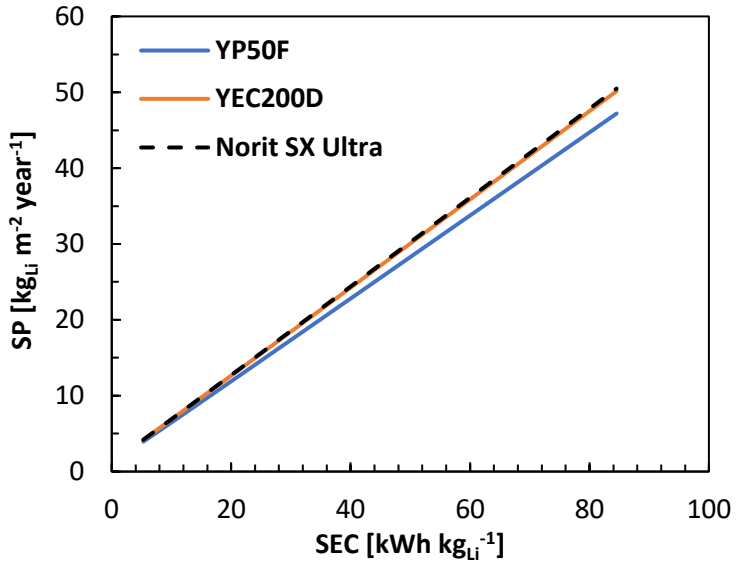

Figure 57 SP versus SEC for different flow electrode compositions. The simulations were performed changing the applied voltage in the range 0.5-8 V.

3.1.2.10 Effect of LiSM properties

Based on the previous analysis, the performance of the Li-MFCDI unit is only marginally affected by the operating conditions and the composition of the flow electrodes. In contrast, it is strongly influenced by the properties of the selected LiSM, particularly by its ionic conductivity. To assess this influence, simulations were performed to compare the performance of the lithium recovery process when different LiSMs were employed.

As a first case, the commercial Selemion CSO membrane was selected. This polymeric cation-exchange membrane (CEM) exhibits a preferential selectivity toward monovalent cations due to a thin positively charged surface layer that hinders the transport of multivalent cations, thereby reducing their partitioning coefficient through Donnan exclusion

[13,180]. The main properties of this membrane are reported in Table 13. To further elucidate the dependence of process performance on the LiSM properties, additional simulations were carried out using an *ideal* LiSM, characterized by the same ionic conductivity as the polymeric Selemion CSO membrane but with a lithium selectivity comparable to that of the Ohara AG-01 membrane. As previously discussed, the main limitation of the Ohara AG-01 membrane lies in its relatively low ionic conductivity, which markedly restricts the specific productivity.

The transport properties of both the Selemion CSO and the ideal LiSM were derived from literature data on lithium-selective recovery from multi-ionic solutions using an ED set-up [200], following the procedure described elsewhere [163]. The corresponding transport numbers are reported in Table 16.

To quantify the effect of LiSM transport properties on the lithium recovery process, a separation selectivity $S_{Li,i}^{p}$ was defined as follows:

$$S_{Li,i}^{p} = \frac{C_{Li,r,out}(t_{tot}) \Big/ C_{Li,f,out}(0)}{C_{i,r,out}(t_{tot}) \Big/ C_{i,f,out}(0)} \tag{3.27}$$

In equation (3.27), $C_{Li,f,out}(0)$ and $C_{i,f,out}(0)$ represent, respectively, the initial concentrations of lithium and of the generic ionic species i in the feed tank at the beginning of the test, while $C_{i,r,out}(t_{tot})$ and $C_{i,r,out}(t_{tot})$ correspond to their concentrations in the receiver tank at the end of the test. The process selectivity values obtained for the three LiSMs investigated are reported in Figure 58.

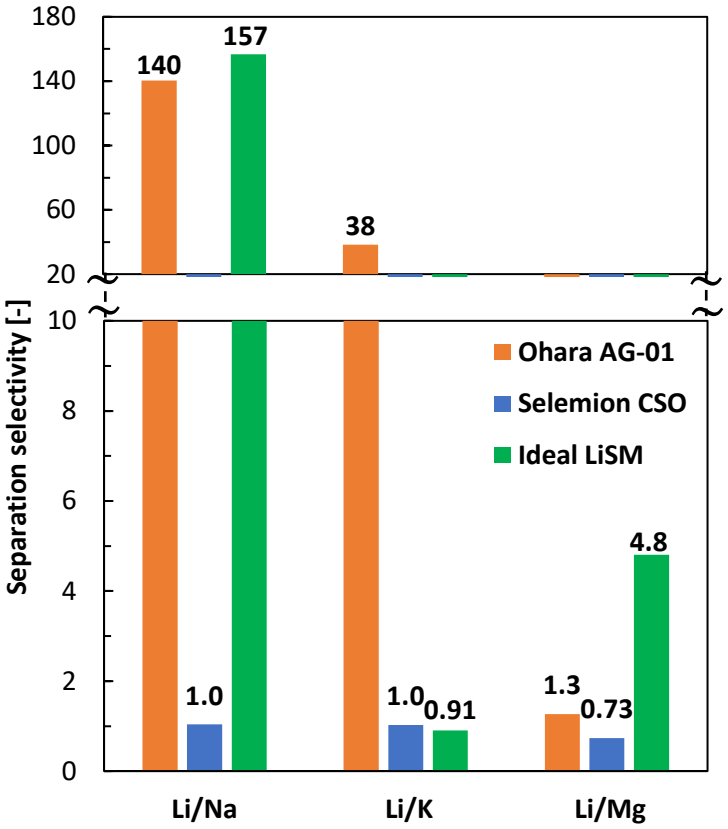

Figure 58 Process selectivity achieved using different LiSMs. All the simulations were performed at similar process conditions in terms of test duration (7 days), applied voltage (1.2 V) and flow rates (10 mL min^{-1} for feed and receiver, 100 mL min^{-1} for flow electrodes)

Clearly, among the simulated membranes, the Selemion CSO exhibits the poorest performance. In particular, its Li/Na and Li/K selectivity values approach unity, indicating the absence of preferential

transport among monovalent cations. The limited lithium selectivity can be ascribed to the polymeric nature of the membrane: in such charged polymers, ion selectivity is primarily governed by electrostatic and dielectric interactions. Due to its higher charge density, Li^+ exhibits a lower affinity for the membrane compared to Na^+ and K^+. These results clearly demonstrate that conventional polymeric membranes are not suitable for the effective separation of lithium from competing monovalent cations.

Conversely, the Ohara AG-01 membrane shows excellent Li/Na and Li/K selectivity. Its selectivity mechanism is mainly based on steric, size-dependent exclusion, which hinders the transport of ions with an effective radius larger than that of Li^+. However, a major limitation of this ceramic membrane lies in its poor ability to reject Mg^{2+}, whose ionic radius is comparable to that of Li^+, resulting in a low Li/Mg selectivity. This difference in selectivity behaviour reflects the fundamentally distinct nature of the two membrane types. From an industrial perspective, employing a ceramic LiSM such as the Ohara AG-01 would likely require a preliminary treatment step to remove Mg^{2+} ions, for example through reactive crystallization technologies [212]. When considering the performance of the ideal LiSM, the Li/Na and Li/K selectivity values are comparable to those of the Ohara AG-01 membrane, while its Li/Mg selectivity is significantly higher. This behaviour arises from the fact that the ideal LiSM was designed to possess transport properties equivalent to those of the Selemion CSO equilibrated with an equimolar $Na^+/K^+/Li^+/Mg^{2+}$ mixture. Since the CSO membrane is intrinsically monovalent-selective, the ideal LiSM effectively hinders the transport of Mg^{2+} ions via electrostatic repulsion. Such a membrane could, in principle, be realized by doping polymeric monovalent-selective IEMs with solid-state electrolytes [9] thereby achieving lithium selectivity comparable to that of ceramic membranes.

Further comparison of the three LiSMs in terms of SEC and lithium productivity was carried out through simulations under different applied voltages and feed/receiver flow rates. The results are presented in Figure 59.

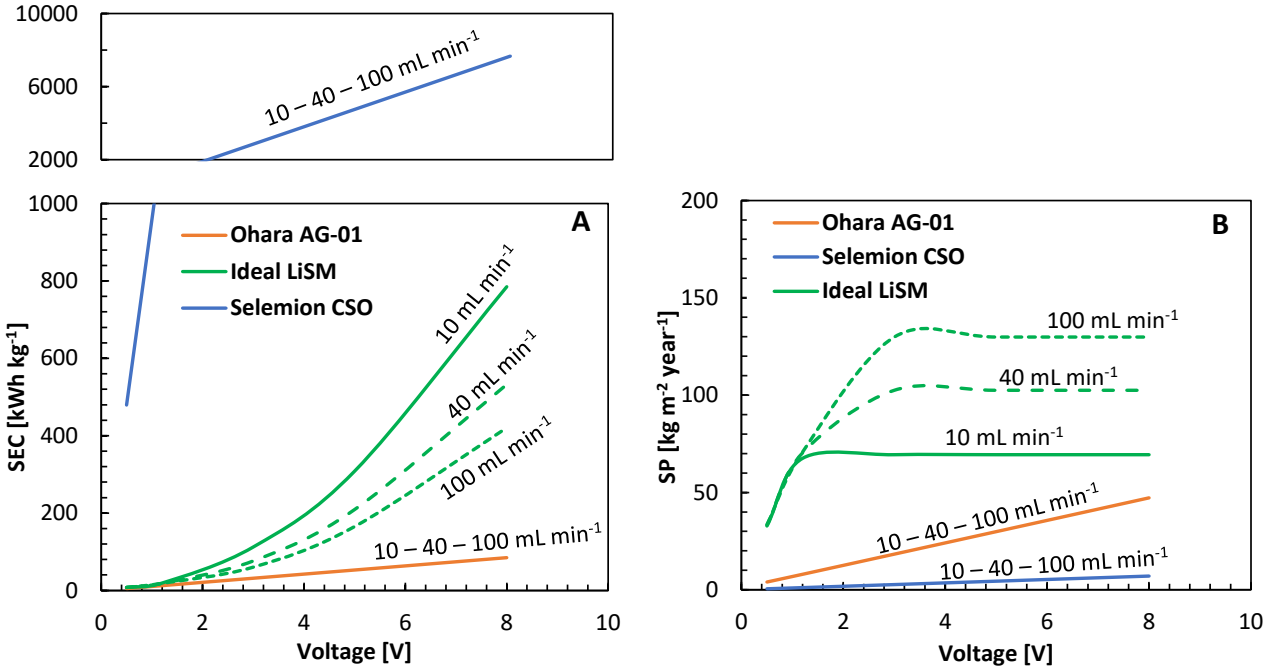

*Figure 59 (**A**) Ohara AG-01, Selemion CSO and Ideal LiSM SEC versus external voltage at different feed and receiver flow rates. (**B**) Ohara AG-01, Selemion CSO and Ideal LiSM SP versus external voltage at different flow rates. Feed and receiver flow rates are set equal and changed simultaneously.*

As shown in Figure 59A, the SEC obtained with the Selemion CSO membrane is almost two orders of magnitude higher than that achieved with the ceramic AG-01 membrane, mainly due to the different current densities. Although the CSO membrane exhibits a much higher ionic conductivity, its poor Li/Na selectivity causes most of the electrical current to be carried by Na^+ ions, resulting in a very low lithium recovery efficiency and consequently a high SEC. The SEC of the CSO membrane is also insensitive to flow rate variations, confirming that polarization phenomena are negligible since Na^+, the most abundant species, dominates charge transport.

Similarly, the productivity and SEC of the AG-01 membrane are nearly unaffected by the flow rate because its high resistance limits current density and minimizes interfacial polarization. Conversely, the ideal LiSM, with ionic resistance comparable to that of a polymeric membrane, shows a marked dependence on flow rate, particularly at high applied voltages. At 4 V and 10 mL min^{-1}, polarization accounts for approximately 63% of the SEC, while increasing the flow rate to 100 mL min^{-1} reduces this contribution to about 30%. This stronger influence arises from the higher current densities achieved with the ideal LiSM (≈1.2 A m^{-2} vs 0.1 A m^{-2} for AG-01 at 1.2 V), which enhance polarization effects.

These observations are consistent with the productivity trends in Figure 59B. The AG-01 membrane exhibits low and flow-rate-independent productivity due to its limited current density, whereas the

ideal LiSM achieves higher productivity, strongly affected by the flow rate. At high applied voltages, a plateau in lithium productivity is observed, corresponding to the onset of the lithium limiting current, beyond which further voltage increase does not enhance Li^+ flux. Nevertheless, increasing the flow rate raises the limiting productivity by approximately 89% (from 1.31 A m^{-2} at 10 mL min^{-1} to 2.82 A m^{-2} at 100 mL min^{-1}). Consequently, at high voltages and low flow rates, a decrease in lithium selectivity is expected. This behaviour is confirmed in Figure 60 , which reports the lithium selectivity of the ideal LiSM as a function of applied voltage and flow rate.

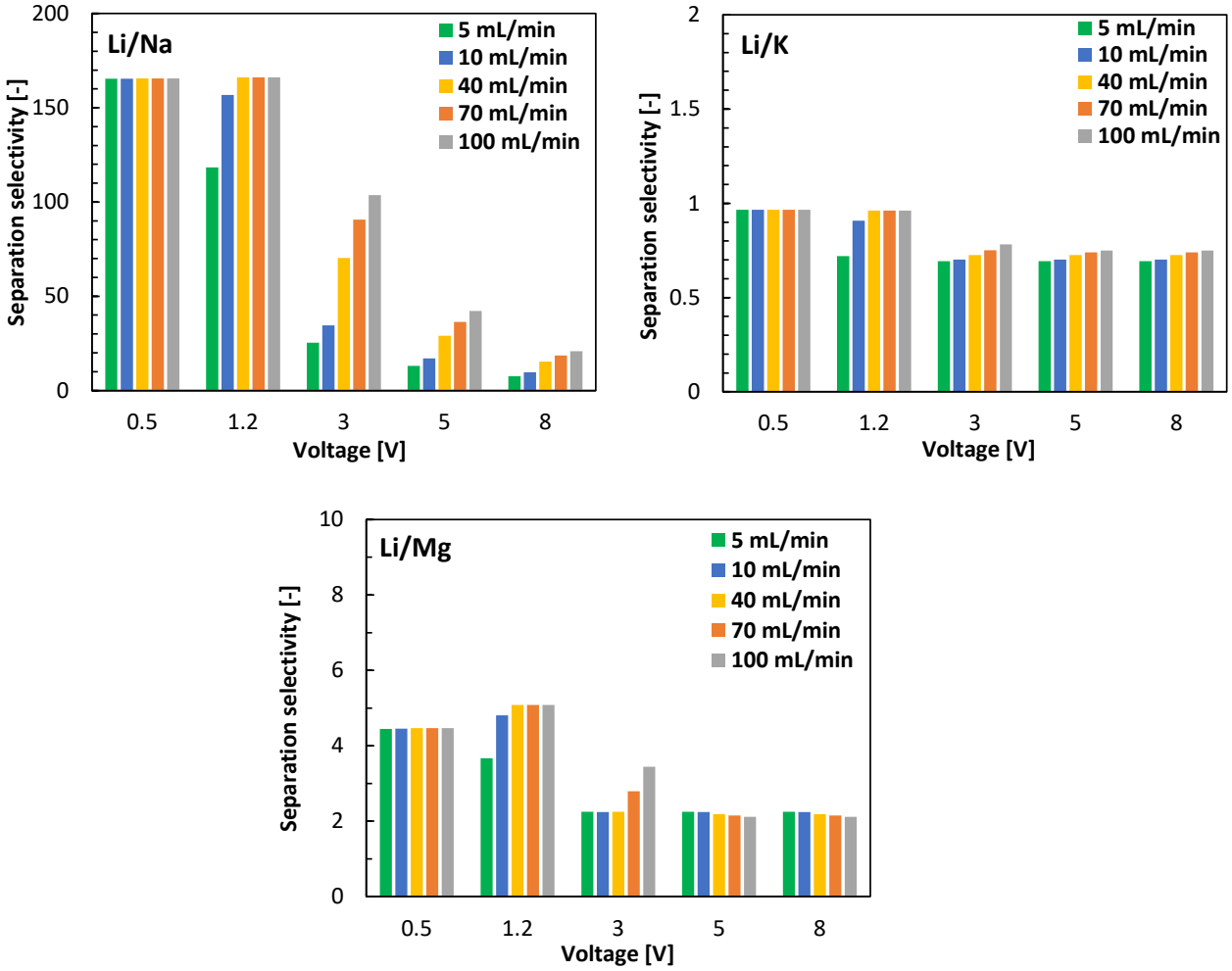

Figure 60 Li/Na, Li/K and Li/Mg selectivity of the ideal LiSM versus applied voltage and feed and receiver flow rates.

From Figure 60 it is evident that lithium selectivity decreases at high applied voltages, i.e., at high current densities, confirming that operating under such conditions is energetically inefficient. This behaviour arises because the limited lithium concentration in the feed restricts the maximum lithium partial limiting current density. According to the definition of the polarization coefficient , polarization effects are more pronounced for species with either higher transport numbers,

corresponding to greater membrane selectivity [82] or lower bulk concentrations. Consequently, at fixed voltage, increasing the flow rate enhances Li/Na and Li/K selectivity, since the reduction in the DBL thickness benefits Li^+ transport more than Na^+ or K^+.

Regarding Li/Mg selectivity, the higher values observed at 1.2 V compared to 0.5 V can be explained by the different charge stoichiometry: for identical transport numbers, the moles of Li^+ recovered per unit charge are twice those of Mg^{2+}. Thus, an increase in applied voltage, and consequently in current density, enhances the apparent process selectivity. This trend, however, disappears at low flow rates (e.g., 5 mL min^{-1}), where polarization limits Li^+ flux and reduces overall selectivity. Interestingly, at high voltages, Li/Mg selectivity slightly decreases with increasing flow rate.

This non-trivial behaviour is consistent with previous studies [13,194] , which reported that increasing flow rates enhance the selectivity of cations with lower aqueous mobility. In the present system, the bulk mobility order ($K^+ > Na^+ > Li^+ > Mg^{2+}$) correlates with the hydrated ionic radii. Since Mg^{2+} has a lower mobility than Li^+, increasing the flow rate improves its transport rate across the DBL more effectively, leading to a small reduction in Li/Mg selectivity. Indeed, the polarization coefficient decreases as ionic diffusivity increases.

Overall, polarization phenomena must be carefully considered in selective recovery processes for trace elements such as lithium. For instance, with the ideal LiSM, increasing the applied voltage from 1.2 V to 3 V can improve productivity but simultaneously cause a substantial drop in selectivity, potentially to unacceptable levels. Under limiting-current conditions, process selectivity tends to approach a value governed not by membrane properties but by the applied current density and hydrodynamic regime [13].

3.2 Macroscale modelling and simulations of ion-exchange membranes processes: valorisation of seawater brines

One of the most promising fields of application for electromembrane technologies currently under investigation concerns the post-treatment of industrial waste effluents, such as the concentrated brines generated by reverse osmosis plants. The implementation of these technologies can significantly reduce the net production of liquid waste and contribute achieving Zero Liquid Discharge (ZLD) conditions, thereby transforming traditionally linear processes into circular and sustainable ones.

In this context, the integration of electromembrane units within a circular treatment chain for the valorisation of seawater-derived brines is presented in the following as a case study of macroscale modelling. This treatment chain was conceptualised and developed within the SEArcularMINE project, a Horizon 2020 Research and Innovation Action coordinated by the University of Palermo (UniPa) in collaboration with several academic and industrial partners across Europe.

The present section begins with a concise description of the project framework and objectives, followed by an overview of the implemented technologies. The core of this work focuses on the preliminary modelling of the individual process units and on the development of an integrated, multi-scale simulation platform designed to model the overall process chain and to support its design, optimisation, and scale-up.

3.2.1 The SEArcularMINE project

The SEArcularMINE project ("Sustainable Extraction and Circular Valorisation of Critical Raw Materials from Seawater Brines"), funded under the Horizon 2020 programme aimed to develop a circular, resource-efficient process for the recovery of critical raw materials, primarily magnesium, lithium, and other trace elements (TEs), from saltworks bitterns, i.e., the concentrated residual brines obtained after NaCl crystallization in traditional solar saltworks.

The project addressed one of the main challenges of the European raw materials strategy: the dependence of the EU on imported critical minerals and the need for sustainable, low-impact extraction routes. SEArcularMINE introduced an innovative circular process chain that valorises existing saline waste streams without producing additional waste or requiring external chemical inputs. The process integrates advanced electromembrane technologies, including EDBM, RED, Li-MFCDI and Membrane Distillation (MD), with reactive crystallization and selective sorption techniques for high-purity mineral recovery.

3.2. Macroscale modelling and simulations of ion-exchange membrane processes: valorisation of seawater brines

Among the main objectives of the project was the increase of the technological readiness level (TRL) of the adopted technologies, with the ultimate goal of enabling a future industrial implementation of the integrated recovery system. In this framework, the experimental construction and testing of pilot-scale units were complemented by extensive modelling and simulation activities, addressing both individual unit operations and the overall integrated treatment chain.

In particular, one dedicated work package focused on the development of advanced multi-scale modelling tools to support the design, scale-up, and optimisation of all the technologies involved in SEArcularMINE. The models were developed from first-principle equations, supported by targeted laboratory investigations.

For each process unit, the project partners developed two complementary modelling approaches: a detailed model, designed to accurately reproduce the laboratory-scale behaviour of the system, and a simplified pilot-scale model, implemented within the integrated simulation platform of the entire SEArcularMINE process. This platform was conceived as a predictive and optimisation tool capable of assessing system performance under various operating and environmental conditions, while also supporting prototype design and process control strategies.

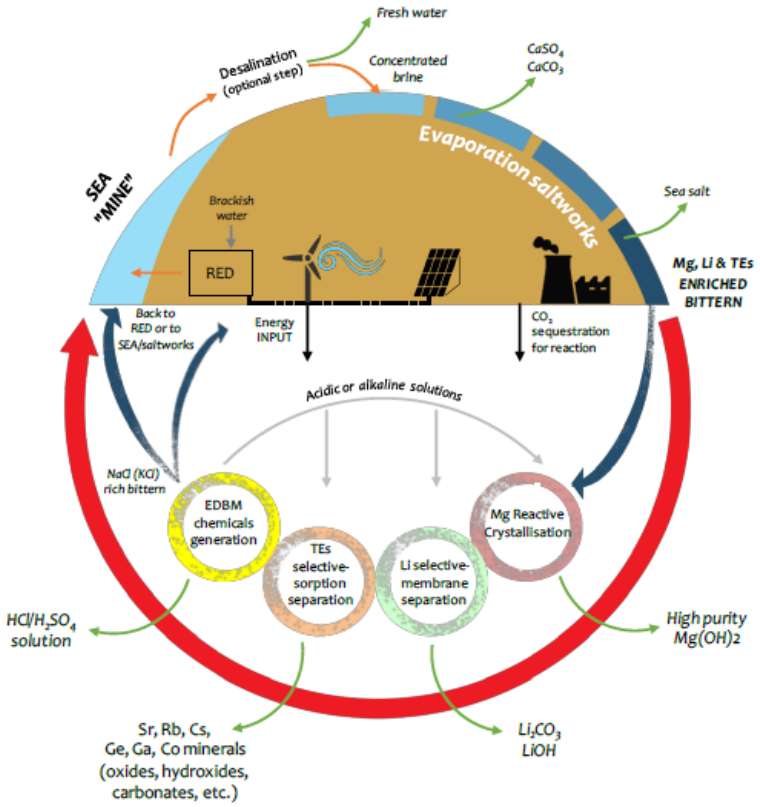

Figure 61 Schematic of the SEArcularMINE integrated process for the valorisation of seawater bitterns

3.2.2 Description and modelling of the units

In the following section, a brief description of the auxiliary and core units of the process chain is provided, along with a schematic description of the developed physical mathematical models. These latter are simplified yet effective models i.e., physical descriptions of any phenomenon not directly affecting the species' concentration in the process streams are therefore dropped for the sake of simplicity.

3.2.2.1 pH-SA units

The pH-SWING adsorption (pH-SA) unit consists of an adsorption column packed with selective ion-exchange resins designed to recover specific trace elements from an aqueous stream. The resins contain ionisable functional groups that exchange ions with the target species in solution. Consequently, the adsorption selectivity depends primarily on the ionic charge of the species and, to a lesser extent, on their chemical affinity for the functional groups. Owing to its tunable selectivity, the pH-SWING unit is employed within the treatment chain to selectively recover several target elements, including B, Sr, Rb, Cs, Co, and Ge.

The operating principle of the unit is analogous to that of a conventional adsorption column. It is, therefore, an intrinsically unsteady system, as the resins become progressively saturated and must be periodically regenerated by shifting the adsorption equilibrium. In this specific technology, the adsorption dynamics are pH-dependent, enabling the regeneration of the resins by adjusting the solution pH. Typically, acidic eluents of low pH are used during regeneration to promote desorption and recover the previously adsorbed species. In practical operation, two or more adsorption columns are alternated in a parallel configuration to prevent downtime during regeneration. This arrangement allows the process to approach a pseudo-steady-state condition, where the outlet composition of the treated stream remains nearly constant over time.

The pH-SA model developed by the project partners at the Universitat Politècnica de Catalunya (UPC) is based on mass balance equations coupled with adsorption–desorption reactions, each characterised by species-specific equilibrium constants. The model predicts the temporal evolution of concentration profiles along the column and identifies the breakthrough point, i.e., the time at which the saturation front reaches the outlet. For steady-state simulations, the outlet concentration is assumed constant and equal to the equilibrium value before breakthrough. Further details on the specific pH-SA columns adopted in the process are provided in the following section.

Three distinct pH-SA units are implemented within the treatment chain (see Figure 61).

The first pH-SA column, located downstream of the ultrafiltration (UF) unit (not included in the integrated platform) and upstream of the Mg-CGCR unit, is dedicated to the removal and recovery of boron, present in the inlet brine as $B(OH)_3$. Boron removal is essential because it can interfere with the crystallisation kinetics of $Mg(OH)_2$ in the subsequent reactor. The high affinity of the resins for boron corresponds to a high adsorption constant for this species, resulting in a boron-depleted effluent.

The second pH-SA column is positioned between the Mg-CGCR and EDBM units. Its purpose is to soften the hypersaline stream leaving the crystalliser, which may still contain residual Ca^{2+} and Mg^{2+} ions. This step is critical to ensure the efficient operation of the downstream EDBM unit, as the presence of divalent cations significantly reduces its NaOH production efficiency due to their higher affinity for cation-exchange membranes compared to monovalent ions such as Na^+ and K^+. Consequently, the effluent from this unit is strongly depleted in Mg^{2+}, Ca^{2+}, and also Sr^{2+}, which is present in solution in a divalent oxidation state.

Finally, the third pH-SA column represents one of the core units for the recovery of trace elements such as Rb, Cs, Ge, and Co. This column is located downstream of the Li-MFCDI unit, and its feed stream, already purified in the preceding steps, mainly contains Na^+ and K^+. The eluent, enriched in the recovered trace elements, is subsequently directed to the post-treatment section for further purification and valorisation.

3.2.2.2 Mg-CGCR unit

The Magnesium Crystals Granulometry Controlled Reactor (Mg-CGCR) represents one of the core technologies within the SEArcularMINE treatment chain. Its main purpose is the recovery of magnesium in the form of $Mg(OH)_2$, characterised by a controlled particle size distribution. The reactive crystallisation of Mg^{2+} is triggered by the increase in pH resulting from the addition of an NaOH stream at the reactor inlet, which is produced in situ by the EDBM unit. The granulometry of the produced particles is primarily governed by the hydrodynamic regime inside the reactor; however, the overall $Mg(OH)_2$ recovery ratio is not affected by flow conditions.

For this reason, the nucleation and crystal growth kinetics are not explicitly included in the model developed in this work and implemented within the simulation platform. The reaction proceeds extremely fast and can therefore be reasonably assumed to occur under equilibrium conditions. Consequently, the outlet concentrations of Mg^{2+} and Ca^{2+} depend exclusively on the amount of NaOH fed to the reactor. A stoichiometric quantity of NaOH is sufficient to precipitate all the magnesium contained in the inlet bittern.

The model takes as input the flow rates and concentrations of both the bittern and the alkaline streams, originating respectively from the boron removal stage and the EDBM unit, and computes the outlet composition by solving the solubility equilibria of pH-sensitive species such as Mg^{2+} and Ca^{2+}. The resulting effluent is typically depleted in magnesium and almost free of calcium, exhibiting a slightly alkaline character due to a modest excess of NaOH.

In terms of energy consumption, the Mg-CGCR unit is among the most energy-demanding in the treatment chain, mainly because of the high flow rates of both the bittern and the recirculating liquid streams. The power consumption of the reactor is estimated from the specific pumping energy required for fluid circulation. The reactor outlet stream consists of a $Mg(OH)_2$ slurry, which is sent to a thickener to separate the solid phase from the magnesium-free brine that is subsequently directed to downstream units. The wet solids are then processed in a drum filter to remove the residual water. The energy demand of the filtration stage depends on the slurry flow rate and on the separation efficiency of the thickener. For completeness, the solid–liquid separation stage is explicitly included in the Mg-CGCR model, allowing the overall energy consumption of the reactor and filtration steps to be consistently accounted for.

3.2.2.3 EDBM unit

EDBM is an electromembrane process used to produce acidic and alkaline solutions from saline feeds (see section 1.1.2.3). Within the SEArcularMINE treatment chain, the EDBM unit serves as an auxiliary subsystem designed to minimise the consumption of external reactants through the in situ generation of soda (NaOH) and hydrochloric acid (HCl) required in the various treatment stages. Among these products, NaOH represents the key output, as it is directly supplied to the Mg-CGCR unit for the precipitation of $Mg(OH)_2$.

The simplified model of the EDBM unit developed in the present work is a lumped model based on mass balance equations for each compartment, the ionic transport equations across the ion-exchange membranes, and the electrical relations governing voltage drops and total power consumption. Ionic transport is modelled according to the Nernst-Planck framework (see 2.1.2), while Nernst and Kirkoff's equations (eq. (3.15) and (3.13)) are employed to describe the electrical behaviour of the unit.

3.2.2.4 MVC unit

The Mechanical Vapour Compression (MVC) unit is a low-pressure evaporative desalination technology driven by a mechanical compressor. In this unit, the seawater brine is first pre-heated by recovering residual heat from the produced distillate. After pre-heating, the brine is sprayed as a

falling film over the surface of heat exchanger tube bundles. Through this heat exchange, a portion of the brine evaporates, while the water vapour inside the tubes condenses into permeate. The generated vapour is removed from the evaporator–condenser through mist eliminators, assisted by a mechanical compressor, which constitutes the core component of the MVC system.

The compressor plays a crucial role in sustaining the process: it continuously handles the produced water vapour, compresses it to a higher pressure and temperature, and recirculates it into the heat transfer tubes. This recirculation provides the latent heat required for continuous evaporation, thereby ensuring the energy efficiency of the system. While MVC technology is typically employed for the production of desalinated water, in the SEArcularMINE treatment chain it is instead used to pre-concentrate the saline effluent from the EDBM unit before it is fed to the downstream processes.

Due to the high latent heat of water evaporation, the MVC unit is among the most energy-intensive operations within the treatment chain. In the present work, the brine concentration process was modelled using PhreeqC, an open-source software for geochemical and aqueous solution modelling. Specifically, the model calculates the flow rate and composition of the outlet stream based on the inlet stream characteristics and a defined concentration factor, expressed as the ratio between the inlet and outlet brine flow rates, respectively. The outlet composition depends on the initial concentration, the amount of water removed, and the solubility limits of the solid phases that may precipitate during the concentration process.

3.2.2.5 Li-MFCDI unit

Lithium Membrane Flow Capacitive De-Ionization (Li-MFCDI) is implemented in the SEArcularMINE treatment chain for the selective recovery of Lithium from the multi-ionic brines, after the removal of other competing species such as Mg^{2+}. The working principle and the mathematical model of the unit was thoroughly presented in section 3. The model implemented in the integrated platform is a simplified, pseudo-steady state lumped model

3.2.2.6 DD unit

Diffusion Dialysis (DD) is a membrane separation process primarily used for the recovery of acids or bases from aqueous salt solutions. Within the SEArcularMINE treatment chain, DD units are employed to recover hydrochloric acid (HCl) from the draw solutions of the Li-MFCDI units, as well as from the acidic eluents used to regenerate the ion-exchange resins in the pH-SA columns.

A diffusion dialysis cell used for acid recovery consists of a series of AEMs arranged in parallel to form repetitive elements known as cell pairs. Each cell pair comprises two compartments separated

by the AEMs: one for the feed solution, containing both acid and salt, and one for the stripping solution (typically DI water).

In this process, the driving force for mass transfer is the concentration gradient across adjacent compartments, which induces the diffusive flux of species from the acid–salt feed solution through the ion-exchange membrane into the stripping solution. The anion-exchange membrane selectively allows the transport of anions while retaining most cations. However, protons can still permeate through the AEM, despite their positive charge, due to the Grotthuss hopping mechanism of proton conduction that confers protons and exceptionally high mobility.

The mathematical model of the DD unit is based on mass balance equations for water and acid species, coupled with ion transport relations across the membrane. The acid and salt fluxes are evaluated by multiplying a constant permeability coefficient, determined from the experimental campaign, by the corresponding driving force, expressed either as the osmotic pressure difference or as the salt concentration difference between the feed and receiver compartments.

3.2.2.7 MD unit

Membrane Distillation (MD) is a promising thermally driven membrane technology for seawater desalination, characterised by very high salt rejection. In this process, two chambers maintained at different temperatures are separated by a microporous hydrophobic membrane. Due to the hydrophobic nature of the membrane, liquid water cannot penetrate its pores; only water vapour can pass through. As a result, salts and non-volatile solutes are completely retained on the feed side.

The driving force of the MD process is the difference in water vapour pressure across the membrane surface, which arises from the temperature gradient between the hot feed and the cold permeate compartments. The feed solution, typically a saline stream, is heated using waste low-temperature heat or solar thermal energy, while the permeate vapour condenses on the cooler side of the membrane to form the distillate.

Within the SEArcularMINE treatment chain, the MD unit is employed in the post-treatment stage to further concentrate the process streams containing the target species recovered in the upstream steps. A simplified model, based on mass balance equations, was implemented to estimate the outlet flow rates of volatile components such as water and acid. The average transmembrane fluxes of water and acid were obtained from experimental measurements and used as model parameters for the simulations.

3.2.3 Results and discussion

In the following section, the structure of the integrated simulative platform is reported. The platform was developed in Python following a modular approach; each unit is modeled separately, and all the models are summoned in the master program as external functions. Therefore, each unit can be schematized as a black box, communicating with the other units by means of exchange variables, which represent the main process variables such as flow rates, concentrations and temperatures of each stream.

Two different versions of the platform were developed in order to perform demonstrative simulations of seawater bittern treatment both in transient steady-state and simulations. In the following sections, the main outcomes in terms of products composition, energy consumption and operation time will be discussed.

3.2.3.1 Steady-state simulations

The scheme of the steady-state simulation platform is shown in Figure 62. The core of the system is represented by the recirculation loop established between the Mg-CGCR and the EDBM units, which provides the reactor with the required soda flow rate.

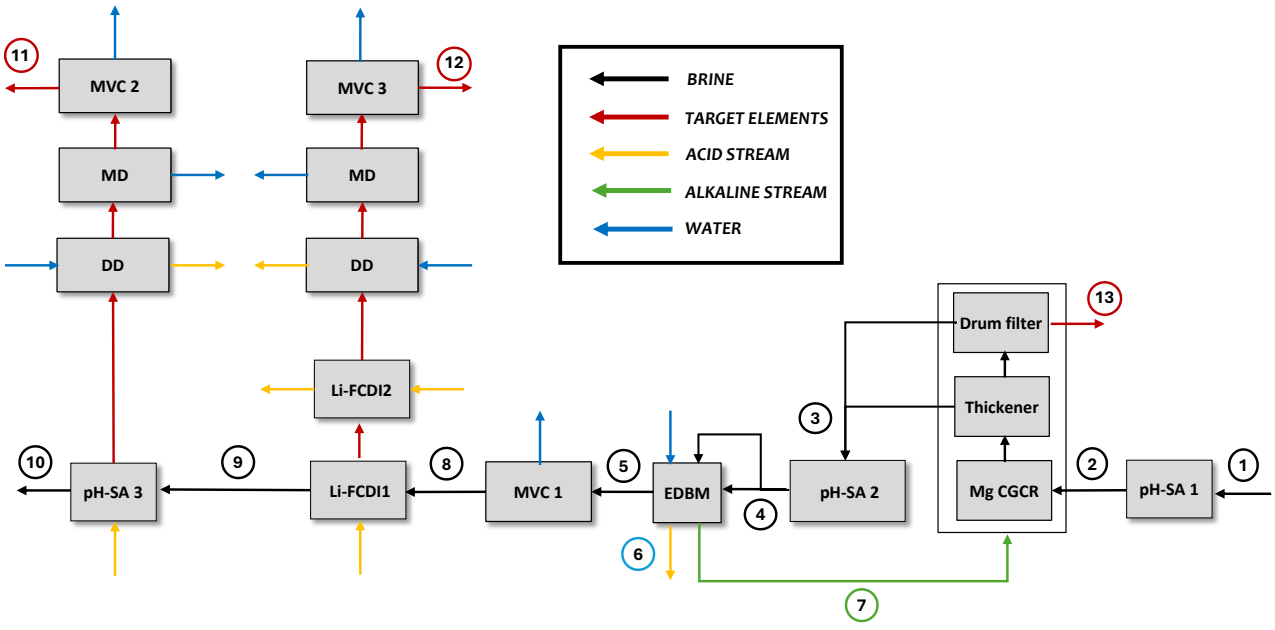

Figure 62 Block flow diagram of the SEArcularMINE simulation platform

In the simulated process configuration, the outlet brine from the second pH-SA unit is split and directed to the alkaline and salt compartments of the EDBM unit. Assuming constant volumetric flow rates in all EDBM compartments, the splitting ratio (α), defined as the fraction of the inlet brine sent

to the salt channel, can be related to the target hydroxide concentration in the alkaline outlet stream and to the total concentration of divalent cations in the brine by the following equation:

$$\alpha = \frac{2\left(C_{Mg^{2+}} + C_{Ca^{2+}}\right)}{C_{OH}^{target} + 2\left(C_{Mg^{2+}} + C_{Ca^{2+}}\right)} \tag{3.28}$$

From a numerical standpoint, recirculation loops may lead to model divergence and must therefore be handled carefully. At the beginning of the simulation, an initial guess is assigned to the EDBM current density, corresponding to a specific NaOH concentration in the recirculating soda stream. By imposing a target soda concentration of 1 mol L^{-1} in the alkaline outlet, a while-loop routine is implemented to iteratively adjust the current density until the stoichiometric requirement of soda production is met. This iterative procedure is necessary because, at each calculation step, the composition of the EDBM inlet salt and alkaline streams changes due to the recirculation effect. Consequently, the final EDBM current density, and thus the applied voltage, depends on the magnesium and calcium concentrations in the inlet brine.

Two different simulations were carried out considering different feed compositions to the treatment chain, in order to evaluate the influence of the feed composition on the overall process performance.

In the first scenario, the treatment of a bittern of a given composition called *Margi* was simulated. The simulation results for the treatment of this latter are reported in Table 19.

As observed from the composition of the inlet stream, Margi bittern is poor in sodium but rich in magnesium, which enables a higher $Mg(OH)_2$ production yield. In particular, 4.35 kg·h^{-1} of $Mg(OH)_2$ are produced from an inlet brine flow rate of 30 L·h^{-1}, achieving an Mg recovery approaching 100% (Figure 63C). The amount of soda required for this production is approximately 6 kg·h^{-1}, corresponding to an EDBM current density of 320 A·m^{-2}. This current density results in an electrical power consumption of 10.4 kW, as illustrated in Figure 63A.

If the electrical power consumption of the Mg-CGCR pumps and the drum filter is also considered, the total energy demand for magnesium hydroxide production amounts to 14.4 kW. Nevertheless, the MVC unit remains the most energy-intensive component of the process. Considering both the pre- and post-concentration steps, the total power consumption associated with brine concentration reaches 23.3 kW. Regarding the other target elements, nearly complete recovery of Li, Rb, and Cs is achieved, as shown in Figure 63C, while only minor recoveries of Co and Ga are observed.

The simulation results for the treatment of the Margi bittern are reported in Figure 63. The inlet flow rate was kept equal to that used in the previous simulation to allow a direct comparison of the effects

of the different feed compositions. Unlike Margi, Galia is a bittern rich in sodium and contains a moderate amount of magnesium. Consequently, the production rate of magnesium hydroxide decreases to 1.68 kg/h. As a result, the EDBM unit operates at a lower current density of 125 $A \cdot m^{-2}$, with a corresponding reduction in power consumption to 2.24 kW. The drum filter power demand is also reduced, as shown in Figure 63B, whereas the Mg-CGCR pumping power remains nearly unchanged, since the inlet flow rate was kept constant.

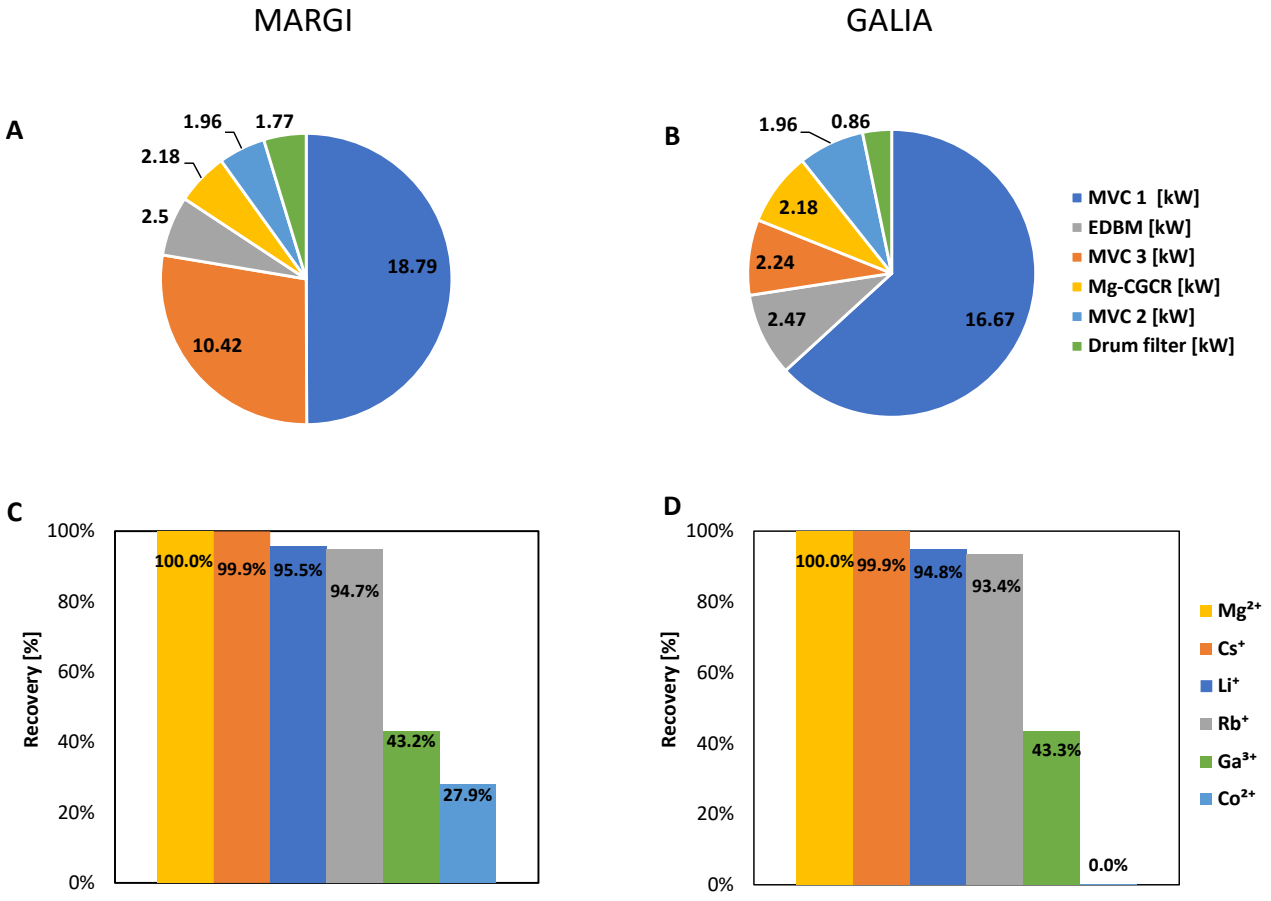

*Figure 63 Power consumption for the treatment of 30 L h-1 of (**A**) Margi bittern and (**B**) Galia bittern. Target elements recovery from (**C**) Margi bittern and (**D**) Galia bittern*

Table 19 Flow rate and composition of the streams in the steady-state treatment of Margi bittern. The number of the stream is referred to the scheme in Figure 62

	Streams											
	1	**2**	**3**	**4**	**5**	**6**	**7**	**8**	**9**	**10**	**11**	**12**
Flow rate [L h^{-1}]	30.00	30.00	180.00	180.00	30.00	220.00	150.00	3.40	3.40	3.40	0.28	0.35
pH	7.00	5.43	11.14	11.14	11.14	0.16	14.00	9.17	8.38	3.24	6.96	7.35
Macro-elements concentration × 10^{-3} [mol m^{-3}]												
Na^{+}	1.90	1.90	6.30	6.30	2.00	0.00	7.10	5.70	5.60	5.60	0.00	0.00
K^{+}	0.30	0.30	0.96	0.96	0.30	0.00	1.10	0.98	0.98	0.98	0.00	0.00
Mg^{+2}	2.50	2.50	0.00	0.00	0.00	0.00	0.00	0.00	0.00	0.00	0.00	0.00
Cl^{-}	5.50	5.50	5.50	5.50	1.20	0.60	5.50	4.90	4.90	4.90	0.01	0.09
SO_4^{-2}	0.86	0.86	0.86	0.86	0.52	0.05	0.86	0.72	0.72	0.72	0.00	0.00
Micro-elements concentration [mol m^{-3}]												
Ca^{+2}	3.5	3.5	0.0	0.0	0.0	0.0	0.0	0.0	0.0	0.0	0.0	0.0
B	17.0	3.5	3.5	3.5	3.5	0.0	3.5	32.0	32.0	32.0	0.0	0.0
Sr^{+2}	0.2	0.2	0.2	0.2	0.2	0.0	0.2	0.0	0.0	0.0	0.0	0.0
Li^{+}	1.0	1.0	1.0	1.0	1.0	0.0	1.0	9.3	0.8	0.8	0.0	83.0
Br^{-}	31.0	31.0	31.0	31.0	31.0	0.0	31.0	280.0	280.0	280.0	0.0	0.0
Trace-elements concentration × 10^{4} [mol m^{-3}]												
Cs^{+}	0.13	0.13	0.13	0.13	0.13	0.10	0.13	1.20	1.20	0.04	14.00	0.00
Rb^{+}	690.00	690.00	690.00	690.00	690.00	0.10	690.00	6300.00	6300.00	630.00	71000.00	0.00
Co^{+2}	0.80	0.21	0.21	0.21	0.21	0.10	0.21	2.00	2.00	0.02	24.00	0.00
Ga^{+3}	6.70	3.20	3.20	3.20	3.20	0.10	3.20	29.00	29.00	3.60	320.00	0.00
Ge^{+4}	8.00	1.70	1.70	1.70	1.70	0.10	1.70	15.00	15.00	15.00	0.00	0.00

Table 20 Flow rate and composition of the streams in the steady-state treatment of Galia bittern. The number of the stream is referred to the scheme in Figure 62

	Streams											
	1	2	3	4	5	6	7	8	9	10	11	12
Flow rate [L h^{-1}]	30.00	30.00	88.00	88.00	30.00	220.00	58.00	3.20	3.20	3.20	0.28	0.36
pH	7.00	6.80	11.62	11.62	11.62	0.57	14.00	13.10	12.30	12.30	6.96	7.31
Macro-elements concentration × 10^{-3} [mol m^{-3}]												
Na^{+}	3.60	3.60	5.50	5.50	3.70	0.00	6.40	5.60	5.60	5.60	0.00	0.00
K^{+}	0.19	0.19	0.28	0.28	0.19	0.00	0.33	0.96	0.96	0.96	0.00	0.00
Mg^{+2}	0.96	0.96	0.00	0.00	0.00	0.00	0.00	0.00	0.00	0.00	0.00	0.00
Cl^{-}	5.00	5.00	5.00	5.00	3.20	0.25	5.00	5.00	4.90	4.90	0.00	0.27
SO_4^{-2}	0.37	0.37	0.37	0.37	0.30	0.01	0.37	0.73	0.73	0.73	0.00	0.00
Micro-elements concentration [mol m^{-3}]												
Ca^{+2}	5.8	5.8	0.0	0.0	0.0	0.0	0.0	0.0	0.0	0.0	0.0	0.0
B	10.0	2.1	2.1	2.1	2.1	0.0	2.1	20.0	20.0	20.0	0.0	0.0
Sr^{+2}	0.3	0.3	0.3	0.3	0.3	0.0	0.3	0.0	0.0	0.0	0.0	0.0
Li^{+}	3.4	3.4	3.4	3.4	3.4	0.0	3.4	32.0	1.8	1.8	0.0	270.0
Br^{-}	16.0	16.0	16.0	16.0	16.0	0.0	16.0	160.0	160.0	160.0	0.0	0.0
Trace-elements concentration × 10^{4} [mol m^{-3}]												
Cs^{+}	0.14	0.14	0.14	0.14	0.14	0.10	0.14	1.30	1.30	0.05	15.00	0.00
Rb^{+}	310.00	310.00	310.00	310.00	310.00	0.10	310.00	2900.00	2900.00	290.00	31000.00	0.00
Co^{+2}	0.10	0.01	0.01	0.01	0.01	0.10	0.01	0.00	0.00	0.00	0.00	0.00
Ga^{+3}	0.07	0.03	0.03	0.03	0.03	0.10	0.03	0.31	0.31	0.03	3.30	0.00
Ge^{+4}	0.15	0.03	0.03	0.03	0.03	0.10	0.03	0.28	0.28	0.28	0.00	0.00

3.2.3.2 Unsteady-state simulations

A dynamic version of the simulation platform was also developed to reproduce the actual configuration of the SEArcularMINE pilot plant, which actually operated in batch mode. The block flow diagram of the simulated treatment chain is illustrated in Figure 64.

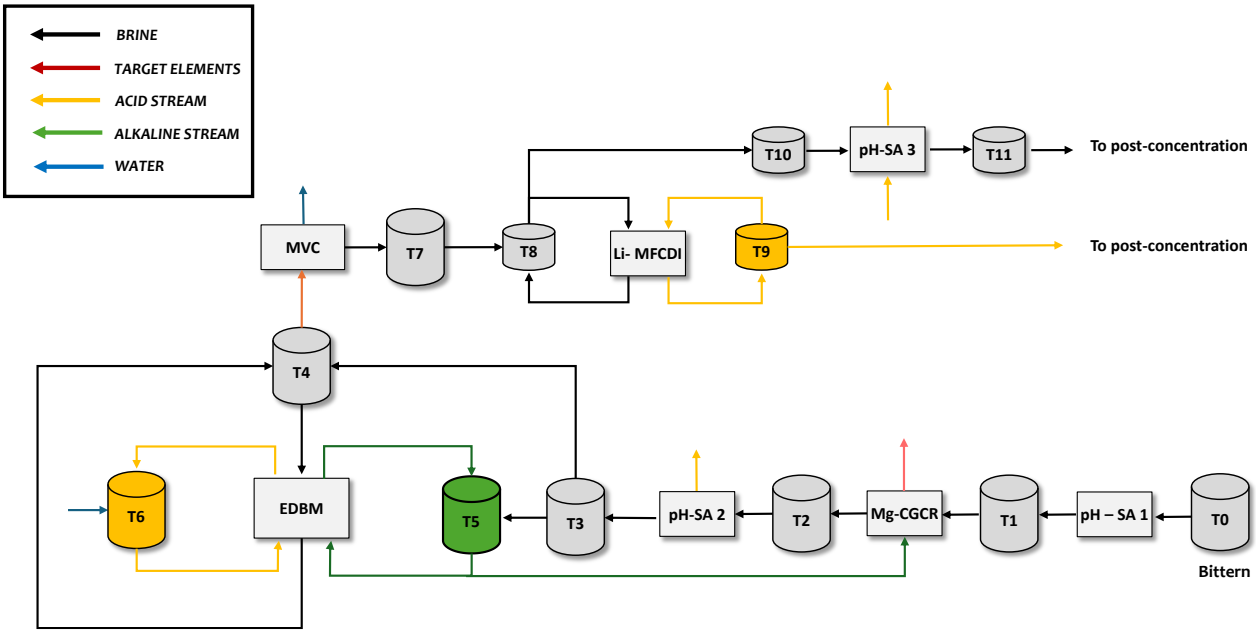

Figure 64 Block flow diagram of the treatment chain simulated in unsteady-state

The main difference between the dynamic and steady-state versions lies in the inclusion of storage and buffer tanks for the various process solutions. In addition, the post-treatment units are not considered in the dynamic model, as they are not part of the pilot plant layout. Another relevant difference concerns the configuration of the EDBM and Li-MFCDI units, which are arranged in a closed-loop rather than a single-pass mode. As a consequence, the composition of the solutions in the accumulation tanks varies over time (Figure 65).

Although the overall platform is dynamic, the models of the individual units are inherently steady-state, under the assumption that their internal dynamics are negligible compared to the slower filling and emptying dynamics of the tanks. In this version of the platform, the tank levels control the flow between units: each tank starts discharging when its liquid level exceeds 50% of its total volume, as illustrated in Figure 67. The discharged solution is then transferred to the downstream unit for further processing.

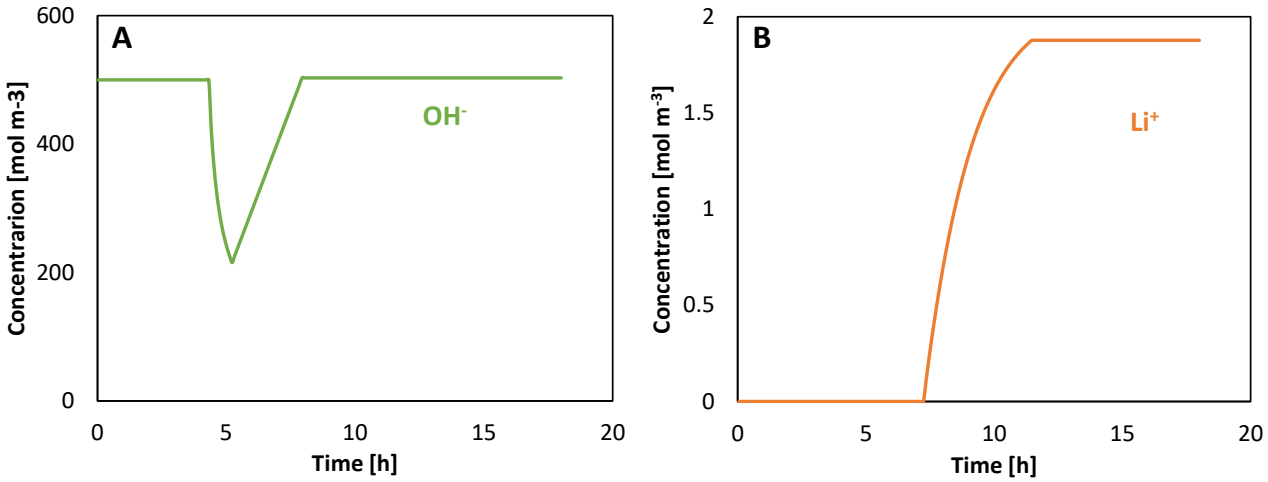

*Figure 65 (**A**) OH^- concentration in the EDBM alkaline tank (T5) vs time. (**B**) Li^+ concentration in the Li-MFCDI receiver tank (T9) vs time*

The filling and emptying dynamics reported in Figure 67 were obtained from the dynamic simulation of the treatment of 100 L of "Margi" bittern. The simulated process lasted 13.5 hours, resulting in a total production of 4.4 kg of $Mg(OH)_2$ and a Li^+ recovery of 27.4% in the Li-MFCDI receiver tank. As shown in Figure 66, the MVC unit represented the main energy-consuming component. The total energy demand of the main units amounted to 257 kWh, corresponding to a specific energy consumption of 2575 kWh m^{-3}.

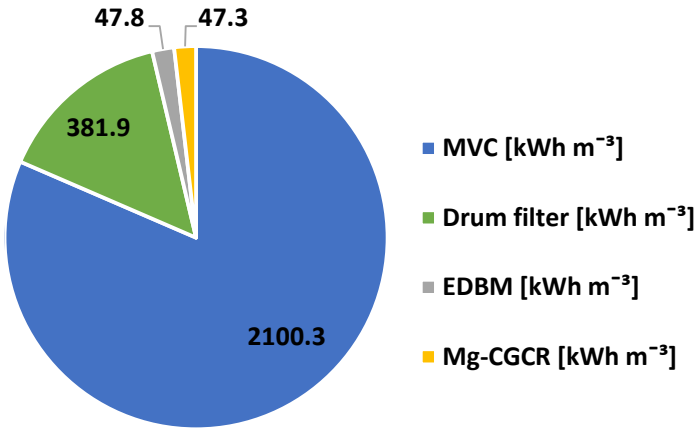

Figure 66 Energy consumption of the most demanding units per cubic meter of processed bittern

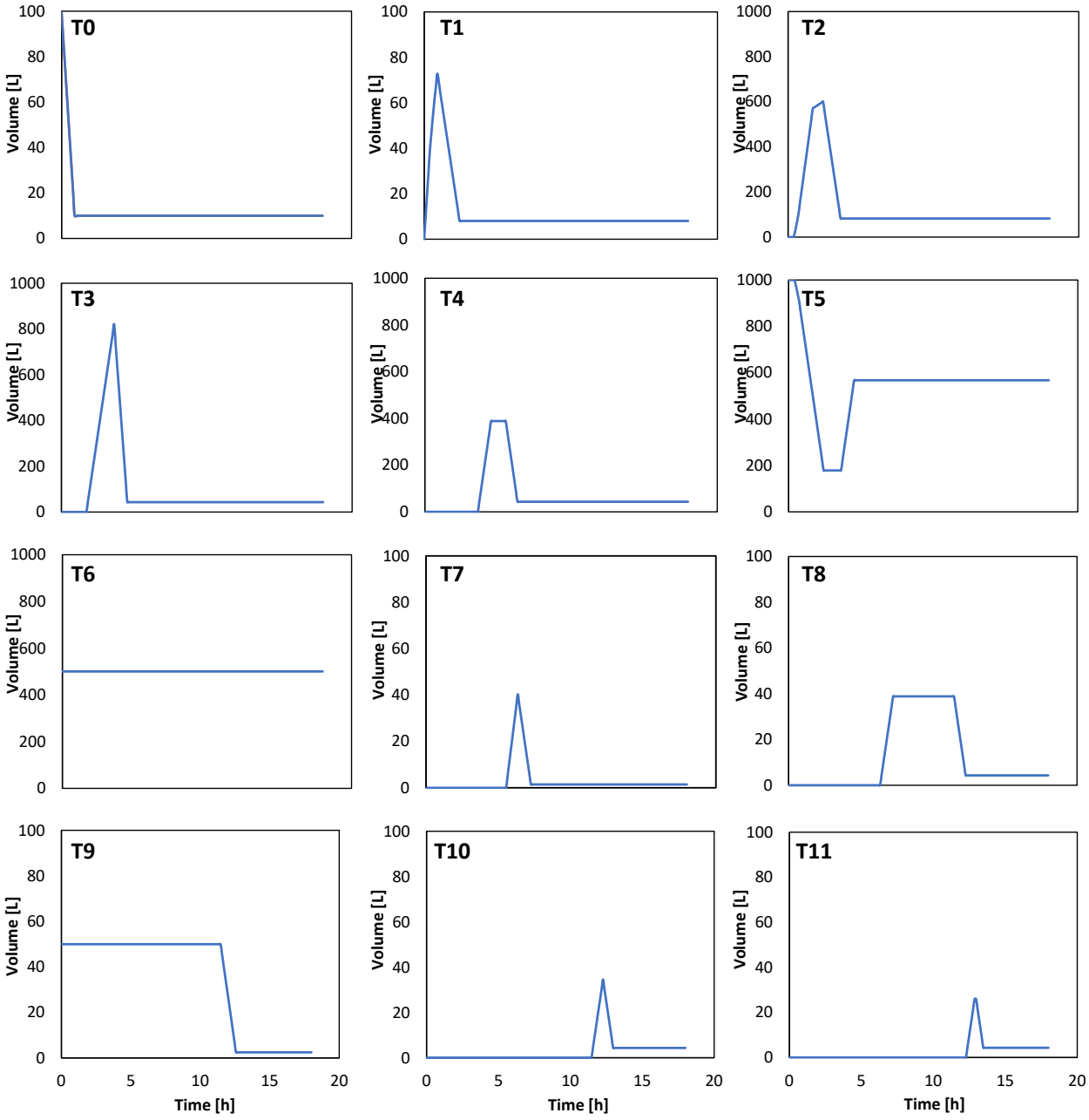

Figure 67 Tanks' volume as a function of time during an unsteady-state simulation

In conclusion, the simulations performed allow to assess the feasibility of the process and to provide and estimation for the recovery of target elements and of the associated energy consumption.

Conclusions, outlooks and perspectives

In the present thesis, ionic transport in IEMs systems was extensively investigated from both experimental and theoretical standpoints, with the overarching goal of developing novel and comprehensive modelling tools to advance the current understanding of mass and charge transport phenomena in highly concentrated systems.

Chapter 1 focused on the thermodynamics of ion exchange. The fundamentals of electrolyte thermodynamics were critically reviewed, highlighting crucial yet often overlooked aspects. An extensive experimental campaign was carried out on commercial IEMs to elucidate how ion-partition equilibria are influenced by the concentration and composition of the external solution, particularly in the presence of multiple counterions at high total ionic strength.

Experimental results revealed that ion activity coefficients in the membrane phase largely exceed unity at high external salt concentrations (i.e., > 1 mol L^{-1}), indicating the development of an increasingly unfavourable partitioning environment. This thermodynamic behaviour was attributed to short-range, unfavourable interactions between mobile ions and fixed-charge groups in the polymer matrix, which cannot be captured by traditional models based on the Debye–Hückel framework, such as the Manning model.

The collected data were employed to develop and validate a novel thermodynamic model for the estimation of ion activity coefficients in the membrane phase, applicable to highly concentrated multi-ionic systems. This model combined a multi-ionic extension of the Manning model with an adapted version of the eNRTL model specifically designed for IEMs. Simulations confirmed the inability of the classical Manning model to describe ion partition at high external concentrations, due to its structural limitation of accounting solely for long-range electrostatic interactions. Conversely, the extended peNRTL model successfully captured the observed behaviour, demonstrating the key role of short-range, non-electrostatic interactions responsible for the increase of activity coefficients above unity.

Further investigations should be conducted to validate the developed model for more complex systems and membranes with well-characterized structures, in order to identify the specific nature of these interactions. Moreover, future work should address the equilibrium of water partition in IEMs, a fundamental yet often neglected topic.

Building on the thermodynamic characterization of the studied membranes, Chapter 2 addressed ion transport in IEMs from both experimental and theoretical perspectives. section 2.1 critically revisited the traditional Nernst–Planck framework, identifying its intrinsic limitations. Subsequently, an

alternative theoretical formulation based on the Maxwell–Stefan transport theory was introduced. This physically grounded approach, referred to as the Binary Friction Model, enables a more rigorous and comprehensive description of charge and mass transport in IEMs. To implement the model, a novel procedure was proposed to accurately extract fundamental ions and water transport coefficients from carefully collected experimental data.

Ion-transport simulations performed with the BFM allowed decoupling the effects of the various interactions among system components on ionic fluxes. Moreover, the dependence of these parameters on the salt concentration was quantified, revealing that at high external concentrations, a significant contribution to ion diffusion and conductivity arises from binary interactions between mobile ions and fixed charges but also from frictional forces between counter-ions and water molecules, which are not properly captured by the Nernst–Planck model.

Furthermore, the Nernst–Planck ionic diffusivities and the Maxwell–Stefan binary diffusivities were found to differ significantly, further elucidating that NP diffusivities lack a specific physico-chemical meaning, even though, in some cases, they can be effectively employed to reproduce the experimental values of salt diffusivity and ionic conductivity in IEMs

Overall, the proposed theoretical framework proved to be a valuable tool for interpreting the physics of ion transport in IEMs. In the future, complementary experimental data, such as ion transport numbers, membrane potentials, and pressure-driven water fluxes, could be analysed within this framework to further elucidate how mutual interactions depend on composition and concentration. Building on this fundamental understanding, future efforts should focus on the development of predictive electrochemical models for the estimation of key transport properties.

Additionally, particular attention should be devoted to modelling water transport and the influence of non-ideal thermodynamic phenomena on this process. For instance, fluid–structure interaction models could be developed to relate solvent activity in the membrane phase to the swelling degree of the polymer matrix. Ultimately, such analyses will pave the way for comprehensive electrochemical–mechanical models capable of capturing the inherent physical complexity of mass and charge transport in IEMs, thereby enabling predictive performance assessment and guiding the design of next-generation, tailor-made membranes.

Finally, in Chapter 3, two case studies of macroscale modelling of electromembrane units were investigated. Fundamental thermodynamic and mass transport models in IEMs were employed to predict the performance of the modelled unit, thus demonstrating how the development of reliable and physically grounded fundamental models is also crucial to optimize operative conditions and configuration of electromembrane processes.

Nomenclature

Variables

A	*Area [m^2]*
A_φ	*Debye-Hückel constant [-]*
a	*Activity [-]*
b	*Average distance between fixed charges [m]*
C	*Molar concentration [mol m^{-3}]*
$\bar{C}$	*Mean ionic concentration [mol m^{-3}]*
C_{el}	*Specific capacitance [F kg^{-1}]*
$c_{i,j}$	*Debye-Hückel's ion-ion binary diffusion coefficient fitting parameter [-]*
$D_{I,J}$	*Multicomponent Fickian diffusivity [m^2 s^{-1}]*
D_i	*Nernst-Planck ionic diffusivity [m^2 s^{-1}]*
$\overline{D}_{ij}$	*Nernst-Hartley mean electrolyte diffusion coefficient [m^2 s^{-1}]*
$Đ_{i,j}$	*Maxwell-Stefan binary diffusion coefficient [m^2 s^{-1}]*
$\vec{d}$	*Driving force per unit of volume [N m^{-3}]*
d	*Channel width [m]*
$\vec{E}$	*Electric field [V m^{-1}]*
e	*Elementary charge [C]*
emf	*Electromotive force [V]*
F	*Helmholtz free energy [J]*
$\mathcal{F}$	*Faraday constant [C mol^{-1}]*
$\vec{F}$	*Drag force per unit of volume [N m^{-3}]*
$f_{i,j}$	*Maxwell-Stefan binary friction coefficient [s m^{-2}]*
G	*Gibbs free enthalpy [J]*
h	*Height [m]*

I	*Ionic strength [eq m^{-3}]*
IEC	*Ion-Exchange Capacity [mol $kg_{dry\ polymer}^{-1}$]*
$\vec{J}$	*Current density [C m^{-2} s^{-1}]*
j	*Current [C s^{-1}]*
K^p	*Partition coefficient [-]*
$K_{i,j}$	*Maxwell-Stefan friction factor [J s m^{-5}]*
k_B	*Boltzman's constant [J K^{-1}]*
L	*Length [m]*
$\mathcal{L}_{i,j}$	*Inverted Maxwell-Stefan friction factor [m^5 J^{-1} s^{-1}]*
l	*Phenomenological transport coefficient [mol^2 m^{-1} s^{-1} J^{-1}]*
M	*Mass [kg]*
$\mathcal{M}_{i,j}$	*Maxwell-Stefan composed friction factor [mol s m^{-5}]*
m	*Molal concentration [mol kg^{-1}]*
MW	*Molar mass [kg mol^{-1}]*
N	*Number of data points [-]*
$\vec{N}$	*Flux in a stationary reference frame [mol m^{-2} s^{-1}]*
N_a	*Avogadro's number [mol^{-1}]*
n	*Number of moles [mol]*
P	*Pressure [Pa]*
P_s	*Salt permeability [m^2 s^{-1}]*
$\mathrm{p_s}$	*Relative salt permeability [-]*
P_{tot}	*Total pressure (hydrostatic-osmotic) [Pa]*
P_w	*Water permeability [m s^{-1}]*
Q	*Flow rate [m^3 s^{-1}]*
R	*Ohmic resistance [Ω]*
R_g	*Universal gas constant [J mol^{-1} K^{-1}]*

r	*Radial position[m]*
r_0	*Debye-Hückel ion's radius [-]*
r_B	*Born radius [m]*
S	*Entropy [J K^{-1}]*
S^p	*Partition selectivity [-]*
S^c	*Condensation selectivity [-]*
S^s	*Separation selectivity [-]*
S_{bet}	*Specific surface [m^2 kg^{-1}]*
s	*Specific entropy [J K^{-1} m^{-3}]*
SEC	*Specific Energy Consumption [J kg^{-1}]*
SP	*Specific Productivity [kg m^{-2} s^{-1}]*
T	*Temperature [K]*
t	*Time [s]*
t_i	*Transport number [-]*
u	*Electrophoretic mobility [m^2 mol J^{-1} s^{-1}]*
V	*Volume [m^{-3}]*
$\vec{v}$	*Velocity [m s^{-1}]*
$\vec{\bar{v}}$	*Molar average velocity [m s^{-1}]*
v_s	*Fluid velocity in the solution channel [m s^{-1}]*
w	*Mass fraction [-]*
w_u	*Water uptake [kg$_{water}$ kg$_{dry\ polymer}^{-1}$]*
w_{el}	*Electrical work [J mol^{-1}]*
X	*Effective molar fraction [-]*
x	*Molar fraction [-]*
Z	*Impedance [Ω]*
Z'	*Impedance real part (Resistance) [Ω]*
Z''	*Impedance imaginary part (Reactance) [Ω]*

z	*Ion valence [-]*

Greek letters

α	*Nonrandomness parameters [-]*
β	*Debye-Hückel's equation lumped parameter [$m^{3/2}$ $mol^{-1/2}$]*
$\beta_{i,j}$	*Debye-Hückel's ion-ion binary diffusion coefficient fitting parameter [$m^{3/2}$ $mol^{-1/2}$]*
$\Gamma_{i(n)}$	*Diffusion coefficient thermodynamic correcting factor [-]*
γ	*Activity coefficient [-]*
$\bar{\gamma}$	*Mean ionic activity coefficient [-]*
$\tilde{\gamma}$	*Absolute activity coefficient [-]*
δ	*Thickness [m]*
ε	*Relative dielectric constant [-]*
ε_0	*Vacuum dielectric constant [F m^{-1}]*
ε_c	*Condensed phase dielectric constant [-]*
ε_u	*Uncondensed phase dielectric constant [-+*
ϵ	*Membrane porosity [-]*
ζ	*Debye-Hückel's equation lumped parameter [$m^{3/2}$ $mol^{-1/2}$]*
$\zeta_{i,j}$	*Debye-Hückel ion-ion binary diffusion coefficient fitting parameter [$m^{3/2}$ $mol^{-1/2}$]*
η_r	*Relative viscosity [-]*
θ	*Condensed fraction [-]*
$\bar{\theta}$	*Uncondensed fraction [-]*
ϑ	*Polarization coefficient [-]*
$\varkappa$	*Debye screening parameter [m^{-1}]*
$\bar{\varkappa}$	*Uncondensed phase Debye screening parameter [m^{-1}]*
κ	*Ionic conductivity [S m^{-1}]*
λ	*Absolute activity [-]*

λ_b	*Bjerrum length [m]*
μ	*Chemical potential [J mol^{-1}]*
$\tilde{\mu}$	*Electrochemical potential [J mol^{-1}]*
μ^{chem}	*Chemical component of electrochemical potential [J mol^{-1}]*
μ^{cond}	*Condensation free energy [J mol^{-1}]*
μ^{hyd}	*Hydration free energy [J mol^{-1}]*
ν	*Stoichiometric coefficient [-]*
ξ	*Reduced linear charge density [-]*
ξ_c	*Reduced critical linear charge density [-]*
Π	*Osmotic pressure [Pa]*
ρ	*Mass density [kg m^{-3}]*
ρ_{el}	*Charge density [C m^{-3}]*
ρ_{bulk}	*Particles bulk density [kg m^{-3}]*
ρ_{tot}	*Solution mass density [kg m^{-3}]*
ϱ	*Pitzer closest approach parameter [-]*
σ_{el}	*Charge density per unit of mass [C kg^{-1}]*
ς_{el}	*Volumetric fraction of suspended solids [-]*
τ	*Membrane tortuosity [-]*
τ_{ij}	*Binary asymmetric interaction parameters [-]*
υ	*Partial molar volume [m^3 mol^{-1}]*
Φ_γ	*Non-ideal partition coefficient contribution [-]*
$\Phi_{\Delta\varphi}$	*Electrostatic partition coefficient contribution [-]*
$\Phi_{\Delta P}$	*Osmotic partition coefficient contribution [-]*
φ	*(Quasi-)Electrostatic potential [V]*
ϕ_w	*Swelling degree [-]*
ϕ	*Osmotic coefficient [-]*

$\Delta\varphi$	*Donnan potential [V]*
$\chi_{i,j}$	*Activity coefficient partial derivative [-]*
Ψ	*Specific entropy production rate [J K^{-1} s^{-1} m^{-3}]*
ψ_i	*Effective viscous molar volume [m^3 mol^{-1}]*
ω	*Frequency [Hz]*
ϖ	*Standard deviation [variable]*

Superscripts

$*$	*Secondary thermodynamic reference state*
$\#$	*Non-stationary reference frame*
$'$	*Interstitial/per unit of pore surface area*
$+$	*Left side*
$-$	*Right side*
∞	*Bulk*
∞_0	*Infinite dilution state*
0	*Primary reference state*
α, β	*Generic phases*
AEM	*Anion-Exchange membrane*
(C)	*Molar-based*
ds	*Desorption solution*
ex	*Excess (i.e., non-ideal)*
$exp.$	*Experimental point*
id	*Ideal*
int	*Interface*
LC	*Local contribution*
$LiSM$	*Lithium-Selective Membrane*
M	*Manning contribution*

m	*Membrane phase*
(m)	*Molal-based*
p	*Unit of volume of swollen membrane*
$pred.$	*Predicted point*
$pure$	*Pure state/component*
PDH	*Pitzer-Debye-Hückel contribution*
s	*Solution phase*
w	*Unit of volume of sorbed solution*
(x)	*Molar fraction-based*

Subscripts

i, j, k	*Components*
a	*Anionic species*
AEM	*Anion-Exchange Membrane*
B	*Blank*
C	*Concentration*
c	*Cationic species*
CEM	*Cation-Exchange Membrane*
co	*Co-ions*
cou	*Counter-ions*
$cloud$	*Ionic cloud*
$chain$	*Linear charge distribution*
$cond$	*Conductive component*
DBL	*Diffusion Boundary Layer*
$diff.$	*Diffusion/Diffusive component*
dry	*Dry membrane*
el	*Electrode/Electrode channel*
ext	*Externally applied*

F	*Feed*
fix	*Fixed charges*
in	*Inlet*
ij	*Electrolyte*
m	*Membrane*
N	*Nernst contribution*
(n)	*Quasi-electrostatic potential reference species*
ohm	*Ohmic/Conductive*
out	*Outlet*
p	*Ion containing polymer*
$pure$	*Pure component*
R	*Receiver*
s	*Solution/Solution channel*
$salt$	*Salt*
tot	*Total*
V	*Volume*
w	*Water*
wet	*Wet membrane*

Acronims

AC	Alternating Current / Activated Carbon
AEL	Anion-Exchange Layer
AEM	Anion-Exchange Membrane
ARED	Assisted Reverse ElectroDialysis
BF	Binary Friction
CDI	Capacitive De-Ionization
CE	Counter Electrode
CED	Capacitive Electrodialysis

CEL	Cation-Exchange Layer
CEM	Cation-Exchange Membrane
DBL	Diffusion Boundary Layer
DC	Direct Current
DI	DeIonized
ED	ElectroDialysis
EDBM	Bipolar Membrane ElectroDialysis
EDL	Electric Double Layer
EIS	Electrochemical Impedance Spectroscopy
FCDI	Flow Capacitive De-Ionization
FRA	Frequency Response Analyzer
IEC	Ion-Exchange Capacity
IEM	Ion-Exchange Membrane
LC	Local Contribution
Li-MFCDI	Lithium Membrane Flow Capacitive De-Ionization
LiSM	Lithium Selective Membrane
MRD	Mean Relative Deviation
MS	Maxwell-Stefan
NP	Nernst-Planck
PDH	Pitzer-Debye-Hückel
RE	Reference Electrode
RED	Reverse Electrodialysis
SC	Single Cycle
SE	Sense Electrode
SEC	Specific Energy Consumption
SP	Specific Productivity

WE	Working Electrode
ZLD	Zero Liquid Discharge

References

[1] H. Fan, Y. Huang, N.Y. Yip, Advancing the conductivity-permselectivity tradeoff of electrodialysis ion-exchange membranes with sulfonated CNT nanocomposites, J. Memb. Sci. 610 (2020) 118259. https://doi.org/10.1016/j.memsci.2020.118259.

[2] H. Fan, Y. Huang, I.H. Billinge, S.M. Bannon, G.M. Geise, N.Y. Yip, Counterion Mobility in Ion-Exchange Membranes: Spatial Effect and Valency-Dependent Electrostatic Interaction, ACS ES T Eng. 2 (2022) 1274–1286. https://doi.org/10.1021/acsestengg.1c00457.

[3] Y. Huang, H. Fan, N.Y. Yip, Influence of electrolyte on concentration-induced conductivity-permselectivity tradeoff of ion-exchange membranes, J. Memb. Sci. 668 (2023) 121184. https://doi.org/10.1016/j.memsci.2022.121184.

[4] A. Kumar, F. Du, J.H. Lienhard, Caustic Soda Production, Energy Efficiency, and Electrolyzers, ACS Energy Lett. 6 (2021) 3563–3566. https://doi.org/10.1021/acsenergylett.1c01827.

[5] A. Filingeri, J. Lopez, A. Culcasi, T. Leon, A. Tamburini, J. Luis Cortina, G. Micale, A. Cipollina, In-depth insights on multi-ionic transport in Electrodialysis with bipolar membrane systems, Chem. Eng. J. 468 (2023). https://doi.org/10.1016/j.cej.2023.143673.

[6] H. Strathmann, Ion-Exchange Membrane Processes: Their Principle and Practical Applications, 2016.

[7] Y. Tanaka, Ion Exchange Membranes: Fundamentals and Applications: Second Edition, 2015. https://doi.org/10.1016/C2013-0-12870-X.

[8] M.C. Martí-Calatayud, M. García-Gabaldón, V. Pérez-Herranz, S. Sales, S. Mestre, Ceramic anion-exchange membranes based on microporous supports infiltrated with hydrated

zirconium dioxide, RSC Adv. 5 (2015) 46348–46358. https://doi.org/10.1039/c5ra04169d.

[9] H.M. Saif, R.M. Huertas, S. Pawlowski, J.G. Crespo, S. Velizarov, Development of highly selective composite polymeric membranes for Li+/Mg2+ separation, J. Memb. Sci. 620 (2021) 118891. https://doi.org/10.1016/j.memsci.2020.118891.

[10] R.S. Kingsbury, S. Zhu, S. Flotron, O. Coronell, Microstructure Determines Water and Salt Permeation in Commercial Ion-Exchange Membranes, ACS Appl. Mater. Interfaces 10 (2018) 39745–39756. https://doi.org/10.1021/acsami.8b14494.

[11] V.I. Zabolotsky, V. V. Nikonenko, Effect of structural membrane inhomogeneity on transport properties, J. Memb. Sci. 79 (1993) 181–198. https://doi.org/10.1016/0376-7388(93)85115-D.

[12] N. Kononenko, V. Nikonenko, D. Grande, C. Larchet, L. Dammak, M. Fomenko, Y. Volfkovich, Porous structure of ion exchange membranes investigated by various techniques, Adv. Colloid Interface Sci. 246 (2017) 196–216. https://doi.org/10.1016/j.cis.2017.05.007.

[13] T. Luo, S. Abdu, M. Wessling, Selectivity of ion exchange membranes: A review, J. Memb. Sci. 555 (2018) 429–454. https://doi.org/10.1016/j.memsci.2018.03.051.

[14] S. Jiang, H. Sun, H. Wang, B.P. Ladewig, Z. Yao, A comprehensive review on the synthesis and applications of ion exchange membranes, Chemosphere 282 (2021) 130817. https://doi.org/10.1016/j.chemosphere.2021.130817.

[15] S. Koter, P. Piotrowski, J. Kerres, Comparative investigations of ion-exchange membranes, J. Memb. Sci. 153 (1999) 83–90. https://doi.org/10.1016/S0376-7388(98)00242-7.

[16] N. Yan, D.R. Paul, B.D. Freeman, Water and ion sorption in a series of cross-linked AMPS/PEGDA hydrogel membranes, Polymer (Guildf). 146 (2018) 196–208. https://doi.org/10.1016/j.polymer.2018.05.021.

[17] R.W. Baker, Membrane Technology and Applications, Wiley, 2004. https://doi.org/10.1002/0470020393.

[18] F. Giacalone, P. Catrini, A. Tamburini, A. Cipollina, A. Piacentino, G. Micale, Exergy analysis of reverse electrodialysis, Energy Convers. Manag. 164 (2018) 588–602. https://doi.org/10.1016/j.enconman.2018.03.014.

[19] Y. Mei, C.Y. Tang, Recent developments and future perspectives of reverse electrodialysis technology: A review, Desalination 425 (2018) 156–174. https://doi.org/10.1016/j.desal.2017.10.021.

[20] A. Culcasi, Electrical energy storage devices based on pH and salinity gradients: modelling, experiments and piloting, (2021).

[21] M. Herrero-Gonzalez, P. Diaz-Guridi, A. Dominguez-Ramos, R. Ibañez, A. Irabien, Photovoltaic solar electrodialysis with bipolar membranes, Desalination 433 (2018) 155–163. https://doi.org/10.1016/j.desal.2018.01.015.

[22] K. Kontturi, L. Murtomäki, J.A. Manzanares, Ionic Transport Processes: In Electrochemistry and Membrane Science, Ion. Transp. Process. Electrochem. Membr. Sci. 9780199533 (2008) 1–304. https://doi.org/10.1093/acprof:oso/9780199533817.001.0001.

[23] P.C. Hiemenz, Principles of Colloid and Surface Chemistry, Revised and Expanded, CRC Press, 2016. https://doi.org/10.1201/9781315274287.

[24] K.G. Denbigh, C. V. King, The Principles of Chemical Equilibrium, J. Electrochem. Soc. 103 (1956) 137C. https://doi.org/10.1149/1.2430318.

[25] K.S. Pitzer, Activity Coefficients in Electrolyte Solutions, CRC Press, 2018. https://doi.org/10.1201/9781351069472.

[26] C.W. Monroe, C. Delacourt, Continuum transport laws for locally non-neutral concentrated electrolytes, Electrochim. Acta 114 (2013) 649–657. https://doi.org/10.1016/j.electacta.2013.10.006.

[27] Y. Song, C.C. Chen, Symmetric electrolyte nonrandom two-liquid activity coefficient model,

Ind. Eng. Chem. Res. 48 (2009) 7788–7797. https://doi.org/10.1021/ie9004578.

[28] C.-C. Chen, L.B. Evans, A local composition model for the excess Gibbs energy of aqueous electrolyte systems, AIChE J. 32 (1986) 444–454. https://doi.org/10.1002/aic.690320311.

[29] T.S. Sørensen, V. Compañ, On the Gibbs-Duhem equation for thermodynamic systems of mixed Euler order with special reference to gravitational and nonelectroneutral systems, Electrochim. Acta 42 (1997) 639–649. https://doi.org/10.1016/S0013-4686(96)00209-5.

[30] J.O. Bockris, A.K.N. Reddy, Modern Electrochemistry vol. I: Ionics, Springer US, Boston, MA, 1973. https://doi.org/10.1007/978-1-4613-4560-2.

[31] E.A. Guggenheim, H.W. Woolley, Thermodynamics: An Advanced Treatment for Chemists and Physicists, Phys. Today 10 (1957) 36–36. https://doi.org/10.1063/1.3060168.

[32] N.P.B. John Newman, Electrochemical systems, fourth edition, fourth, 2021. http://catalysis.eprints.iitm.ac.in/3600/1/%28Electrochemical Society series%29 John S. Newman_ Nitash P. Balsara - Electrochemical systems %282021%29.pdf.

[33] W.H. Smyrl, J. Newman, Potentials of cells with liquid junctions, J. Phys. Chem. 72 (1968) 4660–4671. https://doi.org/10.1021/j100859a051.

[34] C.W. Monroe, Ionic Mobility and Diffusivity, 2014. https://doi.org/10.1007/978-1-4419-6996-5.

[35] E.J. Lam, M.N. Alvarez, M.E. Galvez, E.B. Alvarez, A model for calculating the density of aqueous multicomponent electrolyte solutions, J. Chil. Chem. Soc. 53 (2008) 1404–1409. https://doi.org/10.4067/S0717-97072008000100015.

[36] M. Laliberté, W.E. Cooper, Model for calculating the density of aqueous electrolyte solutinos, J. Chem. Eng. Data 49 (2004) 1141–1151. https://doi.org/10.1021/je0498659.

[37] A.A. Rashin, B. Honig, Reevaluation of the Born model of ion hydration, J. Phys. Chem. 89

(1985) 5588–5593. https://doi.org/10.1021/j100272a006.

[38] Y. Marcus, G. Hefter, Ion pairing, Chem. Rev. 106 (2006) 4585–4621. https://doi.org/10.1021/cr040087x.

[39] Y. Marcus, Thermodynamics of Solvation of Ions, 87 (1991) 2995–2999. https://doi.org/10.1039/FT9918702995.

[40] E.R. Nightingale, Phenomenological theory of ion solvation. Effective radii of hydrated ions, J. Phys. Chem. 63 (1959) 1381–1387. https://doi.org/10.1021/j150579a011.

[41] B.Y.J.W. Akitt, Limiting Single-ion Molar Volumes, i (1980) 2259–2284.

[42] J.O. Bockris, A.K.N. Reddy, Modern Electrochemistry vol. I: Ionics, Springer US, Boston, MA, 1973. https://doi.org/10.1007/978-1-4613-4560-2.

[43] J.E. Biesheuvel, P. M., & Dykstra, Physics of Electrochemical Processes, 2020.

[44] R. Wang, P.M. Biesheuvel, M. Elimelech, Extended Donnan model for ion partitioning in charged nanopores: Application to ion-exchange membranes, J. Memb. Sci. 705 (2024) 122921. https://doi.org/10.1016/j.memsci.2024.122921.

[45] A. Campione, L. Gurreri, M. Ciofalo, G. Micale, A. Tamburini, A. Cipollina, Electrodialysis for water desalination: A critical assessment of recent developments on process fundamentals, models and applications, Desalination 434 (2018) 121–160. https://doi.org/10.1016/j.desal.2017.12.044.

[46] A.H. Galama, J.W. Post, M.A. Cohen Stuart, P.M. Biesheuvel, Validity of the Boltzmann equation to describe Donnan equilibrium at the membrane-solution interface, J. Memb. Sci. 442 (2013) 131–139. https://doi.org/10.1016/j.memsci.2013.04.022.

[47] S.M. Bannon, G.M. Geise, Influence of Donnan and dielectric exclusion on ion sorption in sulfonated polysulfones, J. Memb. Sci. 694 (2024) 122396.

https://doi.org/10.1016/j.memsci.2023.122396.

[48] A.Z. Weber, J. Newman, Transport in Polymer-Electrolyte Membranes, J. Electrochem. Soc. 151 (2004) A311. https://doi.org/10.1149/1.1639157.

[49] A.R. Crothers, R.M. Darling, A. Kusoglu, C.J. Radke, A.Z. Weber, Theory of Multicomponent Phenomena in Cation-Exchange Membranes: Part I. Thermodynamic Model and Validation, J. Electrochem. Soc. 167 (2020) 013547. https://doi.org/10.1149/1945-7111/ab6723.

[50] J. Kamcev, M. Galizia, F.M. Benedetti, E.S. Jang, D.R. Paul, B.D. Freeman, G.S. Manning, Partitioning of mobile ions between ion exchange polymers and aqueous salt solutions: Importance of counter-ion condensation, Phys. Chem. Chem. Phys. 18 (2016) 6021–6031. https://doi.org/10.1039/c5cp06747b.

[51] J. Kamcev, D.R. Paul, B.D. Freeman, Equilibrium ion partitioning between aqueous salt solutions and inhomogeneous ion exchange membranes, Desalination 446 (2018) 31–41. https://doi.org/10.1016/j.desal.2018.08.018.

[52] V. Freger, Ion partitioning and permeation in charged low-T* membranes, Adv. Colloid Interface Sci. 277 (2020) 102107. https://doi.org/10.1016/j.cis.2020.102107.

[53] Z.J. Lim, M. Kho, W. Toh, X. Chen, K.B. Goh, Coion exclusion properties of cation exchange membranes in 2:1 divalent salt solutions, Desalination 574 (2024) 117179. https://doi.org/10.1016/j.desal.2023.117179.

[54] P. Aydogan Gokturk, R. Sujanani, J. Qian, Y. Wang, L.E. Katz, B.D. Freeman, E.J. Crumlin, The Donnan potential revealed, Nat. Commun. 13 (2022). https://doi.org/10.1038/s41467-022-33592-3.

[55] K.S. Pitzer, Thermodynamics of electrolytes. I. Theoretical basis and general equations, J. Phys. Chem. 77 (1973) 268–277. https://doi.org/10.1021/j100621a026.

[56] K.S. Pitzer, G. Mayorga, Thermodynamics of electrolytes. II. Activity and osmotic coefficients

for strong electrolytes with one or both ions univalent, J. Phys. Chem. 77 (1973) 2300–2308. https://doi.org/10.1021/j100638a009.

[57] K.S. Pitzer, G. Mayorga, Thermodynamics of electrolytes. III. Activity and osmotic coefficients for 2-2 electrolytes, J. Solution Chem. 3 (1974) 539–546. https://doi.org/10.1007/BF00648138.

[58] K.S. Pitzer, J.J. Kim, Thermodynamics of electrolytes. IV Activity and osmotic coefficients for Mixed Electrolytes, J. Solution Chem. 3 (1974) 539–546. https://doi.org/10.1007/BF00648138.

[59] K.S. Pitzer, Thermodynamics of electrolytes. V. effects of higher-order electrostatic terms, J. Solution Chem. 4 (1975) 249–265. https://doi.org/10.1007/BF00646562.

[60] S. Tanveer, C.C. Chen, A comprehensive thermodynamic model for high salinity produced waters, AIChE J. 66 (2020) 3–7. https://doi.org/10.1002/aic.16818.

[61] C.C. Chen, Y. Song, Generalized electrolyte-NRTL model for mixed-solvent electrolyte systems, AIChE J. 50 (2004) 1928–1941. https://doi.org/10.1002/aic.10151.

[62] R. Wang, R. Duddu, S. Lin, Extended Donnan-Manning theory for selective ion partition and transport in ion exchange membrane, J. Memb. Sci. 681 (2023) 121782. https://doi.org/10.1016/j.memsci.2023.121782.

[63] M. Galizia, G.S. Manning, D.R. Paul, B.D. Freeman, Ion partitioning between brines and ion exchange polymers, Polymer (Guildf). 165 (2019) 91–100. https://doi.org/10.1016/j.polymer.2019.01.026.

[64] M. Galizia, F.M. Benedetti, D.R. Paul, B.D. Freeman, Monovalent and divalent ion sorption in a cation exchange membrane based on cross-linked poly (p-styrene sulfonate-co-divinylbenzene), J. Memb. Sci. 535 (2017) 132–142. https://doi.org/10.1016/j.memsci.2017.04.007.

[65] R.S. Kingsbury, K. Bruning, S. Zhu, S. Flotron, C.T. Miller, O. Coronell, Influence of Water Uptake, Charge, Manning Parameter, and Contact Angle on Water and Salt Transport in Commercial Ion Exchange Membranes, Ind. Eng. Chem. Res. 58 (2019) 18663–18674. https://doi.org/10.1021/acs.iecr.9b04113.

[66] G.M. Geise, D.R. Paul, B.D. Freeman, Fundamental water and salt transport properties of polymeric materials, Prog. Polym. Sci. 39 (2014) 1–42. https://doi.org/10.1016/j.progpolymsci.2013.07.001.

[67] D.R. Paul, Relation Between Hydraulic Permeability and Diffusion in Homogeneous Swollen Membranes., J Polym Sci Part A-2 Polym Phys 11 (1973) 289–296. https://doi.org/10.1002/pol.1973.180110210.

[68] G.M. Geise, B.D. Freeman, D.R. Paul, Sodium chloride diffusion in sulfonated polymers for membrane applications, J. Memb. Sci. 427 (2013) 186–196. https://doi.org/10.1016/j.memsci.2012.09.029.

[69] H. Fan, M. Heiranian, M. Elimelech, The solution-diffusion model for water transport in reverse osmosis: What went wrong?, Desalination 580 (2024) 117575. https://doi.org/10.1016/j.desal.2024.117575.

[70] J.G. Wijmans, R.W. Baker, The solution-diffusion model: a review, J. Memb. Sci. 107 (1995) 1–21. https://doi.org/10.1016/0376-7388(95)00102-I.

[71] V. Freger, G.Z. Ramon, The solution-diffusion model: “Rumors of my death have been exaggerated,” J. Membr. Sci. Lett. 4 (2024) 100084. https://doi.org/10.1016/j.memlet.2024.100084.

[72] S. Ozkul, J.J. van Daal, N.J.M. Kuipers, R.J.M. Bisselink, H. Bruning, J.E. Dykstra, H.H.M. Rijnaarts, Transport mechanisms in electrodialysis: The effect on selective ion transport in multi-ionic solutions, J. Memb. Sci. 665 (2023) 121114.

https://doi.org/10.1016/j.memsci.2022.121114.

[73] P.M. Biesheuvel, S. Porada, M. Elimelech, J.E. Dykstra, Tutorial review of reverse osmosis and electrodialysis, J. Memb. Sci. 647 (2022) 120221. https://doi.org/10.1016/j.memsci.2021.120221.

[74] L. Wang, T. Cao, J.E. Dykstra, S. Porada, P.M. Biesheuvel, M. Elimelech, Salt and Water Transport in Reverse Osmosis Membranes: Beyond the Solution-Diffusion Model, Environ. Sci. Technol. 55 (2021) 16665–16675. https://doi.org/10.1021/acs.est.1c05649.

[75] J.C. Díaz, J. Park, A. Shapiro, H. Patel, L. Santiago-Pagán, D. Kitto, J. Kamcev, Understanding Monovalent Cation Diffusion in Negatively Charged Membranes and the Role of Membrane Water Content, Macromolecules 57 (2024) 2468–2481. https://doi.org/10.1021/acs.macromol.3c02655.

[76] S.M. Bannon, B.M. Tremblay, A. Boudreau, N. Sreedhar, C. Morin, C.R. Leroux, P. Phan, A. Roy, M. Paul, G.M. Geise, Characterizing Hydrated Polymers via Dielectric Relaxation Spectroscopy: Connecting Relative Permittivity, State of Water, and Salt Transport Properties of Sulfonated Polysulfones, Macromolecules (2025). https://doi.org/10.1021/acs.macromol.5c00616.

[77] D. Kitto, J. Kamcev, Manning condensation in ion exchange membranes: A review on ion partitioning and diffusion models, J. Polym. Sci. 60 (2022) 2929–2973. https://doi.org/10.1002/pol.20210810.

[78] M.L. Vera, W.R. Torres, C.I. Galli, A. Chagnes, V. Flexer, Environmental impact of direct lithium extraction from brines, Nat. Rev. Earth Environ. 4 (2023) 149–165. https://doi.org/10.1038/s43017-022-00387-5.

[79] G. Purpura, E. Papiewska, A. Culcasi, A. Filingeri, A. Tamburini, M.C. Ferrari, G. Micale, A. Cipollina, Modelling of selective ion partitioning between ion-exchange membranes and

highly concentrated multi-ionic brines, J. Memb. Sci. 700 (2024) 122659. https://doi.org/10.1016/j.memsci.2024.122659.

[80] G.S. Manning, Limiting laws and counterion condensation in polyelectrolyte solutions I. Colligative properties, J. Chem. Phys. 51 (1969) 924–933. https://doi.org/10.1063/1.1672157.

[81] J. Kamcev, D.R. Paul, B.D. Freeman, Ion activity coefficients in ion exchange polymers: Applicability of Manning's counterion condensation theory, Macromolecules 48 (2015) 8011–8024. https://doi.org/10.1021/acs.macromol.5b01654.

[82] T. Luo, F. Roghmans, M. Wessling, Ion mobility and partition determine the counter-ion selectivity of ion exchange membranes, J. Memb. Sci. 597 (2020) 117645. https://doi.org/10.1016/j.memsci.2019.117645.

[83] Z. Zou, L. Wu, T. Luo, Z. Yan, X. Wang, Assessment of anion exchange membrane selectivity with ionic membrane conductivity, revised with Manning's theory or the Kohlrausch's law, J. Memb. Sci. 635 (2021) 119496. https://doi.org/10.1016/j.memsci.2021.119496.

[84] S. Ozkul, O. Arbabzadeh, R.J.M. Bisselink, N.J.M. Kuipers, H. Bruning, H.H.M. Rijnaarts, J.E. Dykstra, Selective adsorption in ion exchange membranes: The effect of solution ion composition on ion partitioning, Water Res. 254 (2024) 121382. https://doi.org/10.1016/j.watres.2024.121382.

[85] G.Q. Chen, K. Wei, A. Hassanvand, B.D. Freeman, S.E. Kentish, Single and binary ion sorption equilibria of monovalent and divalent ions in commercial ion exchange membranes, Water Res. 175 (2020) 115681. https://doi.org/10.1016/j.watres.2020.115681.

[86] G.S. Manning, Limiting laws and counterion condensation in polyelectrolyte solutions. 8. Mixtures of counterions, species selectivity, and valence selectivity, J. Phys. Chem. 88 (1984) 6654–6661. https://doi.org/10.1021/j150670a030.

[87] E. Sireci, G. De Luca, J. Luque Di Salvo, A. Cipollina, G. Micale, Prediction of equilibrium

water uptake and ions diffusivities in ion-exchange membranes combining molecular dynamics and analytical models, J. Memb. Sci. 668 (2023) 121283. https://doi.org/10.1016/j.memsci.2022.121283.

[88] R. Sujanani, O. Nordness, A. Miranda, L.E. Katz, J.F. Brennecke, B.D. Freeman, Accounting for Ion Pairing Effects on Sulfate Salt Sorption in Cation Exchange Membranes, J. Phys. Chem. B 127 (2023) 1842–1855. https://doi.org/10.1021/acs.jpcb.2c07900.

[89] R.S. Kingsbury, O. Coronell, Modeling and validation of concentration dependence of ion exchange membrane permselectivity: Significance of convection and Manning's counter-ion condensation theory, J. Memb. Sci. 620 (2021) 118411. https://doi.org/10.1016/j.memsci.2020.118411.

[90] G.S. Manning, Counterion Binding in Polyelectrolyte Theory, Acc. Chem. Res. 12 (1979) 443–449. https://doi.org/10.1021/ar50144a004.

[91] S. Paoletti, J. Benegas, A. Cesàro, G. Manzini, F. Fogolari, V. Crescenzi, Limiting-laws of polyelectrolyte solutions. Ionic distribution in mixed-valency counterions systems. I: The model, Biophys. Chem. 41 (1991) 73–80. https://doi.org/10.1016/0301-4622(91)87211-M.

[92] J.R. Bontha, P.N. Pintauro, Water orientation and ion solvation effects during multicomponent salt partitioning in a Nafion cation exchange membrane, Chem. Eng. Sci. 49 (1994) 3835–3851. https://doi.org/10.1016/0009-2509(94)00205-3.

[93] K. Chang, H. Luo, G.M. Geise, Influence of Salt Concentration on Hydrated Polymer Relative Permittivity and State of Water Properties, Macromolecules 54 (2021) 637–646. https://doi.org/10.1021/acs.macromol.0c02188.

[94] S.M. Bannon, G.M. Geise, Application of the Born Model to Describe Salt Partitioning in Hydrated Polymers, ACS Macro Lett. 13 (2024) 515–520. https://doi.org/10.1021/acsmacrolett.4c00048.

[95] J.D. Wells, Thermodynamics of Polyelectrolyte Solutions., Biopolymers 12 (1973) 223–227.

[96] Y. Yu, Y. Li, N. Hossain, C.C. Chen, Nonrandom two-liquid activity coefficient model for aqueous polyelectrolyte solutions, Fluid Phase Equilib. 497 (2019) 1–9. https://doi.org/10.1016/j.fluid.2019.05.009.

[97] Y. Yu, N. Yan, B.D. Freeman, C.-C.C. Chen, Mobile ion partitioning in ion exchange membranes immersed in saline solutions, J. Memb. Sci. 620 (2021) 118760. https://doi.org/10.1016/j.memsci.2020.118760.

[98] K.S. Pitzer, J.M. Simonson, Thermodynamics of multicomponent, miscible, ionic systems: theory and equations, J. Phys. Chem. 90 (1986) 3005–3009. https://doi.org/10.1021/j100404a042.

[99] H. Renon, J.M. Prausnitz, Local compositions in thermodynamic excess functions for liquid mixtures, AIChE J. 14 (1968) 135–144. https://doi.org/10.1002/aic.690140124.

[100] H. Yasuda, C.E. Lamaze, L.D. Ikenberry, Permeability of solutes through hydrated polymer membranes. Part I. Diffusion of sodium chloride, Die Makromol. Chemie 118 (1968) 19–35. https://doi.org/10.1002/macp.1968.021180102.

[101] X. Chen, K.B. Goh, Quantifying the coupled monovalent and divalent ions sorption in dense ion-exchange membranes, J. Memb. Sci. 666 (2023) 121140. https://doi.org/10.1016/j.memsci.2022.121140.

[102] A.A.E. Elozeiri, R.G.H. Lammertink, S. Lin, H.H.M. Rijnaarts, J.E. Dykstra, Counter-ion mobility in cation-exchange membranes: Single electrolytes versus mixtures, J. Memb. Sci. 718 (2025) 123636. https://doi.org/10.1016/j.memsci.2024.123636.

[103] J. Kamcev, E.S. Jang, N. Yan, D.R. Paul, B.D. Freeman, Effect of ambient carbon dioxide on salt permeability and sorption measurements in ion-exchange membranes, J. Memb. Sci. 479 (2015) 55–66. https://doi.org/10.1016/j.memsci.2014.12.031.

[104] E.-S.S. Jang, J. Kamcev, K. Kobayashi, N. Yan, R. Sujanani, S.J. Talley, R.B. Moore, D.R. Paul, B.D. Freeman, Effect of Water Content on Sodium Chloride Sorption in Cross-Linked Cation Exchange Membranes, Macromolecules 52 (2019) 2569–2579. https://doi.org/10.1021/acs.macromol.8b02550.

[105] J.C. Díaz, J. Kamcev, Ionic conductivity of ion-exchange membranes: Measurement techniques and salt concentration dependence, J. Memb. Sci. 618 (2021) 118718. https://doi.org/10.1016/j.memsci.2020.118718.

[106] G.M. Geise, B.D. Freeman, D.R. Paul, Characterization of a sulfonated pentablock copolymer for desalination applications, Polymer (Guildf). 51 (2010) 5815–5822. https://doi.org/10.1016/j.polymer.2010.09.072.

[107] A.A.E. Elozeiri, J.E. Dykstra, H.H.M. Rijnaarts, R.G.H. Lammertink, Multi-component ion equilibria and transport in ion-exchange membranes, J. Colloid Interface Sci. 673 (2024) 971–984. https://doi.org/10.1016/j.jcis.2024.06.025.

[108] S.M. Bannon, E. Kutner, B. Garretson, G.M. Geise, Understanding the influence of sodium chloride concentration on ion diffusion in charged polymers, J. Memb. Sci. 712 (2024) 123197. https://doi.org/10.1016/j.memsci.2024.123197.

[109] J. Kamcev, R. Sujanani, E.S. Jang, N. Yan, N. Moe, D.R. Paul, B.D. Freeman, Salt concentration dependence of ionic conductivity in ion exchange membranes, J. Memb. Sci. 547 (2018) 123–133. https://doi.org/10.1016/j.memsci.2017.10.024.

[110] FuelCell store, FKE-50 Techincal specification, (n.d.). https://www.fuelcellstore.com/spec-sheets/fumasep-fke-50-technical-specifications.pdf.

[111] FuelCell store, FKS-50 technical specifications, (2021) 24–25. https://www.fuelcellstore.com/spec-sheets/fumasep-fks-50-technical-specifications.pdf.

[112] P.J. Flory, J. Rehner, Statistical mechanics of cross-linked polymer networks II. Swelling, J.

Chem. Phys. 11 (1943) 521–526. https://doi.org/10.1063/1.1723792.

[113] C. Espinoza, D. Kitto, J. Kamcev, Counter-ion Conductivity and Selectivity Trade-Off for Commercial Ion-Exchange Membranes at High Salinities, ACS Appl. Polym. Mater. 5 (2023) 10324–10333. https://doi.org/10.1021/acsapm.3c02102.

[114] D. Kitto, J. Kamcev, Predicting the Conductivity-Selectivity Trade-Off and Upper Bound in Ion-Exchange Membranes, ACS Energy Lett. 9 (2024) 1346–1352. https://doi.org/10.1021/acsenergylett.4c00301.

[115] D. Kitto, C. Espinoza, J.C. Díaz, J. Zamora, J. Kamcev, Fast and selective ion transport in ultrahigh-charge-density membranes, Nat. Chem. Eng. 2 (2025) 252–260. https://doi.org/10.1038/s44286-025-00205-x.

[116] V. Freger, Dielectric exclusion, an éminence grise, Adv. Colloid Interface Sci. 319 (2023). https://doi.org/10.1016/j.cis.2023.102972.

[117] H. Fan, M. Elimelech, P.M. Biesheuvel, Theory of expansion and compression of polymeric materials: Implications for membrane solvent flow under compaction, J. Memb. Sci. 697 (2024) 122576. https://doi.org/10.1016/j.memsci.2024.122576.

[118] T. Luo, Y. Zhong, D. Xu, X. Wang, M. Wessling, Combining Manning's theory and the ionic conductivity experimental approach to characterize selectivity of cation exchange membranes, J. Memb. Sci. 629 (2021) 119263. https://doi.org/10.1016/j.memsci.2021.119263.

[119] E.N. Bird, R.B., Stewart, W.E. and Lightfoot, Transport phenomena, 2nd ed., Wiley, New York, 2002.

[120] K. Kontturi, L. Murtomäki, J.A. Manzanares, Ionic Transport Processes, Oxford University Press, 2008. https://doi.org/10.1093/acprof:oso/9780199533817.001.0001.

[121] O. Medvedev, Diffusion Coefficients in Multicomponent Mixtures, Technical University of Denmark., 2005. https://core.ac.uk/download/pdf/13690545.pdf.

[122] T. Ross, R. Krishna, Multicomponent Mass Transfer, Wiley, 1993.

[123] O. Medvedev, Diffusion Coefficients in Multicomponent Mixtures, Technical University of Denmark., 2005.

[124] A.R. Felmy, J.H. Weare, Calculation of multicomponent ionic diffusion from zero to high concentration: II. Inclusion of associated ion species, Geochim. Cosmochim. Acta 55 (1991) 133–144. https://doi.org/10.1016/0016-7037(91)90406-U.

[125] M. Tedesco, H.V.M. Hamelers, P.M. Biesheuvel, Nernst-Planck transport theory for (reverse) electrodialysis: I. Effect of co-ion transport through the membranes, J. Memb. Sci. 510 (2016) 370–381. https://doi.org/10.1016/j.memsci.2016.03.012.

[126] R. Kubo, The fluctuation-dissipation theorem, Reports Prog. Phys. 29 (1966) 255–284. https://doi.org/10.1088/0034-4885/29/1/306.

[127] P. Lu, G. Zhang, J. Apps, C. Zhu, Comparison of thermodynamic data files for PHREEQC, Earth-Science Rev. 225 (2022) 103888. https://doi.org/10.1016/j.earscirev.2021.103888.

[128] J. Kamcev, D.R. Paul, G.S. Manning, B.D. Freeman, Accounting for frame of reference and thermodynamic non-idealities when calculating salt diffusion coefficients in ion exchange membranes, J. Memb. Sci. 537 (2017) 396–406. https://doi.org/10.1016/j.memsci.2017.05.034.

[129] S.H. Li, H. Mao, Y.N. Feng, L.H. Xu, H. Qi, Z.P. Zhao, A fundamental mass transport model based on molecular insights for pervaporation desalination, Nat. Commun. 16 (2025) 1–12. https://doi.org/10.1038/s41467-025-62664-3.

[130] A. Mazumder, B.M. Dobyns, M.P. Howard, B.S. Beckingham, Theoretical and Experimental Considerations for Investigating Multicomponent Diffusion in Hydrated, Dense Polymer Membranes, Membranes (Basel). 12 (2022) 942. https://doi.org/10.3390/membranes12100942.

[131] J. Fimrite, H. Struchtrup, N. Djilali, Transport Phenomena in Polymer Electrolyte Membranes, J. Electrochem. Soc. 152 (2005) A1804. https://doi.org/10.1149/1.1952627.

[132] A.R. Crothers, R.M. Darling, A. Kusoglu, C.J. Radke, A.Z. Weber, Theory of Multicomponent Phenomena in Cation-Exchange Membranes: Part II. Transport Model and Validation, J. Electrochem. Soc. 167 (2020) 013548. https://doi.org/10.1149/1945-7111/ab6724.

[133] J.A. Wesselingh, P. Vonk, G. Kraaijeveld, Exploring the Maxwell-Stefan description of ion exchange, Chem. Eng. J. Biochem. Eng. J. 57 (1995) 75–89. https://doi.org/10.1016/0923-0467(94)02932-6.

[134] L. Pisani, M. Valentini, D.H. Hofmann, L.N. Kuleshova, B. D'Aguanno, An analytical model for the conductivity of polymeric sulfonated membranes, Solid State Ionics 179 (2008) 465–476. https://doi.org/10.1016/j.ssi.2008.03.029.

[135] P. Knauth, L. Pasquini, R. Narducci, E. Sgreccia, R.A. Becerra-Arciniegas, M.L. Di Vona, Effective ion mobility in anion exchange ionomers: Relations with hydration, porosity, tortuosity, and percolation, J. Memb. Sci. 617 (2021) 118622. https://doi.org/10.1016/j.memsci.2020.118622.

[136] J.S. Mackie, P. Meares, The Diffusion of Electrolytes in a Cation-Exchange Resin Membrane . I . Theoretical, (1955) 498–509. https://doi.org/10.1098/rspa.1955.0234.

[137] J. Kamcev, D.R. Paul, G.S. Manning, B.D. Freeman, Predicting Salt Permeability Coefficients in Highly Swollen, Highly Charged Ion Exchange Membranes, ACS Appl. Mater. Interfaces 9 (2017) 4044–4056. https://doi.org/10.1021/acsami.6b14902.

[138] V. Vitagliano, P.A. Lyons, Diffusion Coefficients for Aqueous Solutions of Sodium Chloride and Barium Chloride, J. Am. Chem. Soc. 78 (1956) 1549–1552. https://doi.org/10.1021/ja01589a011.

[139] C. Delacourt, J. Newman, Mathematical Modeling of a Cation-Exchange Membrane

Containing Two Cations, J. Electrochem. Soc. 155 (2008) B1210. https://doi.org/10.1149/1.2977960.

[140] T.F. Fuller, S o l id - Pol ym e r-E l ect : r o ly t e Departme m of Chemical Engineering University of Calif o rnia Materials Sciences Division t o / Zo, 0 (n.d.). http://www.osti.gov/scitech/servlets/purl/7001224-oTjrVt/.

[141] D.R. Paul, Reformulation of the solution-diffusion theory of reverse osmosis, J. Memb. Sci. 241 (2004) 371–386. https://doi.org/10.1016/j.memsci.2004.05.026.

[142] C.P. Ribeiro, B.D. Freeman, D.R. Paul, Modeling of multicomponent mass transfer across polymer films using a thermodynamically consistent formulation of the Maxwell-Stefan equations in terms of volume fractions, Polymer (Guildf). 52 (2011) 3970–3983. https://doi.org/10.1016/j.polymer.2011.06.042.

[143] A.Z. Weber, J. Newman, Transport in Polymer-Electrolyte Membranes, J. Electrochem. Soc. 150 (2003) A1008. https://doi.org/10.1149/1.1580822.

[144] L. Wu, H. Jiang, T. Luo, X. Wang, On the Ionic Conductivity of Cation Exchange Membranes in Mixed Sulfates Using the Two-Phase Model, Membranes (Basel). 13 (2023). https://doi.org/10.3390/membranes13100811.

[145] P.J.A.M. Kerkhof, A modified Maxwell-Stefan model for transport through inert membranes: the binary friction model, Chem. Eng. J. Biochem. Eng. J. 64 (1996) 319–343. https://doi.org/10.1016/S0923-0467(96)03134-X.

[146] N.D.G. Pinto, E.E. Graham, Evaluation of diffusivities in electrolyte solutions using Stefan-Maxwell equations, AIChE J. 32 (1986) 291–296. https://doi.org/10.1002/aic.690320216.

[147] T. Chapman, The Transport Properties of Concentrated Electrolytic Solutions, Univ. California, Berkeley (1967).

[148] A.H. Galama, N.A. Hoog, D.R. Yntema, Method for determining ion exchange membrane

resistance for electrodialysis systems, Desalination 380 (2016) 1–11. https://doi.org/10.1016/j.desal.2015.11.018.

[149] P. Długołecki, P. Ogonowski, S.J. Metz, M. Saakes, K. Nijmeijer, M. Wessling, On the resistances of membrane, diffusion boundary layer and double layer in ion exchange membrane transport, J. Memb. Sci. 349 (2010) 369–379. https://doi.org/10.1016/j.memsci.2009.11.069.

[150] B.J. Christensen, T. Coverdale, R.A. Olson, S.J. Ford, E.J. Garboczi, H.M. Jennings, T.O. Mason, Impedance Spectroscopy of Hydrating Cement-Based Materials: Measurement, Interpretation, and Application, J. Am. Ceram. Soc. 77 (1994) 2789–2804. https://doi.org/10.1111/j.1151-2916.1994.tb04507.x.

[151] J.S. Park, J.H. Choi, J.J. Woo, S.H. Moon, An electrical impedance spectroscopic (EIS) study on transport characteristics of ion-exchange membrane systems, J. Colloid Interface Sci. 300 (2006) 655–662. https://doi.org/10.1016/j.jcis.2006.04.040.

[152] A.C. Lazanas, M.I. Prodromidis, Electrochemical Impedance Spectroscopy─A Tutorial, ACS Meas. Sci. Au 3 (2023) 162–193. https://doi.org/10.1021/acsmeasuresciau.2c00070.

[153] L. Gómez-Coma, V.M. Ortiz-Martínez, J. Carmona, L. Palacio, P. Prádanos, M. Fallanza, A. Ortiz, R. Ibañez, I. Ortiz, Modeling the influence of divalent ions on membrane resistance and electric power in reverse electrodialysis, J. Memb. Sci. 592 (2019) 117385. https://doi.org/10.1016/j.memsci.2019.117385.

[154] A. Kozmai, V. Sarapulova, M. Sharafan, K. Melkonian, T. Rusinova, Y. Kozmai, N. Pismenskaya, L. Dammak, V. Nikonenko, Electrochemical impedance spectroscopy of anion-exchange membrane amx-sb fouled by red wine components, Membranes (Basel). 11 (2021) 1–17. https://doi.org/10.3390/membranes11010002.

[155] T.M.E. Orazem, Bernard, Electrochemical impedance spectroscopy, 2nd ed., Wiley, 2017.

[156] R.S. Kingsbury, S. Flotron, S. Zhu, D.F. Call, O. Coronell, Junction Potentials Bias Measurements of Ion Exchange Membrane Permselectivity, Environ. Sci. Technol. 52 (2018) 4929–4936. https://doi.org/10.1021/acs.est.7b05317.

[157] G.J. Sloggett, N.G. Barton, S.J. Spencer, Fringing fields in disc capacitors, J. Phys. A. Math. Gen. 19 (1986) 2725–2736. https://doi.org/10.1088/0305-4470/19/14/012.

[158] J. Kamcev, D.R. Paul, G.S. Manning, B.D. Freeman, Ion Diffusion Coefficients in Ion Exchange Membranes: Significance of Counterion Condensation, Macromolecules 51 (2018) 5519–5529. https://doi.org/10.1021/acs.macromol.8b00645.

[159] Kuldeep, J.A. Manzanares, P. Kauranen, S. Mousavihashemi, L. Murtomäki, Determination of Ionic Diffusion Coefficients in Ion-Exchange Membranes: Strong Electrolytes and Sulfates with Dissociation Equilibria, ChemElectroChem 9 (2022) 1–11. https://doi.org/10.1002/celc.202200403.

[160] V. Sarapulova, I. Shkorkina, S. Mareev, N. Pismenskaya, N. Kononenko, C. Larchet, L. Dammak, V. Nikonenko, Transport Characteristics of Fujifilm Ion-Exchange Membranes as Compared to Homogeneous Membranes AMX and CMX and to Heterogeneous Membranes MK-40 and MA-41, Membranes (Basel). 9 (2019) 84. https://doi.org/10.3390/membranes9070084.

[161] O. Scialdone, C. Guarisco, S. Grispo, A.D. Angelo, A. Galia, Investigation of electrode material - Redox couple systems for reverse electrodialysis processes. Part I: Iron redox couples, J. Electroanal. Chem. 681 (2012) 66–75. https://doi.org/10.1016/j.jelechem.2012.05.017.

[162] M.L. La Cerva, M. Di Liberto, L. Gurreri, A. Tamburini, A. Cipollina, G. Micale, M. Ciofalo, Coupling CFD with a one-dimensional model to predict the performance of reverse electrodialysis stacks, J. Memb. Sci. 541 (2017) 595–610.

https://doi.org/10.1016/j.memsci.2017.07.030.

[163] G. Purpura, H.M. Saif, A. Culcasi, S. Pawlowski, J.G. Crespo, A. Cipollina, Modelling selective lithium recovery from brines via membrane flow electrode capacitive de-ionization, Sep. Purif. Technol. 364 (2025) 132400. https://doi.org/10.1016/j.seppur.2025.132400.

[164] S. Pawlowski, P. Sistat, J.G. Crespo, S. Velizarov, Mass transfer in reverse electrodialysis: Flow entrance effects and diffusion boundary layer thickness, J. Memb. Sci. 471 (2014) 72–83. https://doi.org/10.1016/j.memsci.2014.07.075.

[165] E. Volodina, N. Pismenskaya, V. Nikonenko, C. Larchet, G. Pourcelly, Ion transfer across ion-exchange membranes with homogeneous and heterogeneous surfaces, J. Colloid Interface Sci. 285 (2005) 247–258. https://doi.org/10.1016/j.jcis.2004.11.017.

[166] A. Yaroshchuk, M.L. Bruening, E. Zholkovskiy, Modelling nanofiltration of electrolyte solutions, Adv. Colloid Interface Sci. 268 (2019) 39–63. https://doi.org/10.1016/j.cis.2019.03.004.

[167] H. Zhang, G.M. Geise, Modeling the water permeability and water/salt selectivity tradeoff in polymer membranes, J. Memb. Sci. 520 (2016) 790–800. https://doi.org/10.1016/j.memsci.2016.08.035.

[168] J. Crank, The mathematics of diffusion. 2nd Edn., (1979). https://doi.org/10.1088/0031-9112/26/11/044.

[169] B.I. Shklovskii, Screening of a macroion by multivalent ions: Correlation-induced inversion of charge, Phys. Rev. E - Stat. Physics, Plasmas, Fluids, Relat. Interdiscip. Top. 60 (1999) 5802–5811. https://doi.org/10.1103/PhysRevE.60.5802.

[170] T.T. Nguyen, B.I. Shklovskii, Adsorption of charged particles on an oppositely charged surface: Oscillating inversion of charge, Phys. Rev. E - Stat. Physics, Plasmas, Fluids, Relat. Interdiscip. Top. 64 (2001) 9. https://doi.org/10.1103/PhysRevE.64.041407.

[171] N. Marioni, Z. Zhang, E.S. Zofchak, H.S. Sachar, S. Kadulkar, B.D. Freeman, V. Ganesan, Impact of Ion-Ion Correlated Motion on Salt Transport in Solvated Ion Exchange Membranes, ACS Macro Lett. 11 (2022) 1258–1264. https://doi.org/10.1021/acsmacrolett.2c00361.

[172] D.G. Miller, J.A. Rard, L.B. Eppstein, J.G. Albright, Mutual diffusion coefficients and ionic transport coefficients lij of magnesium chloride-water at 25.degree.C, J. Phys. Chem. 88 (1984) 5739–5748. https://doi.org/10.1021/j150667a056.

[173] D.G. Miller, Application of Irreversible Thermodynamics to Electrolyte Solutions. I. Determination of Ionic Transport Coefficients l ij for Isothermal Vector Transport Processes in Binary Electrolyte Systems 1,2, J. Phys. Chem. 70 (1966) 2639–2659. https://doi.org/10.1021/j100880a033.

[174] G. Purpura, H. Muhamad, A. Culcasi, S. Pawlowski, Modelling selective lithium recovery from brines via membrane flow electrode capacitive de-ionization, 364 (2025). https://doi.org/10.1016/j.seppur.2025.132400.

[175] J. Si, C. Xue, S. Li, L. Yang, W. Li, J. Yang, J. Lan, N. Sun, Selective membrane capacitive deionization for superior lithium recovery, Desalination 572 (2023) 117154. https://doi.org/10.1016/j.desal.2023.117154.

[176] X. Guo, J. Zhang, Q. Tian, Modeling the potential impact of future lithium recycling on lithium demand in China: A dynamic SFA approach, Renew. Sustain. Energy Rev. 137 (2021) 110461. https://doi.org/10.1016/j.rser.2020.110461.

[177] A. Cipollina, D. Winter, G. Battaglia, L. Berkemeyer, J.L. Cortina, M.F. de Labastida, J.L. Rodriguez, Recovery of Lithium Carbonate from Dilute Li-Rich Brine via Homogenous and Heterogeneous Precipitation, Ind. Eng. Chem. Res. 61 (2022) 13589–13602. https://doi.org/10.1021/acs.iecr.2c01397.

[178] S. Randazzo, F. Vicari, J. López, M. Salem, R. Lo Brutto, S. Azzouz, S. Chamam, S. Cataldo,

N. Muratore, M. Fernández de Labastida, V. Vallès, A. Pettignano, G. D'Alì Staiti, S. Pawlowski, A. Hannachi, J.L. Cortina, A. Cipollina, Unlocking hidden mineral resources: Characterization and potential of bitterns as alternative sources of critical raw materials, J. Clean. Prod. 436 (2024). https://doi.org/10.1016/j.jclepro.2023.140412.

[179] Y. Guo, Y. Ying, Y. Mao, X. Peng, B. Chen, Polystyrene Sulfonate Threaded through a Metal–Organic Framework Membrane for Fast and Selective Lithium-Ion Separation, Angew. Chemie - Int. Ed. 55 (2016) 15120–15124. https://doi.org/10.1002/anie.201607329.

[180] J.G. Gamaethiralalage, K. Singh, S. Sahin, J. Yoon, M. Elimelech, M.E. Suss, P. Liang, P.M. Biesheuvel, R.L. Zornitta, L.C.P.M. De Smet, Recent advances in ion selectivity with capacitive deionization, Energy Environ. Sci. 14 (2021) 1095–1120. https://doi.org/10.1039/d0ee03145c.

[181] S. Il Jeon, H.R. Park, J.G. Yeo, S. Yang, C.H. Cho, M.H. Han, D.K. Kim, Desalination via a new membrane capacitive deionization process utilizing flow-electrodes, Energy Environ. Sci. 6 (2013) 1471–1475. https://doi.org/10.1039/c3ee24443a.

[182] A. Rommerskirchen, B. Ohs, K.A. Hepp, R. Femmer, M. Wessling, Modeling continuous flow-electrode capacitive deionization processes with ion-exchange membranes, J. Memb. Sci. 546 (2018) 188–196. https://doi.org/10.1016/j.memsci.2017.10.026.

[183] L. Wang, C. Zhang, C. He, T.D. Waite, S. Lin, Equivalent film-electrode model for flow-electrode capacitive deionization: Experimental validation and performance analysis, Water Res. 181 (2020) 115917. https://doi.org/10.1016/j.watres.2020.115917.

[184] J. Ma, C. Zhang, F. Yang, X. Zhang, M.E. Suss, X. Huang, P. Liang, Carbon Black Flow Electrode Enhanced Electrochemical Desalination Using Single-Cycle Operation, Environ. Sci. Technol. 54 (2020) 1177–1185. https://doi.org/10.1021/acs.est.9b04823.

[185] F. Yang, Y. He, L. Rosentsvit, M.E. Suss, X. Zhang, T. Gao, P. Liang, Flow-electrode

capacitive deionization: A review and new perspectives, Water Res. 200 (2021) 117222. https://doi.org/10.1016/j.watres.2021.117222.

[186] C. Zhang, J. Ma, L. Wu, J. Sun, L. Wang, T. Li, T.D. Waite, Flow Electrode Capacitive Deionization (FCDI): Recent Developments, Environmental Applications, and Future Perspectives, Environ. Sci. Technol. 55 (2021) 4243–4267. https://doi.org/10.1021/acs.est.0c06552.

[187] H.M. Saif, T.H. Gebregeorgis, J.G. Crespo, S. Pawlowski, The influence of flow electrode channel design on flow capacitive deionization performance: Experimental and CFD modelling insights, Desalination 578 (2024) 117452. https://doi.org/10.1016/j.desal.2024.117452.

[188] H.M. Saif, J.G. Crespo, S. Pawlowski, Lithium recovery from brines by lithium membrane flow capacitive deionization (Li-MFCDI) – A proof of concept, J. Membr. Sci. Lett. 3 (2023) 100059. https://doi.org/10.1016/j.memlet.2023.100059.

[189] A. Culcasi, L. Gurreri, A. Zaffora, A. Cosenza, A. Tamburini, G. Micale, On the modelling of an Acid/Base Flow Battery: An innovative electrical energy storage device based on pH and salinity gradients, Appl. Energy 277 (2020) 115576. https://doi.org/10.1016/j.apenergy.2020.115576.

[190] Fumatech, f u m a s e p ® F A B - P K - 1 3 0, (2018) 24–25. http://www.fuelcellstore.com/spec-sheets/fumasep-fab-pk-130-technical-specifications.pdf.

[191] M.J. Rice, W.L. Roth, Ionic transport in super ionic conductors: a theoretical model, J. Solid State Chem. 4 (1972) 294–310. https://doi.org/10.1016/0022-4596(72)90121-1.

[192] O.L. ANDERSON, D.A. STUART, Calculation of Activation Energy of Ionic Conductivity in Silica Glasses by Classical Methods, J. Am. Ceram. Soc. 37 (1954) 573–580. https://doi.org/10.1111/j.1151-2916.1954.tb13991.x.

[193] H. Strathmann, Ion-Exchange membrane separation processes, First, Elsevier B.V., 2004.

[194] D. Ding, L. Yang, J. Wang, A. Yaroshchuk, J.L. Schaefer, M.L. Bruening, Selective transport of trivalent lanthanide in electrodialysis: Limitations due to concentration polarization, J. Memb. Sci. 685 (2023) 121949. https://doi.org/10.1016/j.memsci.2023.121949.

[195] R. De Levie, The influence of surface roughness of solid electrodes on electrochemical measurements, Electrochim. Acta 10 (1965) 113–130. https://doi.org/10.1016/0013-4686(65)87012-8.

[196] S. Fletcher, V.J. Black, I. Kirkpatrick, A universal equivalent circuit for carbon-based supercapacitors, J. Solid State Electrochem. 18 (2014) 1377–1387. https://doi.org/10.1007/s10008-013-2328-4.

[197] A.K.E. Rommerskirchen, Continuous Flow-Electrode Capacitive Deionization, Aachener Verfahrenstechnik Ser. AVT.CVT – Chem. Process Eng. 12 (2021). https://doi.org/10.18154/RWTH-2021-02093.

[198] S. Porada, D. Weingarth, H.V.M. Hamelers, M. Bryjak, V. Presser, P.M. Biesheuvel, Carbon flow electrodes for continuous operation of capacitive deionization and capacitive mixing energy generation, J. Mater. Chem. A 2 (2014) 9313–9321. https://doi.org/10.1039/c4ta01783h.

[199] R.B. McCleskey, D.K. Nordstrom, J.N. Ryan, J.W. Ball, A new method of calculating electrical conductivity with applications to natural waters, Geochim. Cosmochim. Acta 77 (2012) 369–382. https://doi.org/10.1016/j.gca.2011.10.031.

[200] X.Y. Nie, S.Y. Sun, Z. Sun, X. Song, J.G. Yu, Ion-fractionation of lithium ions from magnesium ions by electrodialysis using monovalent selective ion-exchange membranes, Desalination 403 (2017) 128–135. https://doi.org/10.1016/j.desal.2016.05.010.

[201] A. Filingeri, M. Philibert, E. Filloux, N. Moe, A. Poli, A. Tamburini, A. Cipollina, Valorization

of surface-water RO brines via Assisted-Reverse Electrodialysis for minerals recovery: Performance analysis and scale-up perspectives, Desalination 541 (2022) 116036. https://doi.org/10.1016/j.desal.2022.116036.

[202] C. Shi, H. Wang, A. Li, G. Zhu, X. Zhao, F. Wu, Process model for flow-electrode capacitive deionization for energy consumption estimation and system optimization, Water Res. 230 (2023). https://doi.org/10.1016/j.watres.2022.119517.

[203] D.Y. Butylskii, V.A. Troitskiy, N. V. Smirnova, N.D. Pismenskaya, Y. Wang, C. Jiang, T. Xu, V. V. Nikonenko, Review of recent progress on lithium recovery and recycling from primary and secondary sources with membrane-based technologies, Desalination 586 (2024). https://doi.org/10.1016/j.desal.2024.117826.

[204] H.J. Cassady, E.C. Cimino, M. Kumar, M.A. Hickner, Specific ion effects on the permselectivity of sulfonated poly(ether sulfone) cation exchange membranes, J. Memb. Sci. 508 (2016) 146–152. https://doi.org/10.1016/j.memsci.2016.02.048.

[205] K. Zhang, J. Sun, L. E, C. Ma, S. Luo, Z. Wu, W. Li, S. Liu, Effects of the Pore Structure of Commercial Activated Carbon on the Electrochemical Performance of Supercapacitors, J. Energy Storage 45 (2022) 103457. https://doi.org/10.1016/j.est.2021.103457.

[206] N. Ganfoud, A. Sene, M. Haefele, A. Marin-Laflèche, B. Daffos, P.L. Taberna, M. Salanne, P. Simon, B. Rotenberg, Effect of the carbon microporous structure on the capacitance of aqueous supercapacitors, Energy Storage Mater. 21 (2019) 190–195. https://doi.org/10.1016/j.ensm.2019.05.047.

[207] H. Wu, M. Genovese, K. Ton, K. Lian, A Comparative Study of Activated Carbons from Liquid to Solid Polymer Electrolytes for Electrochemical Capacitors, J. Electrochem. Soc. 166 (2019) A821–A828. https://doi.org/10.1149/2.0141906jes.

[208] Kuraray Coal Tm, (2019) 2019. https://www.calgoncarbon.com/app/uploads/YP-brochure-

draft_final_08_2019.pdf.

[209] Fuzhou Yihuan Carbon, (2024). http://www.yhcarbon.com/index.php?m=home&c=View&a=index&aid=89 (accessed April 19, 2024).

[210] B. Fang, Hierarchical Nanostructured Carbon Materials for Ultrahigh Electrical Charge Storage, ECS Meet. Abstr. MA2013-02 (2013) 655–655. https://doi.org/10.1149/MA2013-02/9/655.

[211] Lerochem - Chemical supply, No Title, (2019). https://lerochem.eu/en/pagrindinis/336-1136-activated-carbon-farm-grade-kg.html (accessed April 28, 2024).

[212] G. Battaglia, L. Ventimiglia, F.P.M. Viggiano, F. Vassallo, A. Cipollina, A. Tamburini, G. Micale, Mg(OH)2 Recovery from Real Bitterns: a Proof of Concept at Pilot Scale, Chem. Eng. Trans. 105 (2023) 1–6. https://doi.org/10.3303/CET23105001.

[213] A.K. Covington, The principles of ion-selective electrodes and of membrane transport. Studies in analytical chemistry 2, Electrochim. Acta 29 (1984) 283. https://doi.org/10.1016/0013-4686(84)87061-9.